ORNL/HTSPC-17

ORNL Superconducting Technology Program for Electric Power Systems

Annual Report for FY 2005

SUPERCONDUCTIVITY FOR ELECTRIC SYSTEMS

ORNL/HTSPC-17

ORNL SUPERCONDUCTING TECHNOLOGY PROGRAM FOR ELECTRIC POWER SYSTEMS

ANNUAL REPORT FOR FY 2005

Compiled by
R. A. Hawsey
D. F. Lee
A. W. Murphy

Edited by
W. S. Koncinski
D. M. Kroeger

Manuscript Completed: April 2006
Date Published: May 2006

Prepared for the
Office of Electricity Delivery and Energy Reliability
U.S. DEPARTMENT OF ENERGY
(TD 5001)

Prepared by the
OAK RIDGE NATIONAL LABORATORY
P. O. Box 2008
Oak Ridge, Tennessee 37831-6283
Managed by
UT-Battelle, LLC
for the
U. S. DEPARTMENT OF ENERGY
Under contract DE-AC05-00OR22725

Contributors

Left to right: M. Reeves, L. Heatherly, Jr., D. F. Lee, F. A. List, M. P. Paranthaman, D. R. James, M. J. Gouge, A. Goyal, I. Sauers, E. D. Specht, E. Tuncer, P. M. Martin, R. Feenstra, R. C. Duckworth, A. R. Ellis, S. Kang, J. Li, H. M. Christen, C. M. Rey, B. Demps, T. Aytug, D. K. Christen, S-H. Wee, J. A. Demko, S. W. Schwenterly, S. Sathyamurthy, Y. Zhang, D. M. Kroeger, and R. A. Hawsey

Not shown: D. B. Beach, S. Bhuiyan, C. Cantoni, S. W. Cook, K. Kim, B. W. McConnell, A. W. Murphy, and J. R. Thompson

Contents

Contributors iii

List of Figures vii

List of Tables xiii

Abbreviated Terms xv

Executive Summary xix

1. Technical Progress in Applications Development 1-1

1.1 Ultera/ORNL HTS Cable SPI 1-1

1.2 SuperPower Matrix Fault Current Limiter CRADA 1-6

1.3 Waukesha Electric Systems (WES) HTS Transformer SPI 1-10

1.4 General Electric Co. HTS Generator SPI 1-11

1.5 Second-Generation Conductor Applications 1-13

1.6 Cryogenic Dielectrics Initiative 1-21

1.7 HTS Motor R&D with Reliance Electric 1-21

1.8 SPI Oversight/Readiness Reviews 1-22

1.9 Applied Superconductivity Group Laboratories Move from Y-12 to ORNL 1-23

2. Technical Progress in Wire Development 2-1

2.1 Superconductor Wires 2-1

2.2 Irradiation-Free Columnar Defects Composed of Self-Assembled Nanodots and Nanorods Result in Strongly Enhanced Flux Pinning in YBCO Films 2-5

2.3 Controllable Angular Dependence of Critical Current Density in ex situ YBCO Coated Conductors 2-11

2.4 Temperature and Magnetic Field Dependence of Critical Currents in YBCO Coated Conductors with Processing-Induced Variations in Pinning Properties 2-13

2.5 Deposition of $(Y_2BaCuO_5/YBa_2Cu_3O_{7-x})xN$ Multilayer Films on Ni-Based Textured Substrates 2-18

2.6 Reel-to-Reel Low-Pressure ex situ Conversion of BaF_2 Precursor 2-23

2.7 Conversion of ex situ YBCO Superconductor on RABiTS™ on a Novel Precursor Deposited by a Pulsed Electron Beam 2-27

2.8 Limits of the Pulsed Electron Deposition Approach for YBCO Precursors 2-31

2.9	Long-Range Current Flow and Percolation in RABiTS™-Type Conductors and the Relative Importance of Out-of-Plane and In-Plane Misorientations in Determining Critical Current Density	2-36
2.10	Development of Nonmagnetic, Cr-Containing Substrates and Development of Appropriate Buffer Layers	2-42
2.11	Assessment of Chemical Solution Synthesis and Properties of $Gd_2Zr_2O_7$ Thin Films as Buffer Layers for Second-Generation HTS Wires	2-44
2.12	Iridium: An Oxygen Diffusion Barrier and a Conductive Seed Layer for RABiTS™-Based Coated Conductors	2-51
2.13	All MOD buffer/YBCO Approach to Coated Conductors	2-54
2.14	Solution-Processed Lanthanum Zirconium Oxide as a Barrier Layer for High-I_c Coated Conductors	2-58
2.15	Reverse Micellar Synthesis of Cerium Oxide Nanoparticles	2-62
2.16	Characterization of $BaZrO_3$ Nanoparticles Prepared by Reverse Micelle Synthesis	2-67
2.17	Growth of Rare Earth Niobate Based Pyrochlores on Textured Ni-W Substrates with Ionic Radii Dependency	2-77
3.	Summary of Technology Partnership Activities	3-1
3.1	Background	3-1
3.2	Relationship to the DOE Mission	3-1
3.3	Funding	3-1
3.4	Technology Partnership Approach	3-1
3.5	Program Inventions	3-2
4.	Events, Honors, and Awards	4-1
4.1	Amit Goyal Edits Book on Second-Generation High-Temperature Superconductors	4-1
4.2	Team Members Elected Fellows	4-1
4.3	Joint US-Japan Workshop on AC Losses	4-2
4.4	International Energy Agency Committee on Superconductivity	4-3
4.5	Three New CRADAs Signed During Quarter	4-3
4.6	Summer Interns in Superconductivity Program	4-4
4.7	Goyal Receives “Outstanding Young Tennessean (OYT)” Award	4-5
4.8	ORNL Scientists Co-organized and Led the 2005 DOE Superconducting Wire Development Workshop	4-5
5.	Presentations/Publications	5-1

List of Figures

Figure		*Page*
1.1	Measured voltages across the phase 1 main conductor of the 30-m HTS cable.	1-1
1.2	Three-phase termination housings.	1-2
1.3	Cross section of the manufactured three-phase cable.	1-2
1.4	Cable insertion into cryostat	1-2
1.5	Cable in the cryostat with a three-phase termination housing.	1-2
1.6	Triaxial HTS cable and termination assembly bent 90 degrees.	1-3
1.7	Measured superconducting characteristics of the three phases in the triaxial HTS cable at currents up to 7000 A.	1-3
1.8	Measured inlet and outlet temperatures of the circulating liquid nitrogen with the application of 3 kA dc on all three phases	1-3
1.9	Response of the triaxial HTS cable to a dc overcurrent fault	1-4
1.10	Cable system inlet and outlet temperatures while carrying ac currents of 2500 A and 3000 A.	1-4
1.11	High-voltage testing of phase 1 to 110 kV	1-4
1.12	T-section of half-scale model termination instrumented with temperature sensors for partial discharge and voltage withstand tests in liquid nitrogen.	1-5
1.13	Full-scale prototype termination housing	1-5
1.14	G-10 testing	1-7
1.15	Effect of pressure on breakdown voltage in liquid nitrogen in a nonuniform gap	1-7
1.16	Alvin Ellis (ORNL) applies a safety ground to upper stages of the upgraded impulse generator	1-8
1.17	Heat capacity sample installation.	1-9
1.18	Heat capacity (C_p) of bulk Bi-2212 vs temperature	1-10
1.19	Thermal shield in relation to silver-plated copper sample for the emissivity test setup.	1-11
1.20	Emissivity vs time for a silver-plated copper sample with an emissivity of 0.01 at 30 K	1-11
1.21	Comparison of water degradation of emissivity for silver-plated copper samples with different room-temperature emissivities.	1-12
1.22	Quench test coil.	1-12
1.23	Sketch of cross configuration used to test voltage breakdown between a pair of YBCO coated conductors.	1-13
1.24	High-voltage breakdown test setup for YBCO tapes	1-13
1.25	Weibull plot of likelihood of voltage breakdown at room temperature for as-slit and copper-surround-stabilized samples.	1-14

1.26 Liquid nitrogen test setup for stability determination of HTS samples. 1-15

1.27 Measured resistance per unit length for samples 1 and 2 as a function of temperature. 1-15

1.28 Estimated resistance per unit length for samples 1 and 2 as a function of temperature, assuming a 100-μm Hastelloy substrate 1-16

1.29 Profiles of the total sample current and measured resistance unit length vs time for sample 1 under two separate 0.5-s dc current pulses 1-16

1.30 Profiles of the total sample current and estimated average sample temperature vs time for sample 1 under two separate 0.5-s dc current pulses 1-16

1.31 Degradation of sample 1 before and after the 247.4-A, 0.5-s current pulse 1-16

1.32 AC losses in a YBCO tape sample with a critical current at 77 K of 75 A..... 1-17

1.33 Single monolithic YBCO coil. 1-18

1.34 DC V-I curve in LN at 77 K..... 1-19

1.35 A rotor field coil from the 1000-hp motor that was damaged from a quench event. 1-22

1.36 Applied Superconductivity Laboratory. 1-23

2.1 Schematics of HTS wires 2-2

2.2 Cross-section TEM of a YBCO film on RABiTS™ with self-assembled BZO nanodots and nanorods 2-7

2.3 Plan-view TEM images of the YBCO film on RABiTS™ with self-assembled BZO nanodots and nanorods 2-8

2.4 Superconducting transport properties of YBCO films on RABiTS™ 2-8

2.5 Superconducting transport properties of YBCO films on RABiTS™ 2-9

2.6 Superconducting transport properties of YBCO films on RABiTS™ 2-9

2.7 Cross-section TEM images for YBCO films on RABiTS™. 2-10

2.8 Dependence of the normalized ratio of critical current density in applied fields H of 1 T to the self-field critical current density at 77 K on the orientation of the field in ex situ YBCO films on RABiTS™..... 2-13

2.9 An opposite effect on the ratio $J_c(ab)/J_c(c)$ resulting from an alternative processing modification 2-13

2.10 (a) Field dependence of critical current density at temperatures shown for films with and without self-doping. 2-14

2.11 The angular dependence of critical current density at 77 K for nondoped films produced by slow (standard) processing compared with that for films produced by fast processing..... 2-15

2.12 Improved isotropy with respect to field orientation as a result of excess Y. 2-16

2.13 Increased orientational isotropy for thicker self-doped film 2-17

2.14 Semi-log plot showing universal temperature dependence of the ratio of critical current density at self-field, 77 K, and at the field typical of motor applications for samples with widely different pinning mechanisms, irreversibility fields, and self-field critical current densities. 2-17

2.15 SEM micrographs of YBCO-only films deposited on ORNL RABiTS™ 2-19

2.16 SEM micrographs of a (211~1.0nm/123~10.0nm)x25 multilayer films deposited on ORNL RABiTS™ 2-20

2.17 High-magnification SEM micrographs of different grains and grain boundaries of a (211~1.0nm/123~10nm)x26 film deposited on AMSC RABiTS™ substrate 2-20

2.18 Transport critical current density (a) at 77 K for multilayer films compared to 123 reference films deposited at the Air Force Research Laboratory and ORNL 2-22

2.19 The low-pressure reel-to-reel conversion system 2-24

2.20 Variation in BaF_2(111) intensity with conversion time at different P(H_2O) in the low-pressure reel-to-reel system. 2-24

2.21 Variations in conversion rate with P(H_2O) for the reel-to-reel and stationary low-pressure systems. 2-25

2.22 Variations in *c*-axis(005) and random (103)/(013) intensities of 1-μm YBCO with ramp-up rate. 2-25

2.23 Variations in XRD intensities and sectional critical currents of a 5.5 cm-wide sample processed in the low-pressure reel-to-reel system. 2-26

2.24 θ-2θ XRD pattern of a 1.2-μm-thick PED precursor converted under nonaggressive conditions 2-29

2.25 Magnetic dependence of J_c of a 0.72 μm-thick PED-derived YBCO film for both B//*a*-*b* and B//*c* directions at 77 K. 2-29

2.26 Cross-sectional TEM image of a quenched PED precursor after a 2-min conversion 2-30

2.27 Variation in in situ EDX diffraction intensity of the YBCO (002) peak of a ~1.4 μm PED precursor (~1 μm YBCO) converted at high rate in the low-pressure system with time. 2-31

2.28 Conversion of different types of precursors on two different CeO_2/YSZ/CeO_2 buffer stacks 2-32

2.29 Sample architectures used to study the effect of interface damage that may occur during the PED process 2-33

2.30 Cross-sectional TEM images of the converted YBCO on buffer B 2-34

2.31 Lower-magnification cross-sectional TEM image of the sample after conversion 2-34

2.32 RABiTS™ grain structure 2-37

2.33 Critical current density of YBCO/RABiTS™ vs the number of grains along the length of the conductor as a function of number of grains along the width of the conductor 2-37

2.34 Critical current density vs location for a meter-long YBCO/RABiTS™ conductor only 100 grains wide 2-38

2.35 FWHMs of the TiN (002) rocking curves vs corresponding FWHMs of the (002) substrate rocking curve for TiN films on different textured substrates 2-39

2.36 EBKP maps showing grain boundaries larger than 3° for (a) a biaxially textured Cu substrate and (b) the same material with a TiN seed layer 2-40

2.37 Log-scale (111) pole figure of a rolled and annealed Ni-13at%Cr substrate showing very good texture development. 2-42

2.38 Multilayer stack corresponding to Case 2. 2-43

2.39 Cross-section TEM image of the Ni-Cr-W/TiN/MgO/LMO/CeO2/YBCO stack after the YBCO deposition, annealing, and measurement of transport properties 2-43

2.40 (111) pole figure of substrate after deposition of a 1-μm-thick Ni-9at%W coating. 2-44

2.41 Dependence of the normalized XRD FWHM peak widths on processing temperatures, quantifying the crystallinity of sol-gel $Gd_2Zr_2O_3$ films 2-46

2.42 XRD pole figures for $Gd_2Zr_2O_7$ layers on pure Ni substrates, plotted on a logarithmic scale, for processing at various temperatures 2-46

2.43 Pole figure cube-texture percentages as determined by the quantitative analysis of the pole intensities for the samples processed at various temperatures. 2-46

2.44 XRD θ-2θ spectra of one to three coats of GZO layers on textured Ni-W substrates, showing a monotonic increase in the (004) intensity with the number of coats. 2-47

2.45 Surface microstructure of a single-coat GZO film 2-48

2.46 MOD processed $Gd_2Zr_2O_7$ films on Ni-W substrates 2-48

2.47 The interface between $Gd_2Zr_2O_7$ and Ni-W 2-48

2.48 SIMS depth profile of the three-coat MOD processed GZO/Ni-W sample, showing major element distributions throughout the sample 2-49

2.49 Current-voltage curve of a YBCO/CeO2/ YSZ/GZO/Ni/Ni-W sample 2-50

2.50 Magnetic field dependence of critical current density, measured at 77 K, for two YBCO films deposited by PLD 2-50

2.51 XRD θ-2θ patterns of Ir films grown on biaxially textured Ni-W substrates before and after anneals under simulated YBCO conditions. 2-52

2.52 Net resistivity of Ir coated substrates as a function of temperature before and after simulated YBCO annealing 2-52

2.53 Plan view SEM images for the Ir layers (a) before and (b) after YBCO post-anneals. 2-53

2.54 The XRD θ-2θ patterns of YBCO films on LSMO/Ir/Ni-W architecture 2-54

2.55 Magnetic field dependence of transport J_c at 77 K for a 0.2-μm-thick YBCO film on LSMO/Ir/Ni-W 2-54

2.56 A typical θ-2θ scan for a 100-nm-thick (one coat) and 200-nm-thick (two coats) $La_2Zr_2O_7$ film grown on 10-nm-thick Y_2O_3 buffered Ni-5W substrates by MOD 2-55

2.57 The ω and ϕ scans for a 200-nm-thick $La_2Zr_2O_7$ film grown on a 10-nm-thick Y_2O_3 buffered Ni-5W substrate using metal-organic deposition 2-56

2.58 (222) pole figure for a 200-nm-thick $La_2Zr_2O_7$ film grown on a 10-nm-thick Y_2O_3 buffered Ni-5W substrate using metal-organic deposition. 2-56

2.59 Typical θ-2θ scan for a 0.8-μm-thick YBCO film grown on MOD-CeO_2/MOD-$La_2Zr_2O_7/Y_2O_3$/Ni-5W substrate using metal-organic deposition 2-56

2.60 The field dependence of critical current for a 0.8-μm-thick YBCO film grown on MOD-CeO2/MOD-$La_2Zr_2O_7/Y_2O_3$/Ni-5W substrate using metal-organic deposition 2-57

2.61 XRD patterns from multiple-coat LZO/Ni-W samples in thickness increments of 40 to 50 nm per coat, showing proportional increase in LZO (400) peak intensity with thickness. 2-59

2.62 Texture map of a 4-cm-wide LZO/NiW sample coated by dip-coating 2-59

2.63 Area under the NiO (111) peak plotted as a function of annealing time in simulated YBCO ex situ annealing experiments 2-60

2.64 SIMS depth profile of CeO_2/LZO/Ni-W samples after high-temperature annealing in O^{18} for 15 min. 2-60

2.65 All-solution coated conductor with an architecture MOD-YBCO/MOD-CeO_2/ Sol-gel LZO/Ni-W showing a self-field critical current of 140 A/cm at 77 K for a 0.8-μm YBCO film. 2-60

2.66 Critical current vs field for MOD-YBCO/Sputt. CeO_2/LZO/Y_2O_3/Ni-W showing a self-field critical current of 255 A/cm and MOD-YBCO/MOD-CeO_2/ LZO/Y_2O_3/Ni-W showing a self-field critical current of 200 A/cm. 2-62

2.67 Comparative XRD patterns of MOD-YBCO on RF-sputtered CeO_2 and MOD-CeO_2 cap layers. 2-62

2.68 Schematic illustration of nanoparticle synthesis using water-in-oil inverse microemulsions 2-63

2.69 XRD pattern of as-processed CeO_2 nanoparticles 2-64

2.70 Electron diffraction pattern of CeO_2 nanoparticles. 2-64

2.71 High-magnification image of CeO_2 particle agglomeration showing a lattice image of [110] oriented particle 2-65

2.72 (a) UV-visible absorption spectrum of CeO_2 nanoparticles. 2-66

2.73 Photoluminescence spectra of CeO_2 nanoparticle dispersions in methanol (λ_{ex} = 290 nm). 2-66

2.74 Comparison of XRD scans for the as-processed and 700°C heat-treated samples showing the development of $BaZrO_3$ (BZO) 2-70

2.75 TEM micrographs of the as-processed Ba-Zr-O sample 2-71

2.76 EDS spectra 2-72

2.77 TEM micrographs of nanoparticles following heat treatment at 700ºC for 0.5 h in air 2-72

2.78 Nanoparticle size distribution histograms after a 700ºC, 0.5-h exposure in air for measured diameters of $BaZrO_3$ plus ZrO_2 particles from bright-field TEM images and of ZrO_2 particles measured from dark-field images. 2-73

2.79 (a) HREM image of $BaZrO_3$ particle 2-74

2.80 (a) HREM image of a ZrO_2 particle aligned with its [010] parallel to the beam 2-74

2.81 $BaZrO_3$ perovskite structure 2-74

2.82 Schematic views of the ideally cleaved (110) oxygen terminated surface of $BaZrO_3$ 2-75

2.83 Schematic views of the ideally cleaved (111) BaO_3^{4-} terminated surface of the $BaZrO_3$ crystal 2-75

2.84 Schematic of a pyrochlore structure (one-eighth of unit cell). 2-77

2.85 A typical θ-2θ scan for RE_3NbO_7 (RE = Sm, Eu, Gd, Ho, Y, and Yb) films grown on biaxially textured Ni-W substrates using chemical solution deposition 2-80

2.86 Lattice parameters of the solution-grown RE_3NbO_7 films on Ni-W substrates 2-80

2.87 The ω and ϕ scans obtained for a 80-nm-thick Eu_3NbO_7 film grown on textured Ni-W substrate 2-80

2.88 Typical (222) log scale pole figures 2-81

2.89 80-nm-thick Eu_3NbO_7 film surface 2-81

4.1 *Second-Generation High-Temperature Superconductors*, published in FY 2005, is the first book in the field. 4-1

4.2 Amit Goyal and Parans Paranthaman. 4-1

4.3 Attendees to US-Japan Workshop on AC Losses. 4-2

4.4 Front row (l–r): O. Tsukamoto (Japan), J. F. Daley (United States), P. Komarek (Germany), R. Flukiger (Switzerland), and M. Hoshino (IEA-Paris). 4-3

4.5 CRADA partner Metal Oxide Technologies, Inc. (Houston, Texas) visited ORNL's Metals and Ceramics Division to evaluate using a unique rolling mill facility for preparation of RABiTS™ templates. 4-3

4.6 Namita Bisaria, Princeton University. 4-4

4.7. Kartik Venkataraman, University of Wisconsin-Madison. 4-4

4.8 Bethany Musgrave (North Carolina A&T University) with Dave Christen and Tolga Aytug. 4-4

4.9. Brandon Killian (North Carolina A&T University) with Mehmet Ertugrul (Ataturk University) and Ron Feenstra. 4-4

4.10. David Gettman, California State University. 4-5

4.11. Jennifer Carney, University of Tennessee, with Mike Gouge and Robert Duckworth. 4-5

List of Tables

Table		*Page*
1.1	Critical current and n-values	1-3
1.2	Requirements for a 15-kV glass dielectric termination	1-4
1.3	Voltage breakdown data taken for copper-surround-stabilized and as-slit YBCO tapes	1-14
1.4	Summary of sample performance before and after degradation current and associated peak temperature, measured by the thermometry and estimated from the sample resistance	1-17
2.1	Status of the 2G HTS wire technology as of July 2005	2-3
2.2	Specifications for 2G HTS wires to be developed for power applications by 2010	2-4
2.3	Critical current per centimeter width of 1-μm YBCO converted under various conditions	2-25
2.4	Characteristics of YBCO films of various thicknesses converted from PED precursors	2-29
2.5	In-plane and out-of-plane textures of the YBCO layers.	2-40
2.6	Texture data for the Case 3 sample	2-44
2.7	Effect of Y_2O_3 seed layer on LZO epitaxy.	2-61
2.8	Measured interplanar spacing (*d*) from selected area diffraction pattern of CeO_2 nanoparticles compared with reference values of different cerium oxide forms (Å)	2-65
2.9	Measured interplanar spacing (*d*) from selected area diffraction pattern showing a mixture of $BaZrO_3$ and ZrO_2 phases compared with values for $BaZrO_3$ and ZrO_2 from powder diffraction file numbers 6-0399 and 88-1007, respectively.	2-73
2.10	Starting chemicals, solvents, and molarities for the RE_3NbO_7 precursors	2-79
2.11	Texture data of RE niobate films on Ni-W substrates	2-81
2.12	List of lattice parameters for RE3NbO7	2-82
3.1	Superconductivity Program summary of cooperative agreements as of September 30, 2005	3-3
3.2	Invention disclosures during FY 2005	3-4
3.3	Patents issued in FY 2005	3-4
3.4	Cumulative listing of patents	3-5
4.1	2005 Summer Intern Program information	4-4

NOMENCLATURE

$\Delta\phi$	in-plane texture
$\Delta\omega$	out-of-plane texture
ρ	normal-state resistivity
σ	standard deviation
B_{irr}	irreversibility field
$c\ (2 \times 2)$	centered (2×2) superstructure
G_P	precursor growth rate
H	magnetic field
H_{max}	maximum magnetic field
I_c	critical current
I_p	peak current
I_{mp}	propagation current
I_{rms}	root mean square cable current
J_c	critical current density
J_c^{GB}	intergrain critical current density
J_c^{G}	intragrain critical current density
J_E	engineering critical current density
K_c	critical current per unit width of conductor
langmuir	10^{-6} Torr/s
ML	surface adsorbate atoms per surface substrate atoms
M_{sat}	saturation magnetization
Pa.s	pascal.second
P_{base}	base pressure
$P(CO_2)$	CO_2 partial pressure
P(CO)	CO partial pressure
$P(H_2O)$	water vapor partial pressure
$P(O_2)$	oxygen partial pressure
T	tesla
T_c	critical temperature/transition temperature
t	thickness
θ_{mis}	misorientation angle
C_p	heat capacity
P_{tot}	total pressure
R_a	root mean square roughness

ACRONYMS AND INITIALISMS

ac	alternating current
acac	acetylacetonate
AEA	Applied Energy Analysis
AEP	American Electric Power
AFM	atomic force microscopy
AFRL	Air Force Research Laboratory
AMSC	American Superconductor Corporation

ANL	Argonne National Laboratory
APS	Advanced Photon source
ASTM	American Society for Testing and Materials
BIL	basic impulse level
BSCCO	Bi-Sr-Ca-Cu-O
BZO	$BaZrO_3$
CCAS	Coalition for the Commercial Application of Superconductors
CCVD	combustion chemical vapor deposition
CEC	Cryogenic Engineering Conference
CEIDP	Conference on Electrical Insulation and Dielectric Phenomena
CRADA	cooperative research and development agreement
CSD	chemical solution deposition
CTAB	cetyl trimethyl ammonium bromide
CTFE	chlorotrifluoroethylene
CZO	$CaZrO_3$
dc	direct current
DMF	dimethyl formamide
DOE	U.S. Department of Energy
DOE-HQ	DOE Headquarters
DSM	diffraction space mapping
e-beam	electron beam
EBKP	electron backscattering Kikuchi pattern
EBSD	electron backscatter diffraction
EDS	energy-dispersive spectroscopy
EDX	energy-dispersive X-ray diffraction
fcc	face-centered cubic lattice
FFT	fast Fourier transform
FM	ferromagnetism
FRP	fiberglass-reinforced plastic
FWHM	full width at half maximum
GBMD	grain-boundary misorientation distribution
GE	General Electric
GE-CRD	General Electric Corporate R&D
GM	Gifford-McMahon
GZO	gadolinium zirconium oxide
HR-PLD	high-rate pulsed-laser deposition
HRTEM	high-resolution transmission electron microscope
HTS	high-temperature superconductivity/superconductor/superconducting
IBAD	ion-beam-assisted deposition
ICP-MS	inductively coupled plasma mass spectroscopy
IEEE	Institute of Electrical and Electronics Engineers, Inc.
ISD	inclined substrate deposition
ISTEC	International Superconductivity Technology Center
LANL	Los Alamos National Laboratory
LMO	$LaMnO_3$
LN	liquid nitrogen
LNO	$LaNiO_3$
LPE	liquid-phase epitaxy
LSMO	$La_{0.7}Sr_{0.3}MnO_3$
LTS	low-temperature superconductor

LZO	lanthanum zirconium oxide ($La_2Zr_2O_7$)
MCP	melt-cast processed
MFCL	matrix fault current limiter
MgO	magnesium oxide
MLI	multiple-layer insulation
MOCVD	metal-organic chemical vapor deposition
MOD	metal organic decomposition
MRCAT	Materials Research Collaborative Access Team
MRS	Materials Research Society
OIM	orientation image micrograph
OPIT	oxide powder-in-tube
ORNL	Oak Ridge National Laboratory
PD	partial discharge
PDIV	partial discharge inception voltage
PED	pulsed-electron deposition
PLD	pulsed-laser deposition
PSD	position-sensitive detector
PTFE	polytetrafluoroethylene
PVC	polyvinyl chloride
PVD	physical vapor deposition
R&D	research and development
RABiTS™	Rolling-Assisted Biaxially Textured Substrate
RBCO	rare-earth element + $Ba_2Cu_3O_x$
RBS	Rutherford backscattering spectroscopy/spectrum
RE	rare earth
rf	radio frequency
RHEED	reflection high-energy electron diffraction
rms	root mean square
SAD	select area diffraction
SAED	selected-area electron diffraction
SCE	standard calomel electrode
SD	standard deviation
SEM	scanning electron microscopy
SIMS	secondary ion mass spectrometer
SPI	Superconductivity Partnership with Industry
SQUID	superconductivity quantum interference device
SRO	$SrRuO_3$
STEM	scanning transmission electron micoscope
STO	$SrTiO_3$
TBAP	tetrabutylammonium perchlorate
TEM	transmission electron microscopy
TFA	trifluoroacetate
TMAP	trimethyl acetate salts and proponic acid
WES	Waukesha Electric Systems
XPS	X-ray photoelectron spectroscopy
XRD	X-ray diffraction
YBCO	yttrium barium copper oxide ($YBa_2Cu_3O_{7-d}$)
YNO	Y_3NbO_7
YSZ	yttria-stabilized zirconia
Z-STEM	Z-contrast scanning transmission electron microscopy

Executive Summary

This report presents the results of projects conducted at Oak Ridge National Laboratory (ORNL) and its industry and university partners working in the U.S. Department of Energy's (DOE's) Superconducting Technology Research Program for Electric Systems. Funded primarily by DOE's Office of Electricity Delivery and Energy Reliability, ORNL projects include research and development toward second-generation high-temperature superconducting (HTS) wires, the Superconductivity Partnerships with Industry (SPI), and strategic research in materials and process development. Many of the articles in this report are adapted from papers submitted for open-literature publications; presentations at the annual DOE Peer Review in August 2005; and presentations given at the Materials Research Society meetings, the American Ceramics Society meetings, and other conferences and workshops held during FY 2005.

Among the SPI projects included in this report is the HTS cable project with long-time partner Southwire Company. Progress is reported on the testing of a prototype 5-m-long, 3-kA triaxial cable. For this testing, all three phases of the cable are concentric with one another, and the outer shield layer can be made of nonsuperconducting metal such as copper. This design has the potential to revolutionize the development of distribution-voltage-level cables, as it is the most compact and uses half the superconducting wire used in competing technologies. Progresses on the SuperPower HTS matrix fault current limiter project, the Waukesha Electric Systems HTS transformer project, and the General Electric Company HTS generator project are also reported.

In the areas of second-generation HTS wire materials and process research, substantial progress has been achieved, as described in the many articles in this report. Significant flux-pinning enhancement has been achieved in short lab-scale samples with thick YBCO films. This improvement, achieved through nano-defect engineering using aligned nanorods, demonstrated that second-generation wires have the potential to satisfy the demanding performance requirements of most applications. Collaborative works with American Superconductor Corp. and the Wire Development Group in FY 2005 have also yielded essential insights in the means to control the angular dependence of critical current density in these second-generation HTS wires. This is of significance because the response of critical current to external magnetic fields may be tailored to specific applications. Important insights have also been obtained in the long-range percolative behavior of supercurrents in a textured material as well as in the relative influences of out-of-plane and in-plane textures. These studies are highly pertinent because they can reveal potential limitations and areas of opportunity for second-generation wires. In addition to critical-current performance research, high-voltage and ac-loss characterizations have also been conducted on second-generation wires. The results on high-voltage qualification showed that when a wire is surrounded by a copper subsidizer layer, the breakdown voltage is increased compared with the breakdown voltage of its as-slit counterpart. These and other results indicate that performance and properties of second-generation wires may be altered through conductor design and engineering.

1. Technical Progress in Applications Development

The Applied Superconductivity Group in the ORNL Fusion Energy Division continued to support five Superconductivity Partnership with Industry (SPI) projects via superconductivity pilot center agreements and cooperative research and development agreements (CRADAs) and conducted strategic research in the areas of advanced superconductor engineering and cryogenic dielectrics.

1.1 Ultera/ORNL HTS Cable SPI

J. A. Demko, R. C. Duckworth, A. R. Ellis, P. W. Fisher, M. J. Gouge, D. R. James, C. M. Rey, I. Sauers, and E. Tuncer

1.1.1 Southwire 30-m HTS Cable Critical Current Measurement

The Southwire Co. 30-m HTS cable system has been running since early 2000, providing three-phase power to Southwire manufacturing facilities in Carrollton, Georgia. As part of the operational data collected from this system, the dc critical current has been measured periodically to demonstrate the performance of the HTS tapes. The most recent measurement was made in late January 2005. The connections are made on the external bus and include a significant resistive component in the measurement. The results for the phase 1 main conductor are shown in Fig. 1.1. The results for the main conductor show a linear resistive relationship due to the copper bus work. As in the past measurements, the main HTS conductor continues to have a critical current greater than the rated maximum current of the dc power supply (3000 A).

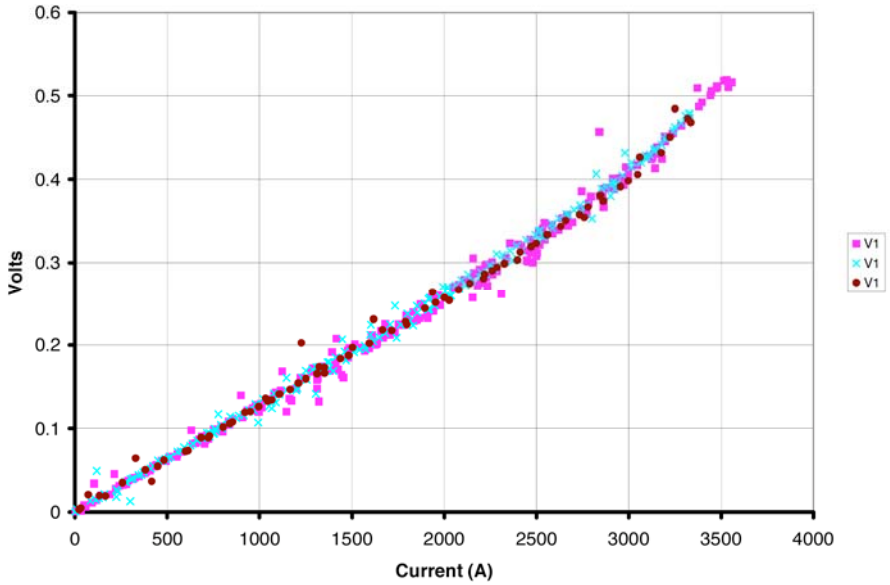

Fig. 1.1. Measured voltages across the phase 1 main conductor of the 30-m HTS cable.

1.1.2 Prototype 5-m, 3-kA HTS Cable Test at ORNL

Design of the triaxial cable terminations was completed at ORNL in late 2004. All parts were then manufactured by seven outside shops in Tennessee, Georgia, and Ohio. The 3-kA, 5-m triaxial cable manufactured by Ultera, a joint partnership between Southwire Company and NKT Cables, arrived at

ORNL from Europe in late January 2005. The major components of the triaxial cable terminations were delivered to ORNL in the first quarter of 2005. Figure 1.2 shows the pressurized termination housings. Figure 1.3 shows a cross section of the manufactured cable.

Fig. 1.2. Three-phase termination housings.

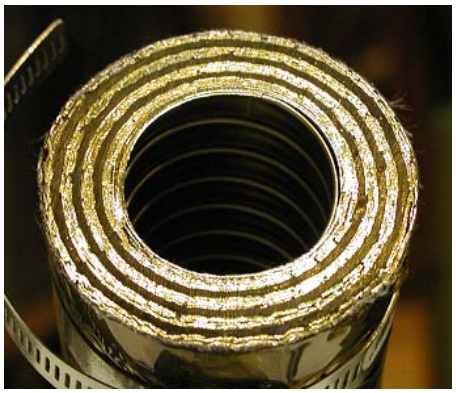

Fig. 1.3. Cross section of the manufactured three-phase cable.

Assembly of the cable and terminations started in February 2005 as fabricated components were delivered. Figure 1.4 shows the HTS cable being inserted into the cryostat provided by Nexans. There were some interferences between fabricated parts that required minor machining. They were resolved, and the termination housings were mounted to the cable cryostat (Fig. 1.5). The final assembly of the current leads, phase and shield bushings was completed in early April 2005.

Fig. 1.4. Cable insertion into cryostat.

Fig. 1.5. Cable in the cryostat with a three-phase termination housing.

The 5-m, 3-kA triaxial cable was assembled, and testing was conducted in the April–June 2005 quarter. Figure 1.6 shows the assembled triaxial cable bent 90 degrees with its associated terminations, which were designed and built by ORNL. The cable was tested in both straight and bent configurations.

Results of dc characterization of the three electrical phases are shown in Fig. 1.7. The measured temperature response to the application of a 3 kA dc current on all three phases is shown in Fig. 1.8. Table 1.1 shows the measured critical current and n-value for the three phases taken at an average cable temperature of 81.3 K. The subcooler was pumped to 0.48 bar (72 K) during the extended (13.7-h) test.

The triaxial HTS cable system was subjected to a series of dc overcurrent tests to simulate fault currents. The measured voltage response to a 0.7-s dc overcurrent of 10 kA on all three phases simultaneously is shown in Fig. 1.9. The innermost phase, with the lowest critical current, showed a slight

Fig. 1.6. Triaxial HTS cable and termination assembly bent 90°.

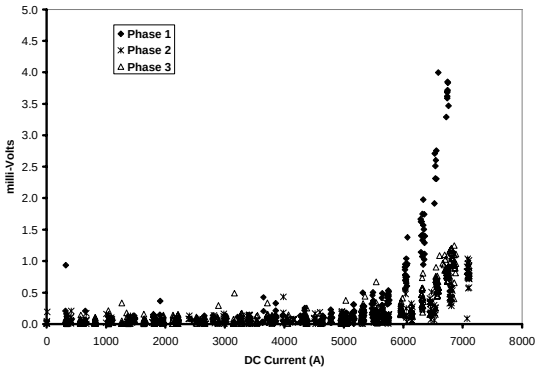

Fig. 1.7. Measured superconducting characteristics of the three phases in the triaxial HTS cable at currents up to 7000 A.

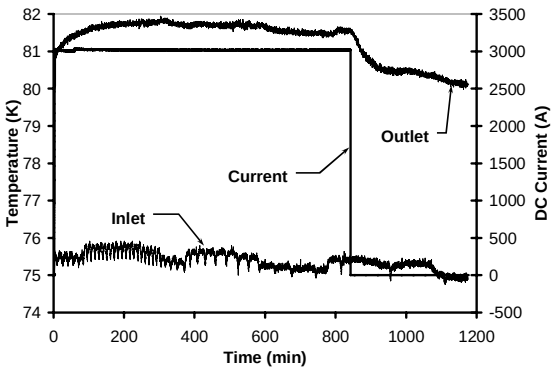

Fig. 1.8. Measured inlet and outlet temperatures of the circulating liquid nitrogen with the application of 3 kA dc on all three phases. The current was turned off at 820 min.

Table 1.1. Critical current and n-values

	Phase 1	Phase 2	Phase 3
Length (cm)	1058	881	716
Critical current (A)	6300	7100	6900
n-value	14.7	14.2	9.6

voltage increase during the pulse, indicating that the phase heated up during the pulse. Phases 2 and 3 showed a flat voltage response. At the end of the pulse, the current was dropped to 2 kA. No voltage was measured across the phases, demonstrating that the cable remained superconducting after the application of the overcurrent.

The cable was held at the 2500 A_{rms} for several hours and at the design ac current of 3000 A_{rms} for shorter periods. The inlet and outlet temperatures of the cable system are shown in Fig. 1.10. The inlet temperature was measured just prior to the entrance of the first termination, and the outlet temperature was measured after the second termination. Figure 1.10 shows the response of the cable system to the application of high currents to all three phases of the cable and terminations. The cable was also maintained at a dc current of 3500 A for three h in another experiment.

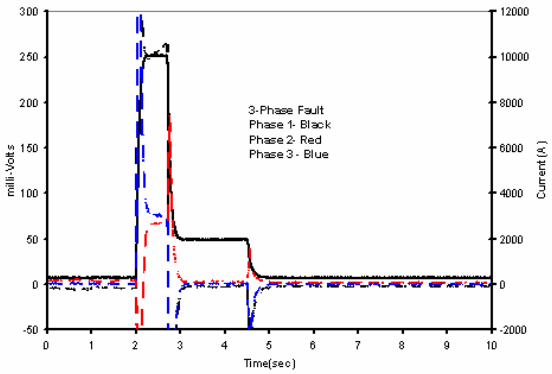

Fig. 1.9. Response of the triaxial HTS cable to a dc overcurrent fault.

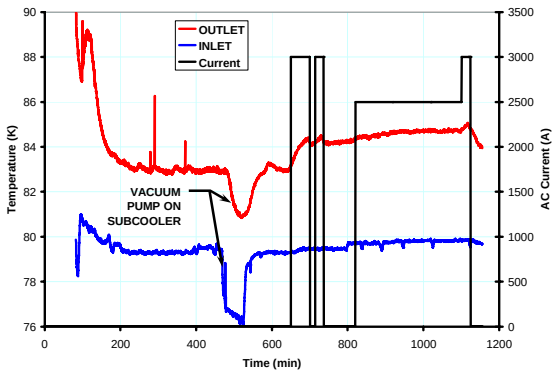

Fig. 1.10. Cable system inlet and outlet temperatures while carrying ac currents of 2500 A and 3000 A.

The cable also underwent extensive high-voltage testing [ac operating voltage, partial discharge (PD) measurements, ac withstand, lightning impulse]. High-voltage tests were successfully completed, and the superconducting cable and terminations met rigorous IEEE performance criteria. The measured wave form of a successful high-voltage impulse test on phase 1 is shown in Fig. 1.11.

A paper summarizing the results from the 3 kA, 5-m triaxial cable was presented at the 2005 Cryogenic Engineering Conference, in Keystone, Colorado. The successful tests support the 200-m HTS triaxial cable to be installed in 2006 at the American Electric Power Bixby substation in Columbus, Ohio.

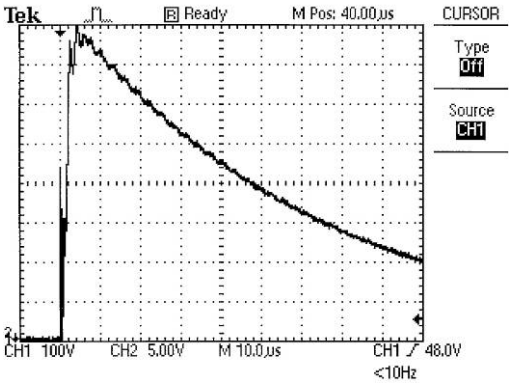

Fig. 1.11. High-voltage testing of phase 1 to 110 kV.

1.1.3 High-Voltage Termination Qualification

A three-phase termination design has been developed and modeled that meets the 3000-A_{rms}, 110-kV basic impulse level (BIL), and fault overcurrent requirements of the AEP Bixby project. Although there are not yet approved standards for HTS cables and terminations, the approach is to follow the existing standard for conventional terminations as a guide (IEEE Standard 48-1996: AC Current Cable Terminations 2.5–765 kV). See Table 1.2 for applicable requirements for 15-kV class dielectric cable terminations.

Table 1.2. Requirements for a 15-kV glass dielectric termination

1-min dry withstand	50 kV_{rms}
6-h dry withstand	35 kV_{rms}
10-s wet withstand[a]	45 kV_{rms}
PD extinction[b]	13 kV_{rms}
lightning impulse (BIL) dry	110 kV (10 ± 10 – polarity)

[a]For outdoor terminations.
[b]Raise to at least 1.2 × 13 kV = 15.6 kV; PD < 5 pC.

Dielectric tests on a half-scale, single-phase model of the cable termination (see Fig. 1.12) have been conducted in a cryostat in liquid nitrogen up to 6 bar pressure. The PD inception was found to increase with pressure, and at 6 bar the PD onset was well above the required phase-to-ground value of 7.6 kV_{rms}.

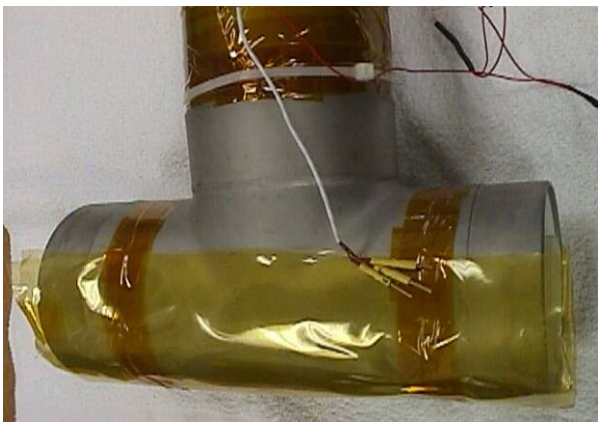

Fig. 1.12. T-section of half-scale model termination instrumented with temperature sensors for partial discharge and voltage withstand tests in liquid nitrogen.

Based on positive results for ac withstand and BIL testing for the half-scale dimensions, fabrication proceeded on the full-scale, single-phase model. The expectation is that going to full-scale where spacings and insulation thicknesses double, will further increase the PD onset and withstand values. However, the scaling in general for surfaces and nonuniform electric fields is not linear with gap separation. Fabrication of a full-scale, single-phase model of the termination was completed, and parts were assembled for testing. Due to the size of the components, the model could not be tested in the available cryostats or open-air dewars. Initial testing therefore has been done in ambient air at room temperature (Fig. 1.13). The system was also tested by sealing the ends with bags and pressurizing slightly (1 psig) with SF_6, which has approximately three times the dielectric strength of air. This provides an intermediate test condition between ambient air and pressurized liquid and gaseous nitrogen and therefore provides a means of testing samples at the equivalent of ~3 bar nitrogen gas. Also, if there is an improvement in PD inception when air is replaced with SF_6, then it is likely that the PD is occurring on an outer surface rather than in an internal void, providing an important diagnostic in identifying the source of PD. Testing in SF_6 at 1 psig indicated a PD onset of 19 to 20 kV_{rms} with a very low level of PD (6–12 pC), which exceeds the standard requirement. The PD extinction voltage is also 19 to 20 kV_{rms}. In addition, negative and positive impulse tests were performed in which the termination successfully withstood impulse voltages of about 115 kV at both polarities. The exterior of the termination bushing was tested in a wet test in which water was sprayed between each shed. The bushing survived 45 kV_{rms} ac for 10 s under the test conditions.

Fig. 1.13. Full-scale prototype termination housing.

1.1.4 Test of 1.25-m HTS Cable Made with Sumitomo Tapes

A nominal 1.25-m HTS cable fabricated by the Southwire Company was delivered to ORNL for cryogenic and electrical testing. The HTS cable was fabricated using Sumitomo Electric Industry HTS Bi-2223 powder-in-tube tape. The HTS cable consisted of forty-eight unlaminated Ag-alloyed Bi-2223 tapes, each tape having a nominal dimension of ~ 4.1 mm wide and 0.25 mm thick. A comprehensive series of tests were performed on the HTS cable to evaluate its performance under various operating and fault conditions:

- dc I-V testing,
- ac loss at 60 Hz (thermal method),
- ac loss at 60 Hz (electrical method), and
- overcurrent excitation.

Four separate thermal cycles were necessary to perform all testing on the cable. Transport critical current measurements were made on the HTS cable in an open liquid nitrogen bath. The transport critical

current measurements were made using a standard low-voltage four-wire technique with a stepped current pulse ramp of ~1-min duration. Using a 1-μV/cm electric field criterion with a voltage tap spacing of 1.35 m, the dc critical current values were 5991 A and 5986 A for the first and second pulses, respectively. The flux flow portion of the I-V curve was fit with a power law function. The measured n-values were 6.1 and 6.5 A for the first and second pulses, respectively. Experimental results of the electrical measurement of the ac loss indicate ~ 2 W/m dissipation at ac current values up to 3600 A_{rms} or a fraction of the dc critical current ($i = I_{op}/I_c$) of ~ 0.6. A series of 14 overcurrent pulses (up to 10.4 kA, 1-s duration) were performed on the HTS cable at 77 K to investigate cable performance and to verify cable reliability in overcurrent conditions. The cable dc critical current was not degraded after this series of overcurrent pulses.

A presentation was made at the 2005 DOE HTS Peer Review on ORNL's support to Ultera; the Ultera cable SPI project was ranked 2/9 in the systems area with a score of 86.5.

1.2 SuperPower Matrix Fault Current Limiter CRADA

S. W. Schwenterly, A. R. Ellis, D. R. James, and I. Sauers

1.2.1 Technical Advisory Board Meetings

ORNL personnel participated as a member of the Matrix Fault Current Limiter (MFCL) Technical Advisory Board at the program review meeting held at SuperPower's plant on November 17, 2004. At the meeting, SuperPower summarized successful proof-of-concept tests on the pre-prototype MFCL unit at KEMA. Other reports summarized progress on design of the 138-kV alpha unit, improvements by manufacturer Nexans to the HTS elements, and high-voltage insulation test results. Utility participant American Electric Power (AEP) summarized studies on specification and application of the commercial beta unit in their system. Another Technical Advisory Board meeting was conducted at SuperPower, Inc., on June 28, 2005, in conjunction with a DOE readiness review. Discussion focused on reliability/lifetime issues of the bulk BSCCO matrix elements and high-voltage R&D and design. There were increasing concerns in these areas as well as concerns about the slower pace of development with the high-voltage design effort and the significantly higher cost anticipated to complete the program. Consequently, the MFCL program has been placed in a "reduced effort" status by SuperPower, with a final decision on the future direction for the program to be made in 2006.

1.2.2 High-Voltage R&D

Experiments were conducted to systematically determine the ac breakdown voltage and the flashover length of fiberglass-reinforced plastic (FRP or G-10) for sphere-plane and rod-plane geometry in liquid nitrogen (LN). Tests were performed at different gap spacings and creepage lengths, providing data that will be used for scaling up to higher voltages. Dr. Kasegn Tekletsadik of SuperPower, Inc., visited the ORNL high-voltage laboratories in March 2005 to perform measurements in collaboration with ORNL staff. Measurements were made at 1 atm pressure in an open LN bath. The sphere diameters for the LN gaps were 0.5, 1, 1.5, and 2 in. with gaps from 1/16 to 5 in. Also studied was surface flashover of FRP (G-10) for sphere- and rod-to-plate on the surface immersed in LN. Flashover lengths were varied from 1 to 13 inches. The rod is a 2-in.-diam cylinder with the end squared off and a sharp edge. Surface flashover along the inside of a G-10 cylinder with sphere and rod were also performed. These nonuniform field geometries were used to simulate practical configurations and to obtain design data for real systems. The 1-atm pressure represents a worst-case condition, where bubbles may form and reduce breakdown strength. In an actual system, the pressure will be higher which will improve breakdown strength up to about 3 bar. Also, the open bath allows testing that would not be possible if a pressurized dewar was used; many measurements can be made in a relatively short time for many different conditions. The preliminary conclusion from this recent work is that for both LN gaps and surface flashover, the breakdown voltage does not increase significantly beyond a certain gap (i.e., there is a saturation effect with gap). We believe

that this is because, for a highly nonuniform electric field at large gaps, the electric field at or near the electrode surface does not decrease significantly as a function of gap. This has been calculated using electric field code software. It may imply that a critical field strength exists at the electrode such that when this value is exceeded, the discharge will initiate and self-propagate across the gap, much like lightning does in the atmosphere. The data are being analyzed to see if this supposition is valid. If so, then we may have a basis for a design rule that will allow, under certain conditions, scaling up to higher voltages; namely, the electric field would have to be kept below this critical field which can be calculated for specific designs (e.g., radii of conductors, gaps).

Figure 1.14(a) shows tracking observed on surface flashover of the G-10 plate from the high-voltage rod to the ground plate. The tracks occur from multiple breakdowns at different gaps. The tracks are similar to lightning discharges that occur in air and appear to be self-propagating. Figure 1.14(b) shows the test rig for surface flashover inside a G-10 tube to the ground plate. There are two G-10 alignment plates with holes to set the flashover gap for the plane G-10 flashover studies. The spacer at the bottom allows LN to enter the inside of the tube. Figure 1.14(c) show tracking along the G-10 spacer plate. These tracks occurred between the high-voltage lead and ground external to the actual test gap and show the treeing, self-propagating nature of the discharge as it seeks a path to ground. These tracks occur when the test gap in LN is very large. Some tracks are 12 in. or more in length and occurred at around 180 to 200 kV_{rms}.

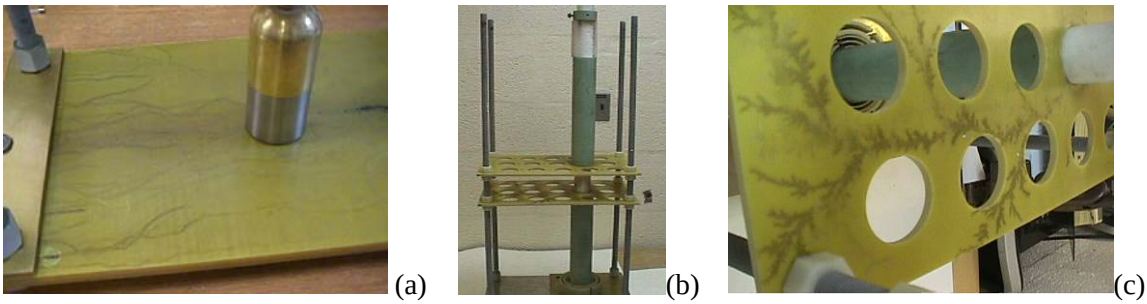

(a) (b) (c)

Fig. 1.14. G-10 testing. (a) Tracking observed from a high-voltage rod to a ground plate. (b) Test rig for surface flashover inside a tube to a ground plate. (c) Close-up of a "treeing" track showing the statistical nature of the discharge as it propagates.

Experiments continued on the ac and impulse breakdown voltages for LN gaps in a nonuniform rod-to-plane electric field. The purpose of that work is to establish baseline data and design guidelines for leads and bushings for the MFCL. Previous data focused on the effect of varying the gap in the rod-plane geometry. Here the focus was on the effect of varying the pressure of LN with a fixed gap. Pressure is an important parameter because it relates to the effect of bubble formation in the liquid. Higher pressures generally increase the breakdown strength which is in part due to suppression of bubbles or reduction in size of the bubbles. Figure 1.15 shows the effect of increasing pressure on the 60-Hz ac breakdown voltage. Consistent with other data in the literature, the breakdown voltage increases with pressure to about 3 atm and then somewhat flattens out. From a design point of view this means that increasing the pressure beyond 3 atm will not substantially increase the breakdown voltage and that other design features, such as gap and triple junction, must be optimized to achieve desired voltage levels.

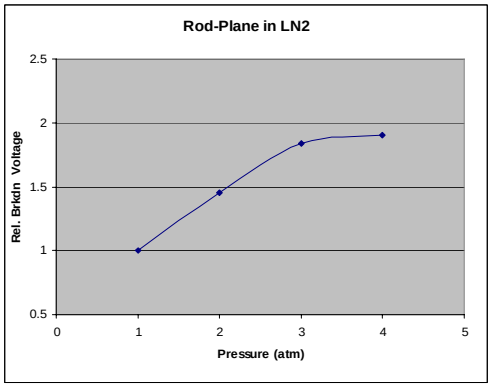

Fig. 1.15. Effect of pressure on breakdown voltage in liquid nitrogen in a nonuniform gap.

During these tests it was observed that initial filling and refilling the LN in the cryostat had a significant effect on the breakdown voltage. Breakdown voltages were lower following a filling cycle and increased over a period of several hours until the value stabilized. This effect may be due to bubble formation caused by turbulence from filling or introduction of gas bubbles from the initial part of the filling operation. Bubbles may also be formed by thermal loading from leads during the initial fill. However, ten successive breakdowns at a given gap and pressure were measured to determine an average breakdown value. Of course, the breakdowns themselves generate some bubbles, and they may contribute to the spread in values.

Impulse voltage measurements (1.2/50 μs) were also performed on the same rod-plane geometry for a small gap as a function of pressure. The up-and-down method was used to determine the 50% probability of breakdown. In this method an impulse is made well below the expected breakdown value. If a withstand occurs, the voltage is raised one step and repeated. If a breakdown occurs, the voltage is decreased one step and repeated. In this way, after a number of withstand shots, the voltage will level out to the 50% probability value. Both positive and negative polarities were measured from 0 to 44 psig. At lower pressures the negative-polarity value was lower than the positive value, but at higher pressures the trend reversed. This effect needs to be examined further.

1.2.3 Upgrade of Haefely Impulse Generator

Arthur Molden of AMEESCO arrived in September 2005 for assembly of Three additional stages to the Haefely Impulse Generator in Building 5500. The added stages will increase the capability from 500 kV to 800 kV. Each stage adds 100 kV or 1 kJ energy. The upgrade includes additional capacitors, resistors, support insulators, shelves, spheres, and sphere gap pole assemblies (see Fig. 1.16). An additional voltage divider section was installed, which increased the rating to 800 kV. Due to the higher voltages, the voltage divider ratio was increased by adding capacitance to the output section of the divider. Assembly of the stages was completed, and commission testing followed. Negative lightning impulse shots using the voltage divider as load (1 nF) were made at 20, 40, 60, and 80% of the total charging voltage. At nominal 80% charging (79 kV dc actual) the peak impulse voltage was 592 kV, which corresponds to an efficiency of 94%. This value is within the acceptable range for impulse generators of this type.

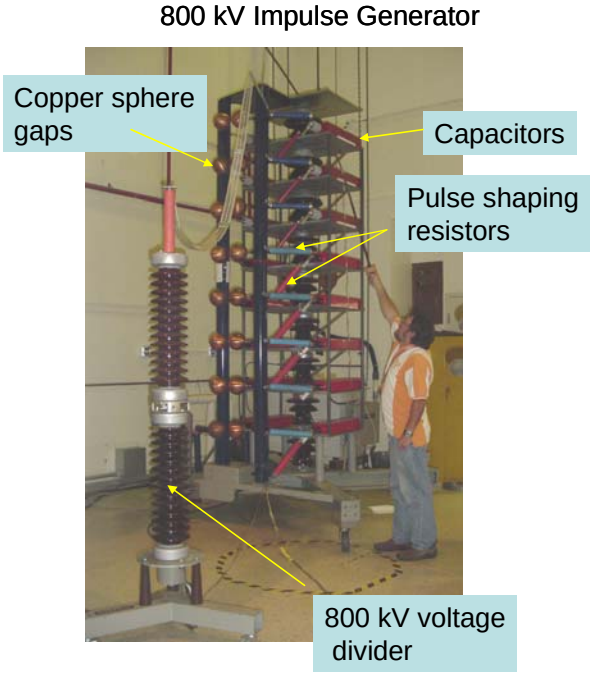

Fig. 1.16. Alvin Ellis (ORNL) applies a safety ground to upper stages of the upgraded impulse generator. Each stage is rated at 100 kV for a total of eight stages or 800 kV.

The waveform had a 0.7-μs rise time and 50-μs fall time. The rise time will increase slightly with a larger capacitive load. A higher value external front resistor will be ordered to fine-tune the rise time to 1.2 μs based on the load being tested. IEEE Standard 82-2002 specifications are as follows: rise time, 1.2 ± 0.36 μs; fall time to half value, 50 ± 10 μs. The upgraded parts of the impulse generator worked well to 80% of the maximum voltage. Based on the efficiency of 94%, we would expect to achieve an ultimate voltage of 744 kV. The BIL for 138-kV-class equipment is 650 kV.

1.2.4 BSCCO Thermal Property Measurements

Heat capacity measurements were completed on a sample bulk HTS MFCL element. The melt-cast Bi-2212 sample tubes were provided by Nexans. The tubes were cast with a centrifugal process at a thickness of several millimeters and were machined off to an outside diameter of 2.5 cm and wall thickness of 1.6 mm. The tubes used in the MFCL device have copper contacts soldered to the ends, but bare tubes were used for these tests. The Bi-2212 tube length was 7.62 cm. An 80-Ω heater of 0.08-cm-diam chromel wire was spirally wound evenly over the tube surface. A 37-Ω thermometer of 0.08-cm-diam, 99.99% Pt wire was wound on between the heater turns. The spacing between individual turns on the sample was about 1 mm. Both the heater and thermometer wires were wound bifilar to reduce noise. A thin layer of Apiezon™ "N" grease was applied over the heater and thermometer wires to promote heat transfer. The mass density of the Bi-2212 material was 5.99 g/cm^3. The mass of the bare sample tube was 54.66 g, and the heater and thermometer added 0.45 g.

The sample tube was mounted in a small Cryo Industries variable-temperature cryostat. The sample volume was a 3.81-cm-ID copper tube with a heat exchanger, silicon diode thermometer, and heater. A flow of LN that was controlled by a valve in the external transfer line cooled the heat exchanger, and the heater could be used for fine temperature control. The coolant gas did not exhaust through the sample volume. Instead, the sample was cooled to the desired temperature by using an exchange gas in the sample volume, and the exchange gas was pumped out to isolate the sample for measurements. Figure 1.17 shows the installation of the heat capacity sample in the cryostat. The sample tube was supported on long threads for thermal isolation, and fine instrumentation wires were used to limit conduction heat loads to about 30 mW.

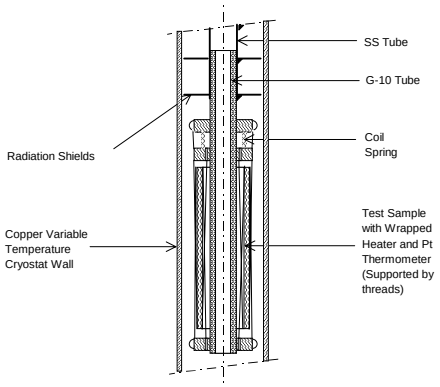

Fig. 1.17. Heat capacity sample installation.

Two separate sets of data were taken, in the high-temperature range and at low temperatures. In the high-temperature range, the sample was cooled down from 300 K to 200 K with exchange gas in 20-K increments. At each temperature, the exchange gas was pumped out and several 1-min heat pulses were applied at 0.5 or 0.75 W. During a pulse the temperature rose by about 2 K. Another low-temperature set of data was taken starting at 88 K. In this case, the sample volume was kept evacuated and the sample heater was pulsed on and off to provide data at increments of about 3 K. The sample volume wall was controlled at about 2 K below the sample temperature to reduce radiation and to provide a slight cooling rate when the heater was off. The heat capacity was calculated from the ratio of the heat input to the difference between the temperature-vs-time slopes when the heater was on and off. Figure 1.18 shows the heat capacity data for the full temperature range between 80 K and 300 K. The two sets of data approach each other in the middle temperature range. The contribution to the heat capacity by the heater and thermometer was about 1% and was not subtracted for the engineering measurements. Measurements by Junod et al.[1] on a single-crystal Bi-2212 sample are shown for comparison. Our results are generally consistent with Junod's; the differences probably stem from the different sample morphologies and the slightly lower density of our sample (5.99 gm/cm^3 vs 6.56 gm/cm^3 for Junod).

The observed heat capacity values have been fitted to the Einstein model, which gives the heat capacity as a function of the temperature T by

$$C_E = 3R\left(\frac{\Theta_E}{T}\right)^2\left(\frac{e^{\Theta_E/T}}{(e^{\Theta_E/T}-1)^2}\right) \quad (1)$$

where R is the gas constant, 8.3145 J/mol-K, and Θ_E is the Einstein characteristic temperature. This approaches the Dulong-Petit value of $3R$ at high temperatures. Using 59.41 gm as the average gram

molecular weight for the 15-atom Bi-2212 unit cell, and the observed sample density of 5.99 gm/cm^3, experimental values of C_p/R are also plotted in Fig. 1.18. These values do tend toward the limiting value of 3 predicted by Eq. (1), but appear to be still rising faster than might be expected at 300 K. The line in Fig. 1.18 shows the best fit of Eq. (1) to the experimental values of C_p/R, using a value of 341 K for Θ_E. This value is comparable to reported Debye temperature values in the range of 370 K.

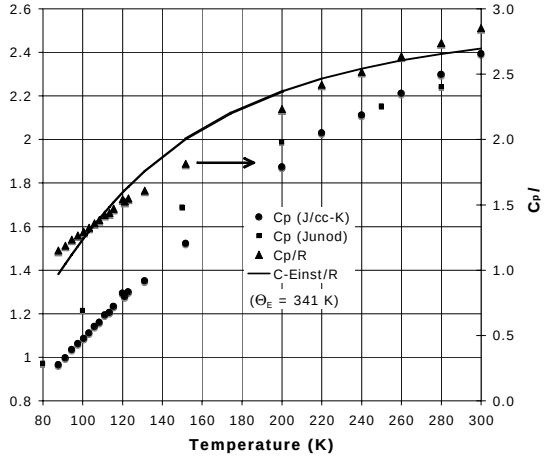

Fig. 1.18. Heat capacity (C_p) of bulk Bi-2212 vs temperature. Source for "Junod": A. Junod et al., "Specific Heat up to 14 Tesla and Magnetization of a $Bi_2Sr_2CaCu_2O_8$ Single Crystal: Thermodynamics of a 2D Superconductor," *Physica C* 229, 209–30 (1994).

In order to verify that the melt-cast-processed Bi-2212 melt-cast tubes can absorb the required fault energy without overheating, we have integrated our experimental heat capacity results in Fig. 1.18 between 80 K and 220 K or 300 K. The total enthalpy change is about 210 J/cm^3 from 80 K to 220 K and 390 J/cm^3 from 80 K to 300 K. Thus, the total 9-cm^3 volume of the sample tube could absorb 1.9 kJ in warming to 220 K and 3.5 kJ for a final temperature of 300 K. The Bi-2212 elements for the MFCL prototype would be considerably longer than the sample tube and should be able to absorb the required energy without excessive heating. However, heat generation in the elements is not completely uniform because additional heat is generated at the copper end connections. Failure of only one element in a series string of several hundred can cause increased losses, and tests at other laboratories have not verified the required reliability of the elements.

1.2.5 References

1. A. Junod et al., "Specific Heat up to 14 Tesla and Magnetization of a $Bi_2Sr_2CaCu_2O_8$ Single Crystal Thermodynamics of a 2D Superconductor," *Physica C* **229**, 209–30 (1994).

1.3 Waukesha Electric Systems (WES) HTS Transformer SPI

S. W. Schwenterly, A. R. Ellis, D. R. James, and I. Sauers

The transformer team led by WES did a comprehensive report on the results of the 2003–2004 test program and a physical inspection of the unit and issued this in the fall of 2004 (the "chronicle" report). The HTS coils were removed and were sent to SuperPower for dissection, which took place in the spring and summer of 2005. A root cause analysis on the low partial discharge inception voltage and high-voltage breakdown in the coils was conducted by SuperPower and a "lessons-learned" readiness review took place on May 11, 2005. These activities were summarized to DOE staff in a meeting at DOE HQ on August 1, 2005. The lessons-learned were also presented to the larger HTS community by Sam Mehta, of WES, at the DOE 2005 Peer Review on August 2. A no-cost extension of the existing pilot center agreement with WES on HTS transformer development was approved for FY 2006. Under the agreement, both parties will continue work on interim transformer development activities using their own funds while an extension of the current HTS transformer SPI is being negotiated. During the year, the conceptual design of the transformer will be updated and modified to include the use of second-generation HTS tapes, to improve reliability, and to conform more closely to WES's standard transformer manufacturing procedures. Further high-voltage tests on dielectric materials for the new conceptual design will be carried out. This work will provide a foundation for a proposed Phase III SPI with the goal of developing a 138-kV HTS transformer.

1.4 General Electric Co. HTS Generator SPI

R. C. Duckworth, A. R. Ellis, M. J. Gouge, D. R. James, C. M. Rey, I. Sauers and S. W. Schwenterly

1.4.1 Emissivity Experiment

Measurement of emissivity degradation has been completed for the case in which a silver-plated copper sample is exposed to a G10 surface. Figure 1.19 shows how the G10 was secured to the test setup and its relationship to the sample. The G10 piece was a disk with a thickness of 1/8 in. (0.317 cm) and an exposed diameter to the silver plated copper sample of 9 in. (22.86 cm). The location of the G10 onto the thermal shield was chosen for two reasons. First it was desired to minimize the obstructions between the water vapor that is produced by the outgassing of the G10. Second, the emissivity of the G10 did not impact the energy balance used to obtain the emissivity significantly. At room temperature, the emissivity of G10 is approximately 0.7, and from modeling the test setup in SINDA-FLUINT, a reduction of the emissivity results in an effect of less than 1% in the sample emissivity with the change in the heat load of 1.0 mW, small when compared to the total heat load of approximately 0.5 W to 1.0 W. Figure 1.20 shows how the emissivity changed as a function of time for two cases. In the first case, the G10 was taken as manufactured and was pumped on for 48 h with a turbomolecular pump before the cryocooler was started. In the second case the G10 piece was removed after the first test was completed and was baked out at a temperature of 110°C for 12 h in a vacuum oven before being pumped on in the test setup for an additional 48 h. Some improvement was achieved from baking the G10; emissivity increased from 0.010 to 0.019 for the first case and from 0.010 to 0.016 for the second case.

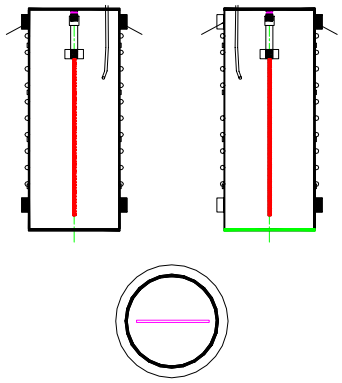

Fig. 1.19. Thermal shield in relation to silver-plated copper sample for the emissivity test setup. The bottom thermal shield panel (ε = 0.97, top left) was replaced by a G10 disk of similar dimensions (ε ≈ 0.7, top right). Bottom: overhead perspective of the relative geometry of the copper sample to the thermal shield.

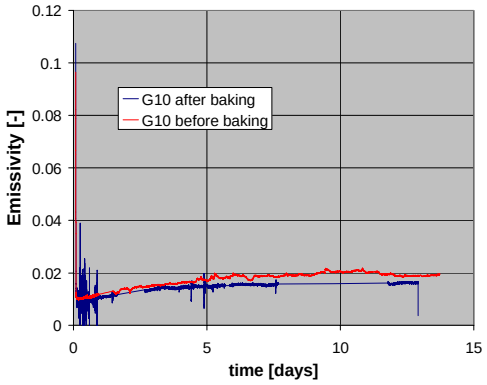

Fig. 1.20. Emissivity vs time for a silver-plated copper sample with an emissivity of 0.01 at 30 K. The two curves represent the same G10 piece, which was used as a source of contamination, except that the G10 after baking represents the G10 contamination after it had been vacuum-baked for approximately 12 h.

In order to determine the extent of water contamination for the outgassed water vapor from the G10, the total amount of water that is need to produce the increase in emissivity is approximated by the previous measurement of emissivity degradation of the silver-plated copper sample due to direct water contamination as shown in Fig. 1.21.

If we assume that the mass of water is approximately 30 μg, the rate of water contamination rate on the silver-plated copper surface is 3.47×10^{-11} g/s. Taking into account that only half of the G10 is outgassing to the silver-plated copper surface directly, this translates into an outgassing rate of

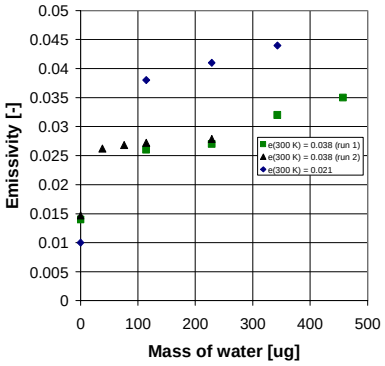

Fig. 1.21. Comparison of water degradation of emissivity for silver-plated copper samples with different room-temperature emissivities.

8.6×10^{-11} torr-L/cm^2-sec. This is still significantly lower than predicted by previous data Los Alamos National Laaboratory, but, as previously mentioned, the G10 temperature is one effect that could reduce the outgassing rate of the G10.

1.4.2 Quench Detection and Protection

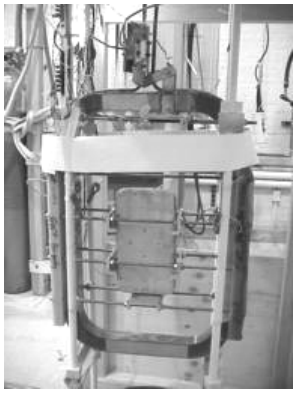

Fig. 1.22. Quench test coil.

A trip was made to General Electric Corporate Research and Development (GE-CRD) during December 2004 to participate in quench detection tests on a new 1.5-MVA generator coil. For simplicity, the coil (see Fig. 1.22) was mounted vertically in a stationary dewar instead of on the rotating cryostat. Forced helium gas cooling was provided from the cryocooled module used for the previous tests on the 1.5-MVA unit. To remove inductive signals and allow detection of a developing resistive zone, a pickup coil was installed in the bore of the HTS coil. The inductive pickup coil signal was multiplied by an appropriate factor of about 100 and was digitally subtracted from the HTS coil signal by the LabVIEW software used for data acquisition. Wide-area platinum thermometers were installed on the two long sides of the coil to observe changes in average temperature over the whole side. ORNL personnel supervised the addition of point ruthenium oxide thermometers at several more locations on the coil to provide additional temperature information. The intent was to induce a global quench in the coil by deliberately exceeding the critical current for a short time. In follow-on tests, localized quenches would be induced by a heater on the coil. Cooldown began on December 15 (the last day of the visit). Unfortunately, a cracked beryllia heat sink on one of the coil leads prevented proper cooldown, and no quench data were obtained on that day. GE repaired the lead insulator in the following week and successfully cooled the coil to 36 K. They verified the critical current of the coil and clearly observed resistive voltages in the range of 150 to 200 mV during current-induced global quenches. ORNL personnel will assist in the data reduction process.

A 2nd trip was made to GE-CRD during March 2005 to participate in quench detection tests on a new 1.5-MVA generator coil. New platinum thermometers were installed (to replace the marginal ones used in the December 2005 tests) on the two long sides of the coil to observe changes in average temperature over the whole side. For the new tests, a local quench heater was installed in the bore of the coil along one side. ORNL personnel assisted in the addition of ruthenium oxide thermometers adjacent to this heater to provide local temperature information. The intent was to use the heater to inject a heat pulse that would induce a local quench in the coil. The coil was successfully cooled down to about 30 K. The critical current of the coil was the same as before. Experiments at currents above the critical current were then conducted, and resistive voltages above 100 mV were observed. ORNL personnel will assist in the data reduction process from the second round of tests and in definition of strategies for quench detection in the much noisier generator environment.

The GE-ORNL CRADA was revised to accommodate the SPI 100-MVA HTS Generator project extension to FY 2008. It was approved by DOE-Oak Ridge in September 2005. Robert Duckworth presented a paper at the Cryogenic Engineering Conference entitled “Measurement of the Emissivity of Clean and Contaminated Silver-Plated Copper Surfaces at Cryogenic Temperatures.”

1.5 Second-Generation Conductor Applications

R. C. Duckworth, J. A. Demko, M. J. Gouge, and C. M. Rey (ORNL); Jennifer Carney (UTK)

1.5.1 High-Voltage Qualification of Copper-Surround-Stabilized YBCO

The high-voltage performance of copper-surround-stabilized YBCO coated conductors was compared to as-slit YBCO coated conductor to determine, from a high-voltage perspective, whether any tangible improvement was gained by copper plating. In a series of tests at room temperature, it was found that for the same dielectric environment, the copper-surround-stabilized tapes had a higher average breakdown voltage (7.0 ± 0.4 kV) than the as-slit YBCO tapes (6.0 ± 2.2 kV). When the results were plotted on a Weibull plot to determine probability of breakdown at a given voltage, the 10% probability occurred at a higher voltage for the copper-surround-stabilized YBCO tapes.

1.5.1.1 Experimental Setup and Procedures

To characterize the dielectric properties for the sample tapes, a cross configuration as shown in Fig. 1.23 was chosen because the test conditions are fairly reproducible and the statistical variation associated with the test setup is minimized. The location and initiation of the high-voltage breakdown for two adjacent tapes or a turn-to-turn configuration is affected by variation of the distance between the tape along the length, defects that occur along the tape length, and the end voltage connections to the tape. In addition, this setup permits for some deviation in the straightness of the sample without affecting the electric field profile between the tapes as the voltage is slowly ramped up to 10 to 20 kV between the two tapes. Breakdown is recorded once a short occurs between the two tapes and the voltage drops to zero.

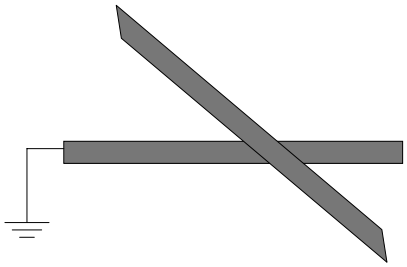

Fig. 1.23. Sketch of cross configuration used to test voltage breakdown between a pair of YBCO coated conductors.

A 0.025-mm-thick piece of kapton was placed between the two tapes (see Fig. 1.24), and the relative height of the sample was adjusted until each tape was flush to the kapton surface. The entire setup was

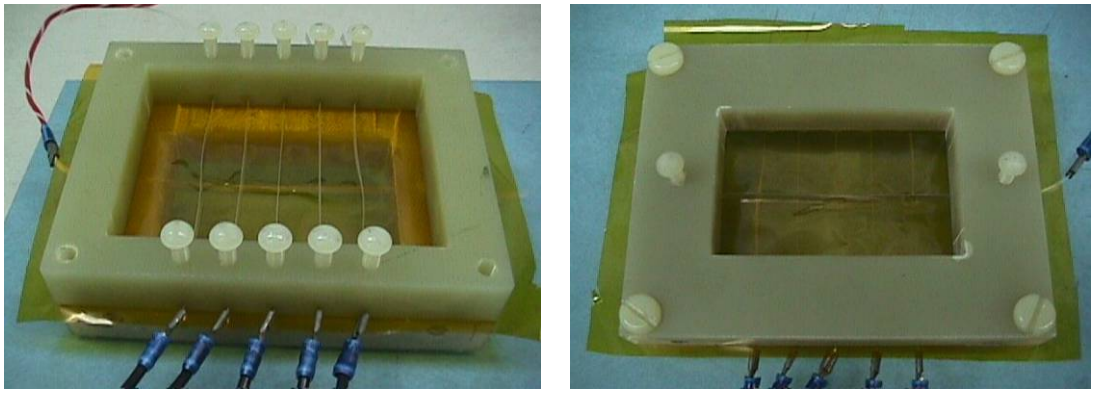

Fig. 1.24. High-voltage breakdown test setup for YBCO tapes. Bottom view (right) shows the single grounded YBCO tape with respect to the array of YBCO tapes. Voltage was supplied to a single tape of the array shown until breakdown occurred between the biased YBCO tape and the single grounded YBCO tape.

immersed in an oil bath to allow for multiple samples to be tested on a systematic basis. The dielectric strengths of the oil and the kapton prevent high-voltage leakage between the voltage-biased tapes and adjacent grounded samples and allow for the electric field to remain concentrated between the two tape edges. The tests were performed on two sample sets of 4-mm-wide YBCO tapes. The samples, which were provided by Superpower, consisted of one set of unstabilized YBCO coated conductor and another of copper-stabilized YBCO with 18 μm of surround copper stabilizer. The breakdown was measured between pairs of YBCO tapes, nominally 15 to 20 cm long, within a sample set (i.e., voltage was applied across a pair of either nonstabilized YBCO or copper-surround-stabilized YBCO).

1.5.1.2 Results

Table 1.3 shows the voltage breakdown that occurred for the as-slit and copper-surround-stabilized YBCO tapes. While there were breakdowns that occurred at high voltages (8 to 10 kV), the copper-surround-stabilized YBCO tapes appeared to have a more predictable response in this preliminary set of measurements. It is believed that the surround stabilizer could be providing a more repeatable interface for the breakdown to occur. However, because the level of voltage breakdown in the as-slit YBCO tapes was higher in some cases, a competing mechanism may be present because the reduction in stress volume in the as-slit tapes should produce a lower breakdown voltage.

Table 1.3. Voltage breakdown data taken for copper-surround-stabilized and as-slit YBCO tapes

Run	Breakdown (kV)	
	As-slit	Copper surround stabilized
1	5.4	6.7
2	6.6	6.5
3	6.4	7.0
4	6.8	6.8
5	9.0	6.7
6	7.8	6.6
7	7.7	6.2
8	6.3	6.7
9	2.8	6.8
10	5.7	7.5
11	2.0	7.7
12	2.6	7.7
13	5.3	7.3
14	7.1	7.2
15	9.9	7.5
Average	6.1 ± 2.2	7.0 ± 0.4 kV

To better appreciate the significance of the results, a Weibull plot has been generated to determine the probably for breakdown to occur at a given voltage based on the sample measurements. Figure 1.25 shows that the variation of the as-slit YBCO contributes to having a 10% probability that voltage breakdown will occur at a lower value than the 6-kV threshold for the copper-surround-stabilized YBCO. The results are preliminary for the copper-surround-stabilized YBCO due to the number of samples tested. Additional measurements are needed to see if the observed trends continue.

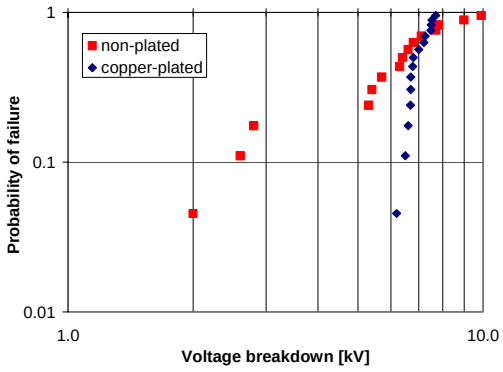

Fig. 1.25. Weibull plot of likelihood of voltage breakdown at room temperature for as-slit and copper-surround-stabilized samples.

Because the test was a fundamental examination of geometry, further testing is required to determine whether the copper-stabilized YBCO has any other benefit from a high-voltage standpoint. When the tape is used in an epoxy-impregnated magnet, the edge-to-edge geometry may show that there is not a significant advantage to the copper-surround-stabilized YBCO due to the dielectric strength of the epoxy and not the tape edges. However, void formation could be harder in copper-surround-stabilized YBCO due to lack of nucleation sites on the sharp edges. A careful set of tests is required to isolate the epoxy and YBCO tape effects.

1.5.2 Effect of Copper Thickness Stabilization on Copper-Surround-Stabilized YBCO

1.5.2.1 Experimental Setup and Procedures

Because applications such as motors and generators desire a high degree of stability without sacrificing the engineering current density of the superconductor, the role of copper stabilization thickness has been examined on a series of copper-surround-stabilized YBCO samples. With two different total copper stabilization thicknesses of 36 and 72 μm, the thermal limits were examined through the application of a dc current pulse at currents greater than the critical current for a period of 0.5 s. The thermal limit was determined based on the measurement after a reduction of critical current was observed.

Each sample was mounted onto a G10 solid rod as shown in Fig. 1.26. Voltage taps and a thermocouple or thin film platinum resistor were attached to the sample before dielectric tape was added to isolate the sample from the liquid nitrogen bath. The voltage taps and the thermocouple or thin-film platinum resistor were used to measure the temperature of the sample during and immediately after the dc current pulse. For the voltage taps this was accomplished by applying a current less than the critical current after the high-current pulse to monitor the sample resistance as the sample either heated up or cooled down. Using a calibration of each sample resistance as a function of temperature, the temperature could be monitored on a more global basis because there is some limitation of the thermocouple due to thermal contact variability and thermocouple mass.

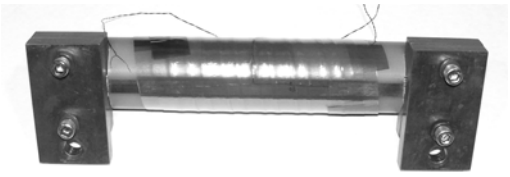

Fig. 1.26. Liquid nitrogen test setup for stability determination of HTS samples.

Before the thermal limits of the sample were examined, the sample resistivities were measured to confirm the composition of the tape and amount of copper stabilization. Figure 1.27 shows the resistance per unit length of sample 1 (36 μm) and 2 (72 μm) from room temperature down to approximately 100 K. A linear fit of the data was used to estimate the average sample temperature between the voltage taps during the 0.5-s impulse and the subsequent sample cooldown at a lower current. The result was unusual in that there is not a significant difference between the resistances even though there is a factor-of-two difference in the amount of copper stabilization between samples 1 and 2. The difference was confirmed with two different methods of resistivity vs temperature measurement with different thermometers; there was no observable disparity in the data. At room temperature the resistance per unit length of sample 1 was 0.053 Ω/m; for sample 2, it was 0.044 Ω/m. Figure 1.28 shows the theoretical resistance per unit length assuming an alloy substrate and the 36 microns of copper for sample 1 and 72 microns for sample 2.

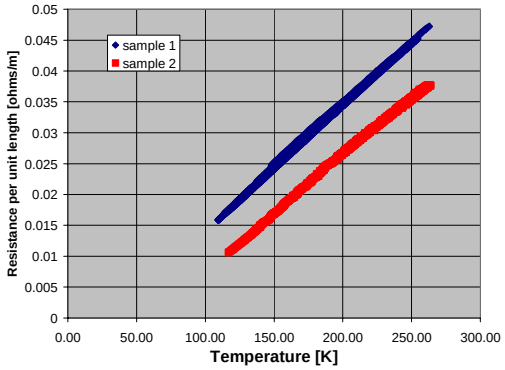

Fig. 1.27. Measured resistance per unit length for samples 1 and 2 as a function of temperature.

Additional measurements were done on other samples with 36 μm and 72 μm of copper plating, and the results were consistent with those shown in Fig. 1.27. It is possible that the composition of the copper-surround stabilized tapes is not pure copper and that it contains some impurities that could be introduced in the copper plating process.

1.5.2.2 Thermal Limits of YBCO as a Function of Copper Thickness

Figures 1.29 and 1.30 show the transient resistance per unit length and estimated temperature for two current pulses of 246 A and 247.5 A. After the 247.5 A current pulse, the critical current degraded from 55 A to 17 A and the n-value went from 30 to 3, as shown in Fig. 1.31. As determined from Fig. 1.30, the

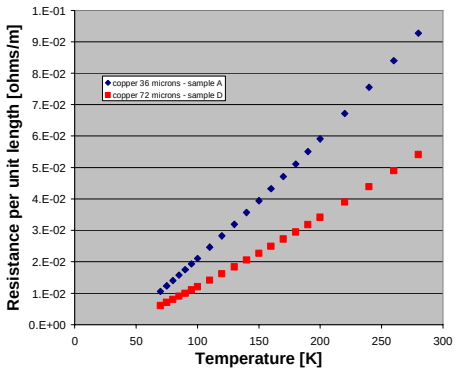

Fig. 1.28. Estimated resistance per unit length for samples 1 and 2 as a function of temperature, assuming a 100-μm Hastelloy substrate. Source: Y. Iwasa et al., *IEEE Transactions on Applied Superconductivity* 15 (2), 1683-86 (June 2005).

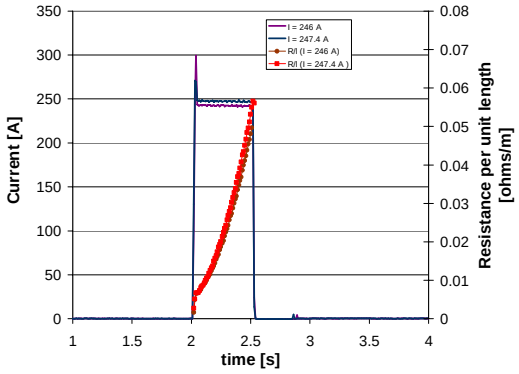

Fig. 1.29. Profiles of the total sample current and measured resistance per unit length vs time for sample 1 under two separate 0.5-s dc current pulses. The 246-A pulse resulted in no damage to the conductor, while the 247.4-A pulse resulted in significant degradation of the conductor.

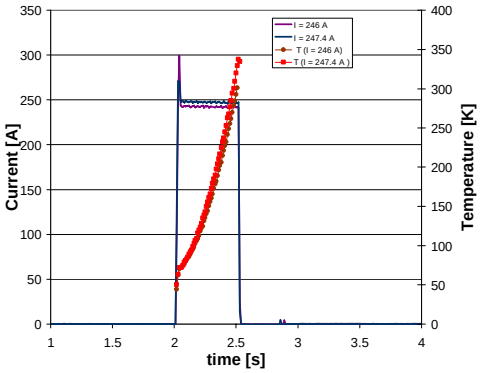

Fig. 1.30. Profiles of the total sample current and estimated average sample temperature vs time for sample 1 under two separate 0.5-s dc current pulses. For the 247.4-A run, the average temperature was approximately 350 K.

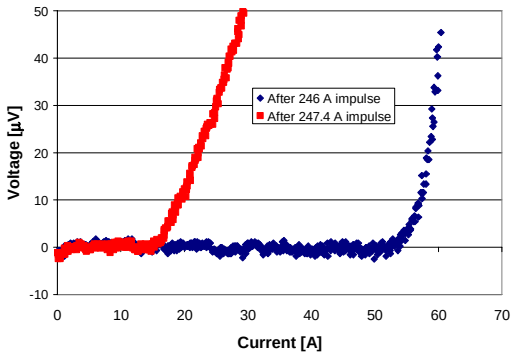

Fig. 1.31. Degradation of sample 1 before and after the 247.4-A, 0.5-s current pulse. The critical current of the tape degraded from 55 A to 17 A.

estimated peak temperature averaged over the 9.5-cm length was approximately 350 K from the resistance of the sample.

Table 1.4 summarizes degradation points for sample 1 and 2. The ratio of the degradation current is inversely proportional to the ratio of the sample resistances, so while the sample resistance was not consistent with the expected sample composition, the degradation current was consistent. Further analysis

Table 1.4. Summary of sample performance before and after degradation current and associated peak temperature, measured by the thermometry and estimated from the sample resistance

Sample	Critical current (A)		n [-]		Degradation current (A)	Average peak temperature (K)	
	Before	After	Before	After		Thermocouple	Resistance
1 (36 μm)	55	17	30	3	247.5	250	350
2 (72 μm)	53	40	30	9	296	275	520

of sample resistances at different copper thicknesses is needed to see if there are compositional abnormalities with the copper plating and how the thickness of the copper plays a role in the resistivity.

The temperatures from the resistances are not consistent with previous modeling results that were reported by Iwasa on copper-surround-stabilized YBCO with similar critical currents [1]. Since the overcurrent pulses (0.5 s) were slightly longer in duration (0.3) and sample was insulated over the entire length, an examination of amount of energy deposited into the sample was performed. This was done by comparing the integration VI product during the current pulse to the maximum energy that could have been absorbed by the sample, or

$$V \int_{T=77K}^{T_{max}} C_p dT = F \cdot I \int_{t=0}^{t=0.5s} V(t) dt \qquad (2)$$

where C_pT is the volumetric specific of heat of the tape and F is the ratio of absorbed heat to generated heat. and When F = 1, which is the case for adiabatic heat transfer, the equivalent peak temperature was 410 K for sample 1 and the equivalent peak temperature was 596 K for sample 2, which are slightly higher than the average peak temperatures measured from the resistances. If the analysis is turned around to compare the integrated specific heat to the measured average peak temperature from the resistance to obtain F, then F is between 0.82 and 0.85 for both samples. The temperatures are still below the modeled limit of 700 K reported by Iwasa [1], and additional analysis will be done through simulation and experiments to see if a localized hot spot can be found.

1.5.3 AC Transport Losses in 4.4-mm-Wide YBCO Tapes

The ac transport losses have been measured electrically and thermally for a 4.4-mm-wide copper-laminated YBCO tape. Agreement between the two methods is good over the overlapping current range. The sample had a critical current of 75 A at 77 K. This conductor was a copper-stabilized, 4.4 mm YBCO conductor with a Ni-5at%W substrate. Figure 1.32 shows the transport ac losses as a function of peak current ratio (I_{peak}/I_c) at a frequency of 60 Hz. The curves in Fig. 1.32 represent the estimated superconducting hysteretic losses found from the Norris elliptical and thin-strip models for a conductor with a critical current of 75 A. Although it is expected that YBCO should approximate the Norris thin-strip model in terms of transport ac losses, the measured losses are considerably higher than either the thin strip or the elliptical model. In previous samples, the ferromagnetic losses of Ni-5at%W contributed to the total ac losses, but the fields that are associated with the sample width of 4.4 mm put the estimated ferromagnetic contribution when I_{peak}/I_c = 1 to be about 3.0 mW/m. To determine the nature of the additional ac loss, two measurements are planned. The first is to repeat the ac loss transport

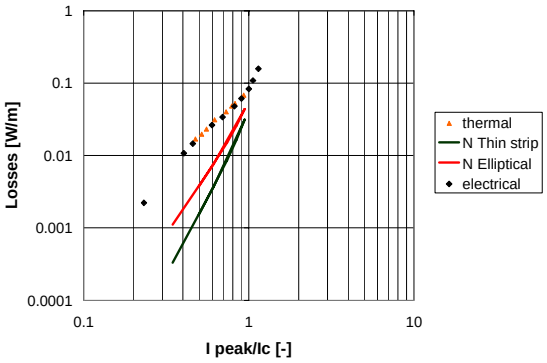

Fig. 1.32. AC losses in a YBCO tape sample with a critical current at 77 K of 75 A.

measurement with a variable-frequency ac source to determine whether the eddy current losses in the copper lamination are contributing. Second, a transport measurement on a nonlaminated, silver-coated, 4.1-mm-wide YBCO sample will be done to determine whether anything occurred in the processing of the YBCO that could have affected the ac loss.

1.5.4 Second-Generation HTS Coil

1.5.4.1 Introduction

ORNL, in collaboration with American Superconductor Corporation and Cryomagnetics, Inc., has designed, fabricated, and tested a nominal 1-T solenoid coil fabricated with a second-generation YBCO coated conductor. The purpose of the 1-T coil project is to gain experience with design and operation of coils made with second-generation conductors and to study quench protection and propagation characteristics in second-generation YBCO coils. A fundamental understanding of the quench phenomena is crucial in the future design and operation of HTS-based electric utility applications and devices.

1.5.4.2 Fabrication

The YBCO coated conductor used in the manufacture of the solenoid coil was fabricated by a process based on the rolling-assisted biaxial textured substrate (RABiTS™). The conductors consisted of a three-ply, copper-laminated YBCO tape with a Ni-5%W substrate. The conductors were about 4.4 mm wide by 0.2 mm thick by 20 m long, and all but one had an internal splice. Each conductor was insulated with 0.025-mm Kapton tape for turn-to-turn insulation and was then wound onto a Cu bobbin into a single pancake coil. The inner diameter of the coil was 35 mm, and the outer diameter was 102 mm. The winding pack, which consisted of about 97 turns, per pancake, was vacuum-impregnated. An external splice was made on the inner diameter to connect two single pancake coils to form a double pancake coil. Three double pancake coils were stacked between top and bottom aluminum end rings and were compressed via axial tie rods. The final external splice was made on the outside diameter of each of the double pancake coils to form a single monolith whose overall height was 35 mm (Fig. 1.33).

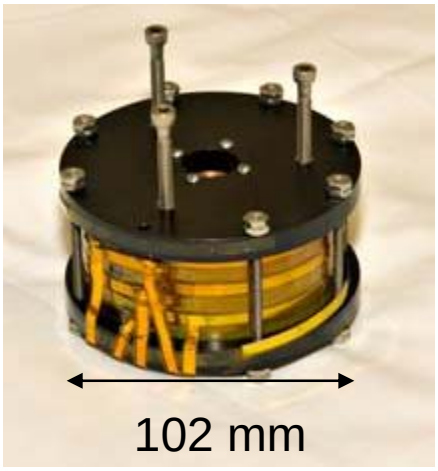

Fig. 1.33. Single monolithic YBCO coil.

1.5.4.3 Experimental

The coil was instrumented with six voltage tap pairs and two Si diode temperature sensors located at the top and bottom end plates of the coil. The voltage taps were located at the beginning and end of each single pancake coil. Thus, voltage taps pairs 1, 3, and 5 included both the double-pancake to double-pancake splice on the outer turn, the single-pancake to single-pancake splice on the inner turn, and the internal splice along the 20-m piece length, while voltage tap pairs 2, 4, and 6 did not include the double-pancake to double-pancake splice joint on the outer turn. The two Si diode temperature sensors located at the top and bottom end rings were able to measure the temperature gradient from the top to the bottom of the YBCO coil. The YBCO coil was tested under two different cooling conditions: bath cooling (with LN) and conduction cooled (i.e. no liquid cryogens).

Thermal Cycle No. 1 (LN Cooling) Initial Test

The YBCO coil was initially tested at 77 K in a bath of pool-boiling LN. Transport critical current measurements were made using standard four-terminal techniques. Using an electric-field criterion of

1 μV/cm, results showed a critical current of 31 A, which corresponded to a central B-field in the coil of 0.32 T (see Fig. 1.34). These results were presented at the DOE 2005 Peer Review in Washington, D.C.

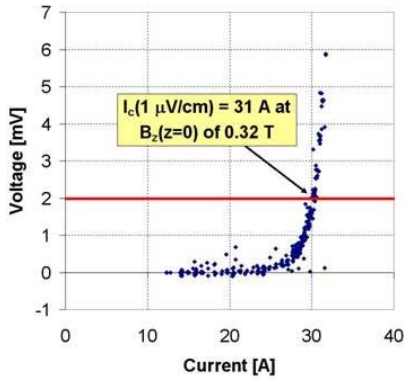

Fig. 1.34. DC V-I curve in LN at 77 K.

Conduction Cooling Test

After the initial testing at 77 K in an LN bath, the YBCO coil was modified to accommodate additional copper end rings attached to the original aluminum end rings of the coil. The new copper ends rings were used to facilitate mounting of the coil to the cryocooler cold head for the conduction cooling test. The new copper top end ring of the YBCO coil was then mounted on a brass spool piece which attached to the cold finger of an Al-330 G-M cryocooler. To keep the top and bottom of the YBCO coil as close to the same temperature as possible, thermally conductive flexible copper straps were attached to the top and bottom end plates of the additional copper end ring. During the modification and subsequent mounting of the YBCO coil for the conduction cooling test, it was noted that a small kink had appeared in the entering and exiting leads of the conductor. The kinks in the YBCO leads were most likely the result of out-of-plane bending that occurred during the conduction cooling modification. An attempt was made to repair the kinks in the entering/exiting leads with the addition of stabilizing conductor.

Thermal Cycle No. 2

During the first thermal cycle the coil was slow to reach thermal equilibrium. The YBCO coil was allowed to cool down for over 24 h prior to the start of the critical current testing. After reaching final thermal equilibrium, the temperatures recorded on the coil were~ 45 K (top) and ~ 51 K (bottom). After reaching a thermal equilibrium point, transport critical current measurements were taken at a wide variety of ramp rates, ranging from 0.01 to 0.5 A/s. Results showed values ranging from 22 to 27 A, depending upon the ramp rate used in the test. The results also indicated that all single pancakes were experiencing large amounts of heat generation during the current excitation. Since higher critical currents were anticipated due to the LN test results, three hypotheses were put forth to explain the disappointing results. First, the YBCO conductor in the coil was actually at a warmer temperature than was being recorded at the top and bottom end rings. Second, there was excessive heat generation in the coil caused by a large ac loss that was not observed during the original LN testing. Third, some type of global damage or degradation had occurred to the coil as a result of the conduction cooling modification or repeated thermal cycling. The critical current tests were halted, the cryocooler was turned off, and the YBCO coil was allowed to warm overnight. Upon warm-up of the YBCO coil, a trickle current was passed through the coil to observe the corresponding superconducting transition temperature. It was noted that the transition temperature of the coils was measured to be ~ 90 K, as would be expected. As a result of the warm-up testing, the hypothesis of the YBCO coil being at a significantly warmer temperature than the top and bottom end rings was ruled out.

Thermal Cycle No. 3

To test the hypothesis that the YBCO coil had either been damaged during modification or degraded as a result of thermal cycling, the critical current of the YBCO coil was once again tested in a bath of pool-boiling LN. After reaching a thermal equilibrium point, transport critical current measurements were taken at a wide variety of ramp rates, ranging from 0.01 to 0.5 A/s. Using the same electric field criterion of 1 μV/cm, results showed critical current values ranging from 28 to 30 A, depending upon the ramp rate used in the test. Although, the critical current was slightly lower by 1 to 2 A than in the previous LN test, it was concluded that no significant global damage or degradation was apparent.

Upon more careful inspection of the YBCO coil, it was noticed that the exposed outer turns of the coil were covered in Kapton tape. It was speculated that the emissivity of the Kapton tapes was quite poor and that the tapes may be acting like a black-body absorber on the outermost turns of the coil, causing them to be at a warmer temperature than the inner windings, resulting in a lower overall critical current for the coil. Therefore, it was determined that a radiation shield may reduce this deleterious effect.

Thermal Cycle No. 4

Prior to the cooldown on the second thermal cycle, two modifications were made to the experimental setup. First, an additional Lakeshore Si diode was placed inside the bore of the solenoid, against the inner copper winding mandrel, to more accurately assess the temperature gradient along the axis of the YBCO coil. Second, a radiation shield consisting of two layers of aluminum foil and six layers of aluminized multiple-layer-insulation (MLI) were wrapped around the coil and were attached to the Al-330 cold head.

Once again another thermal cycle was initiated. This time, however, with the inclusion of the radiation shield the cooldown of the YBCO coil took less than 6 h. After reaching final thermal equilibrium, the recorded temperatures on the coil were ~ 34.2 K, (top), ~ 34.8 K (bottom), and ~ 36 K (center bore). With the inclusion of the radiation shield, the final equilibrium temperature of the YBCO coil was nearly 10 K lower than the previous thermal cycle; the T between the top and bottom end ring was now less than 1 K. (Note: The rated accuracy of the Lakeshore Si diodes is ± 1 K.)

After reaching a thermal equilibrium point, transport critical current measurements were taken at a wide variety of ramp rates, ranging from 0.01 to 0.5 A/s. Using these slow ramp rates and the 1 μV/cm criterion, the critical current was measured to be between 45 and 49 A in the topmost pancake coil. It is believed that the lower-than-expected critical currents at that temperature are because the many nonsuperconducting splices (both internal an external) result in unwanted Joule heating, which cannot be carried away fast enough in the conduction cooling mode. The extremely slow ramp rates further exacerbate the problem by allowing the heating caused by the resistive splices to continually build.

To minimize internal heating within the YBCO coil, the slow current ramps were replaced with rapid "on/off" square wave pulses to the YBCO coil. Duration at full current varied between 2 and 5 s, depending upon the magnitude of the current pulses. Current pulses starting at 60 A were made in 10-A increments all the way to 100 A. the 100-A current corresponds to a B-field of ~ 1 T in the central bore of the coil. After the high on/off current pulses, the experiment was concluded and the YBCO coil was warmed up for 24 h prior to it being removed from the cryostat.

1.5.5 Conclusion

It was not fully determined whether the root cause of the lower-than-expected steady state critical currents is an intrinsic characteristic of the second-generation YBCO conductor in a perpendicular B-field or an extrinsic result of the many internal and external splices or possibly localized damage caused during coil modification. The critical currents of the top and bottom pancake coils were measured to be the lowest, which is consistent with the fact that they experience the peak radial B-field. Hence this is an intrinsic limitation of the YBCO conductor in this solenoid coil configuration. However, extrinsic factors, such as the many splices (both internal and external) and the kinks observed in the entering/exiting leads, may limit the critical current of the coil.

Further experimentation is anticipated to commence in November 2005. It is anticipated that new magnetic permeable end rings will be fabricated to replace the existing copper mounting rings. The purpose of the magnetic permeable end rings is to modify the flux line within the YBCO coil to help reduce the radial B-field at the end pancake region.

1.5.6 References

1. Yukikazu Iwasa et al., "Stability and Quench Protection of Coated YBCO Composite Tape," *IEEE Transactions on Applied Superconductivity* **15** (2), 1683–86 (June 2005).

1.6 Cryogenic Dielectrics Initiative

I. Sauers, M. J. Gouge, D. R. James, A. E. Ellis, S.W. Schwenterly, and E. Tuncer

Cryogenic dielectrics, like cryogenic cooling systems, is an enabling technology for high temperature superconducting (HTS) grid applications. The objective of this initiative is to develop and characterize robust and reliable cryogenic dielectric materials for use in HTS grid-related applications. The driving force for strategic cryogenic dielectrics work is the development of HTS power equipment that can operate at high voltage on the grid reliably for design lifetimes. Proposed work falls into three broad categories, (1) high voltage testing and characterization of currently available materials, (2) the development of new materials, specifically designed for cryogenic HTS applications and (3) high voltage design guidelines (modeling recommendations, model and prototype scaling, minimum thicknesses and gaps, surface finish, volume scaling, LN cleanliness, etc.). The number of available materials that can provide high voltage electrical insulation in typical thermal gradients from 300 to 30-80 K and mechanically compatible with typical conductors and structural materials is not large. There are typically little data on partial discharge and impulse (lightning) performance. Significant partial discharge will eventually produce a breakdown in ac applications. More fully-characterized, cryogenic dielectric materials are needed to allow designers to make engineering tradeoffs in real devices. Proven techniques need to be developed to allow designers to integrate these materials (in some cases with liquid or gaseous nitrogen also serving as a dielectric) in a reasonable and robust insulation package that can meet stringent IEEE requirements (ac withstand, partial discharge, BIL and surge transients) and function at operating voltage for 20-40 years.

Dr. Enis Tuncer from the High Voltage Group at Chalmers University, Sweden, has joined ORNL as a Post-Doctoral Fellow. He has considerable experience in high voltage engineering, dielectric spectroscopy, and modeling of composites using finite element analysis techniques. He has also worked in industry as well. His expertise will be valuable to all of the projects. His initial work is on measuring the dielectric strength of several materials commonly used as cryogenic dielectrics such as cryoflex, kapton, and other prospective candidates which may increase in strength at low temperatures. Measurements are underway using a dielectric spectrometer to obtain the real and imaginary parts of the dielectric constant as a function of frequency and the loss factor at room temperature and 77 K. Similar measurements including breakdown voltages are planned using the cryocooler which has variable temperature from 295 K to near 12 K.

As part of the cryogenic dielectrics initiative ORNL will be hosting the Cryogenic Dielectrics Workshop to be held in Nashville on October 16, 2005 at the Sheraton Downtown Nashville Hotel. The workshop is held in conjunction with the Conference on Electrical Insulation and Dielectric Phenomena (CEIDP), October 16-19, which brings together R&D staff from all over the world to discuss recent advances in electrical insulation, largely aimed at high voltage applications. The workshop will focus on electrical insulation problems that specifically pertain to cryogenic temperatures. Cryogenic dielectrics is an enabling technology for most SPI power applications and many problems need to be resolved in order to achieve success in present and future grid projects, particularly in extending applications to higher voltage ratings. Workshop organizers include Randy James (ORNL), Isidor Sauers (ORNL), Alan Wolsky (ANL), and Toshikatsu Tanaka (Waseda University, Japan).

1.7 HTS Motor R&D with Reliance Electric

C. M. Rey, R. C. Duckworth, M. J. Gouge, and S. W. Schwenterly

A CRADA was implemented in August 2005 between UT-Battelle (ORNL) and Reliance Electric Company (a unit of Rockwell Automation) to perform research related to the commercial viability of industrial motors with HTS windings. Reliance Electric is conducting an SPI project with research focused in eight areas related to commercial viability of industrial motors with HTS windings. The eight areas were identified based upon the past work that Reliance Electric had conducted on development and testing of

HTS motors up to and including the laboratory test of a 1000-hp motor that was later tested in steady state to 1600 hp:

- motor drive interaction
- eddy current heating in end regions
- alternate (second-generation) HTS wire
- alternate HTS motor topologies
- on-board refrigeration
- cryogenic persistent switch
- composite torque tube creep and fatigue
- coil quench protection

One of these R&D areas is the rotor coil quench protection system. A quench is usually an unplanned, rapid transition from the superconducting to the normal conducting state that involves a temperature and voltage spike. If no action is taken, such as the insertion of a dump resistor to dissipate the coil stored energy, the temperature and/or voltage transients could damage the coil conductor or insulation. The objective of the coil-quench focus area is to analyze a quench event in the 1000-hp motor and to develop reliable quench monitoring and protection systems for HTS motors. The purpose of the CRADA project is to conduct R&D on the rotor HTS coil quench model(s) and to provide general technical support to the Reliance Electric team in developing and verifying the quench model. Testing of field coils from the 200-hp and 1000-hp motors at temperatures in the 30 K range will be conducted at ORNL to complement tests in liquid nitrogen (77 K) at Reliance Electric. A picture of the damaged HTS coil from the 1000-hp motor is shown in Fig. 1.35.

Fig. 1.35. A rotor field coil from the 1000-hp motor that was damaged from a quench event.

1.8 SPI Oversight/Readiness Reviews

M. J. Gouge

This risk assessment/reduction program entered its second full year in FY 2005. M. J. Gouge, S. W. Schwenterly, and Paul Bakke (DOE-Golden) participated in the MFCL Technical Advisory Board Meeting with an embedded readiness review on November 17, 2004, at SuperPower. Emphasis was on results from the fault-current testing at KEMA and the initial progress on high-voltage R&D. Feedback was provided to SuperPower management and DOE-HQ.

M. J. Gouge presented a status report on the SPI readiness review program including an overview of 2004 DOE Peer Review comments at the 2005 Wire Development Workshop, St. Petersburg, Florida, on January 19 and 20, 2005. Actions taken in response to the comments of the peer reviewers was also covered. Participation in the Air Force quench and stability workshop in Orlando, Florida, on January 27, 2005, was valuable in that the issues of reliable quench detection and protection in superconducting coils are common to U.S. Department of Defense and DOE HTS applications.

An SPI readiness review was conducted at GE-CRD on April 14, 2005. The scope included HTS field coil excitation, coil turn and layer insulation, and quench protection. Reviewers were Mike Gouge and

Chris Rey, from ORNL, and Charles Oberly from the Air Force Research Laboratory (AFRL). An SPI readiness review of the 5/10-MVA HTS transformer project was conducted at SuperPower, Inc., on May 11, 2005. Reviewers were Mike Gouge and Isidor Sauers (ORNL), Bill Hassenzahl [Applied Energy Analysis (AEA)], and Paul Bakke (DOE-Golden). Most of the discussion focused on the high-voltage failures and dissection of the Phase B coil. It was a review of "lessons learned" that would benefit future HTS transformers as well as all HTS grid applications. An SPI readiness review was conducted at SuperPower, Inc., on June 28, 2005, in conjunction with the MFCL project Technical Advisory Board meeting. Reviewers were Mike Gouge (ORNL), Bill Hassenzahl (AEA), Dave Carruthers (DOE consultant), and Paul Bakke (DOE-Golden). Discussion focused on reliability/lifetime issues of the bulk BSCCO matrix elements and high-voltage R&D and design.

An SPI readiness review was conducted at General Electric Power Systems on July 25 and 26, 2005. The scope included HTS field coil support, electromagnetic shield and vacuum vessel design. Reviewers were Mike Gouge and Brad Nelson, from ORNL, and William Hassenzahl, a consultant from AEA. An SPI readiness review was conducted at General Electric Power Systems on September 27 and 28, 2005. It was the project's preliminary design review whose scope included all generator systems affected by the HTS rotor addition. Reviewers were Mike Gouge, from ORNL, William Hassenzahl, a consultant from AEA, Charles Oberly, from AFRL, and Paul Bakke, from DOE-Golden.

A presentation on the SPI Readiness Review Program was given by M. J. Gouge at the 2005 DOE HTS Peer Review; this activity was ranked 2/9 in the systems area with a score of 85.3.

1.9 Applied Superconductivity Group Laboratories Move from Y-12 to ORNL

J. A. Demko and R. C. Duckworth

1.9.1 Applied Superconductivity Laboratory Moved

In February and March 2005 the Applied Superconductivity Laboratory was moved from the Y-12 NNSA site, where it has been for almost ten years, to a new high-bay laboratory (Building 7625), which is closer to the main X-10 laboratory complex and adjacent to the new ORNL electrical substation. It is a laboratory where experiments on HTS conductors, small cables, and coils are conducted. Equipment includes several Gifford-McMahon (G-M) and pulse-tube cryocoolers, various research cryostats, a 6-T LTS magnet with a large warm bore and several ac and dc high-current power supplies (see Fig. 1.36). The laboratory has been authorized for experimental operations following a rigorous safety review.

Fig. 1.36. Applied Superconductivity Laboratory.

1.9.2 HTS Cable Test Facility Move

The relocation of the cable test facility equipment and the triaxial cable to Building 7625 at the ORNL facility is complete. At the end of the fiscal year, electrical connections were being made to the equipment (power supplies, cryogenic skid, and related equipment) and new casework was being installed. Piping has been installed from the LN tank to the facility. Piping connections to bring LN to the skid, vent line connections, and cooling water connections are planned for October 2005.

2. Technical Progress in Wire Development

2.1 Superconductor Wires

M. P. Paranthaman

2.1.1 Background

High-Temperature Superconductor (HTS) wires are so efficient that they can carry up to 140 times the power of conventional copper wires of the same size. The potential uses for HTS wires in electric power applications include underground transmission cables, oil-free transformers, superconducting magnetic-energy storage units, fault current limiters, high-efficiency motors, and compact generators. Electricity grid losses have grown to be more than 10% of all electricity generated due to resistance and other losses in conventional equipment, and blackouts highlighted transmission bottlenecks in the United States in 2003. Efficiency and reliability will be enhanced when new transmission technologies are used that have reduced line losses and that have the capability to carry more current for a given size of conductor. Superconductors have virtually no electrical resistance; therefore, they can carry current with no electrical energy loss. They come in two types: low-temperature and high-temperature. Low-temperature superconductors (LTSs) work at only very frigid temperatures, near −452°F. Equipment made with LTS wires can be expensive to operate because they need to be chilled with liquid helium. Equipment made with HTS wires, however, work at relatively warmer temperatures (near −320°F) and require less expensive liquid nitrogen to operate.

High-temperature oxide superconductors, discovered in the late 1980s, are moving into the second generation of their development. The first generation relied on bismuth strontium calcium copper oxide (BSCCO); the second generation is based on yttrium barium copper oxide (YBCO), which has the potential to be less expensive and to perform better. One of the main challenges in developing high-performance superconductors has been the brittleness of many of the most promising materials to be drawn into wires that can carry current, yet recent developments allow fabrication of superconductor wires and tapes. This article will provide the present state of superconductor wires and tapes, successes and challenges, and projected applications.

Following the discovery of high-temperature superconductors (HTSs), notably $(Bi,Pb)_2Sr_2Ca_2Cu_3O_{10}$ (BSCCO or 2223) and $YBa_2Cu_3O_{7-x}$ (YBCO or 123), researchers all around the world have searched for ways to fabricate affordable flexible wires that will carry high current density. The U.S. Department of Energy's (DOE's) target cost for the conductor is close to the current copper wire cost of $10/kA-meter. The near-term goal is to fabricate HTS wire in 100-m lengths with current-carrying capacity of 300 A. Robust, high-performance HTS wire will certainly revolutionize the electric power grid and various other electric power equipment as well. American Superconductor Corporation (AMSC) and Sumitomo (Japan) have been widely recognized as the world leaders in manufacturing the first-generation (1G) HTS wires based on BSCCO materials and the oxide-powder-in-tube (OPIT) process. Typically, 1G HTS wires carry critical currents of more than 125 A in piece lengths of several hundreds of meters at the standard 0.41-cm width and ~ 210-μm thickness. However, due to the higher cost of 1G wire and the intrinsic properties of YBCO, the researchers shifted their efforts toward the development of YBCO (second generation – 2G) wires or tapes [1]. One of the main obstacles to the manufacture of commercial lengths of YBCO wire has been the phenomenon of weak links; i.e., grain boundaries formed by the misalignment of neighboring YBCO grains are known to form obstacles to current flow. When the grains are carefully aligned, the low angle boundaries between superconducting YBCO grains allow more current to flow. In fact, below a critical misalignment angle of 4°, the critical current density approaches that of YBCO films grown on single-crystal substrates. The schematics of the 1G and 2G HTS wire architectures are shown in Fig. 2.1. Typically, 2G HTS wires have three components: flexible metal substrate, buffer layers, and YBCO superconductor layers. Several methods were developed to obtain biaxially textured metal substrates suitable for fabricating high-performance YBCO coated conductors. They are ion-beam

assisted deposition (IBAD), Rolling-Assisted Biaxially Textured Substrates (RABiTS™) and inclined-substrate deposition (ISD). The industry standard for characterizing the 2G wire is to divide the current by the width of the wire. With either a 3-μm-thick YBCO layer carrying a critical current density of 1 MA/cm^2 or 1-μm-thick YBCO layer carrying a critical current density of 3 MA/cm^2, the electrical performance would be 300 A/cm-width. Converting these numbers to the industry standard of 0.4-cm-wide HTS wire would correspond to 120 A, which is comparable to that of the commercially available 1G wire. Further increase in YBCO film thickness or finding a way to incorporate two layers of YBCO (either double sided coating or joining two YBCO tapes face to face) in single-wire architecture would then give performance exceeding 1G wire (i.e., high overall engineering critical current density at 77 K). The other important advantages of 2G wires over 1G wire are that YBCO has better in-field electrical performance at higher temperatures, a potentially lower-cost fabrication process, and low alternating-current (ac) losses.

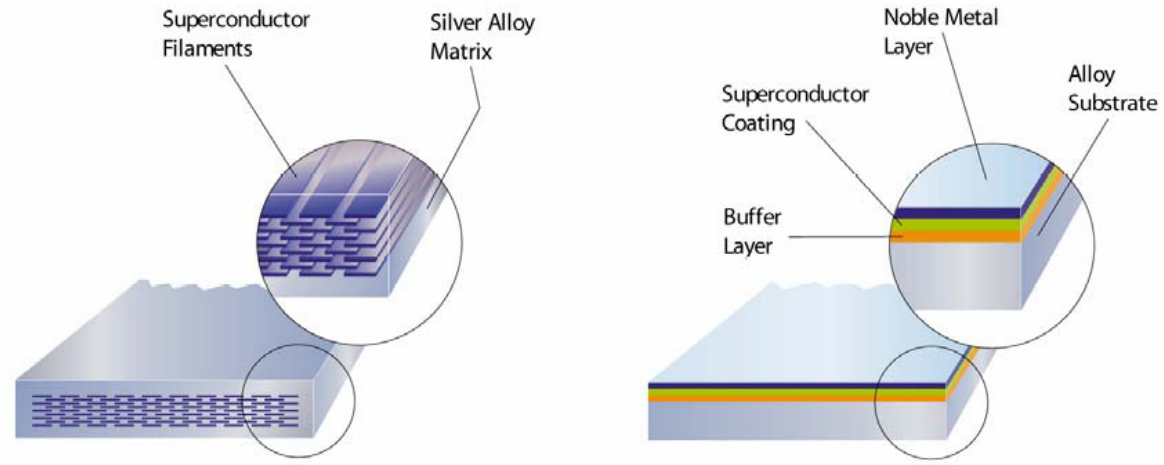

Fig. 2.1. Schematics of HTS wires. Left: first-generation BSCCO wire multifilamentary composite. Right: second-generation YBCO coated conductor tape (courtesy of American Superconductor).

In the IBAD process, the ion beam is used to grow textured buffer layers onto a flexible but untextured metal, typically a nickel superalloy. After the initial announcement by Iijima et al. of the IBAD process to grow textured yttria-stabilized zirconia (YSZ) layers (Fujikura Ltd., Japan, 1992) [2], researchers at Los Alamos National Laboratory (LANL, 1995) perfected the process and achieved high-performance YBCO films on IBAD-YSZ templates [3]. To date, three IBAD templates, namely YSZ, gadolinium zirconium oxide, $Gd_2Zr_2O_7$ (GZO), or magnesium oxide (MgO) are being used to make YBCO tapes. The RABiTS™ process, developed at ORNL (1996), uses thermomechanical processing to obtain flexible, cube-textured nickel-alloy substrates [4]. Both buffers and YBCO superconductors are then deposited epitaxially on the textured nickel alloy substrates. The starting substrate serves as a structural template for the YBCO layer, which has substantially fewer weak links. Wires made by the OPIT process (1G wire) are limited by higher cost because the major component is high-purity silver. In the RABiTS™ and IBAD processes, silver is replaced by a low-cost nickel alloy, which allows for fabrication of less-expensive HTS wires. In the ISD process, the textured buffer layers are produced by vacuum depositing material at a particular angle on an untextured nickel alloy substrate. After the discovery of the ISD-YSZ process by Hasegawa et al. (Sumitomo, Japan, 1996) [5], THEVA and the Technical University of Munich, Germany, perfected the reel-to-reel MgO buffer layer texturing by ISD on Hastelloy tape (2003) [6]. Recently, several industries have demonstrated that they can produce 2G wires in 10– to 100-m lengths with critical currents ranging from 50 to 300 A/cm-width based on either IBAD or RABiTS™ technology. Very recently (2005), the THEVA group produced its first 40-m class

YBCO tape-based ISD-MgO technology. The 37 m × 10 mm wire, based on a nonmagnetic Hastelloy C276 steel tape with ISD-aligned MgO buffers, exhibited an average critical current of 158 A. This demonstration would correspond to 5846 A-m (158 A × 37 m).

Methods to produce textured templates for growing high-performance YBCO coated conductor wires include IBAD-YSZ, IBAD-MgO, IBAD-GZO, ISD-MgO, and RABiTS™. On these five templates, high-deposition-rate YBCO processes such as trifluoroacetate-based metal-organic deposition (MOD), metal-organic chemical vapor deposition (MOCVD) and high-rate pulsed-laser deposition (PLD) are being used to deposit the superconductor films. The main challenge is to combine the oriented template concept and superconductor deposition process to fabricate HTS tapes in kilometer lengths. Industries from the United States and Japan are leading in this area while industries from Europe, Korea, and China are trying to catch up with them. The present status of 2G HTS wires is summarized in Table 2.1.

Table 2.1. Status of the 2G HTS wire technology as of July 2005

Country/organization	Length (m)	Critical current at 77K (A/cm width)	Substrate/HTS deposition process
U.S.: American Superconductor	34	186	RABiTS™/MOD
	10	272	RABiTS™/MOD
	Short samples	~400	RABiTS™/MOD
U.S.: SuperPower	100	70	IBAD/YSZ/PLD
	97	104	IBAD/YSZ/MOCVD
	Short samples	407	IBAD/M_gO/MOCVD
Japan-Sumitomo	35	175	RABiTS™/PLD
	Short samples	357	RABiTS™/PLD
	10	130	RABiTS™/MOD
	Short samples	196	RABiTS™/MOD
	105	NA	RABiTS™
Japan- Showa Electric	6	69	IBAD-GZO/MOD
	230	NA	RABiTS™ (Ni-W)
Japan-Fujikura	105	126	IBAD-GZO/PLD
	Short samples	~300	IBAD-GZO/PLD
	255	NA	IBAD-GZO
Japan-ISTEC	100	159	IBAD-GZO/PLD
	4	270	IBAD-GZO/MOD
	Short samples	413	IBAD-GZO/MOD
	220	NA	IBAD-GZO
Europe-THEVA	37	158	ISD-MgO/Evap.
	5	237	ISD-MgO/Evap.
	1	422	ISD-MgO/Evap.
Europe-Edison Spa	2	120	RABiTS™/Coevap.
	Short samples	220	RABiTS™/Coevap.
Korea- KERI	4	97	RABiTS™/Coevap.
	1	107	RABiTS™/PLD

Coevap. = electron beam co-evaporation.
Evap. = electron beam evaporation
GZO = gadolinium zirconium oxide, $Gd_2Zr_2O_7$
IBAD = ion-beam-assisted deposition
ISD = inclined-substrate deposition
MgO = magnesium oxide
MOCVD = metal organic chemical vapor deposition
MOD = metal organic deposition
PLD = pulsed-laser deposition
RABiTS™ Rolling-Assisted Biaxially Textured Substrates

Courtesy of Oak Ridge National Laboratory and Los Alamos National Laboratory

The following attributes can affect the performance of 2G HTS wire:

- substrate
  - mechanical properties (especially critical tensile stress)
  - ferromagnetism (ac loss caused by ferromagnetic loss)
  - resistivity (eddy current loss)
  - grain size (hysteretic loss)
- HTS deposition process
  - throughput
  - availability of long piece lengths
  - in-field performance, especially perpendicular to tape
  - thick films (small aspect ratio for less hysteretic loss)
- stabilizer
  - fully encapsulating wire or stabilizer on one side
  - rounded edges for direct dielectric integration
  - sharp edges

A number of issues related to the development of power applications for 2G HTS wires by the year 2010 were identified at the DOE Coated Conductor Development Roadmapping Workshop II (Washington D.C., July 28–29, 2003). They included low ac loss, design and current-carrying capacity of the stabilizer, conducting substrates, and alternate conductor designs. (See Table 2.2 for specifications.)

Table 2.2. Specifications for 2G HTS wires to be developed for power applications by 2010

Geometry	Face-to-face; neutral axis; two-sided coating
Length (m)	100–1000
Width (mm)	≤ 4.1
Bend diameter (cm)	2–3.5
Stress (MPa)	200 (300 @ 77 K)
Irreversible strain limit (%)	
Tension	0.4–0.6
Compression (for magnets)	0.3–1
J_E (A/cm^2)	10,000–20,000 at 30–65 K and 3 T (or at operating conditions)
I_c (A)	100–200 at operating conditions
I_c (A/cm-width)	1000 @ 77 K and self-field
ac loss (W/kA-m)	0.25
n value	≥ 14
Large-volume price ($)	10/kA-m

Source: U.S. Department of Energy Coated Conductor Development Roadmapping Workshop II, Washington D.C., July 28–29, 2003.

In summary, five different templates (IBAD-YSZ, IBAD-GZO, IBAD-MgO, ISD-MgO, and RABiTS™) have been developed, and superconductivity companies around the world are in the process of taking the technology to the pilot scale to produce commercially acceptable 100-m lengths. In addition, three different methods (MOD, MOCVD, and high-rate PLD) have been used to fabricate high-critical-current 100-m lengths of YBCO coated conductors. The current research in the area of HTS wire technology is focused on increasing the flux-pinning properties of YBCO superconductor wires and to reduce their ac loss for various military applications [7].

2.1.2 Outlook

DOE has funded three different SPI projects to demonstrate the use of HTS power cables for electric transmission and distribution: Long Island HTS power cable, Albany HTS power cable, and Columbus HTS power cable. The goal of the Long Island HTS power cable project is to demonstrate a 610-m,

600 MW HTS power transmission cable operating at 138 kV in the Long Island power grid, the first-ever installation of a superconductor cable in a live grid at transmission voltages. The goal of the Albany HTS power cable project is to demonstrate the technical and commercial viability of HTS cables by operating a 350-m superconducting cable, including a 30-m section made from 2G HTS wire, between two Niagara Mohawk substations. The goal of the Columbus HTS power cable project is to complete the development, installation, and testing of a 200-m, three-phase HTS power cable at a substation in Columbus, Ohio. This project will demonstrate how a triaxial HTS cable may be used in the future to replace existing oil-filled underground copper cables and greatly increase the capacity of power link. The future of HTS wire technology research depends heavily on the successful demonstration of these power cables.

2.1.3 References

1. M. Paranthaman and T. Izumi, editors, "High-Performance YBCO-Coated Superconductor Wires," *MRS Bulletin* **29**(8), August 2004.
2. Y. Iijima, N. Tanabe, O. Kohno, and Y. Ikeno, *Appl. Phys. Lett.* **60**, 769, 1992.
3. X. D. Wu, S. R. Foltyn, P. N. Arendt, W. R. Blumenthal, I. H. Campbell, J. D. Cotton, J. Y. Coulter, W. L. Hults, M. P. Maley, H. F. Safar, and J. L. Smith, *Appl. Phys. Lett.*, **67**, 2397, 1995.
4. A. Goyal, D. P. Norton, J. D. Budai, M. Paranthaman, E. D. Specht, D. M. Kroeger, D. K. Christen, Q. He, B. Saffian, F. A. List, D. F. Lee, P. M. Martin, C. E. Klabunde, E. Hatfield, and V. K. Sikka, *Appl. Phys. Lett.* **69**, 1795, 1996.
5. K. Hasegawa, K. Fujino, H. Mukai, M. Konishi, K. Hayashi, K. Sato, S. Honjo, Y. Sato, H. Ishii, and Y. Iwata, *Appl. Supercond.* **4**, 487, 1996.
6. W. Prusseit, R. Nemetschek, R. Semerad, Lumkemann, M. Bauer, and H. Kinder, *Physica C* **392**, 801, 2003.
7. J. L. Macmanus-Driscoll, S. R. Foltyn, Q. X. Jia, H. Wang, A. Serquis, L. Civale, B. Maiorov, M. E. Hawley, M. P. Maley, and D. E. Peterson, *Nature Materials* **3**, 439, July 2004.

2.2 Irradiation-Free Columnar Defects Composed of Self-Assembled Nanodots and Nanorods Result in Strongly Enhanced Flux Pinning in YBCO Films

A. Goyal, S. Kang, K. J. Leonard, P. M. Martin, A. A. Gapud, M. Varela, M. Paranthaman, E. D. Specht, D. K. Christen, S. J. Pennycook, and F. A. List (ORNL); J. R. Thompson (ORNL and UTK); A. O. Ijaduola (UTK)

2.2.1. Introduction

The development of biaxially textured, second-generation HTS wires is expected to enable most large-scale applications of HTS materials, in particular electric-power applications.[1] For many potential applications, high critical currents in applied magnetic fields are required. It is well-known that columnar defects generated by irradiating HTS materials with heavy ions significantly enhance the in-field critical current density.[2-4] Hence, for over a decade scientists worldwide have sought means to produce such columnar defects in HTS materials without the expense and complexity of ionizing radiation. Using a simple and practically scalable technique, we have succeeded in producing long, nearly continuous vortex pins along the *c*-axis in YBCO, in the form of self-assembled stacks of $BaZrO_3$ (BZO) nanodots and nanorods. The nanodots and nanorods have a diameter of about 2 to 3 nm and an areal density ("matching field") of 8 to 10 T for 2 vol % incorporation of BZO. In addition, four misfit dislocations around each nanodot or nanorod are aligned and act as extended columnar defects. YBCO films with such defects exhibit significantly enhanced pinning with less sensitivity to magnetic fields (H). In particular, at intermediate field values, the current density varies as $J_c \sim H^{-\alpha}$, with $\alpha \sim 0.3$, rather than the usual values of 0.5 to 0.65. Similar results were also obtained for $CaZrO_3$ (CZO) and YSZ incorporation in the form of nanodots and nanorods within YBCO, indicating the broad applicability of the process. The process could also be used to incorporate self-assembled nanodots and nanorods within matrices of other materials for different applications, such as magnetic materials.

Second-generation HTS conductors or "coated-conductors" comprise a flexible metallic substrate upon which several buffer layers and then the superconducting layer is deposited. The key goal is to have a biaxially textured superconducting layer so that few high-angle, weakly conducting grain boundaries are present. This is accomplished by epitaxial formation of the superconducting layer on biaxially textured oxide surfaces deposited upon the substrate. Three techniques have been developed to accomplish this: ion-beam assisted deposition (IBAD)[5] of biaxially textured buffers on polycrystalline alloy substrates, epitaxial deposition of buffer multilayers on rolling assisted, biaxially textured substrates (RABiTS™),[6] and inclined substrate deposition (ISD)[7] of buffers on polycrystalline alloy substrates. For epitaxial YBCO on substrates fabricated by using all three techniques, the intergranular critical current density is enhanced due to suppression of weak links at grain boundaries. However, for practical application of HTS materials, the in-field performance (intragranular) critical current density also needs to be enhanced further. The first significant progress toward this goal was made by incorporation of randomly distributed 5- to 100-nm BZO nanoparticles with a modal particle size of 10 nm.[8] The incorporation of randomly distributed, heteroepitaxial BZO particles introduces significant strain in the YBCO lattice because of the large lattice mismatch between BZO and YBCO. The strain generates misfit dislocations aligned along the crystallographic *c*-direction of YBCO and an areal density of 400 μm^{-2} (the areal density for an undoped YBCO film is 80 μm^{-2}). These defects resulted in a 1.5 to twofold improvement in the in-field critical current density in the magnetic field range of 1to 5 T. Another recent report, describing depositions of multiple layers of Y_2BaCuO_5 (211) and YBCO, also described how nanoparticles can be incorporated into the YBCO film.[9] In that case, the nanoparticles having an average size of about 15 nm were aligned along the *ab*-planes (i.e., parallel to the Cu-O sheets of the layered superconductor) and had an areal density of about 1.1×10^{11} particles cm^{-2}. Both the self-field and in-field critical current densities were enhanced by the incorporation of such particles.

Here we describe the use of a simple and industrially scalable route to achieve massive enhancements of the in-field critical current density. The technique produced columnar defects that are self-assembled stacks of nanodots and nanorods of nonsuperconducting phases within epitaxially grown YBCO films on RABiTS™ substrates

2.2.2. Experimental Details

Self-assembled nanodots and nanorods of nonsuperconducting phases were incorporated by performing laser ablation from a single target composed of a mixture of YBCO powder and nanoparticles of the chosen nonsuperconducting phase. Nanoparticles of materials such as BZO, CZO, YSZ, and $Ba_xSr_{1-x}TiO_3$ are commercially available from vendors such as Sigma-Aldrich. These nanoparticles, with a sharp particle size distribution ranging from 10 to 100 nm, are well-mixed with YBCO powder. The resulting composite powder is then pressed and sintered to form a target for PLD. All depositions were performed on RABiTS™ substrates with the configuration Ni-5at%W (50 μm)/Y_2O_3 (75 nm)/YSZ (75 nm)/CeO_2 (75 nm).[10] An XeCl (308-nm) excimer laser was used at a repetition rate of 10 Hz to deposit the superconductor (deposition temperature of 790°C, oxygen partial pressure of 120 mTorr). The standard four-point probe method and a voltage criterion of 1 μV/cm were used to measure transport critical current density.

2.2.3. Results and Discussion

Figure 2.2 shows cross-section transmission electron microscopy (TEM) images of the YBCO film. Figure 2.2(a) shows columns of BZO nanodots aligned along the [001] or the crystallographic *c*-axis of YBCO. The red arrows on the image point to the various columns of BZO. The image was taken with the sample tilted along the g=001 vector of the YBCO film so that the columnar properties of the nanoparticles, which are small in comparison with the local thickness of the sample, could be better visualized. Figure 2.2(b), taken from a different region in the sample, indicates that nanorods of BZO are also present. The relative fraction of BZO incorporated as nanodots and nanorods as determined by the TEM observations is about 60% nanodots and 40% nanorods.

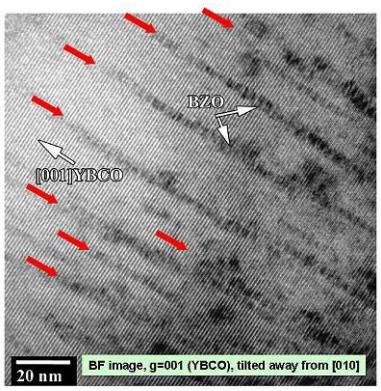

(a)
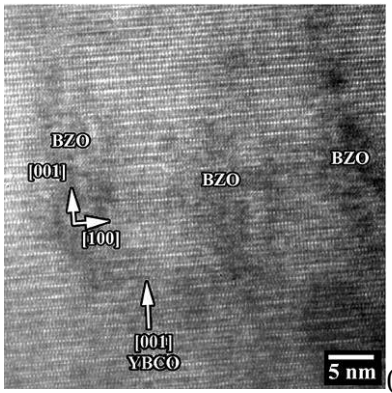

(b)

Fig. 2.2. Cross-section TEM of a YBCO film on RABiTS™ with self-assembled BZO nanodots and nanorods. (a) The BZO nanodots are aligned along the crystallographic *c*-direction in the YBCO and are about 2 to 3 nm in diameter. (b) Cross-section image showing the presence of both nanorods and nanodots.

Figure 2.3(a) shows a plan view TEM image in low magnification, directed down the crystallographic *c*-axis of the YBCO. The image shows the areal distribution of nanodots and nanorods within the thin section of a TEM foil. The intersecting lines within the particles are extinction bands, with the left side of the image being a thicker region of the TEM foil than that of the right. From the areal density of BZO nanoparticles in Figure 2.3(a), one finds a matching field, a magnetic field with equivalent vortex density $B_\phi = \phi_o/a^2$, of about 8 to 10 T, where $\phi_o = 2.07\times10^{-11}$ T-cm^2 is the flux quantum and a is the average in-plane separation of vortices. Figure 2.3(b) is a higher-magnification image, clearly showing that the contrast seen in Figure 2.2 and 2.3(a) is from distinct particles of a different phase. The array of BZO nanodots and/or nanorods can be approximated by a square lattice with a lattice spacing, a ~ 15 nm, as evident from Fig. 2.3(b). Figure 2.3(c) shows a Z-contrast STEM image of a single nanodot within the YBCO matrix. Misfit dislocations can be seen around each BZO nanodot. Since the nanodots and nanorods are aligned along the *c*-direction of YBCO, the strain from the misfit dislocations is also aligned and extended. For this unique configuration, these BZO nanodots and nanorods as well as the correlated misfit dislocations around them may be expected to form ideal flux-pinning sites similar to damage tracks caused by heavy ion-irradiation.[2-4]

The superconducting transport properties of 0.2-μm-thick epitaxial YBCO films fabricated both with and without incorporation of self-assembled nanodots and nanorods are shown in Fig. 2.4. Figure 2.4(a), a plot of transport critical current density vs applied field for YBCO and a YBCO + 2 vol % BZO sample with $H \parallel c$ at 77 K, shows that the dopants reduce the sensitivity to the magnetic field. For example, at an applied field of 1.5 T, the critical current density for undoped YBCO decreases by a factor of about 12, whereas the sample with BZO nanodots and nanorods decreases only by a factor of 5. The enhancement in critical current density can be seen for all fields despite a decrease in the transition temperature of the doped film [T_c ~87 K as determined magnetically via a superconductivity quantum interference device (SQUID) magnetometer; T_c ~ 90 K undoped film]. Figure 2.4(b) shows a log-log plot of critical current density normalized to self-field critical current density vs applied field. It can be seen that the exponent in the power-law relationship $J_c \sim H^{-\alpha}$, is 0.31 for the film containing the BZO nanodots and nanorods, whereas it is 0.5 for the undoped YBCO film. This reduced fall-off in critical current density as a function of applied field shows the strong pinning for $H \parallel c$ for the doped samples.

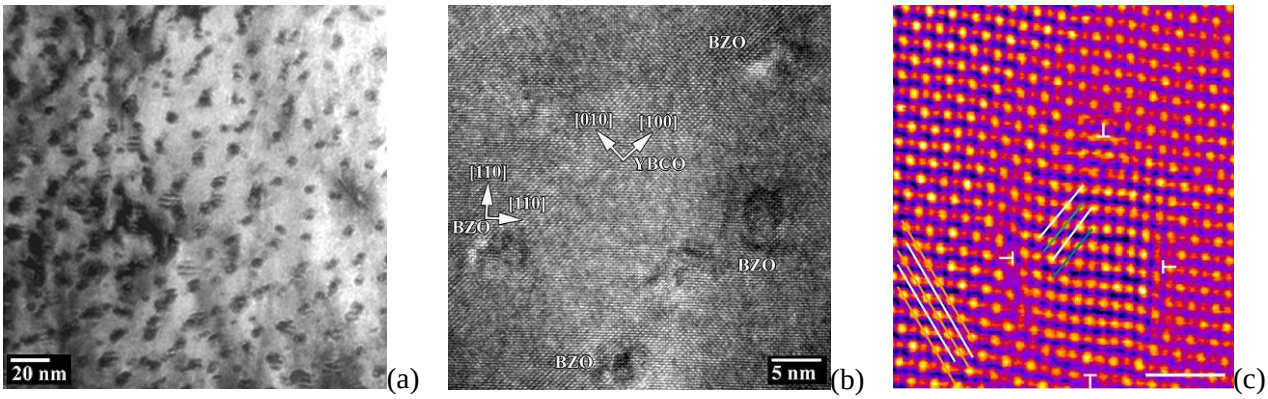

Fig. 2.3. Plan-view TEM images of the YBCO film on RABiTS™ with self-assembled BZO nanodots and nanorods. (a) Low-magnification image showing the high density of nanodots and nanorods. (b) Higher-magnification image showing that the BZO nanodots and nanorods within the YBCO are about 2 to 3 nm in diameter and can be approximated as situated on a square lattice with a spacing of about 15 nm. (c) Z-contrast STEM image of a single BZO nanodot. The extra semiplane in the edge dislocation cores is marked in white. Four misfit dislocations can be seen around the BZO nanodot. Because the BZO nanodots are aligned along the *c*-direction, the strain is also aligned, forming an extended defect. In the YBCO, the BaO planes have been marked with white lines; CuO lines are marked with yellow lines. In the BZO nanoparticle, the ZrO planes have been marked with green lines, and the BaO planes are marked with white lines. The scale bar is 1.5 nm.

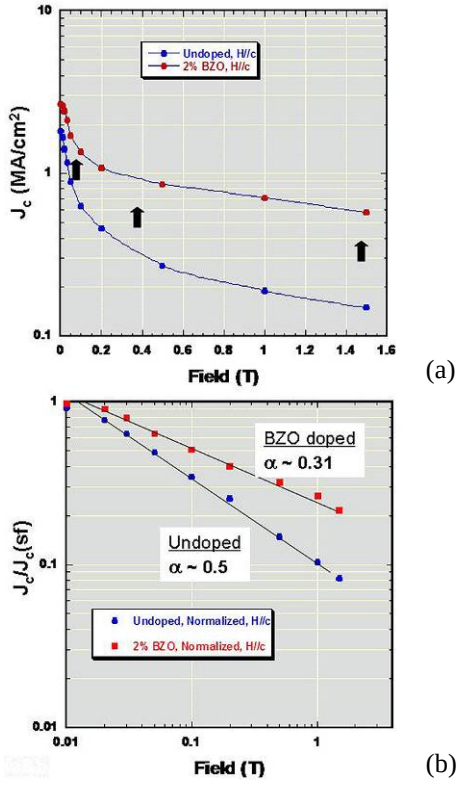

Fig. 2.4. Superconducting transport properties of YBCO films on RABiTS™. (a) Critical current density as a function of applied magnetic field for an undoped YBCO film compared with a YBCO film with 2 vol % incorporation of BZO nanodots and nanorods. A very significant enhancement of critical current density is seen for all fields. (b) A log-log plot of normalized critical current density as a function of applied field shows that the power-law exponent in the relation $J_c \sim H^{-\alpha}$ is only 0.31 for the YBCO film with self-assembled nanodots and nanorods, whereas it is 0.5 for the undoped film.

Figure 2.5 shows the angular dependence of critical current density taken at 77 K and 1T applied field. The angular dependence curve is shifted to a higher critical current density at all angles. In particular, a very pronounced peak for $H \parallel c$ (angle = 0°) can be observed, indicative of strong pinning defects along the *c*-axis for the film containing BZO nanodots and nanorods. A 2-mm-wide bridge was patterned on the samples so that higher-field and lower temperature data could be obtained (the original width of the sample was 5mm) and thus the maximum measuring current restrictions in the system used for these measurements could be met.

During the patterning process and subsequent handling, some sample degradation occurs and the self-field critical current density is reduced slightly. Nevertheless, the data of transport critical current density vs magnetic field at higher applied fields applied parallel to the *c*-axis at 77, 65, and 40 K adequately show the trends and improvement in critical current density (see Fig. 2.6). The data show that the enhancement of critical current density at higher fields (over 7 T) with self-assembled BZO nanodots and nanorods is even more significant, a factor of 6 or more; this improvement also extends to lower temperatures, as is evident in Fig. 2.6.

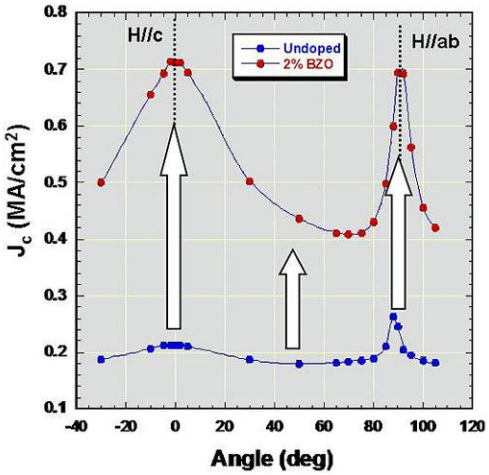

Fig. 2.5. Superconducting transport properties of YBCO films on RABiTS™. Angular dependence of critical current density at 77 K, 1 T for an undoped YBCO film compared with a YBCO film with 2 vol % incorporation of BZO nanodots and nanorods. Measurements were made in a configuration such that the applied field is always perpendicular to the current. A massive enhancement of critical current density is observed at all angles, in particular for *H*//*c* (angle = 0°).

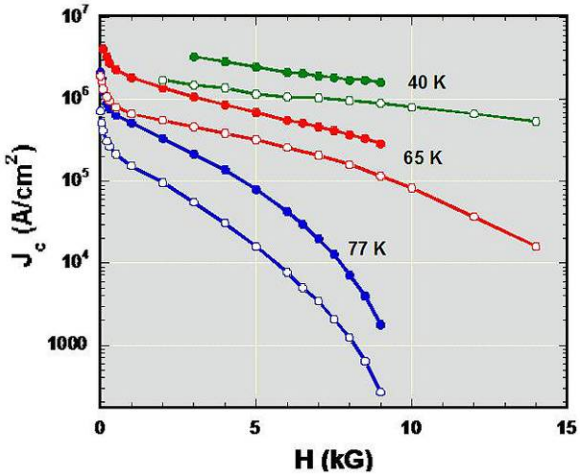

Fig. 2.6. Superconducting transport properties of YBCO films on RABiTS™. Critical current density vs applied magnetic field for high fields as a function of measurement temperature for an undoped YBCO film compared with a YBCO film with 2 vol % incorporation of BZO nanodots and nanorods. Large increases in critical current density can be seen for all fields at all measurement temperatures.

It is not meaningful to compare the magnitude of the transport critical current density shown in Figs. 2.4, 2.5, and 2.6 to the data reported in Ref. 9 because the films here are thinner and critical current density generally depends on thickness, typically decreasing exponentially with increase in thickness.[11,12] However, comparison with the method suggested in Ref. 9 (i.e., multilayering of a YBCO film with 211/123 layers to form rows of 211 nanoparticles perpendicular to the *c*-axis) is possible because films of similar thickness have been grown on RABiTS™ substrates.[13,14]

The angular dependence of critical current density at 77 K and 1 T is markedly different for films on RABiTS™ made by using the 211/123 multilayering approach than for films made according to the approach in this report. Although the peak at $H||ab$ is similar in both samples, the 211/123 multilayered sample has no critical current density peak for $H||c$. Hence, significantly superior pinning is observed over a broad angular range for the present case of self-assembled BZO nanodot and nanorod incorporation. Compared with YBCO films without the incorporation of self-assembled nanodots and nanorods, the data in Fig. 2.4(a), shows a factor of about 5 improvement in critical current density in the field range of 0.4 to 1.5 T at 77 K, and more than a factor of 6 beyond 7 T. This improvement is better than what was reported for incorporation of randomly distributed nanoparticles of BZO in the range of 5 to 100 nm.[8] Driscoll et al.[8] show that incorporation of randomly distributed BZO nanoparticles within epitaxial YBCO films on single-crystal and IBAD substrates results in an enhancement of critical current density by a factor of 1.5 to 2 over a field range of 1 to 5 T and a factor of 5 higher at 7 T.

Detailed X-ray analysis and selected area electron diffraction in TEM show that the BZO nanodots and nanorods are epitaxial with the YBCO matrix. Because BZO and YBCO have about a 9% lattice mismatch, significant strain is expected during the growth of the film. Minimization of this large misfit strain may be the driving force for the vertical self-assembly of BZO nanodots and nanorods within the YBCO film. The question now arises whether this simple method can be extended to allow incorporation of other materials into YBCO films. Figure 2.7(a) shows cross-section TEM images for incorporation of 2 vol % CZO nanodots and nanorods within a YBCO film produced by using the same technique as described above. Figure 2.7(b) is a cross-section TEM image of YBCO film in which 1 vol % YSZ nanodots and nanorods were incorporated by the same method. The YBCO film in Fig. 2.7(b) was tilted off its [010] axis to better visualize the formation of nanorods through the effects of the electron beam interactions through the TEM foil. For the case of CZO, more self-assembled nanodots are seen; for YSZ, more nanorods are seen compared to BZO. The differences in relative volume fractions of nanodots and nanorods is expected to relate to differences in lattice misfit strain as well as reactions of the inclusions with YBCO. For example, in the case of YSZ, the self-assembled nanodots and nanorods have reacted with YBCO to form BZO. The angular dependence of critical current density at 77 K, 1 T shows significant enhancement over undoped YBCO, even though the transition temperatures are significantly reduced for these films (T_c = 85 K for the 1 vol % YSZ and to 80 K 2 vol % CZO doped film). Overall, the TEM images and the observation of angular peaks in critical current density for $H \parallel c$-axis show that this method can produce correlated nanostructures with a variety of dopant materials.

(a)

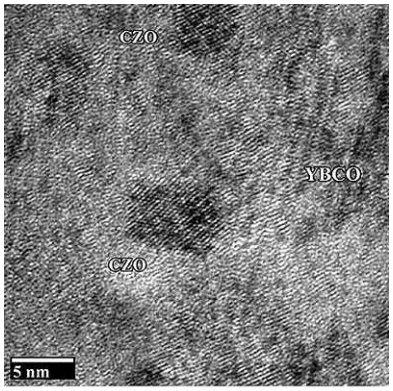

(b)

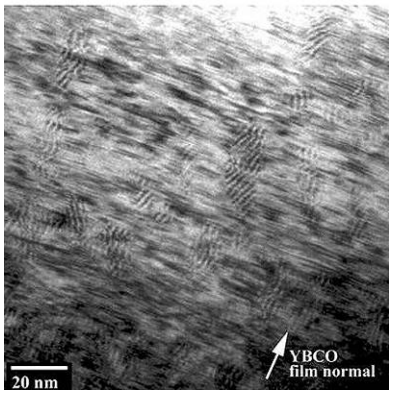

Fig. 2.7. Cross-section TEM images for YBCO films on RABiTS™. (a) Film with 2 vol % CZO nanodots and nanorods. (b) YBCO film with 1 vol % YSZ nanorods.

Since its first public disclosure, in several conferences last year and early this year,[15-18] this work has generated significant interest and worldwide attention. A good confirmation of the results reported here is the very recent work of Yamada et al.,[19] which has reproduced the same microstructure of columnar, self-aligned nanodots.[15-18] Yamada et al. show incorporation of columnar defects of BZO nanodots in 0.25-μm-thick $GdBa_2Cu_3O_{7-x}$ and $SmBa_2Cu_3O_{7-x}$ films on IBAD substrates via PLD. For reasons that are unclear, they found no improvement in critical current density for fields up to 2 T for $GdBa_2Cu_3O_{7-x}$ films

and for fields up to 6 T for the $SmBa_2Cu_3O_{7-x}$ films. At higher fields where improvement in critical current density is observed, the relative effects are smaller than those reported here.

It should be possible to use a similar approach to incorporate nanodots and nanorods of one phase into another for other applications, particularly for ceramic inclusions within a ceramic matrix. Composites of metal/alloy nanodots within a ceramic matrix should also be possible. Significant interest has been shown recently for potential uses of such composites for applications other than superconductivity.[20-22]

2.2.4 References

1. *Second Generation HTS Conductors*, ed. A. Goyal, Kluwer Academic Publishers, Boston, 2004.
2. L. Civale et al., *Phys. Rev. Lett.* **67**, 648–51 (1991).
3. R. Weinstein et al. *Supercond. Sci. Technol.* **18**, S188–93 (2005).
4. Q. Li et al., *IEEE Trans. on Appl. Supercon*. **15**, 2787–89 (2005).
5. J. R. Groves et al., *Physica C* **382**, 43–47 (2002).
6. A. Goyal et al., *Appl. Phys. Lett*. **69**, 1795–97 (1996).
7. M. Bauer, R. Semerad, and H. Kinder, *IEEE Trans. on Appl. Supercon*. **9**, 1502 (1999).
8. J. L. Macmanus-Driscoll et al. *Nat. Mater*. **3**, 439–43 (2004).
9. T. Haugan et al., *Nature* **430**, 867–69 (2004).
10. A. Goyal, U. Schoop, and P. Paranthaman, *MRS Bulletin* **29**, 552–63 (2004).
11. S. R. Foltyn et al., *Appl. Phys. Lett.* **75**, 3692 (1999).
12. B. W. Kang et al., *J. Mater. Res*. **17**, 1750 (2002).
13. T. Haugan et al., *Physica C* **425**, 21–26 (2005).
14. A. Gapud et al. *Appl. Phys. Lett.* (to be submitted).
15. A. Goyal et al., presented at the 2004 Annual Peer Review of the U.S. Superconductivity Program for Electric Systems, July 27–29, 2004.
16. A. Goyal et al., presented at the International Workshop on Coated Conductor for Applications, CCA 2004, Oiso Prince Hotel, Kanagawa, Japan, 19–20 November 2004.
17. A. Gapud et al., presented at the 2005 Wire Development Workshop, January 19–20, St. Petersburg, Florida.
18. S. Kang et al., presented at the MRS Spring Meeting, San Francisco, California, April 2005.
19. Y. Yamada et al., *Appl. Phys. Lett*. **87**, 132502 (2005).
20. J. Narayan and A. Tiwari, *J. Nanoscience and Tech.* **4**, 726–32 (2004).
21. A. Tiwari et al., *J. Nanoscience and Tech*. **3**, 368–71 (2003).
22. D. Kumar et al., *J. Mater. Res*. **17**, 738–42 *(*2002).

2.3 Controllable Angular Dependence of Critical Current Density in ex situ YBCO Coated Conductors

R. Feenstra, A. A. Gapud, P. M. Martin, and D. K. Christen, (ORNL); T. G. Holesinger, B. A. Maiorov, and L. Civale (LANL)

Ex situ processes based on the high-temperature conversion of precursor layers containing BaF_2 are being developed in HTS programs worldwide as a potentially commercial route to depositing the YBCO (or RBCO) layer in coated conductor technology. AMSC has selected a solution-based MOD technique as its primary approach for precursor deposition in their pre-pilot scale-up facilities. The Wire Development Group, led by AMSC, supports this scale-up effort by providing a scientific foundation for continuing properties improvement over time and by providing a platform for evaluating and comparing different approaches toward optimization. ORNL's contribution to the objectives of the Wire Development Group is to utilize the enhanced versatility of a complementary technique to deposit the precursor layer to

explore a broad range of optimization parameters, including the YBCO film thickness, compositional effects, and tailored additions to the precursor layer. This complementary technique uses physical vapor deposition (PVD) from three electron-beam sources in a vacuum system, one source containing BaF_2. Structural investigations by electron microscopy (TEM and SEM) and other techniques have revealed that both precursor types lead to similar, laminar microstructures in the YBCO, induced by closely related thermodynamic conversion and growth mechanisms. Thus, both methods can be used to produce YBCO coatings on RABiTS™ of comparably high structural quality and critical current performance.

An important target set by AMSC is the achievement of controllable dependences of critical current and critical current density in applied magnetic fields (H) on the orientation in which the field is applied. Due to the structural and electronic anisotropy of YBCO, flux pinning provided by featureless defects (e.g. point defects) typically results in a lower critical current density for fields applied parallel to the *c*-axis (perpendicular to the tape surface) than fields parallel to the tape (i.e., parallel to the *a*-*b* planes). Variations in the YBCO microstructure, accompanied by the incorporation of variable defect types or densities, provide a means to modify the angular dependence of critical current density. Based on this notion, a key goal of Wire Development Group research in FY 2004 has been to develop procedures to modify the angular dependence in a reproducible way and identify underlying defect structures. This research is targeted toward large-scale production of application-specific coated conductors. A highlight of ORNL research contributing to the Wire Development Group effort has been the identification of processing parameters by which the ratio of $J_c(H||c)/J_c(H||ab)$ can be controlled in opposite ways, paving the way for engineering of specified characteristics.

Figure 2.8 shows angular dependent critical current density data for films processed ex situ at ORNL. The films were deposited on RABiTS™ metallic templates provided by AMSC and on similar templates prepared at ORNL. To account for slight differences between the different templates and for the differences in film thickness, critical current density is normalized by the self-field critical current density for each film. Angular dependent critical current density data for a standard-processed film are included in Fig. 2.8 as a reference point. Fig. 2.8 shows that, compared with the reference data, the critical current density peak for fields parallel to (a,b) is progressively reduced by certain processing changes and by adding excess Y to the precursor layer. An additional dependence on the YBCO thickness appears to exist as well, resulting in smaller critical current density peaks for $H||(a,b)$ in thicker coatings. For one of the films (red curve), the standard anisotropy with $J_c(a,b)>J_c(c)$ is even reversed. The latter result in particular demonstrates the high flexibility of the ex situ technique, as strong pinning is induced in orientations approximately perpendicular to the film surface, despite the fact that the grain structure is laminar.

Although a relatively flat angular dependence of critical current density may be advantageous for some applications, for others such as coils for magnets or certain motor designs, an anisotropy ratio of $J_c(ab)/J_c(c) \cong 2$ is better suited. For those applications, the critical current density peak along (a,b) may need to be enhanced. Figure 2.9 illustrates the potential to reverse the effects shown in Fig. 2.8 by applying a different processing modification (per agreement with AMSC, the corresponding processing change is not disclosed in this report). Preliminary data suggest that the two effects may be combined, showing the ability, in principle, to engineer the angular dependence of critical current density. Future work aims to demonstrate this explicitly for certain field and temperature ranges consistent with the application-driven specifications.

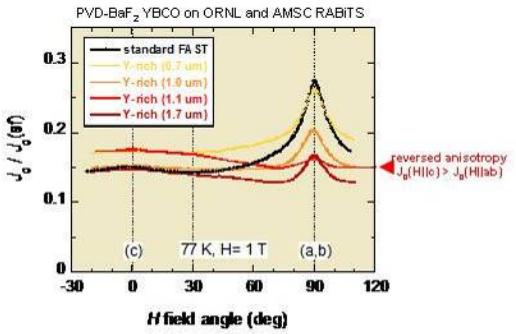

Fig. 2.8. Dependence of the normalized ratio of critical current density in applied fields H of 1 T to the self-field critical current density at 77 K on the orientation of the field in ex situ YBCO films on RABiTS™. Precursors were prepared by the PVD-BaF_2 technique. Different curves were obtained for films with variable Y-concentration and variable thicknesses. "FAST" refers to a fast conversion process used to produce the YBCO layer.

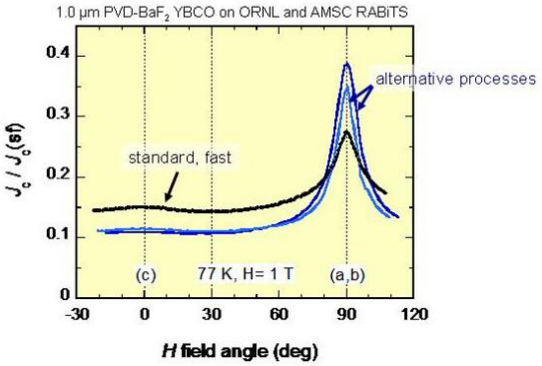

Fig. 2.9. An opposite effect on the ratio $J_c(ab)/J_c(c)$ resulting from an alternative processing modification. The black curve labeled "standard, fast" provides a reference for comparison with Fig. 2.8. A combination of processing changes as applied in both datasets suggests the possibility of engineering the detailed angular dependence of critical current density to application specifications.

2.4 Temperature and Magnetic Field Dependence of Critical Currents in YBCO Coated Conductors with Processing-Induced Variations in Pinning Properties

A. A. Gapud, R. Feenstra, and D. K. Christen (ORNL); J. R. Thompson (ORNL and UTK); T. G. Holesinger (LANL)

Recently there has been a renewal of interest in flux pinning in response to a demand for applying this technology to motors, transformers, and transmission cables, where there is a particular interest in minimizing the decrease of critical current density with increasing dc magnetic field and in making critical current density more uniform with respect to field orientation. At the same time, there have been some recent developments in creating practical "in situ" pinning sites (i.e., tailored defects resulting from modifying the growth conditions of the film) as opposed to having a separate "ex situ" step, such as heavy-ion irradiation. Examples of this include rare-earth doping, self-assembling precipitates, and multilayering.

So far, however, the reported work has been mainly on films made by PLD, and there is as yet little reported on films made by ex situ BaF_2 processing. These films are the subject of this report. We have previously observed that in our ex situ processing, Y_2O_3 precipitates of suitably small dimensions (15–50 nm) may be incorporated in large quantities as inclusions in the laminar YBCO grain structure. Excess yttrium was provided to the precursor in an attempt to control the Y_2O_3 precipitation, a kind of "self-doping." By doing this, the results at 77 K are (a) improved uniformity of critical current density with respect to field orientation $J_c(B,\theta)$ and (b) high self-field critical current density and critical current density for $B \parallel c$.

For the particular application to motors, the interest is in improving the angular dependence of critical current density in the regime of intermediate fields (~ 2–3 T) and temperatures around 30 K. In observing the temperature and field dependence of critical current density, we have found that irrespective of observed variations in the irreversibility field and in angular dependence of critical current density, J_c (H=2 T, T=30 K) scales very well with J_c (self-field, 77 K). We analyze the origin of this result and its important implications.

YBCO films of thickness 0.7 μm were grown on RABiTS™ provided by AMSC. Precursors were formed by e-beam evaporation and were converted by ex situ annealing. In addition to stoichiometric films, two different levels of excess yttrium, +30% ("rich") and +90% ("richer"), were investigated. The films were grown at rates of 5 to 14 Å/s by means of a newly developed, faster conversion process. This process has enabled enhancement of critical current to values > 350 A/cm-width at 77 K.

Transport measurements were made using a standard four-probe method over a range of temperatures (from 30 K to 77 K) in fields of up to 14 T, and at orientation angles spanning a range of 130°. Angular dependence measurements were taken at 77 K at low fields (0.5 to 2 T) in the full Lorentz force configuration. Microstructure was characterized by X-ray diffraction (XRD); TEM analysis is in progress.

The high quality of the films in the study is indicated by $J_c(B,T)$ in Fig. 2.10(a), with B along the c direction, and by the self-field critical current density shown in the inset to Fig. 2.10(b). Various films have been processed under different conditions (e.g., varying levels of excess Y and different processing rates). Significant differences in irreversibility field resulted from this variation,. However, the strongest correlation with respect to irreversibility field was with the critical temperature (for the 77 K operating temperature). For example, for the sample having the lowest irreversibility field (B_{irr} ~ 5.8 T), T_c = 89.4 K; for a Y-rich film ("Y rich fast"), B_{irr} = 6.0 and T_c = 90.2 K; for the superior 123 sample ("123 fast"), B_{irr} = 7.6 T and T_c = 91.1 K. For the sample with the highest irreversibility field (B_{irr} = 8.2 T), T_c = 94.7 K. This film was converted with the shortest processing time, corresponding to 14 Å/s. According to XRD, part of the precursor was left unreacted. This is reflected in the slightly lower critical current density value (self-field, 77 K) of 1.5 MA/cm^2. The origin of the surprisingly high transition temperature is not completely understood but could be related to a dense 123/124 intergrowth.

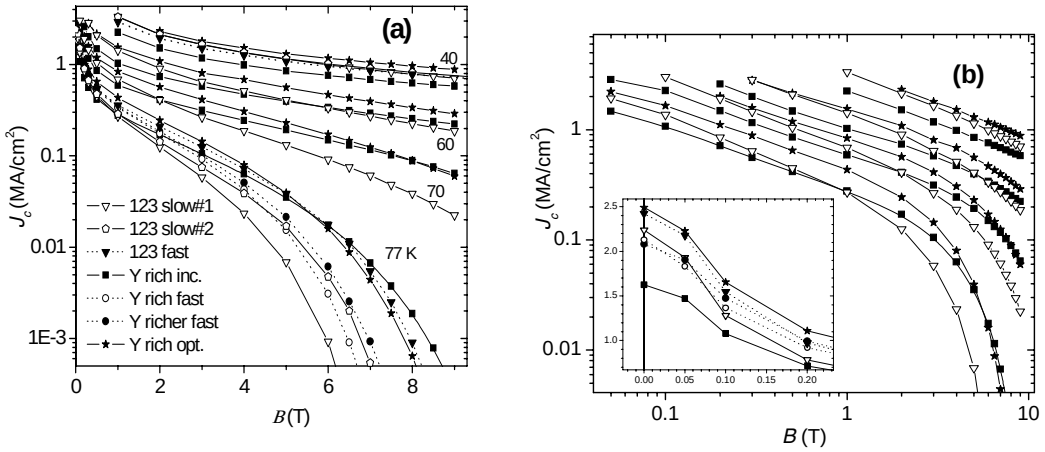

Fig. 2.10(a). Field dependence of critical current density at temperatures shown for films with and without self-doping. "inc.": incompletely converted; "opt": optimal-quality. (b) Log-log version without the additional 77 K data. Inset: 77 K data at low fields.

Aside from the partially unreacted film, the critical current density in self-field is typically around 2 MA/cm^2 or better [see Fig. 2.10(b), inset]. Particularly noteworthy is that the stoichiometric samples labeled "123 slow #2" (B_{irr} = 6.5 T) and "123 fast" have identical critical current densities [J_c (self-field, 77 K) = 2.42 MA/cm^2] despite a significant difference in irreversibility fields. An observation of interest in these curves for $B \parallel c$ is in the power-law regime where $J_c \sim B^{-\alpha}$, which is clearly seen in a log-log plot. In Fig. 2.10(b), the data from Fig. 2.10(a) are plotted with data for three samples at lower temperatures. The power-law regime is seen for fields as low as 0.1 T (for T = 77 K) and at least as high as 1 T. For our data, we have consistently found for stoichiometric films that $\alpha \approx 0.65$, which is close to the predicted value of 5/8 = 0.63 for flux pinning by large, dilute defects. However, the slopes for the Y-rich film are

slightly less, $\alpha \approx 0.6$, or a slightly weaker field dependence. The exponent α is nearly independent of temperature down to 40 K (i.e., the curves are parallel at the different temperatures), indicating that the pinning mechanism does not change with temperature. This is true even for the incompletely converted film. Furthermore, the high-field cutoff for the linear regime moves to higher *B* at lower temperatures, as expected for increasingly stronger pinning due to increasing condensation energy and decreasing coherence length.

We turn now to the dependence of critical current density on field orientation. The first comparison is between two stoichiometric films produced by either the newly developed, faster process ("123 fast") or the slower "baseline" conversion process ("123 slow") (see Fig. 2.11). Both films exhibit the typical behavior of a large critical current density for $B \parallel ab$ and relatively weak variation for other orientations. Specifically, there is no strong peak in critical current density for $B \parallel c$. A strong flattening of the angular dependence is observed for the film produced by the faster process; J_c ($B \parallel ab$) is reduced, while critical current density is enhanced for all other orientations. If we quantify this phenomenon with a parameter $\beta = J_{cmax}/J_{cmin}$, where $\theta = 90^o$ for J_{cmax} and where J_{cmin} is the smallest critical current density regardless of field orientation, we can say that the faster processing has improved β from a value of 3.6 for the slower-processed film to 2.2 for the faster-processed film.

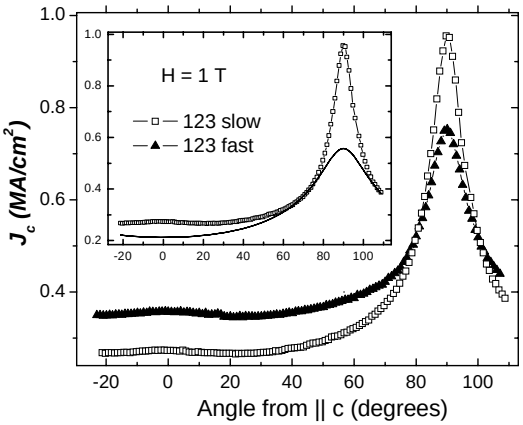

Fig. 2.11. The angular dependence of critical current density at 77 K for nondoped films produced by slow (standard) processing compared with that for films produced by fast processing. Inset: an attempt to fit the data by anisotropic scaling analysis.

It is enlightening to check for the contribution of random pinning array by fitting the data to the scaling curve predicted for electronic mass anisotropy effects alone. In this case, one would expect $J_c = J_c[\varepsilon(\theta)B]$, where $\varepsilon(\theta) = (\cos^2\theta + \sin^2\theta/\gamma)^{1/2}$, where we use $\gamma = 5$ for our YBCO. For a field $B = 1$ T at 77 K, for the entire angular range the scaling field $\varepsilon(\theta)B$ remains in the power-law regime, $J_c \sim B^{-\alpha}$, where we have $\alpha \sim 0.60$, so that $J_c(\theta) = A\,[B\varepsilon(\theta)]^{-\alpha}$, A is an adjustable factor for fitting the scale of critical current density. We have found that for all our films, the resulting curve fails to fit the data, unlike the recent results reported for films made by PLD. This is shown in the inset of Fig. 2.11 for the stoichiometric film, where typically the model curve can be made to intersect the data over only a small angular range. Actually, the poor fit is not surprising because, for the $J_c \sim B^{-\alpha}$ regime, the mass anisotropy model alone predicts a fixed value for the ratio $\beta = \gamma^{\alpha} = 5^{0.65} = 2.85$. All of the faster-processed and/or Y-rich films have much smaller β than this. (Although the critical current density is not always the minimum for $B \parallel c$ due to the presence of a shallow peak in such cases, the critical current density is well within 10% of minimum and β is approximately the same.) Clearly, random pinning is not the dominant mechanism in these films. The broader peak along *ab* for the fast-processed film could be due to the perturbation of *ab*

planes by particles, but the sharper peak for slow-processed film could also be due to correlated disorder, such as planar defects parallel to (*ab*) that grow with longer processing. Another possibility would be the improvement of *ab* plane alignment with longer processing, which in turn would improve the intrinsic pinning component.

Figure 2.12 shows $J_c(\theta)$ for three fast-processed film with variable Y concentration. Clearly, the enhancement in critical current density for $B \parallel c$ is similar over a wide range of angles about *c* direction, down to $\theta \approx 40^o$. Closer to the *ab* direction, we see again a reduction in critical current density as we did in Fig. 2.11. In this case, however, it is due to Y concentration, with β decreasing with increasing Y excess, from 3.6 for stoichiometric to 2.5 for Y-rich, and to 1.8 for Y-richer. However, unlike the recent results from the addition of BZO precipitates, no strong correlation along the *c*-axis is observed; rather, there is enhancement over a wider range of angles around the *c* direction.

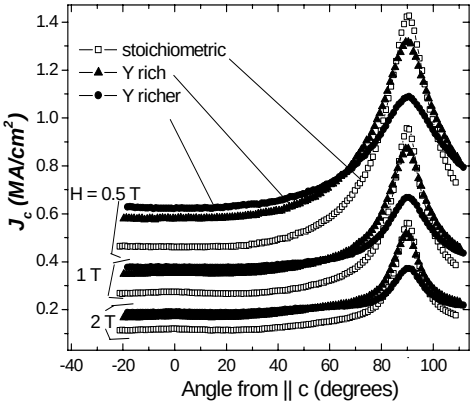

Fig. 2.12. Improved isotropy with respect to field orientation as a result of excess Y.

To check the thickness dependence of Y-doping, we compared a 1.68-μm Y-rich film with a similarly processed 0.7-μm-thick film (Fig. 2.13). For the fast process, we have found that critical current increases approximately linearly with thickness over the interval, $0.2 < d < 1.7$ μm, indicating a nearly constant critical current density. For the 1.68-μm film, the critical current density was 2.3 MA/cm^2. The high critical current of this film, 393 A/cm-width, is equivalent to first-generation multifilamentary HTS wire on a width-normalized basis. This self-field critical current density is also comparable to that of the thinner film, which is 2.1 MA/cm^2. This film also had the highest irreversibility field in our study, at 8.3 T (T_c = 93.6 K). The orientational isotropy also improved, with our smallest being β = 1.3 (β = 1.7 for the thinner film). More importantly, the thicker film shows more structure, especially a higher, broad peak for $B \parallel c$. Clearly, the effect of excess Y is enhanced with thickness.

The above results represent many of the attempted methods for improving the critical current density of HTS film at (*B, T*) ~ (2 T, 30 K), the regime of motor applications: elevating the critical current density and the irreversibilty field, making the critical current density more isotropic with field orientation, increasing the critical current density (self-field, 77 K), and introducing defects for pinning. With this in mind, we sought to determine how J_c(2 T, *T*) scales with J_c(self-field, 77 K), a commonly measured and widely available quantity, for samples made under widely different methods. From the available data, we plotted all the ratios of J_c(2 T, *T*)/J_c(self-field, 77 K) from 77 K down to 30 K. We found that the resulting curves approximately overlap, as shown in Fig. 2.14. At 77 K, there is a spread of about ±50 %, but at 30 K there is convergence, with correlation within ±11%. Considering the diversity of these samples, this is an unexpected and remarkable result. The scaling includes the underconverted sample (solid squares), where we expect a different pinning mechanism from the rest. Therefore, for the films made thus far, this

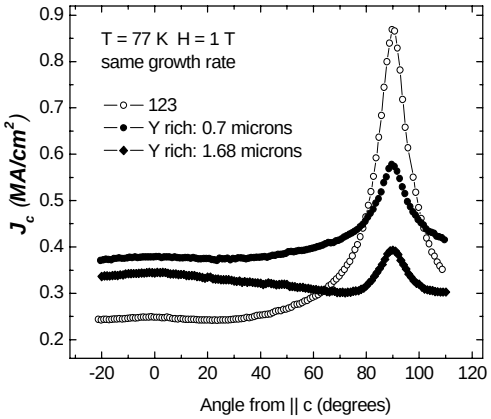

Fig. 2.13. Increased orientational isotropy for thicker self-doped film. The ratio of thickness to total processing time is the same for both films.

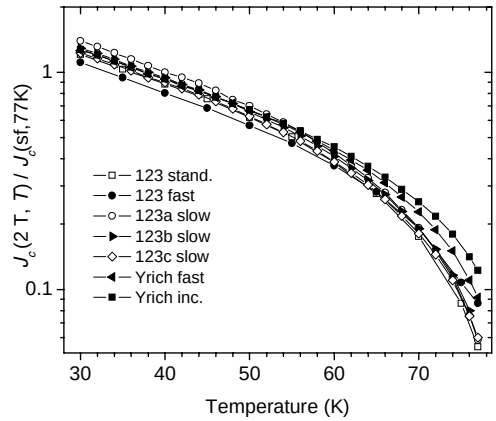

Fig. 2.14. Semi-log plot showing universal temperature dependence of the ratio of critical current density at self-field, 77 K, and at the field typical of motor applications for samples with widely different pinning mechanisms, irreversibility fields, and self-field critical current densities.

scaling is predictive and useful for temperatures of interest in motor/generator applications. Another point of technological interest is that J_c(2 T, 30K)/J_c(self-field, 77 K) turns out to be close to unity.

Because of the results, for these ex situ films on RABiTS™, the value of the self-field critical current density at 77 K could provide a useful benchmark for the expected performance for targeted in-field applications. If true, it implies that any increase in the irreversibility field would increase J_c(2T, 30K) only if elevating the irreversibility field also improves J_c(self-field, 77 K). Conversely, improvement in J_c(2 T, 30 K) would result from upgrading J_c(self-field, 77 K), even if to do so involved degrading the irreversibility field, because 2 T is within the power-law field regime where $J_c \sim B^{-\alpha}$ for most of these samples and because of the small variation of α among samples and its near-independence of temperature. Apparently, the pinning mechanism for this field regime does not change significantly with the variations in processing, and parallel curves are obtained (i.e., the ratio J_c(2 T, T_1)/J_c(B, T_2) is

constant). Furthermore, although the point (self-field, 77 K) is actually outside the power-law regime, we have found uniform, sample-independent scaling of the self-field critical current density with in-field data in the linear regime (0.1 to 1 T at 77 K), so this is a valid point for (B, T_2). As for the increasing scatter toward 77 K, in the case of higher temperatures, B = 2 T is at the edge of the power-law regime, thereby reflecting some sensitivity to the varied irreversibility fields [see Fig. 2.10(b)]. In fact, variations in the irreversibility field have little influence in the power-law regime.

In summary, we have found that by processing the films with excess yttrium and at higher growth rates, ex situ YBCO films made by the BaF_2 method on RABiTS™ show very good uniformity with respect to field orientation at 77 K along with high critical current density for fields along *c* and high self-field critical current density. The critical current density at temperatures and fields of interest to motor applications has revealed a direct relation with critical current density at self field and 77 K, making this a potentially crucial benchmark for the development of HTS film for such applications. As for the nature of the pinning mechanism in these films, although we strongly suspect pinning to be caused by Y_2O_3 precipitates or associated strain fields, the only definitive evidence from this report is the distinct deviation of the angular dependence of critical current density from that predicted by electronic anisotropy and random pinning alone. A more definitive picture will result from correlations of properties with microstructural studies by TEM, which are currently under way.

2.5 Deposition of (Y_2BaCuO_5 /$YBa_2Cu_3O_{7-x}$)xN Multilayer Films on Ni-Based Textured Substrates

T. J. Haugan, P. N. Barnes, and T. A. Campbell (Wright-Patterson AFB); A. Goyal, A. Gapud, L. Heatherly, and S. Kang (ORNL)

2.5.1. Introduction

The development of YBCO thick films on buffer-coated Ni-alloy substrates (coated conductors) with $J_c > 1$ MA/cm^2 offers great promise for incorporation into power applications such as generators or motors operating at 77 K [1–13]. The RABiTS™ process is used to introduce a high degree of grain alignment in the Ni-alloys, which is epitaxially transferred into the buffer and 123 film layers [7–10]. Efforts to improve the critical current density of coated conductors by increasing flux pinning have only recently been initiated [2,3]. This paper presents new improvements of flux pinning of coated conductors by applying a recently developed method to incorporate dispersions of Y_2BaCuO_5 (211) nanoparticles into YBCO by multilayer deposition [14,15].

Growth of (211/123)xN multilayer films was shown to increase critical current density (77 K, ~1–2 T) of YBCO by a factor of 2 to 3 when deposited on single-crystal substrates [14,15]. The (211/123)xN films have a superlattice-type structure of alternating layers of 123 and 211 “pseudo-layers” containing discontinuous 211 nanoparticles that deposit by the island growth method. The 211 nanoparticle size is as small as ~ 8 nm with an areic number density estimated as > 4×10^{11} particles/cm^2 [15]. The resulting composite structure is essentially a layered dispersion of nonsuperconducting 211 nanoparticles inside a 123 matrix.

The issues of how (211/123)xN films will deposit onto RABiTS™ substrates have not been addressed thus far. RABiTS™ has unique features that affect the growth and properties of films deposited on it. Ni grains are not completely *c*-axis oriented but are tilted out of the plane, typically ± 0 to 8°, and higher-angle grain boundaries typically have total misorientations of 0 to 7°. Grain boundaries with in-plane misorientations greater than 5° are expected to result in reduced critical currents, whereas lower-angle grain boundaries may in fact act as flux-pinning sites. The grain boundaries are multifaceted structures at the intersection of irregularly shaped grains that are misaligned in the plane and tilted out of the plane. How these Ni-alloy template structures affect the (211/123)xN composite film coatings is presented in this section.

2.5.2 Experimental

Buffered Ni-W substrates were prepared at ORNL and AMSC by similar procedures [11], and buffered Ni substrates were prepared at the Wright-Patterson Air Force Base Air Force Research Laboratory [16]. The buffer layer architecture on Ni-W was a cap layer of CeO_2 (25 nm thick), an intermediate layer of YSZ (200 nm thick), and a seed layer of Y_2O_3 (30 nm thick). Y_2O_3 layers were deposited by reactive electron beam evaporation, and YSZ and CeO_2 layers were deposited by a radio-frequency (rf) magnetron sputtering process [11,16]. Buffered Ni substrates were prepared by using PLD to deposit all buffer layers: a cap layer of CeO_2 (~70 nm thick), an intermediate layer of YSZ (~500 nm thick), and a seed layer of CeO_2 (~70 nm thick) [16].

Multilayer (211/123)xN and 123 films were deposited onto the buffer-coated substrates by PLD [14–17]. Deposition parameters were 248-nm laser wavelength, ~3.2 J/cm^2 laser fluence, 4-Hz laser repetition rate, a 6-cm target-to-substrate distance, 780°C heater block temperature, 88–90% dense 123-only and 211-only targets, 300 mTorr oxygen partial pressure, and a post-deposition anneal at 500°C and 1 atm of oxygen [17]. An automated target-rotation and pulse-triggering system was used to control the deposition sequences, with a period of about 13 s, during which the deposition was stopped and different targets were rotated into position. The film thickness for every deposition was measured on reference films deposited onto single crystal substrates. The 211 pseudo-layer thickness was calculated assuming a smooth continuous layer, although the thin 211 layer consisted of discontinuous and discrete nanoparticles. Unless noted otherwise, the film thickness was kept in the range of 280 to 350 nm. A 123 reference film was deposited at ORNL with slightly different PLD conditions: 790°C substrate temperature, 120 mTorr O_2 partial pressure, 308-nm laser wavelength, 4-J/cm^2 fluence, 10-Hz repetition rate, and cooling rate 7°C/min in 580 mtorr O_2 pressure.

Critical transition temperatures and transport J_c(H) measurements were made at ORNL and at the Air Force Research Laboratory, with excellent agreement. A 1-μv/cm criterion was used for critical current density. Whole-width measurements and macrobridges of about 0.1 to 0.5 cm width were used for critical current density measurements. Characterization of microstructures was performed with SEM (FEI–Sirion).

2.5.3 Results and Discussion

Microstructural properties of the film surfaces are shown in Figs. 2.15, 2.16, and 2.17 for different SEM magnifications to demonstrate features at varying length scales. The microstructural features of the multilayer films were different from those of the 123-only films.

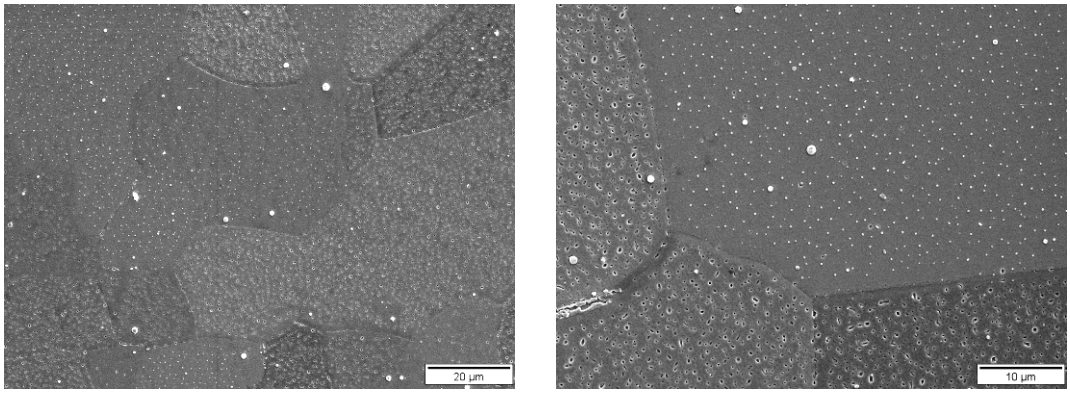

(a) (b)

Fig. 2.15. SEM micrographs of YBCO-only films deposited on ORNL RABiTS™.
(a) Lower magnification. (b) Higher magnification.

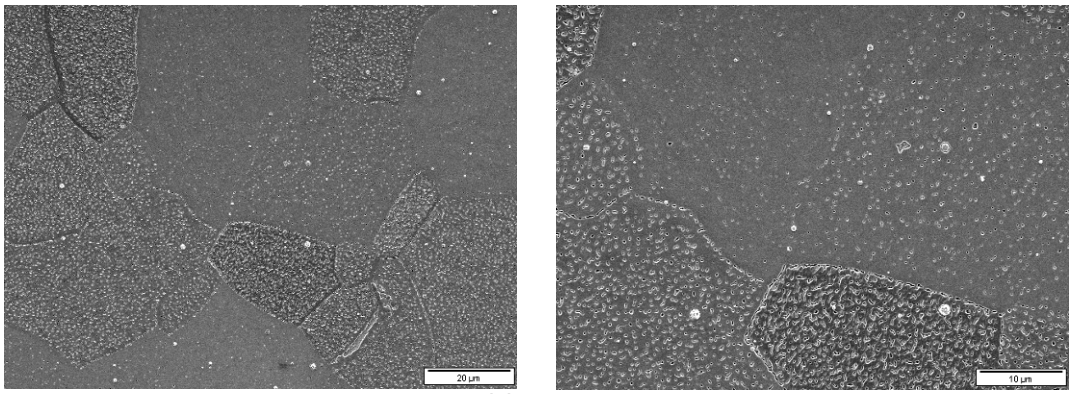

(a) (b)

Fig. 2.16. SEM micrographs of a ($211_{\sim 1.0nm}/123_{\sim 10.0nm}$)x25 multilayer films deposited on ORNL RABiTS™. (a) Lower magnification. (b) Higher magnification.

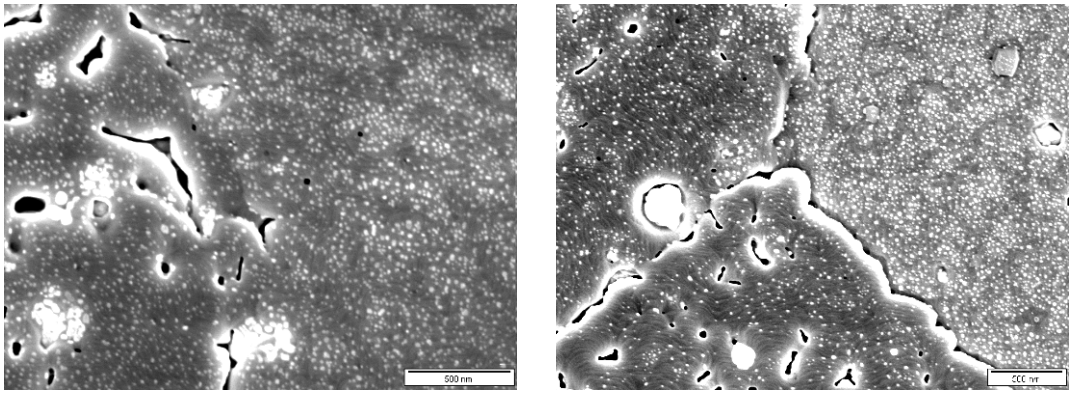

(a) (b)

Fig. 2.17. High-magnification SEM micrographs of different grains and grain boundaries of a ($211_{\sim 1.0nm}/123_{\sim 10nm}$)x26 film deposited on AMSC RABiTS™ substrate. Nanoparticles are white-spherical objects about 10 to 15 nm in size; voids are black objects approximately 0.1-1.0 μm in size.

(1) Void formations (0.1-1) μm in size were notably enhanced for multilayer films, as shown in Figs. 2.15, 2.16, and 2.17. Voids were observed as dark-or-black colored defects in SEM micrographs. Void areic number densities were higher for multilayer films (~ $4x10^8$ defects cm^{-2}) than for YBCO-only films (~ $1x10^8$ defects cm^{-2}), as measured on grains with highest density of voids. Formations of voids occurred particularly on grains with high densities of film-ledge formations, as shown in the bottom and left grains in Fig. 2.17(b). About 30 to 40% of multilayer film grains showed a moderate increase of void densities [e.g., Fig. 2.16(a), lower-left grain], while less than 10% of the grains showed large increases of void defects enough to presumably limit current flow [Fig. 2.16(a), bottom-middle grain].

(2) Surface particulate defects, which typically are observed in PLD films as ~ 0.5 μm size white-color defects [Fig. 2.16(a) bottom, upper right grain], were greatly reduced with multilayer films. However elimination of these defects is not expected to have a great effect on flux pinning, as their areic number density is very low.

(3) Intragrain nanoparticle formations varied noticeably depending on the underlying film and grain structures, as shown in Fig. 2.17. Nanoparticles were observed as white-color spherical-shaped particles, approximately 10 to 15 nm in diameter with areic number densities > 10^{11} particles cm^{-2}, similar to those on single-crystal substrates [15]. Nanoparticle formations were reduced particularly on grains that exhibited high densities or close-spacings of film-ledge formations. Film ledges with close-spacing intervals of about 20 to 40 nm can be observed by close examination in Fig. 2.17(b) bottom-and-left

grains. The film ledges deposited with such close spacings presumably indicate the presence of underlying tilted Ni grains. Film ledges are also observed on single-crystal substrates but with much larger spacing (~200 nm). The positive or negative effects of depositing multilayer films on tilted substrates are unknown yet but are being studied in detail [18]. The reason for reduced nanoparticle formation on (tilted) Ni-grains is not precisely known; however it could result from nonpreferential growth of 211 from relative tilting of the plume and ISD effects [13] or from nonpreferred growth of 211 at the base of film-ledge sites because of the 2 to 7% lattice mismatch of 211 to 123 [15]. The film-ledge bases with 90° step junctions have doubly active 123 film growth surfaces, which may suppress formation of 211 from the vapor phase, whereas the top-edge and top-point-edge of the film-ledge surfaces are energetically attractive sites for 211 coalescence and ripening [15].

(4) Close inspection of grain boundaries (Fig. 2.17) indicated that nanoparticle formation there was varied, with occasional enhancement at the edges. Some preferential growth at the grain boundaries may occur based on the growth processes described above. However only minimal preferential growth was observed, possibly because of the complexity of the grain boundaries.

To summarize the microstructural properties of multilayer films compared to 123-only films, moderate differences were observed on about 30 to 40% of the grains, and severe differences were noted on < 10% of the grains.

Transition temperatures of multilayer {($211_{\sim 1.2nm}$/$123_{\sim 11nm}$)xN, N= 20-25} and 123-only samples measured at the Air Force Research Laboratory by ac susceptibility methods [16] and at ORNL by transport methods were virtually the same (~89–90 K). This is slightly different from transition temperature measurements on single crystals, where a small decrease of ~1 to 2 K was measured for similar multilayer compared to 123 films [15]. This result suggests the template and/or CeO_2 cap buffer layer is having a noticeable effect on the transition temperature values.

The effects of multilayer depositions on J_c(77K, H) properties are shown in Fig. 2.18(a). Multilayer films had significantly increased $J_c(H)$ values for $H > 0.3$ T when compared to 123-only films, and the increase was consistently measured for different 211 and 123 thickness parameters. The increase of $J_c(H)$ was twofold at 2 T, and greater than sixfold at fields of 6 T. Films with thinner 211 layer thicknesses had increased self-field and-intermediate-field critical current densities (e.g., ~ 30% average increase comparing 211 ~ 0.5 nm to 1.0 nm, similar to results on single crystal substrates [15]). Self-field critical current densities were the same for films deposited on Ni-W and Ni substrates prepared at all three laboratories.

The question of whether the pinning enhancements in Fig. 2.18(a) on RABiTS™ substrates were the same as on single crystal substrates was better addressed in Fig. 2.18(b), which compares $J_c(H)/J_c(0\ T)$ plots of multilayer and 123-only films deposited on both substrates. Figure 2.18(b) indicates that the normalized $J_c(H)$ for multilayers was the same for both substrates, at least for fields up to 2 T. The only effect of the RABiTS™ substrates was to decrease the self-field critical current densities (e.g., from about 4 to 5 MA/cm^2 on single-crystal substrates to about 1.3 to 1.5 MA/cm^2 on RABiTS™ for both multilayer (211 ~ 0.5 nm) and 123-only films. The 123-only films had slightly better (relative) pinning at intermediate fields (1–3 T) on RABiTS™ compared to single crystal substrates. Both multilayer and 123-only films had poorer $J_c(H)$ performance at higher fields (>6 T) on RABiTS™ compared to single-crystal substrates.

To fully understand how the $J_c(H)$ properties correlate to the microstructure of the multilayer films on RABiTS™ substrate, both the $J_c(H)$ intragrain properties on every type and orientation of Ni grains and the effect of 211 nanoparticle addition on grain boundary transport mechanisms must be known. Such detailed information is presently not available. Therefore, it is not possible to predict the full-sample-length $J_c(H)$ results on RABiTS™ substrates shown herein. The primary conclusion that can be reached from the present studies is that changing the templates did not significantly change the $J_c(H)$ properties of the multilayer films. The summation of $J_c(H)$ properties across many different Ni grains and grain orientations is remarkably close to the results expected from $J_c(H)$ measured on single crystal substrates, assuming the normal decrease of critical current density expected from grain misorientations on RABiTS™ substrates [4]. Assuming that the intragrain multilayer $J_c(H)$ properties were not strongly

affected by different Ni grain orientations or averaged by a distribution of negative or positive $J_c(H)$ variances, this also indirectly suggests that the addition of nanoparticles does not strongly affect the grain boundary transport current-limiting mechanisms that are already known [4].

2.5.4. Conclusions

In conclusion, the $J_c(H)$ properties of (211/123)xN multilayer films on RABiTS™ showed significant increases (greater than sixfold) compared to 123-only films. Normalized $J_c(H)/J_c(0T)$ plots indicate that the pinning performance was neither (further) enhanced nor decreased as a consequence of switching templates from single-crystal to RABiTS™ substrates. While moderate-to-severe microstructural differences were observed on the RABiTS™ substrates, particularly with enhanced void formations, the differences apparently did not have great effect on the overall pinning performance. For example, while current flows might have been restricted across selected grains, enhancements might have occurred with other grains to offset those effects.

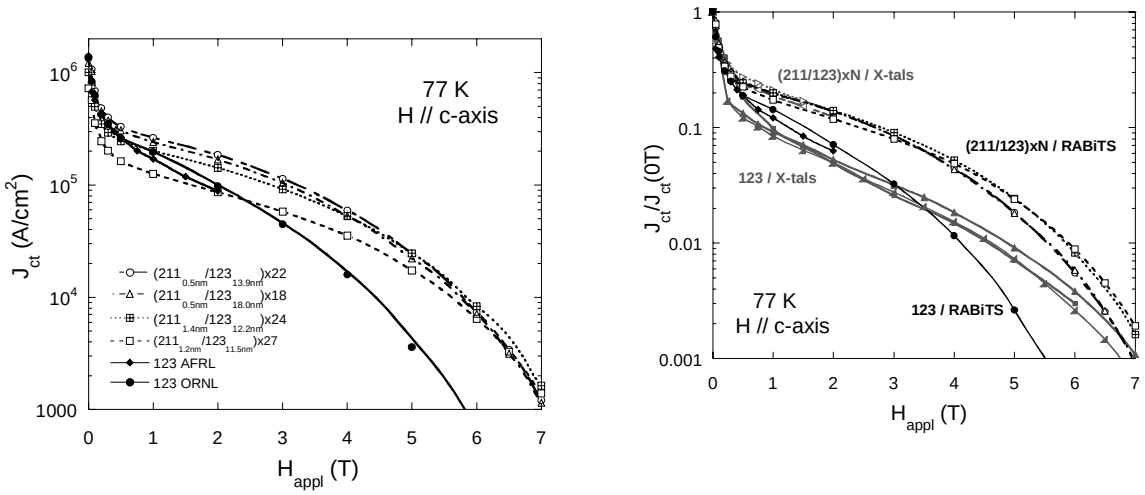

(a) (b)

Fig. 2.18. Transport critical current density (a) at 77 K for multilayer films compared to 123 reference films deposited at the Air Force Research Laboratory and ORNL. All films were deposited on ORNL Ni-W substrates. (b) Normalized for samples from (a) (black) compared with those of similar samples deposited on single crystal substrates (gray). 123-only films have solid lines and multilayer films are dotted lines. 123 films deposited on $LaAlO_3$ at the Air Force Research Laboratory (◢,▲) and processed by the BaF_2 method at ORNL (■) all with $J_{ct}(0T)$ from 4 MA/cm^2 to 5 MA/cm^2 [15], and $(211_{0.6nm}/123_{11.7nm})x21$ on $LaAlO_3$ (▷,◁) with $J_c(0T)$ from 4 MA/cm^2 to 4.5 MA/cm^2 [15]. One film with the lowest J_c (□) was noticeably bent, which could have lowered $J_c(H)$ for all H values. The entire film thickness was used to calculate critical current density.

2.5.5 References

1. P. N. Barnes, G. L. Rhoads, J. C. Tolliver, M.D. Sumption, and K.W. Schmaeman, *Compact, Lightweight Superconducting Power Generators*, presented at the 12th Symposium on Electromagnetic Launch Technology, (May 2004) and to appear in IEEE Trans. Mag.
2. J. L. MacManus-Driscoll, S. R. Foltyn, Q. X. Jia, H. Wang, A. Serquis, L. Civale, B. Maiorov, M. E. Hawley, M. P. Maley, and D. E. Peterson, *Nature Materials* **3**, 439 (2004).
3. J. L. MacManus-Driscoll, S. R. Foltyn, Q. X. Jia, H. Wang, A. Serquis, B. Maiorov, L. Civale, Y. Lin, M. E. Hawley, M. P. Maley, and D. E. Peterson, *Appl. Phys. Lett.* **84**, 5329 (2004).
4. D. Larbalestier, A. Gurevich, D. M. Feldmann, and A. Polyanskii, *Nature* **414**, 368 (2001).

5. Y. Iijima, K. Onabe, N. Tugaki, N. Tanabe, N. Sadakara, O. Kohno, and Y. Ikeno, *Appl. Phys. Lett.* **60,** 769 (1992).
6. X. D. Wu, S. R. Foltyn, P. N. Arendt, W. R. Blumenthal, I. H. Campbell, J. D. Cotton, J. Y. Coulter, W. L. Hults, M. P. Maley, H. F. Safar and J. L. Smith, *Appl. Phys. Lett.* **67**, 2397 (1995).
7. A. Goyal et al, US patent No: 5,739,086; 5,741,377; 5,846,912; 5,898,020.
8. A. Goyal, D. P. Norton, J. D. Budai, M. Paranthaman, E. D. Specht, D. M. Kroeger, D. K. Christen, Q. He, B. Saffian, F. A. List, D. F. Lee, P. M. Martin, C. E. Klabunde, E. Hatfield, and V. K. Sikka, *Appl. Phys. Lett.* **69**, 1795 (1996).
9. A. Goyal et al, U.S. Patent No: 5,964,966; 6,106,615; 6,451,450.
10. A. Goyal, D. F. Lee, F. A List, E. D. Specht, R. Feenstra, M. Paranthaman, X. Cui, S. W. Lu, P. M. Martin, D. M. Kroeger, D. K. Christen, B. W. Kang, D. P. Norton, C. Park, D. T. Verebelyi, J. R. Thompson, R. K. Williams, T. Aytug, and C. Cantoni, *Physica C* **357-360**, 903 (2001).
11. A. Goyal, R. Feenstra, M. Paranthaman, J. R. Thompson, B. Y. Kang, C. Cantoni, D. F. Lee, F. A. List, P. M. Martin, E. Lara-Curzio, C. Stevens, D. M. Kroeger, M. Kowalewski, E. D. Specht, T. Aytug, S. Sathyamurthy, R. K. Williams, and R. E. Ericson, *Physica C* **382**, 251 (2002).
12. S. R. Foltyn, E J. Peterson, J. Y. Coulter, P. N. Arendt, Q. X. Jia, P. C. Dowden, M. P. Maley, X. D. Wu, and D. E. Peterson, *J. Mater. Res.* **12,** 2941 (1997).
13. U. Balachandran, B. Ma, M. Li, B. L. Fisher, R. E. Koritala, D. J. Miller, and S. E. Dorris, *Physica C* **392-396**, 806 (2003).
14. T. Haugan, P. N. Barnes, I. Maartense, E. J. Lee, M. Sumption, and C. B. Cobb, *J. Mat. Res.* **18,** 2618 (2003).
15. T. Haugan, P. N. Barnes, R. Wheeler, F. Meisenkothen, and M. Sumption, *Nature* **430**, 867 (2004).
16. T. Haugan, P. Barnes, R. Nekkanti, J. M. Evans, L. Brunke, I. Maartense, J. P. Murphy, A. Goyal, A. Gapud, and L. Heatherly (private communication).
17. T. Haugan, P. N. Barnes, L. Brunke, I. Maartense, and J. Murphy, *Physica C* **397**, 47 (2003).
18. J. Wu et. al. (private communication).

2.6 Reel-to-Reel Low-Pressure ex situ Conversion of BaF_2 Precursor

D. F. Lee, F. A. List, S. W. Cook, P. M. Martin, E. D. Specht, H. M. Christen, and A. Goyal

Ex situ conversion of YBCO precursor is now one of the major techniques used to produce high-critical-current-density superconducting films on coated conductors. Tremendous progress has been achieved in the past several years, and very high critical current densities have been obtained in long lengths. Physical-vapor-deposited precursors (e.g., e-beam evaporated BaF_2) have the advantage in ease of thick-film deposition and can be used to evaluate the processing parameters necessary for high current capacities. Unfortunately, conversion rate of BaF_2 precursors into high-critical-current-density superconductors under atmospheric condition is typically slow. This is mainly due to the inability of standard precursors to tolerate aggressive high-rate conversion conditions as well as to inefficiency in removal of HF reaction products. Because of the slow conversion rate, a prolonged reaction time was necessary to convert thick precursor films. As such, the quality of the resulting films was typically inferior, partly because of excessive reaction with the buffer material.

Last year, we demonstrated that preconversion annealing of the precursors under controlled oxidation environments can substantially increase their ability to tolerate aggressive conversion conditions. That is, *c*-axis growth of YBCO can be sustained at high growth rates with negligible random YBCO nucleation. Samples having very high critical current densities (~ 3 MA/cm^2) were converted in a simple longitudinal-flow furnace. Dimensions of the samples were limited to ~ 0.3 × 1.5 cm so as to minimize the influence of HF build-up. To increase the sample size to a full 1 cm width, we performed conversions in a stationary low-pressure system. With low pressure, it is expected that gas flow will be more molecular and that gas outlet jetting will be reduced. Also, diffusivities will increase, and total gas as well as energy consumption will decrease. The net benefit of low-pressure conversion will then be a more uniform superconductor that is converted more rapidly and more efficiently. As expected, full

1 × 3 cm samples were successfully converted in this "ideal" stationary low pressure system at rates as high as ~ 14 Å/s. Critical currents of these 1-μm YBCO films varied between ~170 A/cm and ~210 A/cm, depending on the conversion rate.

To move low-pressure conversion beyond being a mere laboratory curiosity, it is necessary to show that the same benefits can be obtained in more complex reel-to=reel systems. We have developed a low-pressure reel-to-reel system to investigate the feasibility of this approach. A photo and schematic of the system are shown in Fig. 2.19. Briefly, the system consists of a 2.5-m-long Inconel 600 chamber that sits in the cradle of a four-zone split furnace. Two turbo pumps are fitted to the spool boxes at either-end of the conversion chamber and provide the pumping capability (base pressure ~ 1F-6 Torr). A single gas-injection tube with nozzle holes is situated to one side of the chamber. The conversion environment (argon, oxygen, and water) is controlled by individual computerized flow meters and valves; tape movement and hot-zone temperatures are also computer controlled.

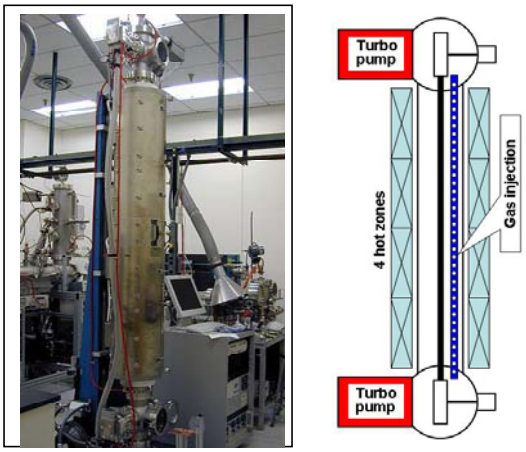

Fig. 2.19. The low-pressure reel-to-reel conversion system. Left: photo. Right: schematic.

To determine the effect of water partial pressure [$P(H_2O)$] on conversion rate in this system, 1 × 3 cm samples were cut from a length of precursor that was deposited reel-to-reel on RABiTS^{TM} and that had been subjected to a low-temperature preannealing treatment. The precursor thickness was targeted to produce 1-μm YBCO films. An individual sample was spot-welded onto Ni leaders and was converted in the low-pressure reel-to-reel unit for different lengths of resident time at selected values of $P(H_2O)$. Following conversion, these samples were examined by XRD θ-2θ scans. Measured values of BaF_2(111) intensities from the samples are shown in Fig. 2.20 as functions of conversion time for $P(H_2O)$ levels of 0.3 mTorr, 0.5 mTorr and 1 mTorr. It can be seen from Fig. 2.20 that BaF_2(111) intensity decreases rapidly with conversion time, reaching a residual level. Intercepts of the decreasing BaF_2(111) intensities with this residual value were used to approximate the conversion times for each $P(H_2O)$, and the calculated growth rates are plotted with $P(H_2O)$ in Fig. 2.21, which also includes the experimental growth rates obtained in the stationary low-pressure unit. As seen in Fig. 2.21, conversion rates in the low-pressure systems vary linearly with $[P(H_2O)^{½}/P_{Total}]$. This is in agreement with the model proposed by Solovyov et al., in which gas-phase HF removal is the rate-limiting step. As such, low-pressure conversion allows for the investigation of the true convertibility of various precursors. These data also show that the furnace (proportionality) constant, which depends on factors such as geometry and gas velocity, of the reel-to-reel system is larger than that of the stationary unit. With the high sensitivity of growth rate to $P(H_2O)$ in the reel-to-reel unit (or any other system that exhibits high furnace constant), it may be prudent to reduce this sensitivity by increasing the P_{Total} by addition of inert gas to avoid

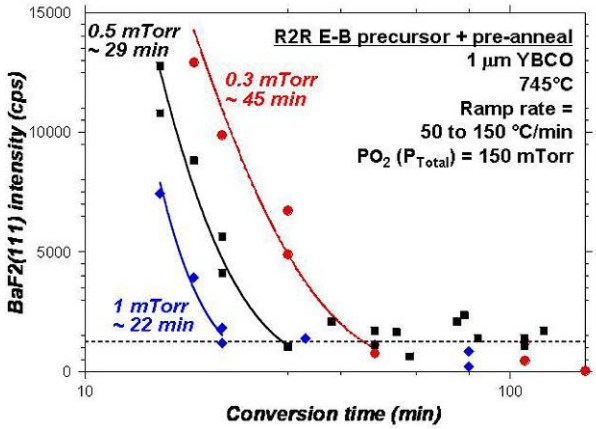

Fig. 2.20. Variation in BaF_2(111) intensity with conversion time at different $P(H_2O)$ in the low-pressure reel-to-reel system.

unintended growth-rate changes caused by $P(H_2O)$ fluctuation. Also, it can be seen in this Fig. 2.21 that the growth rates of both systems are high, one order of magnitude greater than those attainable in our atmospheric systems.

Besides conversion temperature, $P(H_2O)$, $P(O_2)$ and P_{Total}, we have determined that nucleation and growth of YBCO is also affected by the temperature ramp-up rate. To determine its influence, short samples were cut from the same stock material and were converted in the low-pressure reel-to-reel system at various tape speeds while maintaining the total residence time to 50 min. In addition, other parameters were held constant: T = 745°C, $P(H_2O)$ = 0.5 mTorr (growth rate = 5.7 Å/s), and $P_{Total} \sim P(O_2)$ = 150 mTorr. However, because of nonlinearity in furnace temperature profile, the transient nature of moving tapes, and thermal conduction in the metal substrate, a linear ramp-up rate and the instantaneous ramp-up temperature could not be accurately determined. Consequently, the ramp-up rate is presented here using the measured tape speed and the linear portion of furnace profile of 10°C/cm. YBCO *c*-axis (005) and random (013)/(103) XRD intensities of these samples are shown in Fig. 2.22, where c-axis intensity increases with ramp-up rate, reaches a maximum, and then decreases. Concomitant to this *c*-axis growth is the disappearance of random grains. These data show that for a given set of conversion parameters, there is a range of ramp-up rates where high-quality YBCO films can be obtained.

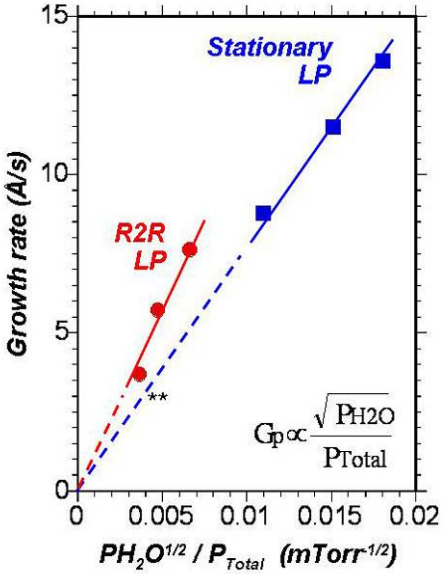

Fig. 2.21. Variations in conversion rate with $P(H_2O)$ for the reel-to-reel and stationary low pressure systems.

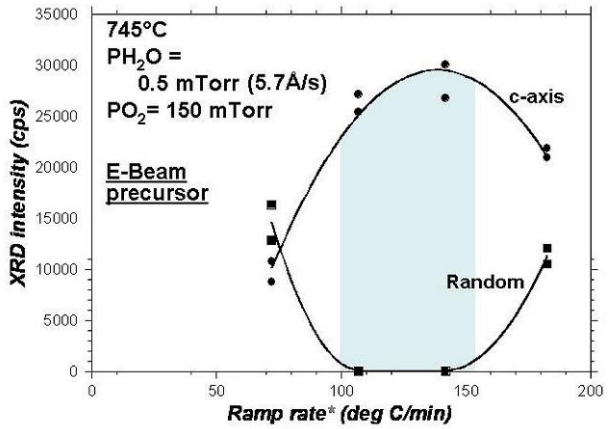

Fig. 2.22. Variations in *c*-axis(005) and random (103)/(013) intensities of 1-μm YBCO with ramp-up rate.

High-quality YBCO films on RABiTS™ were obtained at high conversion rates based on these and similar systems. Best critical current values for various conditions examined thus far are listed in Table 2.3; a high critical current of 148 A/cm was obtained for 1-μm YBCO at a growth rate of 7.6 Å/s [$P(H_2O)$ = 1 mTorr]. This value is similar to that obtained in the stationary low-pressure system at the same level of growth rate. Higher conversion rate conditions have not been examined in the reel-to-reel system. A limited number of 2-μm films have also been converted in the low-pressure reel-to-reel system, with a best value of 200 A/cm. In contrast, slightly lower critical currents (typically 120 A/cm for 1-μm films) were obtained in our "atmospheric"

Table 2.3. Critical current per centimeter width of 1-μm YBCO converted under various conditions[a]

Sample	Growth rate (Å/s)	Ramp (°C/min)	Temperature (°C)	Time (min)	Critical current (A/cm)
A	5.7	107	745	38	131
B	5.7	142	745	38	140
C	7.6	107	780	28	148

[a] $P_{Total} \sim P(O_2)$ = 150 mTorr.

reel-to-reel system. Furthermore, this level of critical current could only be reached by using a much slower conversion rate (0.6 to 1 Å/s). Considering a higher growth rate and much lower gas flow rate, gas use of the low pressure reel-to-reel system is at least 1,500 times lower than it is for its atmospheric counterpart.

One of the expected benefits from low-pressure conversion is a more uniform superconductor. For tapes processed in a reel-to-reel configuration, longitudinal uniformity is expected to be good because different locations along the tape length are subjected to the same conversion history. Uniformity in the transverse direction, however, can be problematic. We have previously shown that for a 100-A/cm-class 1-cm-wide sample converted in our reel-to-reel atmospheric furnace, the transverse variation in critical current from edge-to-edge can be as high as 27%. The sectional transport critical currents were determined by cutting the 1-cm-wide sample into three ~ 3 mm-wide strips. The same type of sectional critical-current measurements were perfumed on the samples listed in Table 2.3. Transverse critical-current variations of the samples (samples A, B, and C) were determined to be 1.3%, 3.1%, and 2.1%, respectively. These values are much lower than that found for the atmospheric-processed reel-to-reel sample.

An approach to increasing the production rate of YBCO derived ex situ is through the conversion of wide tapes followed by slitting. Although we have shown that transverse uniformity of 1-cm-wide samples can be improved by low-pressure processing, whether this beneficial effect can be extended to wider tapes remains to be determined. Since wide tapes were not available to us, we have simulated this condition by spot-welding a 5.5-cm-long sample cross-wise onto Ni leaders for conversion. The tape "width" is limited to 5.5 cm due to the dimensional constraints of our low pressure reel-to-reel chamber. A 1-μm YBCO layer was processed in this fashion using the parameters listed in Table 2.3 for sample A. YBCO(006) and BaF_2(111) XRD intensities were collected using a X-ray beam with 1-mm spot size (see Fig. 2.23). The intensities are very uniform along the tape "width", with only a 5.3% standard deviation (SD) for the *c*-axis YBCO. Sectional critical current measurements were also performed on the sample, with a variation of only 4.7%. While the entire "width" of the tape could not be determined because of the need for transport current tab placements, critical current values at the edges are expected to be similar because of the uniform YBCO(006) intensity (we have previously shown that there is a close correlation between relative changes in XRD YBCO(00l) intensity and critical current variation). These results show that low-pressure processing can be extended to more complex reel-to-reel system, with benefits of faster and more uniform conversion as well as much better conversion efficiency.

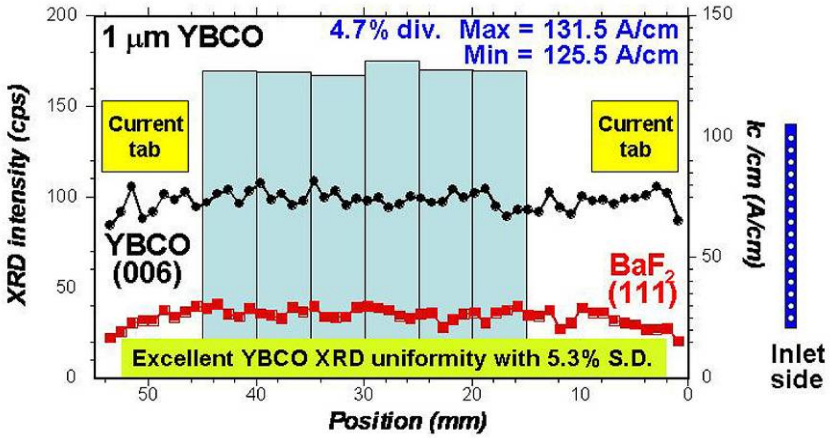

Fig. 2.23. Variations in XRD intensities and sectional critical currents of a 5.5 cm-wide sample processed in the low-pressure reel-to-reel system.

2.7 Conversion of ex situ YBCO Superconductor on RABiTS™ on a Novel Precursor Deposited by a Pulsed Electron Beam

D. F. Lee, H. M. Christen, F. A. List, L. Heatherly, K. J. Leonard, C. M. Rouleau, S. W. Cook, P. M. Martin, M. Paranthaman, A. Goyal

2.7.1 Introduction

The ex situ approach to YBCO formation on RABiTS™ has been shown to be capable of providing high-critical-current coated conductors. In fact, roughly 1-μm-thick YBCO with critical current densities greater than 2 MA/cm^2 have been converted in meter lengths from MOD precursors on RABiTS™ [1]. High-critical-current-density conductors (~1.3 MA/cm^2) with similar YBCO thickness have also been obtained in meter-lengths on PVD BaF_2 precursors [2].

Solution-based MOD is a low cost deposition method, but it is still not known whether it can produce very thick YBCO precursor films for ultrahigh-performance conductors consistently in lengths without cracking. On the other hand, very thick (> 5 μm), dense, and crack-free precursor films can be deposited by PVD techniques such as electron beam co-evaporation (BaF_2 precursor). Unfortunately, e-beam co-evaporation can suffer from inadequacies in long-range compositional control due to cross talk in power level during discharges as well as a lack of proven high-volume thickness monitoring for the Cu source [2–3]. Most importantly, results on high-performance e-beam-derived precursors have mostly been restricted to slow conversion rates, roughly 1 Å/s.

Pulsed electron-beam deposition (PED) is a PVD technique that is based on much simpler equipment and utilizes a single-source target such that long-range compositional uniformity is potentially much easier to achieve. More importantly, different starting precursor phases can be incorporated into the target to alter the phase assemblage of the precursor, which may influence the conversion rate of the film. Similarly, because a single target is used, substitution or doping studies of precursors for pinning enhancement are expected to be straightforward. That is, modifications will be performed during target preparation and additional e-guns are not required. In this report, we show that the new PED precursor can be converted into high-quality superconducting films at both standard slow and rapid conversion rates.

2.7.2 Experimental

2.7.2.1 PED Deposition

AMSC provided the 1-cm-wide RABiTS™ samples used in this study and used its proprietary MOD technique to determine that they were prequalified to sustain a critical current density of ~2 MA/cm^2. PED equipment setup, deposition details, as well as control of composition and deposition stabilities can be found elsewhere [4]. Single 1-in. targets were fabricated in-house by ball-milling the desired ratios of powders of YF_3, BaF_2 and CuO. After mixing, each powder batch was loaded into a stainless steel die and was cold-pressed into 1-in.-diam disc at ~4,000 kg. Densification of the targets was achieved by sintering for several hours in air at 800°C. Multiple iterations of target composition were performed initially to determine a target composition that resulted in a near-stoichiometric precursor film as measured by inductively coupled plasma-mass spectroscopy (ICP-MS).

Precursors were deposited on 30- to 50- cm-long RABiTS™ samples of CeO_2/YSZ/Y_2O_3/Ni-5%W architecture mounted (together with Ni leaders) in a reel-to-reel deposition chamber. The chamber was pumped to a base pressure of 10^{-6} Torr before being backfilled with nitrogen gas to a pressure of 9 mTorr. After tape motion was initiated, e-pulses were triggered at a repetition rate of 10 Hz with a source voltage of 16 kV. The sample traveled between the two reels in a reciprocating action (i.e., multiple passes were performed for a full deposition with the tape traveling at a fixed speed of 9 cm/min).

2.7.2.2 Precursor Conversion

A reel-to-reel transverse-flow conversion chamber situated in a 22-zone furnace was used to study the PED precursor conversion characteristics at standard slow conversion rates (on the order of 1 Å/s. Details of this conversion chamber can be found elsewhere [2–3]. For the ex situ conversion approach, the rate of *c*-axis YBCO growth is, to a large part, determined by the aggressiveness of the conversion parameters, the amount of HF generation and the efficiency of HF removal [2–3, 5–6]. Typically, aggressiveness can be increased by increasing the humidity in the form of water partial pressure [$P(H_2O)$] as well as the conversion temperature for a given oxygen partial pressure [$P(O_2)$]. The amount of HF generated is influenced by the precursor volume and the decomposition rate of fluorine-bearing phases, whereas efficiency of HF removal can be enhanced by increasing the gas flow rate or by reducing the total pressure (P_{Tot}) through pumping. For the present reel-to-reel chamber, no pumping is provided. Also, because of high gas flow rate and the small exhaust nozzles utilized in this system, the typical operation total pressure was ~1140 Torr (1.5 atm).

Sample conversion at higher rates was performed in a custom-designed low-pressure conversion system with in situ XRD. Details of system configuration and operation are available elsewhere [7]. System components include a sample stage in which a 3-cm-long by 1-cm-wide sample was spot-welded to Ni leaders on either end and was suspended under tension between two water-cooled copper electrodes. A 75-μm-diam type K thermocouple was spot-welded to the center edge of the sample to monitor and control the temperature. Sample heating was accomplished by passing a controlled electric current through the metallic leader and substrate. The unit is capable of greater than 1000°C/min linear ramp-up rates, although 50˚C/min was used in this study. After loading the sample stage into the sealed, all-metal hydrocarbon-free vacuum chamber, the pressure was reduced to ~5×10^{-7} Torr. During conversion, the $P(O_2)$ and $P(H_2O)$ were controlled with precision leak valves. Throughout the entire conversion process, development of crystalline phases was continuously monitored by a built-in energy dispersive X-ray (EDX) diffraction unit. In this study, the total pressure was roughly 215 mTorr, which is nearly 5,300 times lower than that of the reel-to-reel chamber.

Once conversion was completed, a standard XRD diffractometer with a 50-kV, 30-mA copper anode and a scintillation detector was used to collect an individual sample XRD θ-2θ measurement. A 1-μm-thick Ag overlayer was then deposited onto the HTS, and the sample was heat-treated at 500°C for 1 h and cooled at a rate of 1.5ºC/min in flowing oxygen. Transport measurements were performed in standard four-probe configuration at 77 K according to the 1-μV/cm criterion. Thicknesses of both the precursor and the converted YBCO film were determined by averaging repeated profilometry scans on chemically etched films.

2.7.3 Results and Discussion

2.7.3.1 Slow Conversion of PED Precursors

Preliminary trial of the convertibility of a PED precursor was first performed on a 3 × 1 cm sample cut from a 30-cm-long stock with 1.2-μm-thick PED precursor deposited in a reel-to-reel apparatus. The sample was spot-welded to Ni leaders and was converted in the reel-to-reel chamber. Baseline processing parameters of this initial trial were chosen based on the processing conditions developed for high-critical-current-density e-beam co-evaporated PVD precursors converted in the same chamber. Before conversion commenced, the temperature, $P(O_2)$, and $P(H_2O)$ were set respectively to 740°C, 120 mTorr, and ~4 Torr increasing to ~30 Torr. The sample was moved through the chamber at a speed of 2.3 m/h in order to achieve a desired conversion time of 100 min. The corresponding ramp-up rate was ~45˚C/min due to a fixed entrance temperature gradient of ~32.5˚C/cm.

The θ-2θ XRD diffraction pattern (Fig. 2.24) revealed that the converted YBCO film is *c*-axis textured, with no detectable YBCO (103)(013) or (h00) *a*-axis peak. However, a small BaF_2 (111) peak was found, indicating that the conversion did not go to completion. With an averaged YBCO film thickness of 0.86 μm (as determined by profilometry), the presence of an unreacted BaF_2 phase indicates

that the conversion rate was less than 1.4 Å/s, given the conversion parameters. Transport measurement on the sample performed at 77 K showed that the film possesses a self-field critical current of 85 A (J_c ~ 1 MA/cm^2) and confirms that PED precursors can produce high-quality ex situ YBCO.

Another PED precursor sample was used to obtain complete conversion. The sample was cut from the same stock material and was reacted under identical conditions except for a conversion rate of 0.7 Å/s. That is, the resident time was increased to 205 min with a corresponding ramp-up rate of ~22°C/min. As expected, the XRD pattern revealed no BaF_2 (111) signal and only *c*-axis YBCO (00l) peaks. Self-field 77 K critical current density of the sample was found to be 1.1 MA/cm^2. Next, PED precursor films of various thicknesses were converted to ensure that the deposition technique could produce thicker high-quality YBCO films (Table 2.4). Samples (3 × 1 cm) of various precursor thicknesses were cut from respective PED stocks deposited in the reel-to-reel chamber. Conversion parameters were identical to those for the sample that had provided the high critical current density; conversion temperature = 740°C, P(O_2) = 120 mTorr, and P(H_2O) increased from ~4 Torr to ~30 Torr. The reaction rate was fixed at ~0.7 Å/s, which translated to resident times ranging from 170 to 310 min and ramp-up rates from ~15 to ~27°C/min. Profilometry measurement of precursor and converted films revealed that substantial reduction in thickness has occurred during YBCO formation. The amount of reduction was found to be quite constant (~28%), within the range of film thickness examined in this study.

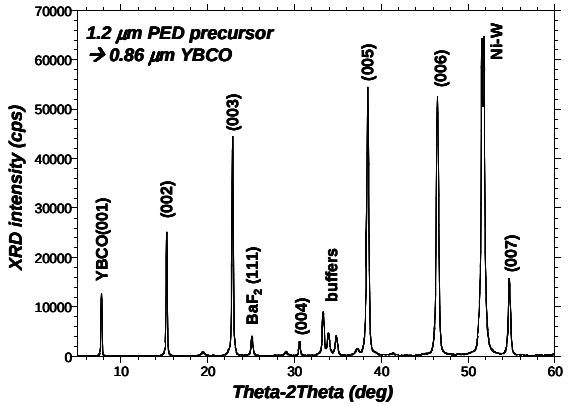

Fig. 2.24. θ-2θ XRD pattern of a 1.2-μm-thick PED precursor converted under nonaggressive conditions. The reaction rate was less than 1.4 Å/s.

Table 2.4. Characteristics of YBCO films of various thicknesses converted from PED precursors

YBCO Thickness (μm)	I_c (A/cm)	J_c (MA/cm^2)
0.72	117	1.6
0.86	92	1.1
0.94	100	1.1
1.30	159	1.2

It can be seen from Table 2.4 that all the samples possess high critical current density and critical current per centimeter performance. Magnetic field dependencies of another 0.72-μm-thick YBCO with self-field (J_c ~1.5 MA/cm^2) were measured at 77 K for both the B//*a*-*b* and B//*c* directions and are shown in Fig. 2.25. The critical current density of the PED sample was reduced by a factor of ~5 at 0.5 T, which is typical of stoichiometric ex situ YBCO films converted at slow rates in the chamber. The inset in Fig. 2.25 shows the angular dependence of critical current density at 0.5 T. The angular dependency of the PED precursor shows no correlated pinning defects for B//*c*, which is also characteristic of typical stoichiometric ex situ YBCO films. Out-of-plane and in-plane texture measurements were performed on the 1.3-μm YBCO sample following conversion, and the Δω full-width-at-half-maximum (FWHM) of Ni-W, YSZ, CeO_2 and YBCO were found to be 5.9°, 5.6°, 5.7° and 5.6°, respectively. The Δϕ FWHM of the corresponding

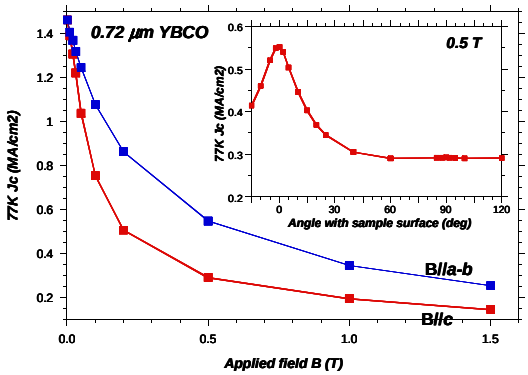

Fig. 2.25. Magnetic dependence of J_c of a 0.72 μm-thick PED-derived YBCO film for both B//*a*-*b* and B//*c* directions at 77 K. Also shown in the insert is the angular dependency at 77 K and 0.5T.

layers were 7.0°, 6.6°, 6.5° and 6.8°, respectively. As such, close epitaxy was attained by the PED precursor after conversion. The variation does not necessarily represent the true reduction in critical current density behavior that is generally associated with increasing thickness, although it appears to decrease with film thickness in Table 2.4. The reason is that optimum processing parameters have been shown to vary with precursor thickness in PVD ex situ precursors [2], and no attempt has been made to optimize the parameters for each thickness in this study.

2.7.3.2 Rapid Conversion of PED Precursors

The large reduction in film thickness after conversion seen in the slow reaction study is an unexpected feature of PED precursors. The average reduction of ~28% is substantially larger than that of e-beam co-evaporated precursors. To determine whether this densification is microstructure related, a PED precursor sample was initially converted in the standard fashion. Two minutes after reaching the conversion temperature, however, the sample was rapidly quenched onto the cold reel within a time frame of ~9 s. As seen in Fig. 2.26, cross-sectional TEM imaging of the precursor revealed that the PED precursor is quite porous. In contrast, a similarly treated e-beam evaporated precursor was found to be considerably denser, whereas MOD precursors are more porous. With this porous microstructure, H_2O in-diffusion and HF out-diffusion may be enhanced, thereby allowing the precursor to react at faster rates. Moreover, owing to the choice of YF_3 as the Y-bearing phase, the fluorine content of the precursor is increased, and may bring the PED precursor reaction trajectory deeper into the partial melt regime [8]. In short, the resemblance of both the microstructure and the initial precursor phase assemblage is closer to the MOD precursor, which is known to be capable of rapid conversion into high-quality YBCO at rates as high as several tens of angstroms per second [8].

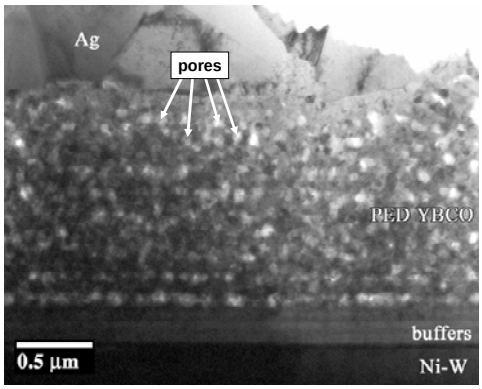

Fig. 2.26. Cross-sectional TEM image of a quenched PED precursor after a 2-min conversion. Numerous ~100-nm-diam pores can be seen.

To determine whether PED precursor can be converted rapidly while simultaneously maintaining high critical current density, several samples were converted in the reel-to-reel system under progressively more aggressive reaction conditions. This was accomplished by increasing both the $P(H_2O)$ and the conversion temperature and decreasing the conversion time. XRD patterns of samples converted thus showed that even with higher reaction rates, the films exhibited only high-intensity YBCO (00l) peaks without a noticeable amount of YBCO (103)(013) components. This is in stark contrast to as-deposited e-beam co-evaporated precursor, where these aggressive conditions would have led to predominantly random YBCO growth with very weak YBCO (00l) peaks. A sample converted at a temperature of 760°C and $P(H_2O)$ increasing from 30 to 40 Torr exhibited a critical current density of 1 MA/cm^2 and showed no BaF_2 (111) peak in the XRD pattern, indicating that the conversion rate was greater than 2.2 Å/s. When the aggressiveness of conversion is further increased to 770°C and the $P(H_2O)$ is increased from 30 to 55 Torr, a substantial amount of BaF_2 (111) remained among high-intensity YBCO (00l) peaks, indicating that the conversion rate was slower than 3.2 Å/s. At this point, the total pressure was found to be above 1520 Torr (> 2 atm) due to increased gas viscosity, and the experiment was stopped due to safety concerns. The conversion rate limit of 3.2 Å/s, however, is believed to be dependent upon the conversion chamber and does not reflect the true limitation of the PED precursor itself. This is because conversion rate of YBCO has been shown to be proportional to the square root of $P(H_2O)$ and inversely proportional to total pressure [6]. In other words, a much higher conversion rate cannot be achieved in the conversion chamber because the total pressure increases faster than the $P(H_2O)$.

Fortunately, high conversion rates can be achieved in our low-pressure stationary-sample conversion system, as previously demonstrated on MOD precursors [9]. Different samples were loaded onto the conversion chamber and were converted at progressively more aggressive conditions. Similar to the results from the reel-to-reel furnace, all the PED precursors exhibited strong YBCO (00l) peaks only. The only differences were that the reactions rates were much higher and that the conversion always went to completion [no BaF_2 (111) peak]. This was the case since each conversion process was continuously monitored by in situ EDX, and the experiment was terminated when YBCO formation was completed. Figure 2.27 shows the in situ EDX counts of the YBCO (002) peak for a 1.4-µm-thick PED sample (~1 µm YBCO) converted at 740°C, ramp-up rate of 50°C/min, PO_2)of 200 mTorr and P(H_2O) of 15 mTorr. It can be seen in Fig. 2.27 that the *c*-axis YBCO phase developed rapidly and the YBCO (002) reaches a high intensity in less than 22 min. This translates to a conversion rate of 7.7 Å/s. More importantly, J_c ~1 MA/cm^2 at 77 K and self field was determined for this sample. In contrast, the YBCO (002) development of an as-deposited 0.9 µm-thick stoichiometric e-beam co-evaporated precursor that was reacted in a substantially similar fashion (also shown in Fig. 2.27), was found to be significantly reduced, with a zero critical current density. Conversions of PED precursors at even more aggressive conditions in the low-pressure system are under way.

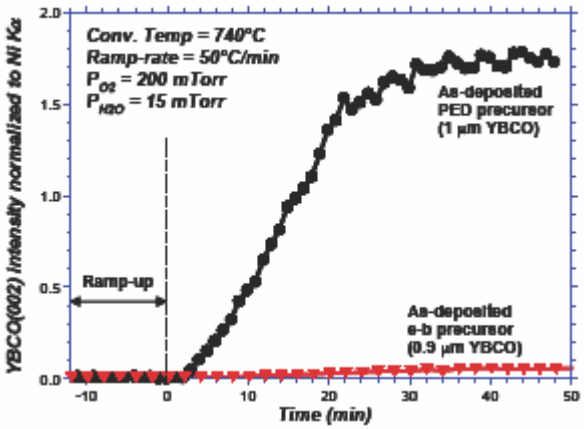

Fig. 2.27. Variation in in situ EDX diffraction intensity of the YBCO (002) peak of a ~1.4 µm PED precursor (~1 µm YBCO) converted at high rate in the low-pressure system with time. Also shown is the reduced *c*-axis YBCO development of a 0.9 µm as-deposited e-beam precursor.

2.7.4 References

1. M. W. Rupich et al., *IEEE Tran. Appl. Supercond.* **13**, 2458 (2003).
2. D. F. Lee et al., *Supercond. Sci. Technol.* **17**, 386 (2004).
3. D. F. Lee et al. pp. 149–77 in *Second Generation HTS Conductors*, ed. A. Goyal, Kluwar Academic Publisher, Boston (2005).
4. H. M. Christen et al. (private communication).
5. T. Izumi et al., *IEEE Tran. Appl. Supercond.* **13** 2500 (2003).
6. V. F. Solovyov et al., *Physica C* **353**, 14 (2001).
7. F. A. List et al., *Physica C* **391**, 350 (2003).
8. M. Yoshizumi et al., *Physica C* **403**, 191 (2004).
9. F. A. List et al. (private communication).

2.8 Limits of the Pulsed Electron Deposition Approach for YBCO Precursors

H. M. Christen, D. F. Lee, F. A. List, S. W. Cook, A. Goyal, P. M. Martin, and J. Li

2.8.1 Introduction

We have shown the potential of PED for the reel-to-reel deposition of precursors for conversion into superconducting tapes on RABiTS™ [1,2]. The main advantage of this ablation-based film growth technique is the comparatively simple equipment, the possibility to work with a single source (hence the absence of sophisticated in situ control requirements for the composition), and the scalability achievable by placing multiple sources in series.

A series of newer experiments now illustrates difficulties encountered with this approach. In particular, the PED approach is not successful when working with certain types of buffered tapes containing a CeO_2 cap, even if other methods (such as e-beam evaporation) yield satisfactory results on the same substrates and even if PED yields high critical currents on other CeO_2-capped buffers of nominally the same architecture.

While a definite identification of the origin of this buffer-layer-dependent reduction of the critical current and crystallinity cannot be made at this point, a comparison to PLD points to the energetics of the approach as one possible cause.

2.8.2 Conversion of PED and e-Beam-Deposited Precursors

Figure 2.28 compares PED-deposited precursors to e-beam-evaporated precursors for two types of CeO_2/YSZ/CeO_2 buffers on RABiTS™. The two types of buffer stacks were obtained in different deposition systems and vary slightly in layer thicknesses, but both contain the CeO_2 cap as routinely used in ex situ work on coated conductors. As shown in Figs. 2.28(a) and (b), e-beam precursors on both substrates yield YBCO with high X-ray intensity of the (002)-reflection (as recorded during conversion), and both samples exhibit high currents in excess of 150 A (J_c > 1.5 MA/cm^2) for 1-µm-thick layers and 1-cm-wide tapes.

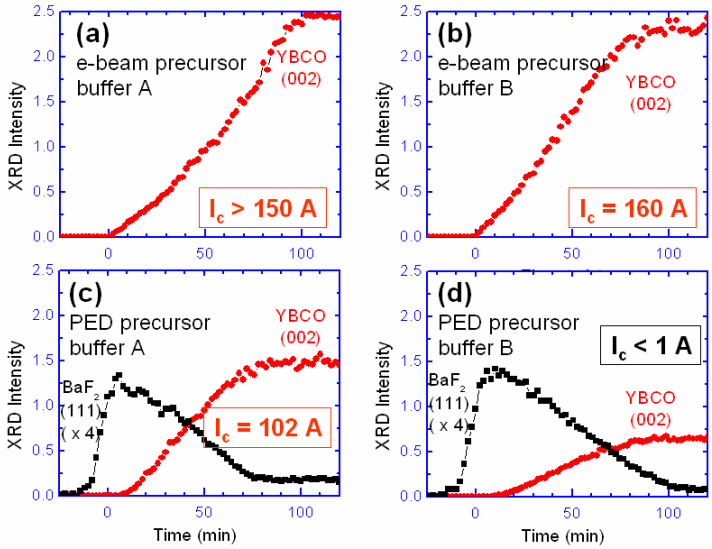

Fig. 2.28. Conversion of different types of precursors on two different CeO_2/YSZ/CeO_2 buffer stacks. High currents are observed in all combinations except for case (d): PED precursor on buffer B.

The PED-deposited layers behave very differently. As in all of our PED precursor work, these layers were obtained by ablating from a slightly Ba-deficient target (as needed due to the nonstoichiometric transfer of material in the PED process) while the tape moves in a reciprocating fashion in the deposition chamber. The two types of buffers were mounted in series on a length of tape, which passed through the deposition zone more than 30 times. This guarantees that the two samples contain an identical PED precursor. Figure 2.28(c) shows the X-ray data recorded during the conversion of the PED layer on buffer A. The sample exhibits a poorer development of the crystallinity (*c*-axis oriented YBCO) [see Fig. 2.28(a)]. Nevertheless, a critical current just above 100 A was measured on the sample. In contrast, the identical precursor material on buffer B [Fig. 2.28(d)] yields poor crystallinity and almost no supercurrent carrying capacity.

An additional interesting observation can be made by more closely inspecting the YBCO(002) traces in Figs. 2.28(c) and (d) with those in Figs. 2.28(a) and (b). A delay is observed in the development of the crystallinity with respect to time when the conversion temperature is reached (t = 0). Such an "incubation time" is not observed for any of the e-beam-evaporated layers but is typical for all PED material.

These observations may indicate poorer nucleation of YBCO in the case of PED precursors and buffer layer B, possibly due to damage that occurs during the deposition of the PED material. However, other interpretations are also possible. For example, different CeO_2 caps may have different types of nucleation sites for YBCO crystallization, and the requirements for PED precursors may be different from those of e-beam-evaporated material.

2.8.3 Damage to Buffer Layer Material in the PED Process

The hypothesis that the PED precursor–CeO_2 cap interface is the limiting element in these structures was tested by comparing two test samples (see Fig. 2.29). Figure 2.29(a) shows the structure with a PED precursor deposited onto buffer B [Fig. 2.28(d)]. A different sample [Fig. 2.29(b)] was fabricated in which e-beam evaporation was first used to deposit a 100-nm-thick "seed" precursor (isolating the buffer from the PED-deposited material) followed by another 1000 nm of PED-deposited material.

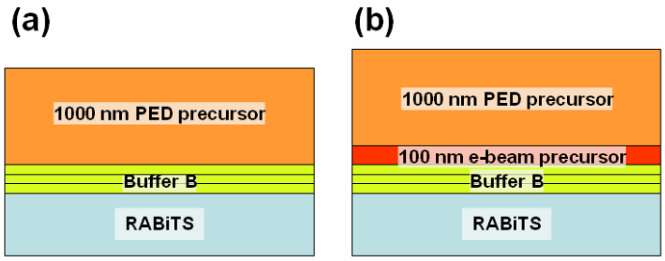

Fig. 2.29. Sample architectures used to study the effect of interface damage that may occur during the PED process. (a) Standard sample. (b) An e-beam-evaporated "seed" layer separates the PED precursor from the buffer in the architecture.

The test structure was converted in the same process, and a value of I_c = 43 A was measured. While this value is significantly lower than that measured for an e-beam precursor, it represents a significant improvement over the PED precursor deposited directly onto buffer B. Multiple interpretations may explain these observations. For example, the kinetics of conversion may differ significantly between e-beam and PED precursors. Therefore, a different type or density of nucleation sites at the surface of the CeO_2 cap may be needed to yield optimum conditions, and the PED-material might be particularly sensitive to these nucleation issues. Alternatively, some damage may occur during the PED process. However, a cross-sectional TEM analysis of the structures showed no visible damage to the YBCO-CeO_2 interface (Figs. 2.30 and 2.31). The interface between the e-beam seed and the PED material is not visible after conversion, indicating that crystallization of PED precursors into high-quality YBCO is possible, as was concluded from the data in Fig. 2.28(c). This points again to the interpretation of damage to some (but not all) buffer layers during the deposition in the PED process, even if it remains invisible in the TEM images, or to differences in the requirement of nucleation sites.

Measurement of the X-ray intensity during the conversion of the sample with the e-beam seed layer (data not shown) also shows an incubation time comparable with those of all PED-based samples. This indicates that the incubation time is not a question of nucleation and crystallization at the interface, but instead may be due to a limited diffusion of gaseous species through the PED material. While this represents a hurdle for scale-up and rapid processing, the reasonable current obtained for the sample shows that it is not the limiting factor for these precursors.

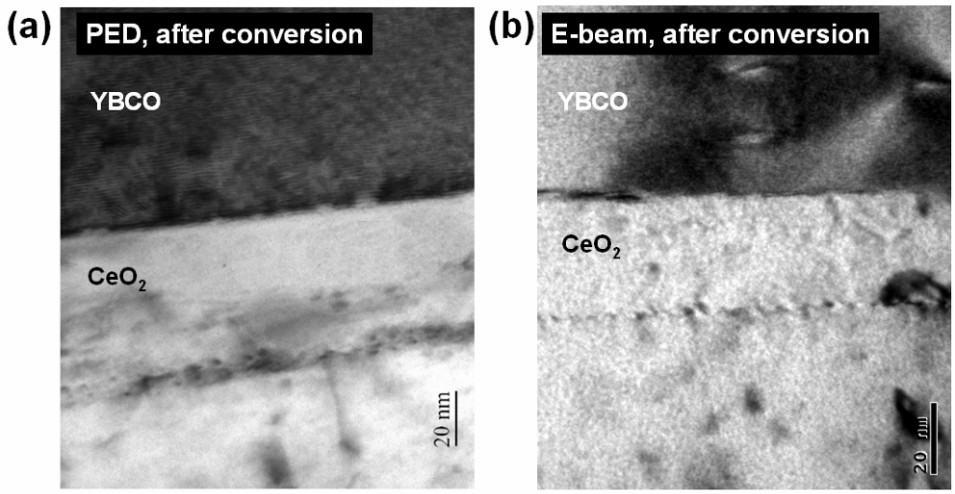

Fig. 2.30. Cross-sectional TEM images of the converted YBCO on buffer B. (a) The standard sample shows the PED material. (b) The interface between the e-beam-evaporated seed layer and the buffer layer shows no visible damage to the CeO_2.

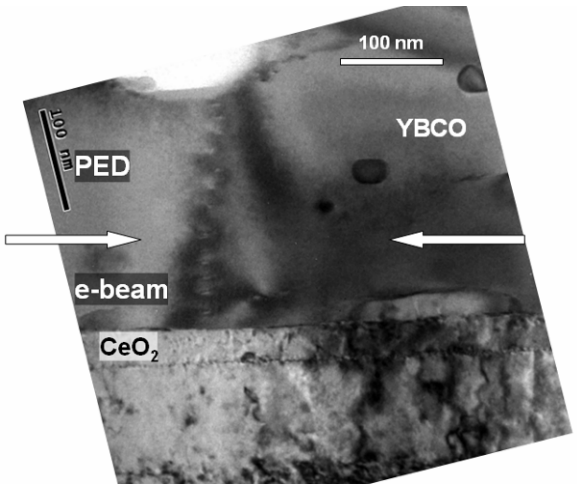

Fig. 2.31. Lower-magnification cross-sectional TEM image of the sample after conversion. Arrows indicate the approximate location of the interface between the e-beam deposited "seed" and the PED-deposited precursor. No contrast is seen, indicating the possibility to fully crystallize the PED-material in a similar fashion to the e-beam deposited precursor.

2.8.4 Energetics of the Approach and Comparison with PLD

As we have shown in our previous annual report, an ion probe can be used to monitor the ionic flux of species impinging on a substrate during the PED process. As our analysis has shown [1], the energies are comparable to those encountered in PLD if operating in vacuum. High energies are particularly damaging in a low-temperature process (as in this room-temperature deposition) because recrystallization and annealing of the created defects during the deposition does not occur.

For comparison, buffer B was used for the PLD deposition of a similar precursor (different target composition due to the more stoichiometric transfer observed typically in PLD). Two conditions were used: deposition in vacuum, and deposition in 30 mTorr of Ar. Introducing a background gas in PLD results in a significant reduction of the energies of the impinging species (which is possible in PED only to a limited extent due to the requirement of an electron discharge). After conversion, the vacuum-deposited precursor carried a current of $J_c = 0.44$ MA/cm^2; the sample deposited in Ar showed $J_c =$ 0.6 MA/cm^2 (actual thicknesses were lower than in the case of the PED precursors). We can immediately conclude from the data that the energetics in the deposition play a key role—in the case here, an increase of 50% in critical current density was observed when a carrier gas was introduced (i.e., when the deposition energetics were reduced.

It is particularly important to note here that PLD-deposited precursors on buffer A carry much higher currents (comparable to the PED samples on the same buffer A), illustrating that the details of the buffer structure determine the degree to which damage is suffered from the energetic species.

Nevertheless, the fact that a vacuum-PLD process, having comparable energetics as the PED approach, yields significantly higher current densities than the PED material, shows that plume damage can only partially explain the observed decreases in currents. Other aspects must be considered. For example, the potential for electron damage (redirected high-energy electrons from the PED source impinging on the substrate).

2.8.5 Summary and Conclusions

An "incubation" period was observed on all PED samples during the conversion, which may be a consequence of inhibited gas diffusion through the PED precursor. More importantly, the PED process appears to cause damage to the buffer layer surface for certain types of CeO_2 cap layers or to result in a precursor that is extremely sensitive to the distribution, density, and type of nucleation sites present at the CeO_2 surface. While the exact details of these mechanisms are not understood, our observations show that they lead to poor crystallinity and, consequently, to low critical currents. The sensitivity of one type of buffers to deposition energetics in particular was further illustrated by PLD experiments under different conditions.

The resulting need to find optimum buffer layers for a PED process significantly reduces the method's value in coated conductor manufacturing, as the gains from simplicity and reduced costs may be offset by increased requirements in other steps of the process. Furthermore, PED is inherently ill-suited for buffer-layer comparisons to provide guidance to other, less energetic, processes, such as e-beam evaporation.

Methods could be devised to change the energetics of the deposition species, but not without serious complications. Increasing the target-substrate distance is one possibility, but doing so would result in reduced control over stoichiometry (when collecting over a large solid angle) or reduced deposition rates. Increasing the pressure in the system is an additional option. However, doing so would require a differentially pumped electron-beam path, which would significantly complicate the process. It may also be possible to fine-tune the conversion conditions and thus control the nucleation kinetics for PED material so as to change the requirement for nucleation sites.

Therefore, our work shows that PED may lack the ease and versatility expected from a candidate deposition method for an industrial coated-conductor process.

2.8.6 References

1. H. M. Christen, D. F. Lee, F. A. List, S. W. Cook, K. J. Leonard, L. Heatherly, P. M. Martin. M Paranthaman, A. Goyal, and C. M. Rouleau, "Pulsed Electron Deposition of Fluorine-Based Precursors for $YBa_2Cu_3O_{7-x}$-Coated Conductors," *Superconductor Science & Technology* **18**, 1168 (2005).

2. D. F. Lee, H. M. Christen, F. A. List, L. Heatherly, K. J. Leonard, C. M. Rouleau, S. W. Cook, P. M. Martin, M. Paranthaman, and A. Goyal, "R & D of RABiTS™-Based Coated Conductors: Conversion of ex situ YBCO Superconductor using a Novel Pulsed Electron-Beam Deposited Precursor," 17th International Symposium on Superconductivity (ISS), Niigata, November 2004. To be published in *Physica C.*

2.9 Long-Range Current Flow and Percolation in RABiTS™-Type Conductors and the Relative Importance of Out-of-Plane and In-Plane Misorientations in Determining Critical Current Density

A. Goyal, C. Cantoni, and D. F. Lee (ORNL); N. Rutter (ORNL and the University of Cambridge, UK)

2.9.1 Introduction

RABiTS™ consists of a biaxially textured metallic substrate and one or more epitaxial buffer layers [1-2]. HTS layers such as YBCO are grown epitaxially on these substrates, and critical current densities of more than 3 MA/cm^2 are now routinely obtained [3–4]. Because the rolled, recrystallized metallic template has a cube texture, {001}<100>, the superconducting film is also made up of a network of grains that have crystallographic orientations that are within a few degrees of {001}<100>. The critical current of such a superconducting grain network is usually assumed to be limited by dissipation at grain boundaries, which generally are able to carry less current than the grains. Current flow in polycrystalline coated conductors therefore relies on percolation around the higher-angle grain boundaries. Hence, calculations of long-range current flow in RABiTS™-type conductors are of interest. It is important to determine how narrow filaments can be made on such conductors without significant reduction in critical current density.

A characteristic of the {001}<100>.cube texture is a FWHM of about 5° for the "true" in-plane texture and 4-8° FWHM for the out-of-plane texture in the YBCO layer [3-4]. The sharper out-of-plane texture is for rocking in the rolling direction; the broader is for rocking about the rolling direction. The finite FWHMs along the *a*, *b*, and *c* crystallographic axes mandate that a number of grain boundaries in the superconductor will have misorientations comprising both in-plane and out-of-plane misorientations. It is of interest to discern the relative effects of in-plane and out-of-plane misorientations on critical current density in order to direct efforts in further improving the performance of the conductors.

In this work results on calculation of long-range critical currents in a RABiTS™-type conductor and the effect of conductor or filament geometry are summarized. In an effort to experimentally probe the effects of conductor geometry, a meter-long, 100-grain-wide conductor of YBCO/RABiTS™ was fabricated and characterized. The relative effects of out-of-plane and in-plane misorientations on critical current density are discussed.

2.9.2 Calculation of Long-Range Current Flow

Many models have been used to calculate or estimate critical currents in RABiTS™-type conductors [5-8]. Each of these models has a number of limitations that have recently been improved upon [9]. In this work, the Monte-Carlo Potts method was used to first generate a realistic grain structure, which is similar to that of real RABiTS™ tapes. Figure 2.32 compares a real RABiTS™ grain structure with one modeled with the Potts method [9]. The grains in the model structure are irregularly shaped and have a range of sizes.

When the physical grain structure has been generated, the crystallographic orientation of each grain is then assigned. As in other simulations, this is done randomly based on a typical X-Ray gaussian distribution. The misorientation angle (θ_{mis}) between adjacent grains is then calculated, and the critical current is assigned based upon the exponential relationship between the misorientation angle and the critical current density. Pixel boundaries that lie within grains are also assigned a critical current value, which represents the critical current density of the grains. This takes into account the low-angle plateau in critical current density vs misorientation angle [9].

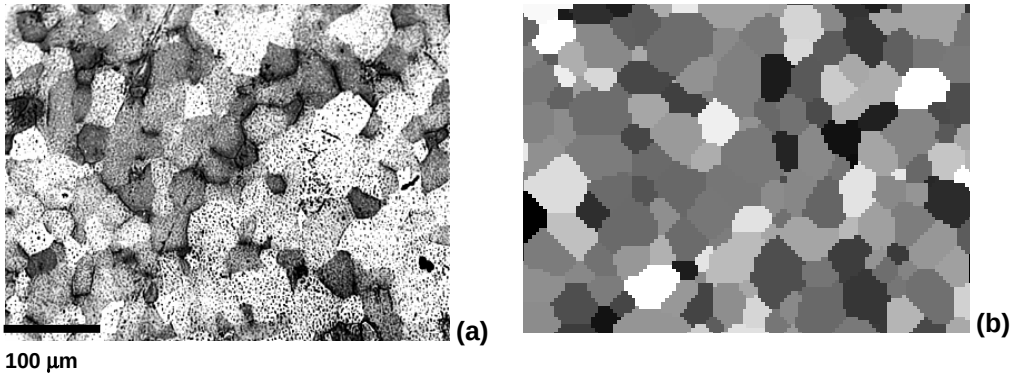

Fig. 2.32. RABiTS™ grain structure. (a) Real. (b) Modeled.

Once the network of grain boundaries, each with an assigned critical current, has been established, the critical current is calculated by determining the path of boundaries across the width of the conductor whose critical current sum is the minimum among all such possible paths (i.e., the limiting path).

2.9.2.1 Calculations for a Conductor with a 10° FWHM

Figure 2.33 shows the results obtained for critical current density as a function of length and width of the conductor. The critical current density is normalized to the intragraunlar critical current density for a zero-degree grain boundary [J_c (0º)]. If the average grain size in a RABiTS™-type conductor is about 40 μm, a 2-km length represents to 5×10^7 grains. One of the axes in the plots is the number of grains along the length and this scale extends to 10^8 grains. Figure 2.33 contains plots of critical current density vs the number of grains along the length of the conductor as a function of the number of grains along the width of the conductor. Plots are included for conductor widths of 10, 30, 100, 300 and 1000 grains. Even for a conductor that is only 10 grains wide, the normalized critical current density only drops from 0.4 to 0.1 in going to kilometer lengths. For conductors 100 grains wide or wider, only a very minimal decrease in critical current density is found.

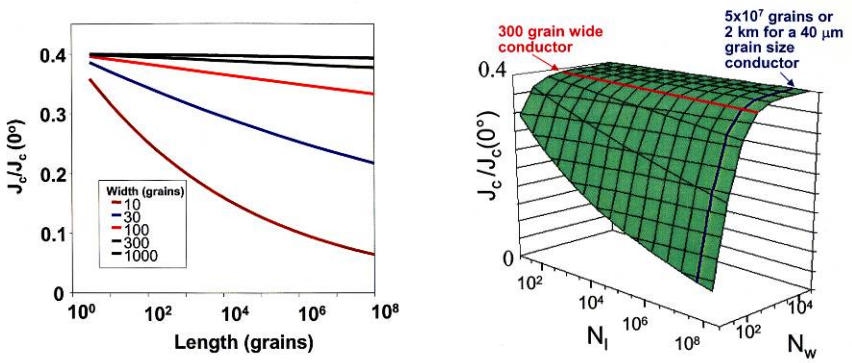

Fig 2.33. Critical current density of YBCO/RABiTS™ vs the number of grains along the length of the conductor as a function of number of grains along the width of the conductor. (a) Two-dimensional plot. (b) Three-dimensional plot.

2.9.2.2 Measurement of Critical Current Density for a 100-Grain-Wide Conductor

A 4-mm-wide, 1-m-long YBCO on RABiTS™ conductor was fabricated. The ex situ BaF_2 process was used to deposit a 0.3-μm YBCO layer [10]. The critical current density was measured at every centimeter along the tape. Figure 2.34 shows a histogram of measured transport critical current densities along the length. The average critical current density was 2.16 MA/cm^2, self-field, 77 K. The standard

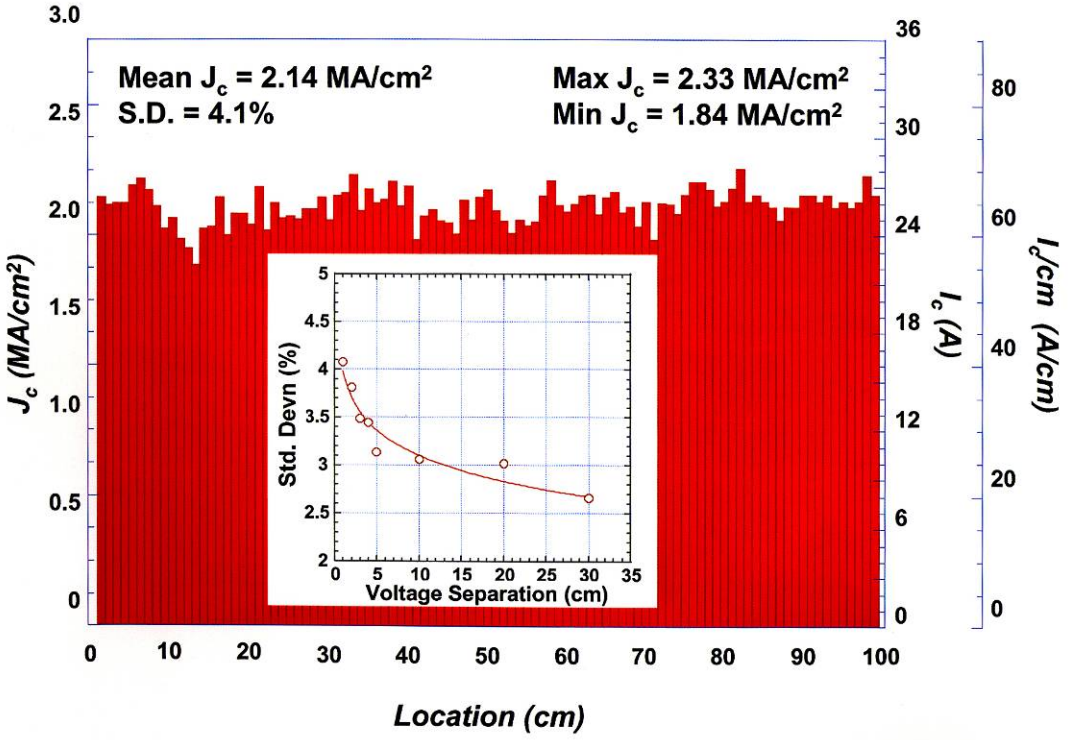

Fig. 2.34. Critical current density vs location for a meter-long YBCO/RABiTS™ conductor only 100 grains wide. The critical current density is indicated for every centimeter of tape. Average J_c = 2.14 MA/cm^2; SD = 4.1%. No evidence of any percolative pinch-off is present. Inset: How the standard deviation would vary with separation between the voltage tabs.

deviation of the 100, 1-cm segments was 4.1%. The low standard deviation for a conductor only 100 grains wide and the high critical current density are in agreement with the predictions of the percolation model in Fig. 2.33. Clearly no percolative pinch-offs in critical current density were observed along the length of the conductor. The inset in Fig. 2.34 shows the standard deviation as a function of measurement length. That the standard deviation decreases with increase in the distance between the voltage tabs is important because it shows that when reporting critical current density and standard deviation in long samples, it may be essential to probe the critical current density at various length scales. Comparing such a plot of standard deviation vs distance between the voltage tabs to the theoretically predicted dependence can give insights into whether the critical current density is still processing-limited. Such an analysis has also been performed on American superconductor tapes [11].

2.9.2.3 Calculations for a Conductor with a 5° FWHM

Typical state-of-the-art, fully buffered RABiTS™ tapes have FWHM of the in-plane texture of 5° [3,4]. This would have a significant effect on Fig. 2.33. As was presented in the 2004 DOE Annual Peer Review in Washington, D.C., the calculated self-field critical current density for a 1 km × 100 grain conductor with a 5° FWHM, is almost an order higher than that with a 10°FWHM. Moreover, the decrease in critical current density in going from a short sample (a few centimeters) to a 1-km sample is significantly reduced. More than 90% of the critical current density of a short sample is expected for a 1-km sample.

2.9.2.4 Calculations for a Conductor with a 5° FWHM in Applied Magnetic Fields

Verebelyi et al. have measured the properties of YBCO bicrystals in applied fields. Using those data, Dimos-type [12] plots of critical current density vs misorientation angle in applied magnetic fields can be generated. The plots are then used to assign critical current densities to individual grain boundaries based on their misorientation angles. Plots of critical current density vs the number of grains along the length of the conductor as a function of number of grains along the width of the conductor in applied fields show that the dependence of critical current density on conductor geometry is almost negligible [13]. As expected, with increase in applied field the effect of conductor geometry on critical current density is reduced further [13]. This suggests that subdivision of epitaxial YBCO layers on a RABiTS™-type conductor into narrow filaments for low-AC loss applications should be possible without significant reduction in critical current density.

2.9.3 Effect of Out-of-Plane Texture

RABiTS™ samples fabricated with TiN as a seed layer were used to test the effect of the out-of-plane texture on critical current density [14]. Significant sharpening of the out-of-plane texture was found for TiN layers on textured metallic substrates. Figure 2.35 shows two graphs of the FWHM values for the (002) rocking curve of TiN films grown at various temperatures and with different thicknesses on Ni-3%W, Ni-5%W, Ni-Cr-W, Cu, and Cu-48%Ni-1%Al substrates. The data are plotted against the corresponding FWHM values of the substrate (002) rocking curves. In Fig. 2.35(a) the FWHMs of films and substrates are measured with azimuth parallel to the transverse direction of the tape; in Fig. 2.35(b) the azimuth is parallel to the rolling direction. In both cases the FWHM values for the TiN films are considerably smaller than the corresponding values for the substrate. The rocking curve sharpening is most evident in the transverse direction where most films exhibit a FWHM ranging between one-half and one-fourth of the substrate value. Particularly impressive is the case of one of the TiN films on Cu for which the FWHM improved by 10.4° (from a value of 13.6° in the substrate to a value of 3.2° in the film). For the same film the corresponding FWHM values in the rolling direction were 6.3° and 2°.

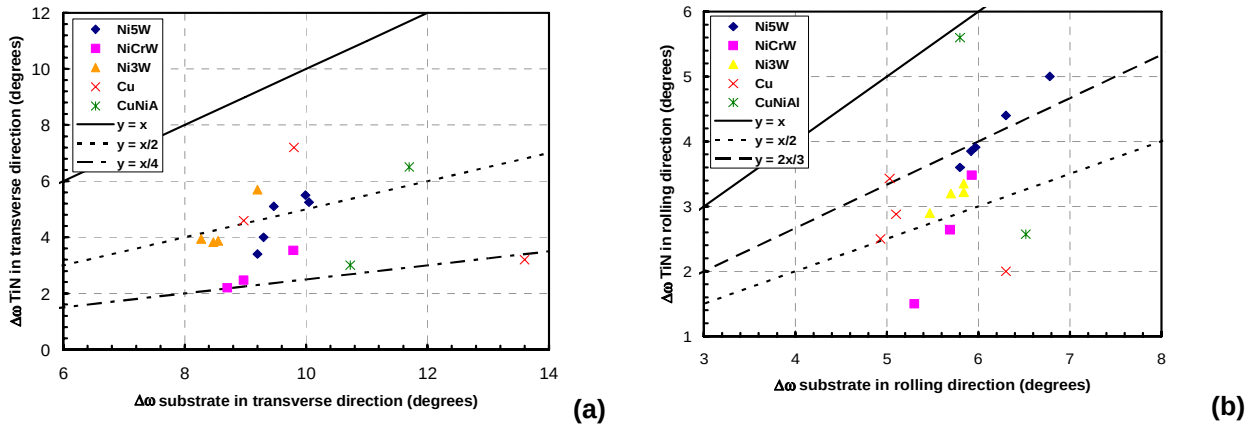

Fig. 2.35. FWHMs of the TiN (002) rocking curves vs corresponding FWHMs of the (002) substrate rocking curve for TiN films on different textured substrates. (a) Rolling direction. (b Transverse direction.

Figure 2.36 shows a comparison between grain boundary maps obtained by electron backscatter Kikuchi patterns (EBKP) of (a) a biaxially textured Cu substrate and (b) a TiN film deposited on the same substrate. The map acquired on the TiN film highlights only grain boundaries that are larger than 3°. It is clear that with this criterion, macroscopic percolation of current is possible and that most of the material is connected by grain boundaries ≤ 3°. If the same criterion is used for the Cu substrate, the distribution of highlighted grain boundaries becomes much denser and current percolation through grain boundaries ≤ 3°

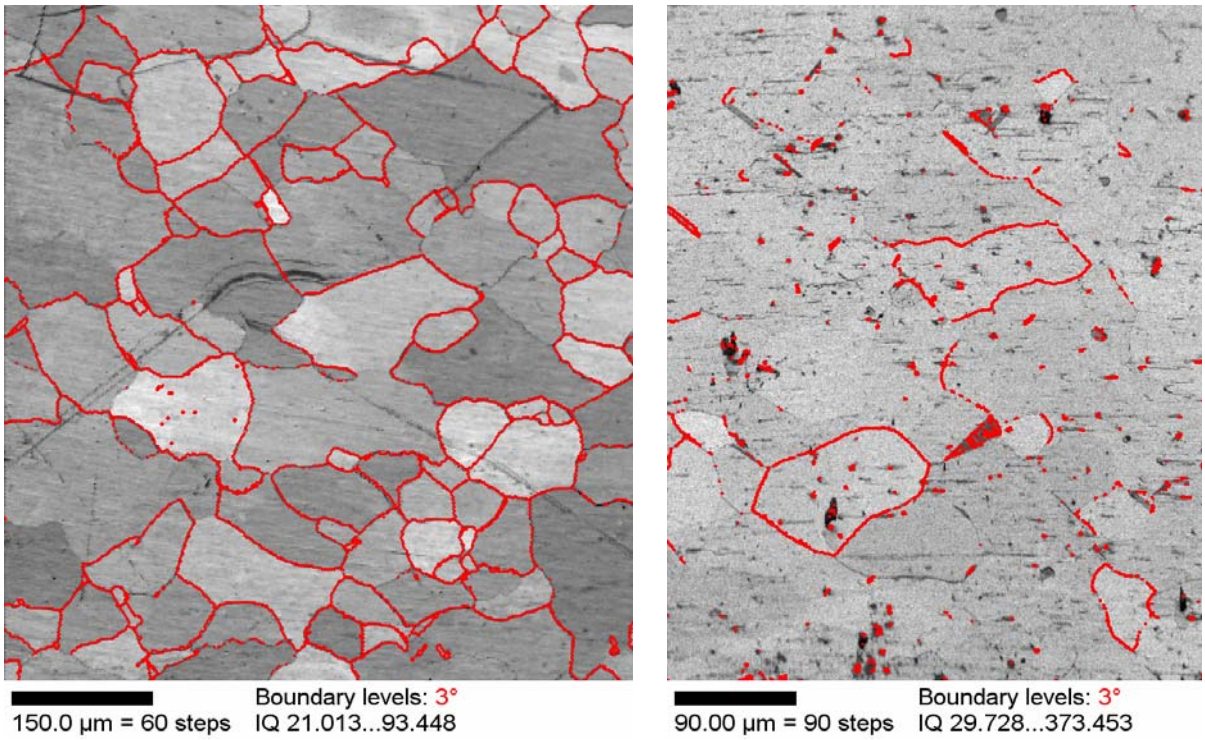

Fig. 2.36. EBKP maps showing grain boundaries larger than 3° for (a) a biaxially textured Cu substrate and (b) the same material with a TiN seed layer.

is not possible. To obtain in the substrate a fraction of connected grains similar to that shown by the TiN film, we have to raise the criterion to an angle of 7°. In other words, if buffers and superconductor were to replicate faithfully the texture of the substrate, macroscopic current percolation would occur by transport through grain boundaries of ≤ 7°. The EBKP maps clearly suggest that the GB distribution has shifted toward much lower angles in the TiN film than in the substrate.

For high-quality YBCO films to grow on TiN seed layers, additional buffer layers that adequately prevent metal diffusion to the YBCO layer and oxygen diffusion to the substrate-seed layer interface are required. For this purpose, epitaxial layers of MgO followed by $LaMnO_3$ (LMO) were deposited, both of which maintain the sharper out-of-plane texture in the TiN seed layer. A 0.2-µm-thick YBCO film was deposited on such a RABiTS™ configuration (consisting of Ni-3at%W/TiN/MgO/LMO). All layers were deposited by PLD. The critical current density of the film was measured to be ~ 3.0×10^6 A/cm^2 and ~ 5.1×10^5 A/cm^2 in self-field and 1 T, respectively, at 77 K. Another RABiTS™ of the same configuration was capped with an epitaxial layer of CeO_2. Because of the particular deposition conditions used during PLD, in the CeO_2 layer, the out-of-plane texture deteriorated and broadened by a few degrees both for rocking in and transverse to the rolling direction. A YBCO layer was also deposited by PLD on the RABiTS™ substrate. The critical current density of the sample was measured to be ~ 2.5×10^6 A/cm^2 and ~ $4.9.0 \times 10^5$ A/cm^2 in self-field and 1 T, respectively, at 77 K. Table 2.5 lists the in-plane and out-of-plane textures of the YBCO layers on the substrates as well as the critical current density in self-field and 1 T at 77 K.

Table 2.5. In-plane and out-of-plane textures of the YBCO layers

	Architecture	Δω, R	Δω, T	Δϕ	J_c, 77 K (MA/cm^2)	
					Self-field	1 Tesla
1	LMO/MgO/TiN/Ni-3at%W	3.1°	4.1°	7.5°	3.0	0.51
2	CeO_2/LMO/MgO/TiN/Ni-3at%W	6.3°	7.5°	7.9°	2.5	0.49

It can be seen from Table 2.4 that the in-plane texture of the YBCO layers is very comparable in the two samples. However, a significant difference of 3° in the out-of-plane FWHM of $\Delta\omega$ for rocking in and about the rolling direction is observed. Despite this significant difference in the texture, the measured critical current density values are similar for the two samples.

2.9.4 Separation of Total Misorientation into In-Plane and Out-of-Plane Misorientations

Typical misorientation angles measured using X-ray microdiffraction or EBKP give the total misorientation at the grain boundary. Hence, thus far all correlations of critical current density with misorientations have been with total misorientations. For over 10 years, attempts have been made to derive crystallographically correct separation of this total misorientation into in-plane and out of-plane components. The difficulty in doing this arises because three distinct rotations are required to describe any misorientation. Moreover, typically orientation data are represented in Euler Space, which is highly nonlinear, particularly along the ϕ axis. Three Euler angles (ϕ_1, ϕ, and ϕ_2) are needed to describe any orientation or misorientation in Euler Space. Hence, making projections in Euler Space is crystallographically incorrect. We have formulated a crystallographically correct methodology in which manipulations are performed in Rodrigues Space [13,15]. Orientation image micrographs (OIM's) of the same region in a fully buffered substrate from AMSC were drawn with the total misorientation, the in-plane misorientation, and the out-of-plane misorientation [13,15]. Upon substrates such as these, AMSC routinely achieves critical current densities in excess of 3 MA/cm^2 in self-field and 77 K. This level on the RABiTS™ substrates is about 70 to 80% of the critical current density typically obtained on single crystals. The only OIM micrograph that correlated well with that level of critical current density is the map of in-plane misorientations, in that about 70 to 80% of the cross-sectional area of the substrate had no grain boundaries with misorientation angles greater than 4°. The grain boundary map corresponding to out-of-plane misorientations had less than 20% of the cross section with no grain boundaries greater than 4°. This observation together with the results obtained in the previous section point toward the more dominant influence of the in-plane misorientation in determining the transport critical current density.

2.9.5 Summary

Calculations of long-range current flow using an advanced percolation model show that with the presently observed texture in RABiTS™ substrates, the dependence of critical current density on length as a function of width is greatly reduced and becomes almost negligible in applied fields. These results suggest that subdivision of a wide conductor into narrow filaments should be possible without loss in critical current density. The relative importance of the out-of-plane texture in affecting intergranular critical current density was explored by fabricating RABiTS™ substrates with different out-of-plane textures but approximately the same in-plane texture by using TiN as a seed layer for which significant sharpening of the out-of-plane texture was observed. Two samples of configuration Ni-3at%W/TiN/MgO/LMO/ YBCO and Ni-3at%W/TiN/MgO/LMO/CeO_2/YBCO were examined. For these two samples, similar critical current densities were found, even though significant differences existed in the out-of-plane texture with approximately the same in-plane texture. Separation of the total misorientation in grain boundary networks into in-plane and out-of-plane misorientations using manipulations in Rodrigues space shows that measured transport critical current density on typical RABiTS™ correlates best with the in-plane texture.

2.9.6 References

1. A. Goyal, D. P. Norton, J. D. Budai, M. Paranthaman, E. D. Specht, D. M. Kroeger, D. K. Christen, Q. He, B. Saffian, F. A. List, D. F. Lee, P. M. Martin, C. E. Klabunde, E. Hatfield, V. K. Sikka, *Appl. Phys. Lett.* **69**, 1795 (1996).
2. A. Goyal, J. D. Budai, D. M. Kroeger, D. P. Norton, E. D. Specht and D. K. Christen, U.S. Patents 5,739,086; 5,741,377; 5,846,912; 5,898,020.

3. A. Goyal in "Second Generation HTS Conductors," ed. A. Goyal, Kluwer Publishing Corporation, USA (October 2004).
4. A. Goyal, M. P. Paranthaman, and U. Schoop, *MRS Bulletin* **29**, 552 (2004).
5. E. D. Specht, A. Goyal, and D. M. Kroeger, *Supercond. Sci. Technol.* **13**, 592 (2000).
6. N. A Rutter, B. A. Glowacki, and J. E. Evetts, *Supercond. Sci. & Technol. 13*, L25 (2000).
7. Y. Nakamura, T. Izumi, and Y. Shiohara, *Physica C* **371**, 275 (2002).
8. B. Holzapfel, L. Fernandez, F. Schindler, B. de Boer, N. Reger, J. Eickemeyer, P. Berberich, and W. Prusseit, *IEEE. Trans. Appl. Supercond.* 11, 3872 (2001).
9. N. A. Rutter and A. Goyal (private communication).
10. D. F. Lee, K. J. Leonard, L. Heatherly, F. A. List, S. W. Cook, J. Yoo, M. Paranthaman, P. M. Martin, A. Goyal, and D. M. Kroeger, *Supercond. Sci. Technol.* **17**, 386 (2004).
11. D. T. Verebelyi, U. Schoop, C. Thieme, X. Li, W. Zhang, T. Kodenkandath, A. P. Malozemoff, N. Nguyen, E. Siegal, D. Buczek, J. Lynch, J. Scudiere, M. Rupich, A. Goyal, E. D. Specht, P. Martin, and M. Paranthaman, *Supercond. Sci. Technol.* **16**, L19 (2003).
12. D. Dimos, P. Chaudhari, J. Mannhart, and F.K. LeGoues, *Phys. Rev. Lett.* **61**, 219 (1988).
13. A. Goyal, "RABiTS™ Substrates Research and Development", presented at the DOE Peer Review on Superconductivity, Washington D.C. July 2003 (http://www.ornl.gov/sci/htsc/documents/pdf/fy2003/RABiTS_Substrates_R&D-Goyal.pdf).
14. C. Cantoni, A. Goyal, U. Schoop, X. Li, C. Thieme, A. A. Gapud, T. Aytug, M. Paranthaman, K. Kim, J. D. Budai, and D. K. Christen (private communication).
15. A. Goyal and D. Field (private communication).

2.10 Development of Nonmagnetic, Cr-Containing Substrates and Development of Appropriate Buffer Layers

A. Goyal, S. Cook, C. Cantoni, L. Heatherly, K. Leonard, D. F. Lee, P. M. Martin, and E. Hatfield

We have developed deformation and annealing conditions for fabrication of nonmagnetic Ni-13at%Cr substrates. The starting material was made via induction skull melting. The casting was then homogenized, hot-rolled, and subsequently cold-rolled to form the starting coil for the final rolling in the ORNL class 100 clean-room facility.

Figure 2.37 shows a (111) pole figure for a reel-to-reel rolled Ni-13at%Cr substrate. The log-scale (111) pole figure is clean with almost a 100% cube texture. The out-of-plane rocking curve FWHMs for the fully annealed substrate for rocking in and about the rolling direction were 4.5º and 6.3º, respectively. The "true" in-plane FWHM as measured by a phi-scan was 6º.

The presence of Cr makes seed buffer layer deposition with the correct orientation challenging due to the tendency for Cr to preferentially oxidize and form undesirable textures. Typically, high-quality cube-on-cube epitaxy of oxide buffers on Ni is made possible by performing the depositions under conditions in which the formation of NiO is thermodynamically unfavorable. However, no such condition exists for deposition of the commonly used oxide buffer layers wherein the formation of Cr oxide is thermodynamically unfavorable while the

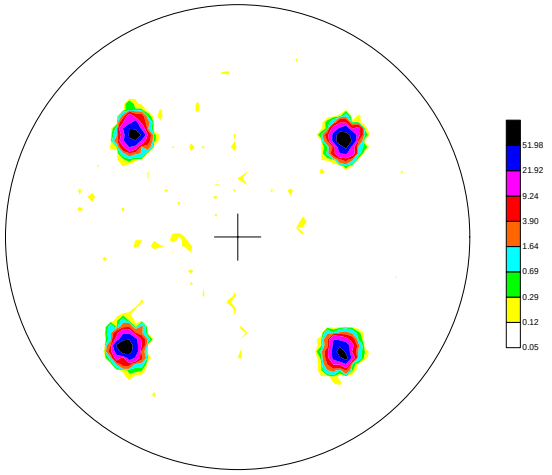

Fig. 2.37. Log-scale (111) pole figure of a rolled and annealed Ni-13at%Cr substrate showing very good texture development.

formation of the desired oxide is thermodynamically favorable. In light of this, three buffer multilayer options have been developed for transferring the texture from Cr-containing substrates to the superconductor:

1. Cr-containing substrate /Pd/MgO/LMO
2. Cr-containing substrate /TiN/MgO/LMO/CeO_2
3. Cr-containing substrate /Ni-9at%W/Y_2O_3/YSZ/CeO_2

For case 1, we have demonstrated that 0.2-μm-thick YBCO films deposited by pulsed laser ablation have a critical current density of 3 MA/cm^2 at 77 K, self-field. It is likely that this stack will also be useful for thicker films (in the range of 1 to 3 μm). However, the high cost of the Pd layer, even though it is very thin, makes this multilayer stack somewhat unattractive. In light of that, we have developed two other buffer layer stacks (Case 2 and 3).

For Case 2, Substrate/TiN/MgO/LMO/CeO_2, wherein the expensive Pd layer was replaced by TiN, a critical current density of 1.8 MA/cm^2 was obtained for a 0.8-μm-thick YBCO film. This film was deposited byAMSC, using its ex situ MOD process. Clearly, the high performance indicates the viability of Case 2. Figure 2.38 shows the multilayer stack used and the thicknesses of each layer.

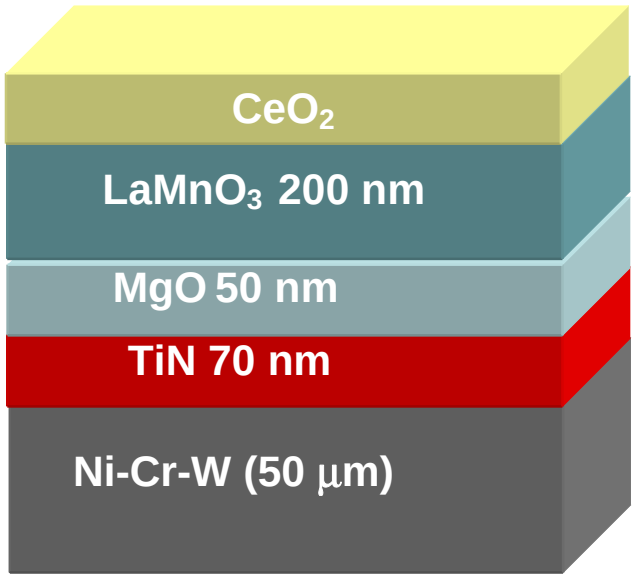

Fig. 2.38. Multilayer stack corresponding to Case 2.

Figure 2.39 shows a TEM cross-section image of the Case 2 stack. It is clear from the micrograph that the interfaces are clean. Higher-magnification examination of the Ni-Cr-W – TiN interface shows that no oxide layer is formed.

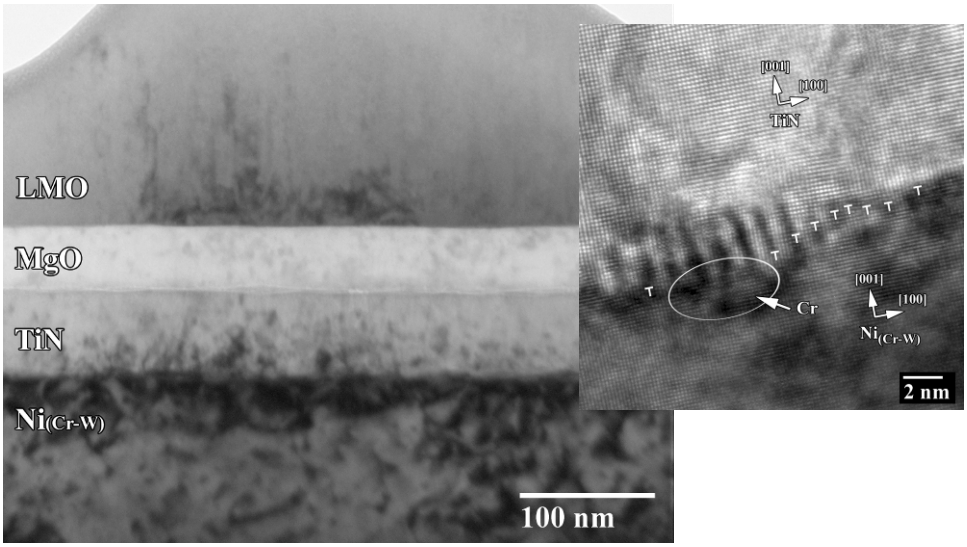

Fig. 2.39. Cross-section TEM image of the Ni-Cr-W/TiN/MgO/LMO/CeO_2/ YBCO stack after the YBCO deposition, annealing, and measurement of transport properties. Inset: higher-magnification image of the Ni-Cr-W–TiN interface.

Case 3 is the most interesting because it does not require perovskite buffer layers containing two cations, such as $LaMnO_3$. Deposition of perovskites containing two cations is difficult using rapid depositions techniques such as e-beam deposition or reactive sputtering. It turns out that the standard buffer stack of Y_2O_3/YSZ/CeO_2 developed for Ni and Ni-W substrates can be used along with a nonmagnetic Ni-9at%W seed layer. Figure 2.40 shows a (111) pole figure of the Ni-13at%Cr substrate after a 1-μm-thick Ni-9at%W coating was deposited on it in a reel-to-reel sputtering system. Clearly, only the cube texture is seen. Upon this Ni-9at%W coating, a standard stack of Y_2O_3/YSZ/CeO_2 was deposited in reel-to-reel systems at ORNL. The texture data obtained is shown for all the layers in Table 2.6.

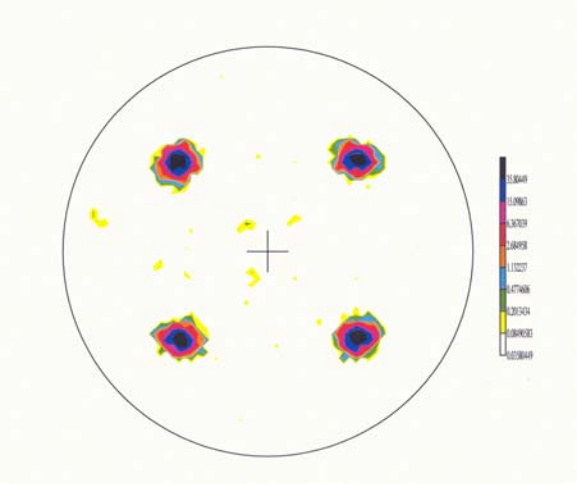

Fig. 2.40. (111) pole figure of substrate after deposition of a 1-μm-thick Ni-9at%W coating.

Table 2.6. Texture data for the Case 3 sample

Layer	Δω		Δϕ	
	ϕ = 0°	ϕ = 90°	Measured	Actual
Y_2O_3	3.94	5.75	6.18	5.14
YSZ	4.23	5.85	6.65	5.61
CeO_2	3.90	5.44	6.43	5.51

A 0.8-μm-thick YBCO film was then deposited by AMSC, using the ex situ MOD process on the Case 3 substrate. A critical current density of 2.4 MA/cm^2 at 77 K, self-field was obtained. The respectable critical current density value at that thickness suggests that deposition of a nonmagnetic, Ni-9at%W coating on top of Cr-containing substrates is a simple way to integrate such substrates with the standard multilayer buffer developed for Ni and Ni-W alloys.

2.11 Assessment of Chemical Solution Synthesis and Properties of $Gd_2Zr_2O_7$ Thin Films as Buffer Layers for Second-Generation HTS Wires

M. Paranthaman, K. J. Leonard, H. Y. Zhai, M. S. Bhuiyan, E. A. Payzant, A. Goyal, D. B. Beach, P. M. Martin, and D. K. Christen (ORNL); T. Aytug and S. Sathyamurthy, (ORNL and UTK); X. Li, T. Kodenkandath, U. Schoop, and M. W. Rupich (AMSC); H. E. Smith, T. Haugan, and P. N. Barnes (Air Force Research Laboratory)

Presently, buffer layer architectures on which high-critical-current-density YBCO films have been consistently obtained comprise the three layers CeO_2/YSZ/(Y_2O_3 or CeO_2) deposited epitaxially on Ni-alloy substrates by PVD. Recently, there have been significant efforts concentrated on chemical-solution-derived $SrTiO_3$, RE_2O_3, $RE_2Zr_2O_7$, and RE_3NbO_7 (RE = rare-earth) films to assess their feasibility as buffer layer materials on RABiTS™. Among these systems, sol-gel–processed single $La_2Zr_2O_7$ (LZO) buffer layers, a $RE_2Zr_2O_7$-based cubic pyrochlore structure, and LZO seeds capped with sputtered CeO_2/YSZ layers have shown the most promise as templates for YBCO with high critical current density. Despite similar precursor processing chemistries, the other solution-based material systems have not yet demonstrated performance levels as effective as $RE_2Zr_2O_7$. Currently, studies to understand the relationship between the processing techniques and the role of various materials are being pursued.

Another $RE_2Zr_2O_7$-based material that has recently been drawing considerable interest is $Gd_2Zr_2O_7$ (GZO), with a pseudocubic lattice parameter of 3.72 Å. To date, fabrication of GZO has been made by using IBAD, a vacuum-based approach for biaxially textured template fabrication by which a factor-of-two increase in the processing rate can be obtained over the original IBAD-YSZ process. The CeO_2 films deposited on IBAD-GZO layers exhibit significantly improved grain alignment (i.e., small in-plane

mosaic spread). Hence, it is of the essence to assess the solution deposition technology for GZO films on the RABiTS™ template.

In this study, we investigated the viability of GZO as a buffer layer via wet chemical precursor approaches. In particular, we examined growth and microstructural behavior of GZO layers. Contrary to the common porous microstructure observed in solution-processed oxide layers, GZO films studied in this initial work were dense and free of pores. We have also demonstrated high-critical-current-density YBCO performance on these GZO buffers with sputtered and MOD-derived CeO_2 cap layers on RABiTS™.

Both sol-gel and MOD routes were used to prepare precursor GZO solutions. Sol-gel solution preparation was carried out under an Ar gas atmosphere in a Schlenck-type apparatus. The MOD precursors were made in ambient atmosphere. In order to avoid premature hydrolysis, which can induce precipitation, the as-received gadolinium acetate (Alfa, purity: 99.9%) powder was first purified by dissolving in a mixture of water and acetic acid at a ratio of 3:1. The solution was filtered and then evaporated to dryness in an oven maintained at 150°C overnight to remove absorbed moisture. For the sol-gel chemistry, a stoichiometric mixture of purified gadolinium acetate and zirconium *n*-propoxide in 70% w/w *n*-proponal (Alfa) were dissolved and refluxed in excess of 2-methoxyethanol (Alfa, 99%) in a 250-mL round-bottom flask. The acetic acid (Alfa, 99.99%) and 2-proponal formed during the exchange reaction were distilled out along with the excess 2-methoxyethanol. The final concentration of the solution was adjusted to 0.25 M of total cations. The MOD solution was prepared from the purified gadolinium acetate by first dissolving it in acetic acid and then mixing with a stoichiometric amount of zirconium acetylacetonate (acac) (Alfa) while continuously stirring at room temperature. The final volume was adjusted to 20 mL to produce a 0.25 M cation precursor solution. The coatings were done by spin-coating on 1-cm-wide substrates at 4000 rpm for 30 s followed by direct heating to the crystallization temperature in a reducing atmosphere of forming gas (Ar + 4%H_2). To optimize the GZO growth conditions, samples were annealed at various temperatures (ranging from 1050 to 1250°C) for 30 min.

The YBCO films were deposited by PLD at 780°C in 200 mTorr oxygen with an average energy density of ~ 2 J/cm^2/pulse. Following deposition, the films were annealed under 550 Torr oxygen during cooldown. The samples were characterized for crystal structure, phase purity, and texture by XRD; high-temperature XRD wase used to document the nucleation and growth. SEM and high-resolution transmission electron microscopy (HRTEM), equipped with energy dispersive spectrometry (EDS), were used for homogeneity, microstructure, and cross-sectional examinations. We employed atomic force microscopy (AFM) for surface roughness analysis. Secondary ion mass spectroscopy (SIMS) depth-profile analyses were conducted to study the chemical compatibility and diffusion of elemental products through the conductor stack, as related to the possible cation contamination of YBCO. For the SIMS, an oxygen primary ion beam was employed. The major isotope of each element was followed, and spectrometer mass resolution was set at $M/\Delta M = 3000$ (10% valley) to exclude the contributions of other possible interferences. Electrical properties such as the resistive superconducting transition temperature, critical current density, and current-voltage characteristics of the composite structures were evaluated by a standard four-probe technique. Values of critical current density were assigned at a 1-μV/cm criterion. While GZO buffer layers processed by both sol-gel and MOD routes were stable up to a maximum processing temperature of 1250°C, sol-gel–synthesized GZO films required temperatures above 1200°C to obtain good crystalline quality. Figure 2.41 shows the XRD out-of-plane ($\Delta\omega$) and in-plane ($\Delta\phi$) FWHM peak-width distributions for GZO (004) and (222) reflections as a function of processing temperature. For direct quantitative comparison between the crystalline quality of the samples, FWHM values are normalized to those of the underlying Ni substrate. While the processing temperature does not have substantial effect on the in-plane alignment of the GZO films, the degree of mosaic spread of the GZO layers sharpens up significantly with increasing temperature above 1100°C and continues to gradually improve up to temperatures around 1200°C. These results are expected because, during the transformation of amorphous to crystalline phase, heterogeneous nucleation events occur preferentially at the substrate interface due to the lower interfacial energy. As such, the in-plane alignment of GZO films is primarily governed by the crystallographic texture of and epitaxy with the underlying substrate. On the

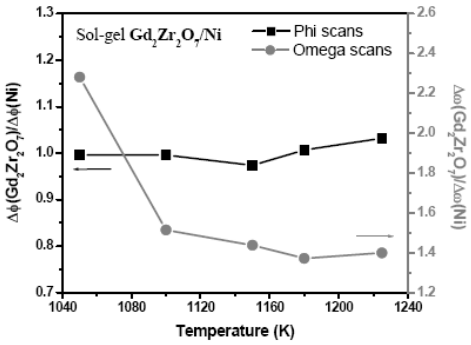

Fig. 2.41. Dependence of the normalized XRD FWHM peak widths on processing temperatures, quantifying the crystallinity of sol-gel $Gd_2Zr_2O_3$ films. (i) The out-of-plane distribution width, $\Delta\omega$. (ii) The in-plane distribution width, $\Delta\phi$.

other hand, the observed improvement in out-of-plane texture of GZO is a direct consequence of the processing temperature, where the thermal energy assists to align misoriented grains, reducing the mosaic spread. In fact, improvement of texture alignment can be clearly observed in the logarithmic scale (222) pole figures for GZO films that were processed between 1050 and 1225°C for 1 h in flowing Ar+4%H_2 (Fig. 2.42). For processing temperatures < 1200°C, significant amount of misoriented grains are present along with less well defined poles; and the quantitative analysis of the pole figure intensities indicates that the samples are < 90% cube textured (Fig. 2.43). On the other hand, a well-developed, 95% single-component cube texture is evident for the sample annealed at 1225°C. It is well known that non-textured materials can result in undesirable high-angle grain boundaries, which are proven to severely limit the supercurrent flow in the HTS film. Despite the development of good texture, the out-of-plane alignment of GZO films did not sharpen to the level of the substrate even upon annealing at 1225°C. This may be a consequence of chemical and physical properties of the substrate surface, thermal processing conditions, and/or the precursor chemistry of the sol-gel process. Besides, such high temperatures could also induce secondary recrystallization in technologically viable Ni-based alloy substrates, resulting in a significant fraction of random texture formation. Hence, these results challenged us to develop more practical solution routes to fabricate GZO layers on Ni-based substrates. Hereafter, the processing conditions and physical properties of GZO layers synthesized only by the MOD solution method will be discussed.

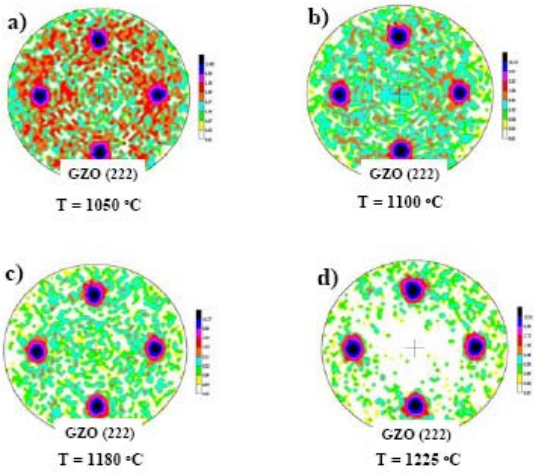

Fig. 2.42. XRD pole figures for $Gd_2Zr_2O_7$ layers on pure Ni substrates, plotted on a logarithmic scale, for processing at various temperatures. (a) 1050°C, (b) 1100°C, (c) 1180°C, (d) 1225°C.

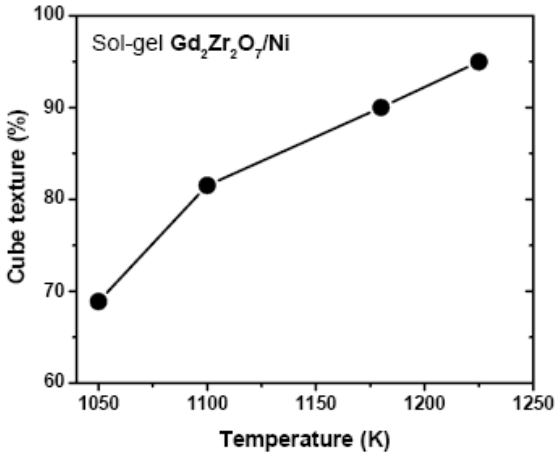

Fig. 2.43. Pole figure cube-texture percentages as determined by the quantitative analysis of the pole intensities for the samples processed at various temperatures.

First, nucleation and growth behavior of MOD GZO layers were determined by in situ XRD studies. Experiments were carried out in a Scintag PAD X diffractometer with a linear position sensitive detector covering a 2θ range of 8° centered at 2θ = 31° in reducing Ar + 2%He atmosphere. A single-coat GZO

film, approximately 15 to 20 nm thick, on a Ni-W substrate was heated from room temperature to 1250°C on a rhodium-platinum strip heater at a heating rate of 400°C/min. XRD patterns were recorded for a series of temperatures (data not shown here). Film crystallization nucleated at about 700°C and phase formation was completed around 1100 to 1150°C, which was evidenced by the saturation of the GZO (004) peak intensity with further increase in temperature up to 1250°C. We have not observed any indication of polycrystalline GZO component formation at the temperature range studied. This result reflects a significantly lower, 75–125°C, processing temperature to form epitaxial structure through MOD precursor chemistry. Even though there is no direct evidence, the reason for the observed decrease in processing temperature could be due to the differences in precursor chemistries of sol-gel and MOD-derived films. Moreover, HTXRD studies also revealed that the film growth is completed within 5 min when heat-treated at 1150°C. For this study, another single coat GZO sample was heated to 1150°C at the same heating rate, with XRD patterns were collected every 30 s for 60 min. In general, decrease in processing temperature should ease the fabrication requirements and provide a more practical synthesis scheme on Ni-W, as well as on other technologically viable substrates.

After having established the basic relationship between the phase nucleation and growth characteristics via the MOD approach, GZO films with thicker coatings were produced by multiple spin coatings with intermediate annealing steps. Thicker coatings are generally required due to the substrate cation diffusion issues associated with bulk porosity in solution-processed buffer layers. Figure 2.44 shows the XRD θ-2θ spectrum of one to three layer coatings processed at 1150°C. Each coat is typically 15 to 20 nm thick. Clearly, the GZO (004) peak intensity increases with each successive coat as the intensity of polycrystalline GZO (111) component remains at the background levels.

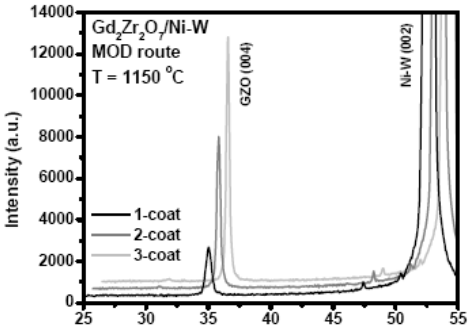

Fig. 2.44. XRD θ-2θ spectra of one to three coats of GZO layers on textured Ni-W substrates, showing a monotonic increase in the (004) intensity with the number of coats.

In Fig. 2.45(a), a typical plan-view high-resolution SEM microstructure of a single-coat GZO film is presented in the vicinity of a grain boundary. The sample exhibits a dense, continuous, and crack-free morphology with uniform coverage at the grain boundary. AFM measurements [Fig. 2.45(b)] show that the GZO film has a narrow distribution of nanoscale growth nuclei. The root-mean-square roughness (R_a) on a 10 × 10 μm area is 3 nm, which is comparable to that of the underlying substrate (R_a = 1 nm). A more detailed roughness profile, obtained without averaging, can be seen from the line scan analysis on a 5 × 5 μm region [Fig. 2.45(c)]. No significant variations in the surface profile along the line scan are observed, indicative of spatially uniform film growth.

Cross-section examination of GZO films on Ni-W substrates revealed a number of interesting growth characteristics. For comparison, TEM images of the thinned cross-sectional area of a single-coat sol-gel film and a three-coat MOD-derived GZO film are shown together in Figs. 2.46(a) and (b). While both samples show a dense microstructure and complete *c*-axis-oriented growth throughout the thickness, the sol-gel GZO sample exhibits a rougher surface. This is likely due to the processing at a higher temperature than processing of the MOD films (T = 1250°C vs 1150°C). For this particular sol-gel sample, the GZO thickness varies between 13 and 23 nm, with an average thickness of 19 nm. Epitaxial orientation of the GZO and Ni-W substrate can be seen within the selected area electron diffraction pattern [Fig. 2.46(c)], showing that the GZO layer was oriented with its direction normal to the interface and producing a rotated cube-on-cube orientation of GZO[110](220)//Ni-W[100](020). A closer look at the interface of both samples [Fig. 2.47(a) for sol-gel and Fig. 2.47(b) for MOD sample] revealed no evidence of reactions between the GZO film and substrate and no presence of any secondary phases within the GZO layers. In fact, an EDS line scan across the boundary between the sol-gel–derived film and Ni-W substrate [Fig. 2.47(c)], using an electron probe of approximately 1.5 nm in diameter, displays

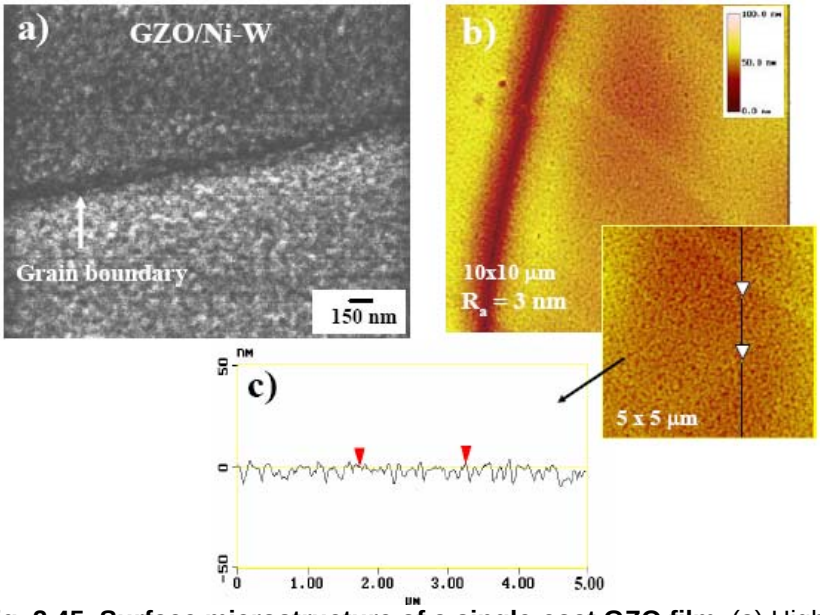

Fig. 2.45. Surface microstructure of a single-coat GZO film. (a) High-resolution SEM, (b) AFM, and (c) AFM surface profile on a 5-μm line scan (small image).

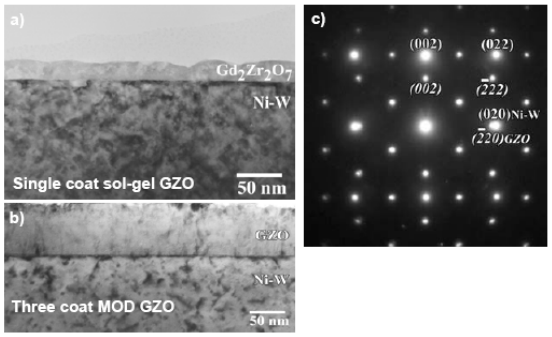

Fig. 2.46 MOD processed $Gd_2Zr_2O_7$ films on Ni-W substrates. Cross-section TEM images of (a) the single-coat sol-gel film and (b) the three coat MOD film. (c) Selected area diffraction pattern illustrating the Ni-W[100](010) // $Gd_2Zr_2O_7$[110](110) rotated cube-on-cube epitaxial relationship between the films and substrates.

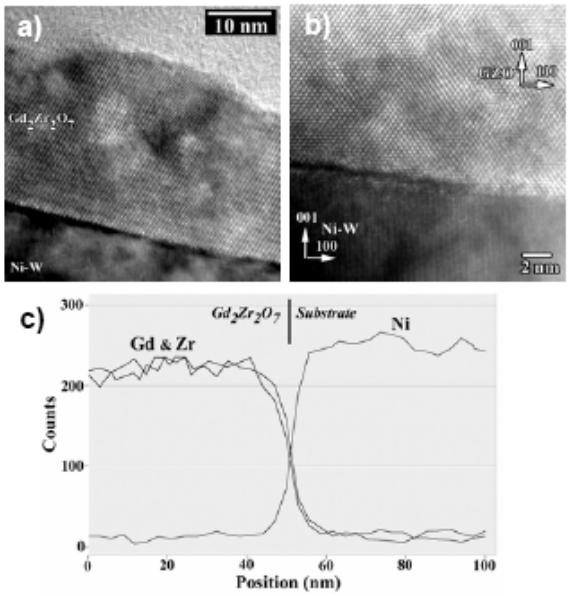

Fig. 2.47. The interface between $Gd_2Zr_2O_7$ and Ni-W. High-resolution TEM images of for (a) the single coat sol-gel film and (b) the three-coat MOD-deposited film revealing a pore-free and dense microstructure. (c) An EDS nanoprobe line scan across the GZO/Ni-W interface, verifying a clean and sharp interface with no interfacial reactions or interdiffusion.

sharp changes in the Gd, Zr, and Ni signals at the interface, providing further support for a clean interface and no significant intermixing.

Most interestingly, unlike the common observations reported in solution-processed films (i.e., sol-gel $La_2Zr_2O_7$ or MOD YBCO), these high-resolution TEM images show no porosity in GZO layers prepared by either technique. Although further work is required to understand the underlying mechanisms for this favorable growth behavior, it may be related in part to the chemical nature of the precursor species, such that the onset of crystallization is delayed to higher temperatures, therefore enhancing the film densification. This observation significant because pores along with other structural defects can act as accelerated pathways for inward diffusion of oxygen to the metal substrate as well as outward diffusion of substrate cations to the HTS layer, degrading the physical properties of the conductor. Obviously, eliminating such defects from any buffer architecture should improve the performance of a coated conductor structure. The SIMS data shown in Fig. 2.48 are consistent with these observations of good growth behavior. The interfaces between layers in the sputter depth profile are sharp and do not show the sputter profile broadening and degradation with increasing depth that is typically observed with porous or rough films. The linear, normalized signal representation used here is chosen as the appropriate representation to reveal any possible cation diffusion. The apparent diffusion of small amounts of copper from the YBCO layer into the GZO layer may be SIMS-beam-induced Cu segregation known to occur in the profiling of oxides. Small amounts of Ce seem to have diffused into the topmost portion of the GZO layer. In that portion of the film, Zr has a greater signal than in the remainder. Gd and C signals are correspondingly low in this portion of the GZO layer, rising to full value in the deeper portion of the layer. In light of a TEM-EDS scan (Fig. 2.47), this may be a SIMS ion enhancement effect due to differing chemical environment through the GZO layer, specifically caused by the variable carbon distribution.

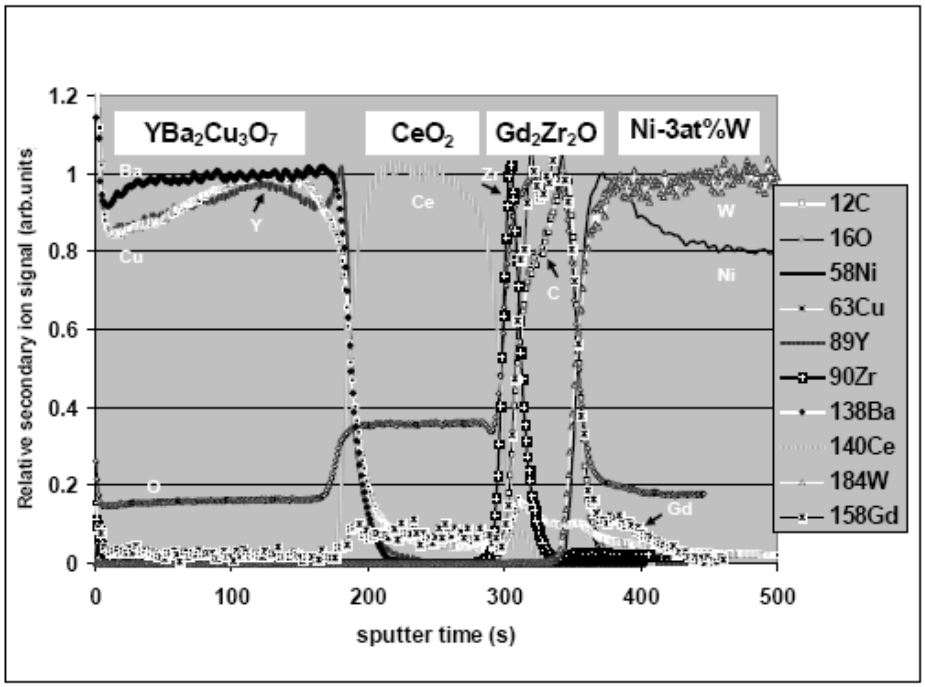

Fig. 2.48. SIMS depth profile of the three-coat MOD processed GZO/Ni-W sample, showing major element distributions throughout the sample. The intensity scale for each element is normalized to its maximum value. Sputter time is proportional to depth, but sputter rates of layers differ.

The performance of the MOD GZO buffer layers was evaluated by depositing both in situ PLD and ex situ metal-organic trifluoroacetate (TFA)-based MOD YBCO coatings. The latter was used in our initial test. First, CeO_2/YSZ buffer layers were deposited by magnetron sputtering on a single-layer GZO coated Ni/Ni-W substrate. A CeO_2 cap layer was used in order to provide an optimized structural and chemical template for TFA YBCO growth. The intermediate YSZ layer serves as a barrier for Ni diffusion.

Chemical compatibility is especially crucial for YBCO films grown ex situ. Figure 2.49 illustrates the current-voltage characteristics of a 0.8-µm-thick TFA-based YBCO film on such a substrate. The sample exhibited a self-field critical current of 100 A/cm-width, which corresponds to a critical current density of 1.25×10^6 A/cm^2. Although this result does not reflect optimum performance, it demonstrates that MOD-synthesized GZO films can act as good templates for further growth of epitaxial oxide layers.

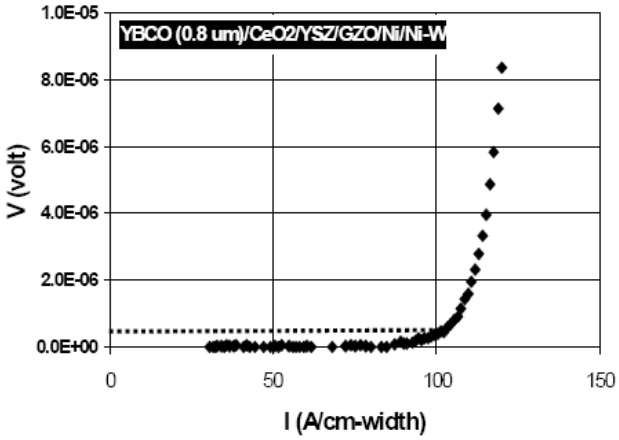

Fig. 2.49. Current-voltage curve of a YBCO/CeO_2/YSZ/GZO/Ni/Ni-W sample. The YBCO was processed via the ex situ TFA approach. The dashed line indicates the voltage criterion for definition of critical current.

Next, in an attempt to simplify the entire structure, we removed the YSZ layer from the buffer architecture for in situ deposition of YBCO. The magnetic field dependence of transport critical current densities at 77 K for two PLD-deposited YBCO films are compared in Fig. 2.50. These films were deposited on three-coat GZO buffers (~ 60 nm thick), capped with both sputtered and solution-derived (MOD) CeO_2 layers (~ 20 nm thick). Measurements are made with the field applied parallel to *c*-axis. The zero-field critical current density for a 0.2-µm-thick YBCO film on an all-solution-processed CeO_2(soln.)/GZO(soln.)/Ni-W is 1×10^6 A/cm^2, and the superconducting transition temperature is around 92 K (see Fig. 2.50, inset). A critical current density (self-field) of 1.1×10^6 A/cm^2 is obtained for a thicker YBCO film (0.5 µm) on CeO_2(sput.)/GZO(soln.)/Ni-W, which reflects a performance comparable to that on standard vacuum-based three-layer CeO_2/YSZ/Y_2O_3 buffer architecture. Since the YBCO is thicker in the latter case, and an exponential decrease in critical current density with thickness for in situ YBCO coatings is well known, the J_c-*H* data suggest that further optimization is required for MOD CeO_2 cap layers. In fact, the surface of some samples showed small amounts of polycrystalline CeO_2. Such random crystallites are possibly a result of surface nucleation associated with competition between the

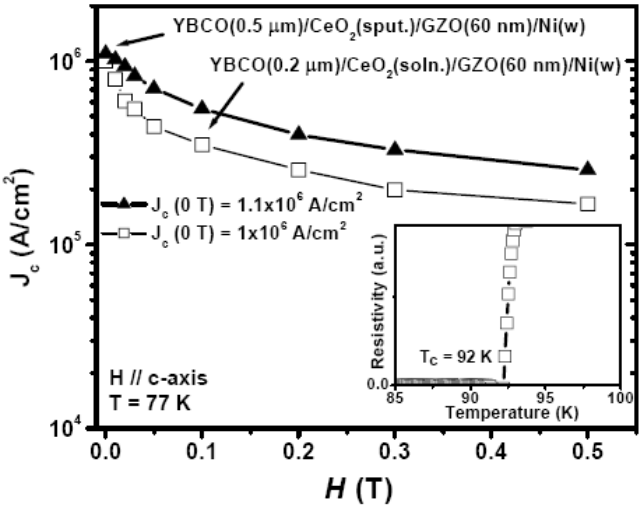

Fig. 2.50. Magnetic field dependence of critical current density, measured at 77 K, for two YBCO films deposited by PLD on (i) the all-solution MOD CeO_2 and (ii) sputtered CeO_2-capped $Gd_2Zr_2O_7$(MOD)/Ni-W. Inset: the resistive superconducting transition region for the former sample.

crystallization driving forces, where the free surface nucleation becomes as plausible as interface nucleation at the growth conditions used for MOD CeO_2 films.

Cross-sectional TEM investigations (not shown) depicted no indication of homogeneous random nucleation. An additional issue is that the out-of-plane texture of MOD GZO films needs further improvement, evidenced by the slight increase in FWHM values of the ω-scans on progressing from substrate to YBCO layer. For instance, while the in-plane alignment of individual layers in YBCO/CeO_2(sput.)/GZO(soln.)/Ni-W structure replicate the texture of the Ni-W substrate ($\Delta\phi = 8°$), the ω-rocking curve FWHMs are progressively broader, with value of 6.2°, 7.4°, 8.5° and 8.6° for the YBCO, CeO_2, GZO, and Ni-W layers, respectively. This broadening in $\Delta\omega$ may have been, in effect, a contributing factor for the nonoptimal transport critical current density. Interestingly, a similar increase is also found in the out-of-plane texture of solution-based LZO and RE_2O_3 buffer systems, but no explanation was given for the cause. Nevertheless, the present preliminary results indicate a strong viability of solution-based GZO buffer layers for practical HTS-wire fabrication.

We have demonstrated that GZO films can be grown epitaxially on Ni-W substrates by sol-gel and MOD-based solution deposition processes. The effects of processing parameters on the growth of these buffers were studied. Remarkably, GZO films synthesized by both techniques showed dense and pore-free microstructure, which were reflected within the examined cross-section microstructures. Studies also indicated that GZO films via MOD route can be processed at temperatures 75 to 125°C lower than the sol-gel counterparts, easing the materials requirements on the technologically viable metal substrates. Using both the PLD and TFA methods, high-quality YBCO films have been obtained on MOD-derived GZO films. On a CeO_2/YSZ/GZO/Ni-W architecture, 0.8-μm-thick TFA YBCO film exhibited a critical current (77 K) value of 100 A/cm-width. On a simplified, all-solution buffer architecture of CeO_2(soln.)/GZO(soln.)/Ni-W, we have achieved self-field critical current density (77 K) of 1.1×10^6 A/cm^2 for PLD-deposited 0.5-μm-thick YBCO films. These observations reflect the strong candidacy of MOD GZO buffers for low-cost, scalable second generation HTS-wire manufacturing.

2.12 Iridium: An Oxygen Diffusion Barrier and a Conductive Seed Layer for RABiTS™-Based Coated Conductors

T. Aytug and J .R. Thompson (ORNL and UTK); M. Paranthaman, H. Y. Zhai, K. J. Leonard, A. A. Gapud, P. M. Martin, A. Goyal, and D. K. Christen (ORNL)

A key issue for the deposition of epitaxial oxides on metal surfaces is the corrosion of metal substrate surfaces in oxidizing environments at elevated temperatures (> 700°C). Generally, at these extreme growth conditions, an unfavorable orientational relationship results between the native oxide and metal substrate, degrading the subsequent nucleation of crystalline oxide buffer layers. Although epitaxial growth of various oxide layers has been successfully achieved over the years by effectively controlling the surface conditions of metallic tapes, insulating interfacial metal-oxide formation during the subsequent deposition of YBCO films has not been completely prevented. Regarding a fully conductive architecture, this problem is a major concern because it causes a partial or total loss of electrical connection between the HTS layer and the underlying substrate material. Hence, it becomes indispensable to protect the metal substrate from oxidation during the high-temperature steps with a barrier layer that blocks oxygen diffusion and remains electrically conductive. While an apparent solution would be the use of one or more noble metals (Pd, Au, Pt, or Ag), so far studies on textured metal tapes showed either poor epitaxial nucleation of subsequent oxides on these materials or undesirable interdiffusion effects such as alloying, compound growth, surface roughening, and defect formation via bulk or grain-boundary diffusion. An alternative approach may be the introduction of an unreactive metal, preferably having a conductive native oxide, as a seed layer into a conductive architecture.

In this study, a conductive $La_{0.7}Sr_{0.3}MnO_3$(LSMO)/Ir film structure is examined regarding its chemical and structural stability and its ability to work as a barrier for inward oxygen and outward metal cation diffusion. Both LSMO and Ir have relatively low oxygen diffusivity, with diffusion coefficients at

800°C ($D = 5 \times 10^{-15}$ and 5×10^{-12} cm^2/s, respectively, nearly two to seven orders of magnitude lower than those of the standard CeO_2, Y_2O_3 and YSZ buffer compounds. Ir is also recognized for its excellent corrosion resistance among platinum metal groups, with high conductivity ($\rho \sim 5$ μΩ-cm). Moreover, its native oxide, IrO_2, under conditions of stability, is characterized by metallic conductivity (bulk resistivity, $\rho \sim$ 30-100 μΩ-cm) and chemical inertness. In this initial work, we have used Ni-3at.%W (Ni-W) substrates for a proof-of-principle assessment of the feasibility of LSMO/Ir as a conductive buffer interface. Epitaxial Ir and LSMO films have been deposited on Ni-W substrates using dc- and rf-magnetron sputtering systems, respectively. Substrate temperatures of 600 to 700°C for LSMO and 500 to 650°C for Ir layers were used and depositions were conducted in a forming gas (Ar+4%H_2) environment. To ensure chemical stability of LSMO layers, a source of oxygen (5×10^{-5} Torr of H_2O) was mixed with the 3 mT of forming gas in the chamber.

The YBCO films were grown by PLD; a KrF excimer laser system, operated at an energy density of ≈2 J/cm^2 and a repetition rate of 10 Hz was used. During film growth, the substrates were maintained at 780°C in 120 mTorr of O_2. After deposition, the samples were first cooled to 500°C at a rate of 5°C/min; then the O_2 pressure was increased to 550 Torr, and the samples were cooled to room temperature at the same rate. YBCO film thicknesses ranged from 0.2 to 2μm. Crystal structures were characterized with a Philips model XRG3100 XRD, and microstructural analyses were conducted on a model JSM-840 SEM. AFM was used to study the surface roughness of the samples. Electrical property characterizations were made by using a standard four-probe technique with values of critical current density assigned at a 1 μV/cm criterion.

First, we have investigated the chemical compatibility and electrical properties of Ir layers under the growth conditions of YBCO films by subjecting an epitaxial as-grown Ir/Ni-W sample to post-annealing at T=780 C under 100 mTorr of oxygen for 30 min. Typical XRD spectra are shown in Fig. 2.51, indicating virtually no change in the spectra before or after the annealing. Only *c*-axis-oriented Ir peaks are present, and there is no evidence of IrO_2 or unwanted NiO and other reaction phases. The free energy of formation for NiO is much lower than that of IrO_2; hence, while the IrO_2 is not thermodynamically stable at YBCO processing conditions, there is a slight possibility that a very small amount of NiO might have been formed at the interface, which the XRD could not detect. As a sensitive indicator of the interface, net resistivity (ρ_{net}) vs temperature measurements were made on several Ir coated samples. The results are shown in Fig. 2.52. Clearly, ρ_{net}-T reveals complete electrical coupling among the Ir/Ni-W

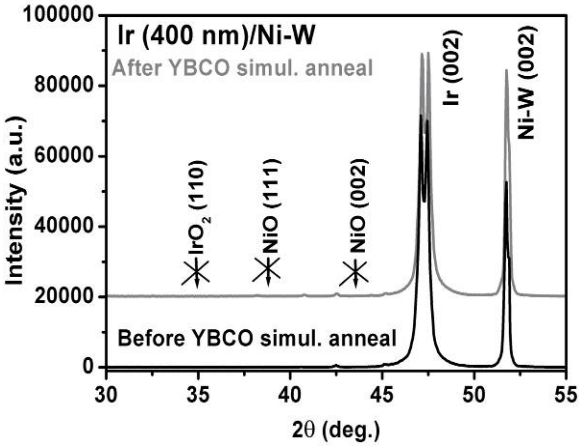

Fig. 2.51. XRD θ-2θ patterns of Ir films grown on biaxially textured Ni-W substrates before and after anneals under simulated YBCO conditions.

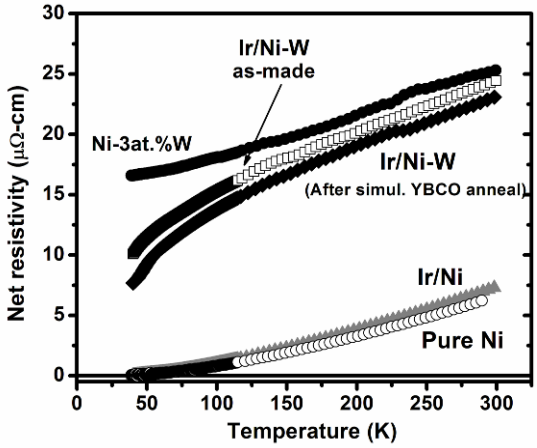

Fig. 2.52. Net resistivity of Ir coated substrates as a function of temperature before and after simulated YBCO annealing. Also shown for comparison are the curves for Ni-W and pure Ni.

layers, even after a simulated YBCO anneal. The slightly lower overall ρ_{net} behavior for Ir-coated samples results from the parallel electrical coupling of a high-conductivity Ir metal with a high-net resistivity Ni-W ($\rho \sim 17$ μΩ-cm). In the lower temperature regime (< 100 K), net resistivity declined because of the much lower residual resistivity of Ir compared to that of Ni-W. In fact, as expected, we did not observe this low-temperature effect when Ir layers were grown on high-conductivity pure Ni tapes.

The above findings are also supported by the fact that there was no evident change in the surface morphology of the Ir films, even after the YBCO anneal. The SEM images (Fig. 2.53), revealed smooth and dense surface microstructure for (a) as-deposited and (b) annealed Ir layers grown on the Ni-W substrates, with no implication of surface roughening or deterioration. However, contrary to these observations, interdiffusion between Ir and Ni was observed when the samples were annealed in forming gas or in vacuum environment at similar conditions. At this time the role of oxygen in retarding the interdiffusion of solute elements is unclear and the details of which are currently under investigation.

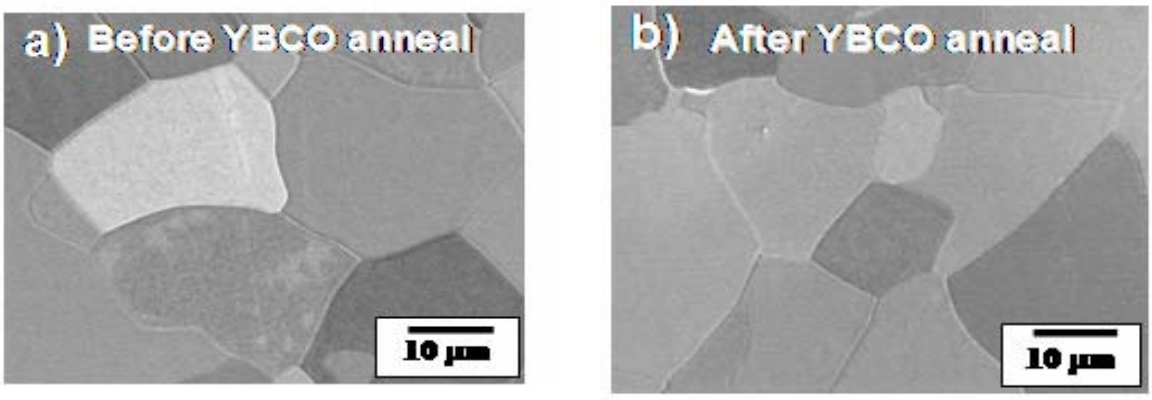

Fig. 2.53. Plan view SEM images for the Ir layers (a) before and (b) after YBCO post-anneals.

To further develop the prospect of implementing Ir as a conductive interface in a RABiTS™ architecture, 50- to 300-nm LSMO layers were deposited on Ir seed layers to provide a structurally and chemically compatible template with YBCO coatings. Figure 2.54 shows typical XRD spectrums for (a) 0.2- and (b) 1-μm-thick YBCO films deposited on the LSMO/Ir/Ni-W structure. All diffraction peaks are (00*l*)-type reflections, indicating *c*-axis growth for each layer. Apparently, even after 1 μm of YBCO growth, there are no NiO or $NiWO_4$ peaks, and no other chemical reaction has occurred among the layers. This is a significant observation in view of our previous conductive buffer-layer studies on Ni-based templates, which always showed some NiO formation at the substrate/buffer-layer interface, even after growth of only 0.2-μm-thick YBCO. For the 0.2-μm YBCO coated sample, the out-of-plane ($\Delta\omega$) FWHM widths for YBCO(006), LSMO(002), Ir(002),and Ni-W(002) were 4.7°, 4.6°, 5.2°, and 5.3°, respectively. The in-plane FWHM in-plane ($\Delta\phi$) scan values on the (111) peak reflections for LSMO, Ir, and Ni-W were 7.2°, 7.7°, and 7.7°, respectively; the (103) reflection was 8° for YBCO. The peak-width sharpening is evident in progressing from Ni-W to YBCO layers, which can be attributed to a smoother substrate surface enabled by the Ir layers as observed by AFM measurements.

The superconducting transition temperatures for both YBCO films are near 88 to 89 K, and the critical current density values at 77 K in self-field are 2.2×10^6 A/cm^2 for the 0.2-μm-thick sample and 1×10^6 A/cm^2 for the 1-μm-thick YBCO sample. For the latter, this value of critical current density corresponds to a critical current of 100 A/cm-width. Figure 2.55 shows the magnetic field performance of critical current density for the 0.2-μm-thick YBCO film at 77 K, with the field applied parallel to *c*-axis. The sample has an irreversibility field of 6.8 Tesla, similar to best YBCO on single-crystal substrates. Such high values for critical current density result from the presence of only low-angle grain-to-grain alignments, along with an overall high-quality YBCO coating, free of cation contamination. Apparently,

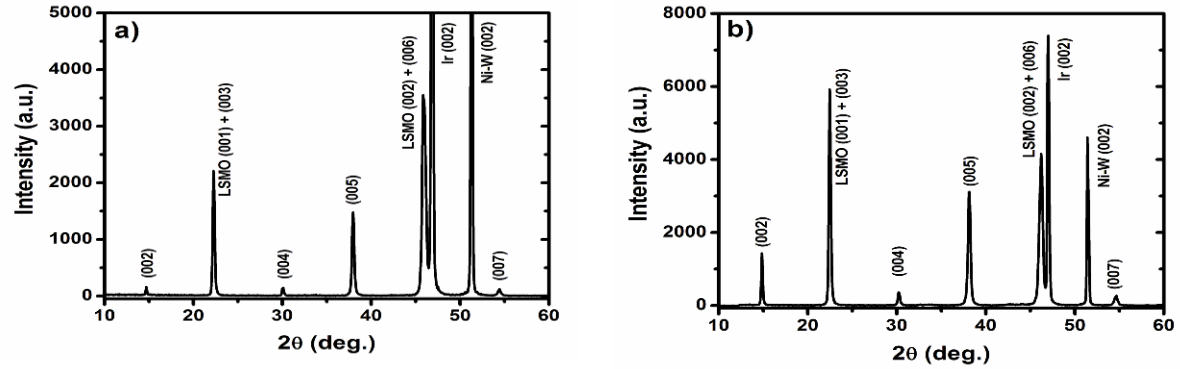

Fig. 2.54. The XRD θ-2θ patterns of YBCO films on LSMO/Ir/Ni-W architecture. The YBCO thicknesses are (a) 0.2 μm, (b) 1 μm.

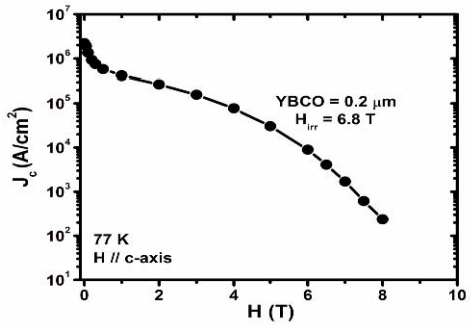

Fig. 2.55. Magnetic field dependence of transport J_c at 77 K for a 0.2-μm-thick YBCO film on LSMO/Ir/Ni-W. The irreversibility field, H_{irr}, is defined by a voltage-current power law exponent of 2.

the LSMO/Ir structure performs effectively to block the oxygen and cation diffusion into and out of the substrate.

The current vs voltage characteristics of the composite structures were also measured to document the electrical stability provided by the LSMO/Ir conductive buffer interface. A complete electrical coupling of the YBCO films with the underlying Ni-W substrate was achieved, and electrical stability to an overcurrent of ~3 I_c was provided at 1 Tesla. However, for a practical high-current-capacity conductor, Ni-W substrates will not be adequate because of their high resistivity. Nevertheless, the present results establish a proof-of-principle for a conductive buffer stack on a metal substrate and provide motivation for the development of a fully conductive Cu-based RABiTS™, for which the metal substrate conductivity is sufficiently high to provide self-stabilization of the conductor while substantially increasing the engineering critical current density values.

In summary, a fully conductive buffer layer architecture employing the layer sequence of LSMO/Ir was developed as a self-stability measure for YBCO coated conductors. This buffer architecture is an excellent diffusion barrier for Ni and oxygen. Subsequent growth of thick YBCO coatings showed high critical current density and superior electrical coupling with the substrate. Our analysis has indicated that the present architecture offers significant advantages for the advancement of Ni-based RABiTS™ technology and for the envisioned development of Cu-based coated conductors.

2.13 All MOD Buffer/YBCO Approach to Coated Conductors

M. P. Paranthaman, S. Sathyamurthy, L. Heatherly, P. M. Martin, A. Goyal (ORNL); T. Kodenkandath, X. Li, C. L. H. Thieme, and M. W. Rupich (AMSC)

2.13.1 Introduction

The main objective of this research is to develop an all-solution buffer/YBCO process to fabricate potentially lower-cost, high-performance second-generation coated conductors, with a goal to demonstrate a critical current of 300 A/cm width for all-solution buffers on RABiTS™ [1]. Efforts are being made to replace the existing three-layer architecture of all-PVD Y_2O_3/YSZ/CeO_2 with simplified layers comprising multifunctional buffers deposited by industrially scalable methods such as chemical solution deposition [2,3]. Chemical solution deposition offers significant cost advantages compared to PVD processes [4–7]. Solution coating is amenable to complex oxides. Slot-die coating and ink-jet

printing techniques can be used to scale up solution processes. Both LZO and CeO_2 buffers have been identified as potential candidates for this study. The challenge is to match the performance of AMSC's current PVD buffer stack with a performance of 250 A/cm in short lengths with buffers deposited using non-vacuum-based solution techniques [8]. Last year, we demonstrated a transport critical current density of 1.75 MA/cm^2 on 0.8-μm-thick MOD-YBCO films grown on all MOD CeO_2 (one coat)/LZO(three coats)/Ni-3W substrates. These translate to a critical currrent of 140 A/cm-width at 77 K and self-field [9,10]. The lattice mismatch between LZO and Ni-W substrate is about 7.9%. The performance of the LZO layer has been further enhanced by reducing the lattice mismatch and by improving the texture by inserting a thin Y_2O_3 seed layer. Here, we report our recent results obtained on the improved MOD-CeO_2/$La_2Zr_2O_7$ templates.

2.13.2 Experimental Procedure

Biaxially textured Ni-W (5 at. %) substrates were obtained by annealing the as-rolled substrates in the presence of Ar/H_2 (4%) gas at 1100 to 1150°C for 1 h. The substrates used were 1 cm wide and 75 μm thick. All the textured substrates were sulfurized by annealing at 750°C and 1×10^{-5} Torr of H_2S gas atmosphere to get the desired sulfur c(2 × 2) superstructures at the Ni-5W surface. Reel-to-reel electron beam evaporation was used to deposit 10-nm-thick Y_2O_3 seed layers [11]. The LZO precursor solution was prepared from lanthanum isopropoxide (Alfa, La 40% assay), zirconium n-propoxide in n-propanol (Alfa, 70%), and 2-methoxyethanol (Alfa, spectrophotometric grade). The details of the solution preparation were reported earlier [9,12]. About 0.75 M total cation concentration was used to grow 100-nm-thick LZO films in a single coat. Spin coating was used to deposit LZO at a spin rate of 2000 rpm for 30 s. The spin-coated films were then crystallized at 1100°C for 15 min in a flowing mixture Ar/H_2 4% gas. To obtain thicker LZO films, the coating and crystallization steps were repeated several times. About 60-nm-thick MOD-CeO_2 and 0.8-μm-thick MOD-YBCO were deposited on MOD-LZO using AMSC's proprietary process [8].

The films were characterized for phase purity and texture by XRD, and the microstructure of both buffers and YBCO were observed by AFM. The resistivity and transport critical current density were measured by using a standard four-point probe technique.

2.13.3 Results and Discussion

Typical θ-2θ XRD patterns for both one coat (100-nm-thick) and two coats (200-nm-thick) of LZO films on Y_2O_3-seeded Ni-5W substrates are shown in Fig. 2.56. These scans indicate the presence of strong *c*-axis (004) aligned films. The ω and ϕ scans for a 200-nm-thick LZO film grown on Y_2O_3-seeded Ni-5W substrates are shown in Fig. 2.57. The FWHM values for LZO (004) and Ni-5W (002) were 4.7° and 5.9°, respectively. Similarly, the FWHM values for LZO (222) and Ni-5W (111) were 6.7° and 7.7°, respectively. Both in-plane and out-of-plane textures of LZO layers were improved over 1°. The (222) X-ray pole figures for 200-nm-thick LZO film grown on Y_2O_3–seeded Ni-5W substrate are shown in Fig. 2.58. The presence of a fourfold symmetry indicates the presence of a single cube-textured LZO film. Highly textured MOD-CeO_2 and MOD-YBCO films were grown on 200-nm-thick LZO/Y_2O_3–seeded Ni-5W substrates.

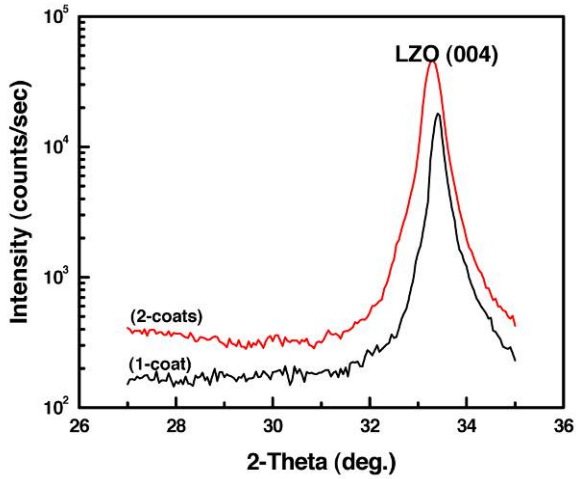

Fig. 2.56. A typical θ-2θ scan for a 100-nm-thick (one coat) and 200-nm-thick (two coats) $La_2Zr_2O_7$ film grown on 10-nm-thick Y_2O_3 buffered Ni-5W substrates by MOD. LZO has a preferred *c*-axis orientation.

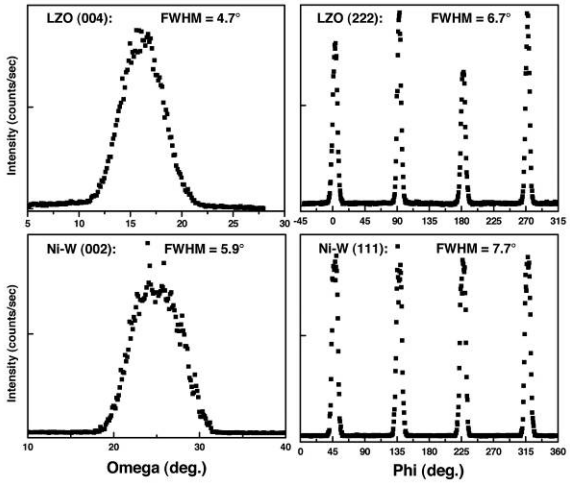

Fig. 2.57. The ω and ϕ scans for a 200-nm-thick $La_2Zr_2O_7$ film grown on a 10-nm-thick Y_2O_3 buffered Ni-5W substrate using metal-organic deposition. The FWHM values for each scan are shown inside the scans.

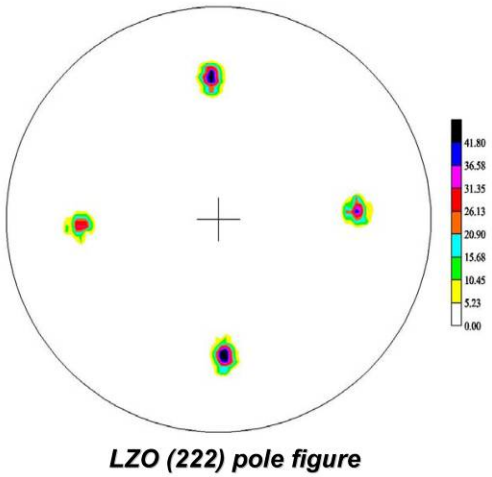

Fig. 2.58. (222) pole figure for a 200-nm-thick $La_2Zr_2O_7$ film grown on a 10-nm-thick Y_2O_3 buffered Ni-5W substrate using metal-organic deposition.

As shown in Fig. 2.59, the typical θ-2θ scan for a 0.8-μm-thick YBCO film grown on MOD-CeO_2/MOD-LZO/Y_2O_3/Ni-5W substrate indicated the presence of a strong *(00l)* reflection of YBCO films. In addition, small impurities of $NiWO_4$, NiO, unreacted BaF_2, $BaCeO_3$, and polycrystalline YBCO were also present. The transport properties of the MOD-YBCO film on MOD-buffer template are shown in Fig. 2.60. The self-field critical current of 200 A/cm (J_c = 2.5 MA/cm^2) was achieved. From the angular measurement data (right side of Fig. 2.60), a strong *ab*-plane peak with a very small *c*-axis peak was observed at 77 K and 1 Tesla.

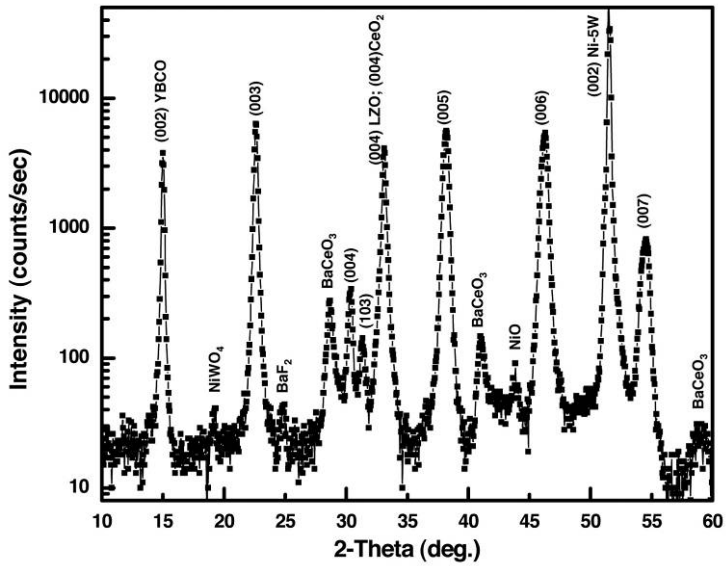

Fig. 2.59. Typical θ-2θ scan for a 0.8-μm-thick YBCO film grown on MOD-CeO_2/MOD-$La_2Zr_2O_7$/Y_2O_3/Ni-5W substrate using metal-organic deposition. YBCO film has a preferred c-axis orientation. In addition, small amounts of $NiWO_4$, BaF_2, $BaCeO_3$, and NiO impurities and polycrystalline YBCO peaks were also identified.

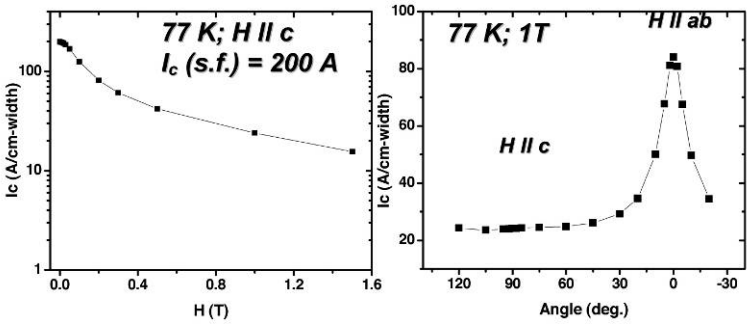

Fig. 2.60. The field dependence of critical current for a 0.8-μm-thick YBCO film grown on MOD-CeO_2/MOD-$La_2Zr_2O_7$/Y_2O_3/Ni-5W substrate using metal-organic deposition (left side). The self-field J_c of 2.5 MA/cm^2 (I_c = 200 A/cm) at 77 K and self-field was obtained. The angular dependence I_c at 77 K and 1T for the same film is shown on the right side. A minimum I_c of 20 A/cm was obtained at all angles.

The enhancement of critical current from 140 A/cm (last year) to 200 A/cm (this work) is mainly due to the combination of both thin e-beam Y_2O_3 and MOD-LZO layers. However, to find out whether the performance of the templates is limited by MOD-LZO or MOD-CeO_2 compared to all PVD templates with a performance of 250 A/cm, we replaced the MOD-CeO_2 with a sputtered CeO_2 cap. MOD-YBCO films grown on sputtered-CeO_2/MOD- LZO/Y_2O_3/Ni-5W carried a critical current of 255 A/cm (J_c = 3.2 MA/cm^2) [13]. This demonstrates that the barrier properties of MOD-LZO/Y_2O_3 layers are comparable to that of PVD-YSZ layers. Detailed X-ray characterization of MOD-CeO_2 and PVD-CeO_2 cap layers indicated that there was no big difference in the texture between the two templates. However, reaction of MOD-CeO_2 with YBCO films resulted in increased amounts of $BaCeO_3$ formation as compared to that on PVD-CeO_2. Further optimization of the MOD-CeO_2 layers are in progress.

2.13.4 Summary

We have developed process conditions to deposit 100-nm-thick MOD-$La_2Zr_2O_7$ layers in a single coat using spin coating on 10-nm-thick Y_2O_3-seeded Ni-5W substrates. To improve the texture, to reduce the lattice mismatch with the Ni-5W substrate, and to enhance the performance of MOD- $La_2Zr_2O_7$, we have inserted a 10-nm-thick Y_2O_3 seed layer. MOD-YBCO film with an I_c of 200 A/cm was achieved on MOD-CeO_2/MOD-$La_2Zr_2O_7$/Y_2O_3/Ni-5W substrates. These results demonstrate that the performance of MOD buffers is approaching that of PVD buffers.

2.13.5 References

1. A. Goyal, D. P. Norton, J. D. Budai, M. Paranthaman, E. D. Specht, D. M. Kroeger, D. K. Christen, Q He, B. Saffian, F. A. List, D. F. Lee, P. M. Martin, C. E. Klabunde, E. Hatfield, and V. K. Sikka, *Appl. Phys. Lett.* **69**, 1795 (1996).
2. M. Paranthaman and T. Izumi, Editors, *MRS Bulletin* **29** (8), 533–36 (2004).
3. A. Goyal, M. Paranthaman, and U. Schoop, *MRS Bulletin* **29**, 552–61 (2004).
4. C. J. Brinker, A. J. Hurd, P. R. Schunk, G. C. Frye, and C. S. Ashley, *J. Non-Cryst. Solids* **147**, 424 (1992).
5. F. F. Lange, *Science* **273**, 903 (1996).
6. R.W. Schwartz, "Chemical solution deposition of perovskite thin films," Chem. Mater. 9 (1997) 2325.
7. M. Paranthaman, T. G. Chirayil, F. A. List, X. Cui, A. Goyal, D. F. Lee, E. D. Specht, P. M. Martin, R. K. Williams, D. M. Kroeger, J. S. Morrell, D. B. Beach, R. Feenstra, and D. K. Christen, *J. Amer. Ceram. Soc.* **84**, 273 (2001).
8. M. W. Rupich, D. T. Verebelyi, W. Zhang, T. Kodenkandath, and X. P. Li, *MRS Bulletin* **29**, 572-78 (2004).

9. S. Sathyamurthy, M. Paranthaman, H. Y. Zhai, S. Kang, T. Aytug, C. Cantoni, K. J. Leonard, E. A. Payzant, H. M. Christen, A. Goyal, X. Li, U. Schoop, T. Kodenkandath, and M. W. Rupich, *J. Mater. Res.* **19**, 2117 (2004).
10. M. Paranthaman, S. Sathyamurthy, M. S. Bhuiyan, A. Goyal, T. Kodenkandath, X. Li, W. Zhang, C. L. H. Thieme, U. Schoop, D. T. Verebelyi, and M. W. Rupich, *IEEE Trans. on Appl. Supercond.* **15**, 2632 (2005).
11. M. Paranthaman, D. F. Lee, A. Goyal, E. D. Specht, P. M. Martin, X. Cui, J. E. Mathis, R. Feenstra, D. K Christen, and D. M. Kroeger, *Supercond. Sci. Technol.* **12**, 319 (1999).
12. S. Sathyamurthy, M. Paranthaman, H. Y. Zhai, H. M. Christen, P. M. Martin, and A. Goyal, *J. Mater. Res.* **17**, 2181 (2002).
13. S. Sathyamurthy, M. Paranthaman, L. Heatherly, P. M. Martin, E. D. Specht, A. Goyal, T. Kodenkandath, X. Li, and M. W. Rupich, "Solution processed Lanthanum Zirconium Oxide as a barrier layer for high Ic coated conductors, *J. Mater. Res.* (submitted).

2.14 Solution-Processed Lanthanum Zirconium Oxide as a Barrier Layer for High-I_c Coated Conductors

S. Sathyamurthy, M. Paranthaman, L. Heatherly, P. M. Martin, E.D. Specht, A. Goyal (ORNL), T. Kodenkandath, X. Li, and M. Rupich (AMSC)

2.14.1 Introduction

To date, in the processing of high-current coated conductors using RABiTS™, the best results have been obtained reproducibly using three layer buffer architectures like CeO_2/YSZ/Y_2O_3/NiW, where Y_2O_3 serves as a seed layer which nucleates a well textured oxide layer, YSZ is a barrier layer which prevents the diffusion of Ni into the superconductor, and CeO_2 is a cap layer which promotes good epitaxy of the superconductor. The fabrication of this multi-layered buffer architecture, however, may present significant roadblocks to the scale-up of the process to long-lengths. Typically, deposition of the buffer layer stack would involve a combination of e-beam and rf-sputter deposition techniques coupled with the exposure of the samples to thermal cycling and ambient environment. These requirements could lead to the degradation of the individual buffer layers and add to the complexity, and cost of the overall process. However, if buffer layers are deposited using a nonvacuum, scaleable technique such as solution deposition, it would significantly decrease the processing time and make the process simpler and could make the coated conductor cheaper.

Several groups are currently working on developing an all-solution processing route to coated conductor fabrication. We have previously reported our results on the sol-gel deposition of lanthanum zirconium oxide (LZO) as a buffer layer to obtain high critical current densities up to 2 MA/cm^2 for 0.2-μm thick pulsed laser ablated YBCO. Using a sputtered CeO_2 cap layer on the sol-gel LZO buffer layers, and using an MOD process for YBCO deposition, we have demonstrated a critical current density of 1.7 MA/cm^2 with a corresponding critical current of 135 A/cm using a 0.8-μm-thick YBCO. This paper presents secondary ion mass spectroscopy (SIMS) depth profiling that demonstrates the performance of LZO as a barrier layer. The compatibility of this sol-gel LZO layer with a sputtered or solution-processed CeO_2 cap layer for the processing of MOD-YBCO with critical current densities comparable to that obtained using an all-PVD buffer stack will be discussed.

The precursor solution for LZO films was prepared from alkoxides of lanthanum and zirconium. Lanthanum isopropoxide (Alfa, La 40% assay), zirconium n-propoxide in n-propanol (Alfa, 70%) and 2-methoxyethanol (Alfa, spectrophotometric grade) were used as received. Stoichiometric quantities of lanthanum isopropoxide and zirconium n-propoxide were dissolved in 60 mL of 2-methoxyethanol in a 250-ml round-bottomed flask. The solution was refluxed in excess 2-methoxyethanol in a Schlenk-type apparatus. The isopropanol formed during the exchange reaction was distilled out along with the excess 2-methoxyethanol. Solutions with a total cation concentration of 0.5 M, 0.75 M, and 1 M were used to process LZO films of a variety of thicknesses, ranging from 40 to 50, 70 to 75, and 90 to 100 nm, respectively. LZO films were deposited on textured Ni-W alloy substrates, typically 3 cm × 1 cm, by

spin-coating the precursor solution at a spin rate of 2000 rpm for 30 s. The spin-coated samples were then crystallized at 1100ºC for 15 min. To obtain thicker coatings the coating and annealing steps were repeated several times.

The phase purity and texture of the LZO films were characterized by XRD, using a Philips XRG3100 diffractometer and a Picker four-circle diffractometer, respectively, using Cu-K_α radiation. The performance of the LZO films as a barrier layer was evaluated using a simulated YBCO annealing treatment. The LZO films of various thicknesses on Ni-W substrates were subjected to standard ex situ or MOD-YBCO processing temperature and oxygen partial pressure and held at that temperature for a fixed amount of time before cooling down to room temperature. The performance of the LZO films was compared with that of the standard all-PVD three-buffer stack of CeO_2/YSZ/Y_2O_3 on Ni-W substrates. The amounts of NiO and $NiWO_4$ formed as a result of the annealing treatment were monitored using XRD. The barrier properties of the LZO films were also evaluated in SIMS studies. The performance of the LZO films as a buffer layer for coated-conductor fabrication was evaluated by depositing a CeO_2 cap layer by sputtering or solution deposition, the details of which are reported elsewhere [1,2]. YBCO films were deposited and processed on the CeO_2 capped LZO films, by the MOD process and the superconducting properties were measured using a four-point probe.

LZO films of various thicknesses were deposited by sol-gel processing directly on Ni-W substrates. In a single coating step crack-free films with thicknesses of up to 100 nm could be deposited. To obtain thicker films, the coating and annealing steps were repeated. Figure 2.61 shows XRD patterns from one such multiple coated sample with LZO film thicknesses from 40 to 160 nm deposited in 40-nm steps. These sol-gel films were found to have a fully crystalline surface as determined by RHEED measurements and a reasonably smooth surface; average roughness was determined by AFM to be between 1.8 and 2 nm. This process could be easily extended to wider substrates. Figure 2.62 shows XRD texture map of a 4-cm-wide substrate dip-coated with sol-gel LZO film, which demonstrates the versatility of solution deposition to obtain uniform coatings.

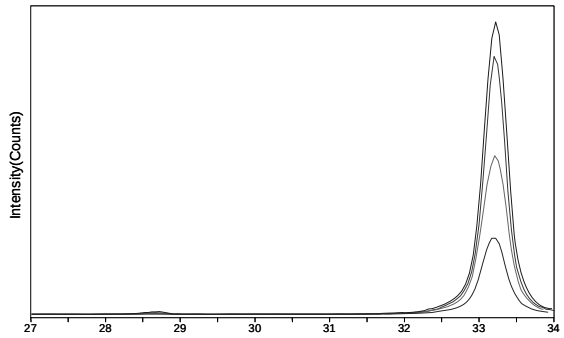

Fig. 2.61. XRD patterns from multiple-coat LZO/Ni-W samples in thickness increments of 40 to 50 nm per coat, showing proportional increase in LZO (400) peak intensity with thickness.

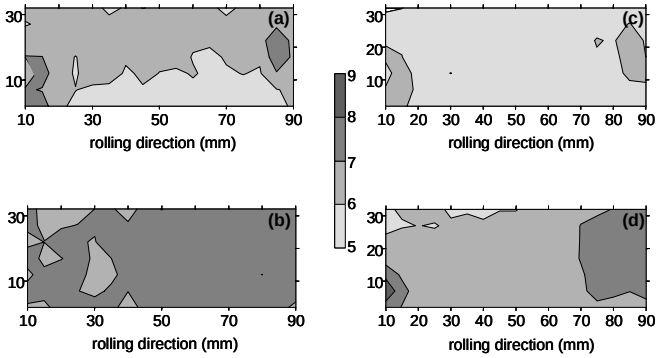

Fig. 2.62. Texture map of 4-cm-wide LZO/NiW sample coated by dip-coating. (a) LZO (004) out-of-plane texture, (b) LZO (222) in-plane texture, (c) Ni (002) out-of-plane texture, (d) Ni (111) in-plane texture.

To evaluate the performance of these films as barrier layers, simulated ex situ YBCO annealing experiments were conducted using standard processing conditions. LZO films having estimated thicknesses of 120 and 160 nm were processed by multiple coating using a 0.5 M precursor solution. These samples along with samples with the standard all-PVD three-layer buffer stack of CeO_2/YSZ/Y_2O_3 with a total buffer layer thickness of 300 nm on Ni-W substrates were annealed under a humid Ar-O_2 atmosphere with 200 ppm of oxygen for different lengths of time.

The amount of NiO formed in the samples, analyzed using XRD, is summarized in Fig.2.63. It is clear in Fig. 2.63 that the barrier properties of 80- to 120-nm-thick LZO layers is comparable to that of the standard all-PVD three-layer buffer stack. This result implies that LZO can be used as the barrier layer

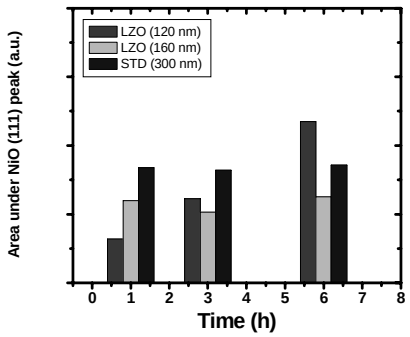

Fig. 2.63. Area under the NiO (111) peak plotted as a function of annealing time in simulated YBCO ex situ annealing experiments. (Legend: LZO = LZO/Ni-W, STD = standard CeO_2/YSZ/Y_2O_3/NiW buffer stack)

for coated conductor fabrication. To further evaluate the barrier layer performance of LZO layers, a 160-nm-thick LZO film was coated with a 20-nm solution-processed CeO_2 layer. The sample was then annealed at typical YBCO process temperature in O^{18} for 15 min, and was then analyzed by SIMS. The SIMS depth profile of the sample illustrated in Fig. 2.64 shows that the LZO film acts as a good barrier to diffusion of tungsten. However, some amount of nickel diffusion through the LZO is observed, but the diffusion of nickel is stopped within the first 80 to 100 nm. This suggests that thicker LZO layers may perform better as buffer layers.

To obtain an all-solution coated conductor, a 120-nm-thick sol-gel LZO film on Ni-W substrate was coated with a 70-nm-thick MOD-CeO_2 film, and on this buffer stack a 0.8-μm-thick MOD-YBCO was deposited. A 120-nm-thick LZO film was used in this buffer stack because a small amount of the randomly oriented LZO (shown by the occurrence of a small (222) peak in the XRD in Fig. 2.61) develops for thicker films. Since this randomly oriented LZO could adversely affect the properties of the YBCO deposited on this buffer stack, a 120-nm LZO layer was used. On this all-solution coated-conductor, a critical current of 140 A/cm (J_c = 1.75 MA/cm^2) was measured (as shown in Fig. 2.65). This is the first time such high critical current values have been measured on an all-solution coated-conductor. Although it is respectable for an all-solution coated-conductor, it is still far from being comparable to the performance of the all-PVD buffer stack. On the all-PVD buffer stack, for similar YBCO thickness critical curent of over 250 A/cm are typically obtained. Therefore, further optimization of the solution buffer stack is warranted.

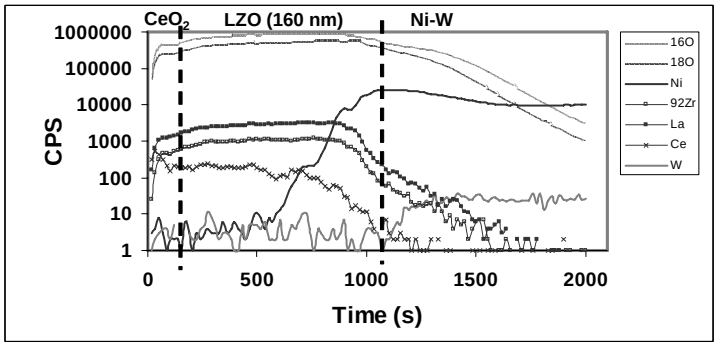

Fig. 2.64 SIMS depth profile of CeO_2/LZO/Ni-W samples after high-temperature annealing in O^{18} for 15 min.

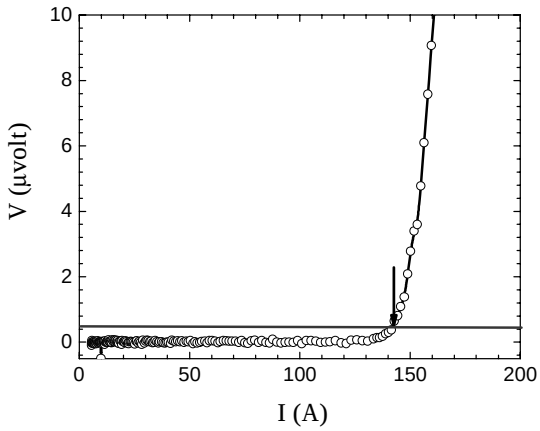

Fig. 2.65. All-solution coated conductor with an architecture MOD-YBCO/MOD-CeO_2/Sol-gel LZO/Ni-W showing a self-field critical current of 140 A/cm at 77 K for a 0.8-μm YBCO film.

One possible reason for the relatively poor performance of the all-solution buffer stack in comparison to the all-PVD buffer stack could be related to the crystallographic texture of the buffer layers. It has been well established that the electron-beam-evaporated Y_2O_3 seed layer on Ni-W substrates gives an improvement of the out-of-plane texture with respect to the metal substrate. This texture improvement gets transferred through the buffer stack to the YBCO layer. However, in case of the all-solution stack, the LZO layer typically shows a marginal deterioration of the out-of-plane texture when deposited directly on Ni-W substrates. Along with the deterioration of out-of-

plane texture, development of a small amount of a randomly oriented LZO in the film is also observed for thicker LZO films. However, as is clear from the results of the SIMS studies, thicker LZO layers may be necessary to prevent the diffusion of Ni into the YBCO layer.

To evaluate the effect of texture improvements, LZO films were deposited on 10-nm-thick Y_2O_3 seed layers. The LZO films deposited on the Y_2O_3 seed layers show improved texture, as shown in Table 2.7. Along with improved out-of-plane texture, it was also determined that using a thin Y_2O_3 seed layer reduced the amount of the polycrystalline LZO phase formation.

Table 2.7. Effect of Y_2O_3 seed layer on LZO epitaxy

	Δω (°)		Δϕ (°)
	Rolling direction	Transverse direction	
Ni-W Substrate	5.2	8.1	7.7
LZO/Ni-W	6.6	10.2	8.1
LZO/Y_2O_3/Ni-W	4.6	6.6	7.5

LZO films with a thickness of 200 to 225 nm could easily be deposited without development of any detectable randomly oriented LZO using three coats of 0.75 M LZO precursor solution. The improvement in texture and the absence of detectable randomly oriented LZO could lead to improved buffer properties. The performance of the LZO films (200–225 nm thick) deposited on 10-nm Y_2O_3 seed layers was evaluated by depositing a 70-nm-thick CeO_2 layer by rf-sputtering followed by a 0.8-μm MOD-YBCO deposition. The field dependence of critical current for this sample is shown in Fig. 2.66. This sample had a self-field critical current of 255 A/cm width, which is comparable to the values obtained on the standard all-PVD buffer layers. This suggests that a 200- to 225-nm-thick LZO buffer layer could perform as effectively as the PVD YSZ layer for deposition of a 0.8-μm-thick MOD-YBCO film. The effect of the Y_2O_3 seed layer on the performance of the sol-gel LZO with an MOD-CeO_2 layer similar to the all-solution buffer stack was also evaluated. These samples with a 10-nm Y_2O_3 seed layer, a 200- to 225-nm LZO layer, and a 70-nm-thick MOD-CeO_2 layer were found to have a self-field critical current of 200 A/cm. The field dependence of the critical of this sample is also illustrated in Fig. 2.66. While the Y_2O_3 seed layer seems to have improved the performance of the solution-LZO/CeO_2 buffer stack, the performance of the sample is still not on par with that obtained with the rf-sputtered CeO_2 layer. Further analysis of the samples indicated that the MOD-CeO_2 films on sol-gel LZO films have a rougher surface and yield more $BaCeO_3$, a reaction product after YBCO processing. Figure 2.67 which illustrates comparative XRD patterns obtained from the MOD-YBCO on rf-sputtered CeO_2 and MOD-CeO_2 shows that the MOD-CeO_2 leads to more reaction and a larger $BaCeO_3$ peak. Hence, further improvement of the sol-gel LZO/ MOD-CeO_2 buffer layers is needed to obtain properties that match the all-PVD buffer stack.

2.14.2 Summary

High-quality LZO films, suitable as barrier layers for ex situ processing of YBCO have been demonstrated by sol-gel processing. Deposition of crack-free LZO films up to 100 nm in thickness in a single step and thicker films, of 200 to 225 nm by multiple coating and annealing, has been demonstrated. Simulated YBCO ex situ processing showed that LZO films thicker than 120 nm have good barrier properties comparable to the standard all-PVD buffer stack. SIMS depth profile studies performed on LZO films on Ni-W substrates after annealing in O^{18} at YBCO processing temperature for 15 min shows that the diffusion of Ni through the buffer layer is contained within the first 80 to 100 nm. An all-solution conductor with a buffer stack YBCO (0.8 μm)/CeO_2 (70 nm)/LZO (120 nm)/Ni-W produced by a MOD approach had a critical current density of 1.75 MA/cm^2 and a corresponding critical current of 140 A/cm. This is the first demonstration of such high critical current on an all-solution conductor. Using an e-beam-evaporated thin Y_2O_3 seed layer to give LZO with improved texture, a 0.8-μm-thick MOD YBCO with a critical current of 255 A/cm on sputtered CeO_2 cap layer and 200 A/cm on MOD CeO_2 cap layer has been obtained. This demonstrates that LZO films could give performance comparable to that of PVD YSZ buffer layers. This offers promise to the development of an all-solution conductor with performance comparable to the all-PVD buffer stack, and thus a potentially low-cost alternative for conductor fabrication.

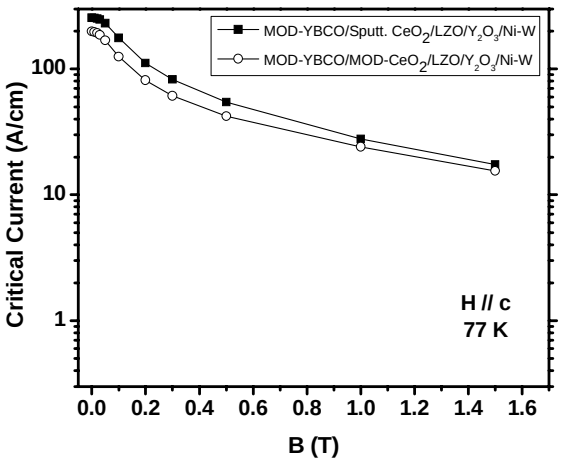

Fig. 2.66. Critical current vs field for MOD-YBCO/Sputt. CeO_2/LZO/Y_2O_3/Ni-W showing a self-field critical current of 255 A/cm and MOD-YBCO/MOD-CeO_2/LZO/Y2O3/Ni-W showing a self-field critical current of 200 A/cm.

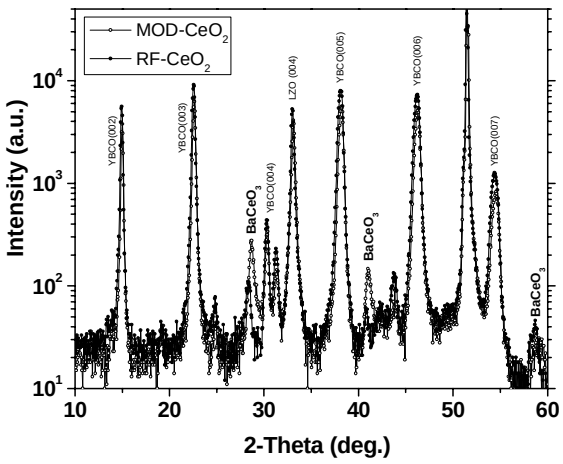

Fig. 2.67. Comparative XRD patterns of MOD-YBCO on RF-sputtered CeO_2 and MOD-CeO_2 cap layers.

2.14.3 References

1. D. T. Verebelyi, U. Schoop, C. Thieme, X. Li, W. Zhang, T. Kodenkandath, A. P. Malezemoff, N. Nguyen, E. Siegel, D. Buczek, J. Lynch, J. Scudiere, M. Rupich, A. Goyal, E. D. Specht, P. M. Martin, and M. Paranthaman, "Uniform performance of continuously processed MOD-YBCO-coated conductors using a textured Ni-W substrate," *Supercond. Sci. Tech.* **16**, L19 (2003).

2. M. S. Bhuiyan, M. Paranthaman, S. Sathyamurthy, T. Aytug, S. Kang, D. F. Lee, A. Goyal, E. A. Payzant, and K. Salama, "MOD approach for the growth of epitaxial CeO_2 buffer layers on biaxially textured Ni-W substrates for YBCO coated conductors," *Supercond. Sci. Tech.* **16**, 1305 (2003).

2.15 Reverse Micellar Synthesis of Cerium Oxide Nanoparticles

S. Sathyamurthy, K. J. Leonard, Reza T. Debastani, and M. P. Paranthaman

2.15.1 Introduction

Cerium oxide (CeO_2) nanoparticles have been extensively investigated for a wide variety of applications, such as catalysis [1], fuel cells [2], polishing media in microelectronics, and luminescent materials [3], and could be used as artificial pinning centers in high-temperature superconductors [4]. The physical and chemical properties of nanometer-sized particles are significantly different from those of the bulk material. Ultrafine particles of CeO_2 have great potential for use as UV-absorbent materials and high-activity catalysts. Many researchers have prepared CeO_2 nanoparticles using various methods, such as gas condensation of Ce metal followed by oxidation in O_2 gas [5], homogeneous precipitation using hexamethylenetetramine [6], sol-gel processing [7], hydrothermal synthesis [8], and electrochemical synthesis [9].

In this work, we describe the use of water-in-oil microemulsions to synthesize nanometer-size CeO_2 particles. A dispersion of two mutually insoluble liquids, such as oil and water, facilitated by the use of surfactants, which serve to decrease the surface tension across the interface between the oil and the water

materials [3], and could be used as artificial pinning centers in high-temperature superconductors [4]. The physical and chemical properties of nanometer-sized particles are significantly different from those of the bulk material. Ultrafine particles of CeO_2 have great potential for use as UV-absorbent materials and high-activity catalysts. Many researchers have prepared CeO_2 nanoparticles using various methods, such as gas condensation of Ce metal followed by oxidation in O_2 gas [5], homogeneous precipitation using hexamethylenetetramine [6], sol-gel processing [7], hydrothermal synthesis [8], and electrochemical synthesis [9].

In this work, we describe the use of water-in-oil microemulsions to synthesize nanometer-size CeO_2 particles. A dispersion of two mutually insoluble liquids, such as oil and water, facilitated by the use of surfactants, which serve to decrease the surface tension across the interface between the oil and the water phases, is called a "microemulsion." The surfactant molecules have a polar head with a nonpolar tail. The polar portion of the surfactant is attracted to the water, and the nonpolar portion is attracted to the oil. The hydrophile-lipophile balance is a convenient measure of these counter-attractions. An ordered arrangement of the surfactant molecules forms as a monomolecular layer around the spherical droplets (see Fig. 2.68). In microemulsions, because the size of the dispersed phase is on the order of a few nanometers, they are optically transparent. These spherical particles can be used as tiny reactor vessels, and the size of the products will be limited to the size of the reactors (a few nanometers). For example, for reactions taking place in an aqueous medium, the reaction can be conducted in a water-in-oil microemulsion. This type of processing approach for nanoparticles is also referred to as the reverse micellar approach.

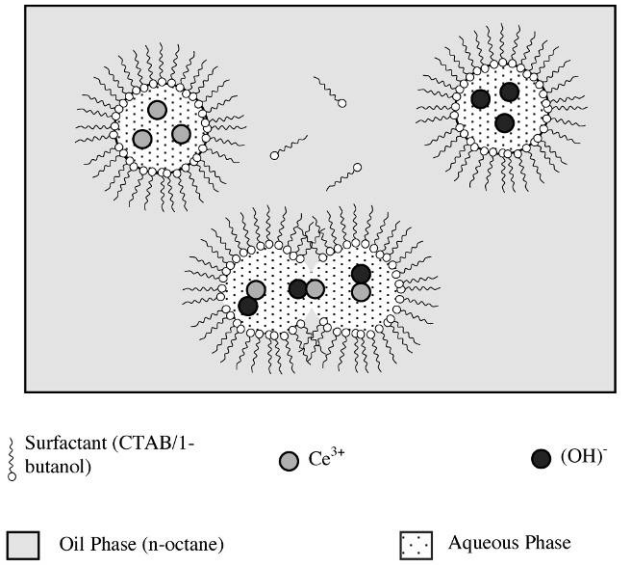

Fig. 2.68. Schematic illustration of nanoparticle synthesis using water-in-oil inverse microemulsions.

Using the above method, several studies have been carried out in recent years to synthesize monodisperse nanoparticles of metals and oxides [10–13]. The use of this method allows the synthesis of particles with uniform small size and narrow size distribution because the reaction volume is limited to the size of the water droplets (typically a few nm). In the present study, we have employed the reverse micellar (microemulsion) technique to prepare nanometer sized Ceria particles. The results obtained on the Ceria nanoparticle size and morphology is reported. In addition, the UV absorption and photoluminescence properties of CeO_2 nanoparticles are also reported.

2.15.2 Experimental Procedure

All chemicals were used as received. Cerium (III) nitrate.$6H_2O$ (Fisher Scientific, 99%) was used as the starting material for the Ceria nanoparticles, and sodium hydroxide (Fisher Scientific 97.7%) was used as the reaction reagent. The microemulsion system used in the present study consisted of n-octane (Alfa Aesar, 99%) as the continuous oil phase, cetyl trimethyl ammonium bromide (CTAB) (Alfa Aesar, 99%) as the surfactant, 1-butanol (Alfa Aesar, 99.4%) as the co-surfactant and an aqueous solution as the dispersed phase. A 0.24M solution of Ce^{3+} was prepared by dissolving 1.0421 g of Ce(III) nitrate.$6H_2O$ in 10 mL of deionized water. The solution was dispersed in a mixture of 14 g of n-octane, 3 g of 1-butanol, and 4 g of CTAB to form a microemulsion. Another microemulsion of similar composition was made from 10 mL of 0.72 M $(OH)^-$ solution (0.288 g of NaOH in 10 mL of deionized water) was prepared.

The two stable microemulsions made from the above compositions were mixed together using a magnetic stirrer for 1 h. The resulting microemulsion developed a yellowish hue, indicating the formation of CeO_2 nanoparticles, which were extracted by centrifuging at 10,000 rpm for 10 min. The CeO_2 nanoparticles were then washed with methanol and stored as dispersion in methanol. The nanoparticles were characterized by XRD, HRTEM, UV-visible spectroscopy using a CARY 5000 UV-VIS-NIR spectrophotometer, and photoluminescence using Jobin-Yvon Fluoromax-P spectrofluorometer. The specific surface area of the nanoparticles was measured by the Brunauer, Emmet, Teller (BET) method, using a Gemini 2375 multi-point surface area analyzer.

2.15.3 Results and Discussion

A typical XRD pattern obtained from the as-processed nanoparticles is shown in Fig. 2.69. The diffraction peaks observed show a good match with those of bulk CeO_2. There is considerable broadening of the peaks, suggesting that the particles are very small in dimensions. Using the Scherrer formula, the average size of the particles was estimated to be around 3.5 nm. Due to the extensive broadening of the peaks, significant overlap between the peaks is also observed. This could lead to error in phase identification and particle size estimation. Further confirmation of the phase purity and particle size estimates was obtained using HR-TEM. Figure 2.70 shows an electron diffraction pattern taken from one particle agglomeration examined. All the rings except one, marked by an asterisk in the image, could be precisely indexed to the cubic CeO_2 phase. The diffraction pattern was further examined for all possible forms of cerium oxide for matches to the unknown ring. It was determined that both pure Ce and CeO have (220) planes diffracting under these conditions (Table 2.8). In addition, these phases also have other planes at near overlapping positions with the CeO_2 phase that further contribute to the CeO_2 patterns observed in the selected area electron diffraction (SAED) pattern. Therefore, an amount of oxygen-lean phase is present within the sample, suggesting that micelle mixing within the solutions was not complete, which is not unexpected as the material is in the as-processed condition. Further annealing of the particles within an oxygen environment will likely fully convert the material, though at the expense of particle size. Nevertheless, the results from Figs. 2.69 and 2.70 show that the nanoparticles obtained from the microemulsions in the reaction of cerium nitrate and sodium hydroxide is predominantly crystalline CeO_2 and may not require further heat treatment.

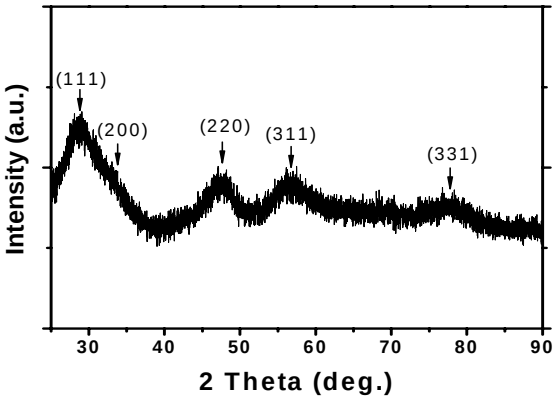

Fig. 2.69. XRD pattern of as-processed CeO_2 nanoparticles.

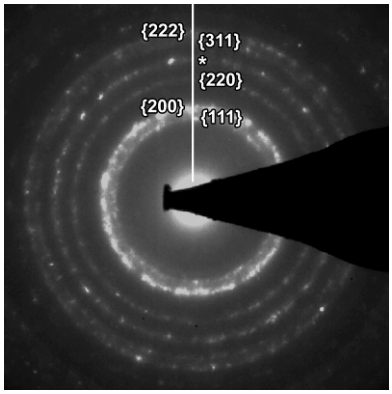

Fig. 2.70. Electron diffraction pattern of CeO_2 nanoparticles.

Table 2.8. Measured interplanar spacing (*d*) from selected area diffraction pattern of CeO_2 nanoparticles compared with reference values of different cerium oxide forms (Å)

Ring	$d_{measured}$	CeO_2	CeO	CeO_{2-x}	Ce_2O_3	Ce
1	3.119	3.124 (111)	2.938 (111)	3.39 (222)	2.945 (01 $\bar{1}$1)	2.97 (111)
2	2.733	2.706 (200)	2.544 (200)		2.254 (10 $\bar{1}$2)	2.57 (200)
3	1.949	1.913 (220)		2.06 (044)	1.9455 (11 $\bar{2}$0)	
4	1.824		1.799 (220)		1.733 (10 $\bar{1}$3)	1.82 (220)
5	1.622	1.632 (311)		1.65 (543)	1.6373 (11 $\bar{2}$2)	
6	1.526	1.562 (222)	1.534 (311)			1.55 (311)

Figure 2.71 shows the high resolution TEM image of the CeO_2 nanoparticles. It is evident that the particle size is very small. The particle size was estimated to be about 3.7 nm with a narrow size distribution. This is consistent with the estimates obtained from XRD. Also evident in the figure is the polyhedral shape of nanoparticles. Most of the particles were found to have well-defined polyhedral shapes. It has been reported in the literature [6,8] that for CeO_2 nanoparticles in the size range of 3 to 10 nm, the particle shape is dominated by a truncated octahedral that is enclosed by the {100} and {111} facets. The observations made in our study also show similar trends in the nanoparticle shape showing {111} and {002} faceted surfaces (Fig. 2.71). Since the microemulsion was broken to extract the nanoparticles, some amount of agglomeration was observed, as is evident in the TEM image. However, since CTAB is a strongly coordinating surfactant, the surface of the CeO_2 is still expected to be protected. This hypothesis was further confirmed using BET surface area measurements.

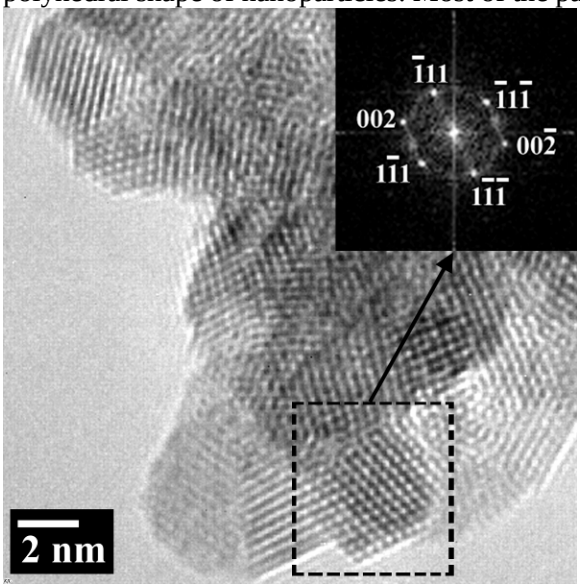

Fig. 2.71. High-magnification image of CeO_2 particle agglomeration showing a lattice image of [110] oriented particle. Inset: fast Fourier transformation of selected particle revealing the {002} and {111} faceted surfaces of the particle.

The specific surface area was measured by the BET method using a Gemini 2375 surface area analyzer. The BET multipoint surface area of the particles was determined to be 168.3 m^2/g. The apparent equivalent diameter of the particles can be estimated from the BET-specific surface area by assuming the particles to be spherical according to the expression

$$d_{BET} = 6/(\rho * S_{BET}) , \quad (1)$$

where d_{BET} is the diameter of the particle, ρ is the bulk density of the solid (7.132 g/cc for CeO_2), and S_{BET} is the specific surface area measured. Using equation (1), the particle size of the CeO_2 was determined to be 5 nm, which is in close agreement with the estimates from XRD and HRTEM.

Figure 2.72(a) shows the UV-visible absorption spectrum of a dispersion of CeO_2 nanoparticles in methanol. These measurements were made by using pure methanol as a blank. The CeO_2 nanoparticles show a strong absorption below 400 nm with a well-defined absorbance peak at around 305 nm. The band gap energy (E_g) for the CeO_2 nanoparticles is determined by fitting the absorption data to the direct transition equation

$$\alpha h\nu = B_d (h\nu - E_g)^{1/2} , \quad (2)$$

where α is the optical absorption coefficient, hν is the photon energy, E_g is the direct band gap, and B_d is a constant [10]. Plotting $(\alpha h\nu)^2$ as a function of photon energy, and extrapolating the linear portion of the curve to absorption equal to zero as shown in Fig. 2.72(b), gives the value of the direct band gap (E_g) to be 3.31 eV. This value is within the range reported in the literature. Yin et al. [17] have reported direct band gap values ranging from 3.03 to 3.68 eV for CeO_2 nanoparticles prepared using sonochemical synthesis. Yu et al. [18] have reported direct band gap value of 3.7 eV for CeO_2 particles synthesized by hydrothermal hydrolysis in the presence of block co-polymers as stabilizing agents. Similarly, Masui et al. [19] have reported direct band gap values ranging from 3.38 to 3.44 eV for CeO_2 nanoparticles prepared using reverse micelles.

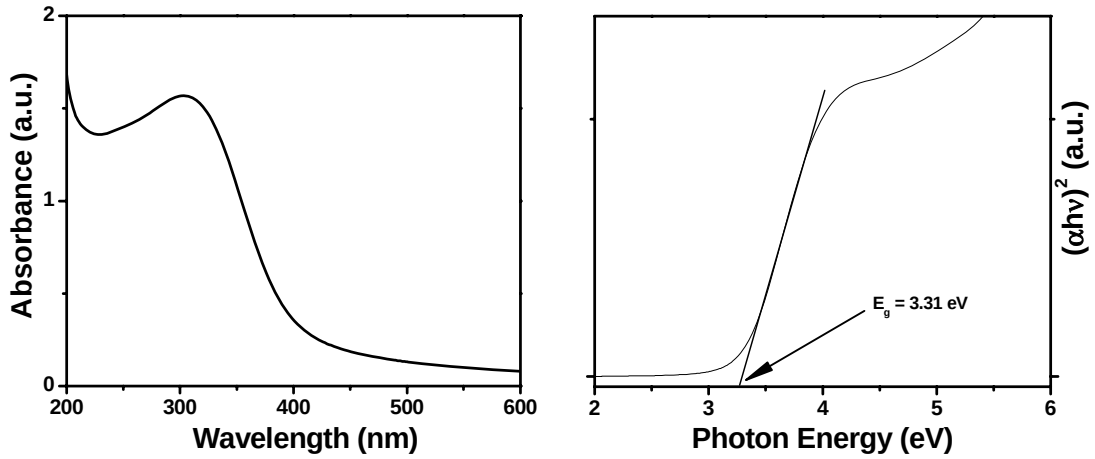

Fig. 2.72. (a) UV-visible absorption spectrum of CeO_2 nanoparticles. (b) Plot of $(\alpha h\nu)^2$ as a function of photon energy for the CeO_2 nanoparticles.

Figure 2.73 shows the room-temperature photoluminescence spectra of CeO_2 nanoparticle dispersion in methanol. The as-prepared nanoparticles at higher concentrations shows a photoluminescence peak around 410 nm. When the solution was diluted to one fiftieth of the original concentration, the emission peak was found to shift toward shorter wavelength (around 360 nm). This observation is consistent with those reported in the literature [20], where the photoluminescence peak observed at 422 nm at high concentrations slowly shifted to 405, 389, 382, and 368 nm as the concentration was decreased. This phenomenon has been explained by charge transitions from the 4f band to the valence band of the CeO_2 in both nanoparticles [18] and thin films [21]. To check for effects of oxygen, the dilute solution of CeO_2nanoparticles was bubbled with ultrahigh-purity Ar gas for several minutes to remove all dissolved oxygen, and the photoluminescence spectra were recorded again. There was no change in the photoluminescence spectra, suggesting that oxygen-related quenching of the photolulminiscence does not take place in these CeO_2 nanoparticles.

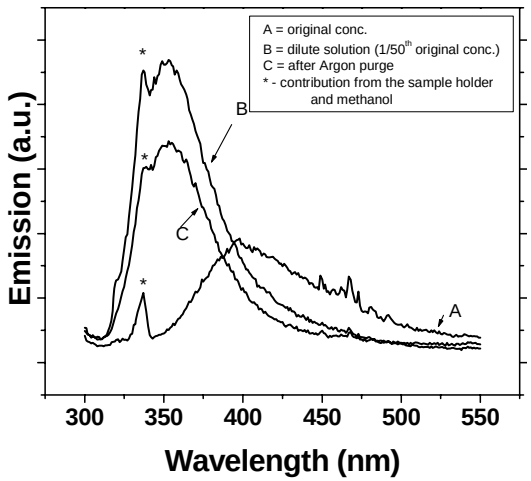

Fig. 2.73. Photoluminescence spectra of CeO_2 nanoparticle dispersions in methanol (λ_{ex} = 290 nm).

2.15.4 Conclusions

CeO_2 nanoparticles have been synthesized using a reverse micellar method. Using XRD and HRTEM, the particles were found to have an average size of 3.7 nm, and the particles have a well defined polyhedral shape. Using BET multi-point surface area of the nanoparticles was measured to be 168.3 m^2/g. The average particle size calculated from the BET specific surface area was 5 nm. The CeO_2 nanoparticles show a strong UV absorption below 400 nm with a well defined absorption peak at 305 nm. The direct band gap for CeO_2 nanoparticles was determined to be 3.31 eV. The particles also exhibited room-temperature photoluminescence. The photoluminescence peak was found to be sensitive to the particle concentration, shifting towards shorter wavelengths as the solution was diluted.

2.15.5 References

1. A. Trovarelli, *Catal. Rev. Sci. Eng*. **38**, 439 (1996).
2. B. C. H. Steele, *Nature* **414**, 345 (2001).
3. X. J. Yu, P. B. Xie, and Q. D. Su, *Phys. Chem. Chem. Phys*. **3**, 5266 (2001).
4. J. L. Macmanus-Driscoll, S. R. Foltyn, Q. X. ,Jia, H. Wang, A. Serquis, L. Civale, B. Maiorov, M. E. Hawley, M. P. Maley, and D. E. Peterson, *Nature Materials* **3**, 439 (2004).
5. N. Guillou, L. C. Nistor, H, Fuess, and H. Hahn, *Nanostructured Materials* **8**, 545 (1997).
6. F. Zheng, Q. Jin, and S.-W. Chan, *J. Appl. Phys.* **95**, 4319 (2004).
7. F. Czerwinski and J. A. Szpunar, *J. Sol-Gel Sci. Tech*. **9**, 103 (1997).
8. Z. L. Wang and X. Feng, *J. Phys. Chem. B* **107**, 13563 (2003).
9. I. Zhitomirsky and A. Petric *Ceram. Int.* **27**, 149 (2001).
10. S. Hingorani, V. Pillai, P. Kumar, M. S. Multani, and D. O. Shah, *Mater. Res. Bull.* **28**, 1303 (1993).
11. J. Wang, J. Fang, S.-C. Ng, L.-M. Gan, C.-H. Chew, X. Wang, and Z. Shen, *J. Am. Ceram. Soc.* **82**, 873 (1999).
12. A. J. Zarur and J. Y. Ying, *Nature* **403**, 65 (2000).
13. R. N. Bhargava, V. Chhabras, T. Som, A. Ekimov, and N. Taskar, *Phys. Stat. Sol. B* **229**, 897 (2002).
14. V. Pillai and D. O. Shah, *Journal of Magnetism and Magnetic Materials* **163**, 243 (1996).
15. G. Palazzo, L. Carbone, G. Colafemmina, R. Angelico, A. Ceglie, and M. Giustini, *Phys. Chem. Chem. Phys.* **6**, 1423 (2004).
16. E. M. Corbeil and N. E. Levinger, *Langmuir* **19**, 7264 (2003).
17. L. Yin, Y. Wang, G. Pang, Y. Koltypin, and A. Gedanken, *J. Colloid and Interface Science* **246**, 78 (2002).
18. S-H Yu, Colfen H, and Fischer A 2004 *Colloids and Surfaces A* **243** 49.
19. Masui T, Fujiwara K, Machida K, and Adachi G 1997 Chem. Mater. **9** 2197.
20. N. Serpone, D. Lawless, and R. Khairutdinov *J. Phys. Chem.* **99**, 16646 (1995).
21. Gao F, Li G.H, Zhang J.H, Qin F.G, Yao Z.Y, Liu Z.K, Wang Z.G, Lin L.Y 2001 *Chem. Phys. Lett.* **18** 443.

2.16 Characterization of $BaZrO_3$ Nanoparticles Prepared by Reverse Micelle Synthesis

K. J. Leonard, S. Sathyamurthy, and M. Paranthaman

2.16.1 Introduction

Research into nanotechnology has exploded over the past several years, carrying with it new ideas in both the processing and utilization of nanostructured materials for a magnitude of applications ranging from common uses to advanced technologies over all scientific and commercial fields. Numerous preparation methods for nano-scaled materials, particularly particles, have been established and documented. These processes include physical methods such as mechanical milling [1] and inert gas condensation [2], along with chemical methods such as oxidative precipitation [3], electro-deposition [4], hydrothermal [5], and

sol-gel synthesis [6]. In general, a major benefit of chemical methods is their relative inexpensive investment of capital equipment. Of these chemical processes, reverse micelle synthesis has been recently demonstrated to be a viable method for producing a wide array of metals and metal oxide compounds, including perovskites [7–12], over a relatively narrow particle size distribution.

Reverse micelle synthesis utilizes a natural phenomenon involving the formation of spheroidal aggregates in a solution when a surfactant is introduced to a polar organic solvent, formed either in the presence or absence of water [7]. Micelle formation allows for a unique encapsulated volume of controllable size through which reactions and subsequent development of metal and metallic compounds can be produced. Aggregates containing water to surfactant molar ratios of less than 15 are called "reverse micelles" and have hydrodynamic diameters in the range of 40 to 100 Å [7,9,10,13], whereas water-to-surfactant molar ratios of greater than 15 constitute microemulsions, which have a hydrodynamic diameter range between 50 to 5000 Å. Within the micelles, reactants for chemical processes can be contained. In developing nanocrystalline materials, solutions of separately prepared reverse micelles containing encapsulate reactants A and B are mixed together. By using sonication or stirring to further enhance collisions between the micelles containing the different reactants, fusion between micelles can occur, producing a transient dimer that exchanges the water cores of the collided micelles. The dimer breaks down again into two reverse micelles with the contents from one micelle transferred into the other [7]. The mixing of the two reactants produces a precipitation reaction, from which nano-particles can be obtained through centrifugal extraction of the solution. The process of micelle exchange, which leads to further growth, continues until the particles reach a terminal size determined by the system and the stabilization of the particles by the surfactant [10]. The size of the metallic particles produced is a function of the reaction time, water content in the micelle, the concentration of the reactant solutions contained within the micelle, and the solvent type [10].

Metal oxide compounds of the perovskite crystal structure are a class of materials that have attracted great attention for their use in the electronics industry due to unique optical, magnetic, and electronic properties [14]. These properties, which have been found to be dependent on the dimensional scale of the materials, are the driving force into research examining these compounds in particle [15,16] or thin-film form [17]. Recently, dispersions of $BaZrO_3$ nanoparticles in laser-ablated YBCO films have been produced through the initial mixing, compacting, and sintering of YBCO with $Ba(NO_3)_2$ and ZrO_2 powders in the ablation targets [18]. The $BaZrO_3$ nanoparticles create stable flux-pinning centers within the superconducting films [19]. Dramatic enhancements to the current-carrying properties of these films under high magnetic fields have been observed. This method also offers an easier processing route than heavy-ion irradiation in producing defect-generated pinning centers, in addition to being more amenable to the production of long-length multi-layered coated conductor tapes [18]. Furthermore, recent work at Oak Ridge has shown that PLD of $BaZrO_3$-doped YBCO targets results in an even finer dispersion of $BaZrO_3$ particles within the YBCO film.

Although synthesis of $BaZrO_3$ particles through solution-based techniques has been reported on [16], particle sizes on the micron scale were produced. The larger particle sizes may create nonuniform distributions or larger particles sizes if used within ablation or sputtering targets. In this section we report on the processing of $BaZrO_3$ nanoparticles produced through reverse micelle synthesis. Emphasis is placed on characterizing two of the processing stages in production through XRD and analytical electron microscopy.

2.16.2. Experimental

All chemicals were used as received. Barium nitrate [$Ba(NO_3)_2$, Alfa Aesar, 99+%] and zirconium dinitrate oxide [$ZrO(NO_3)_2 \times H_2O$, Alfa Aesar, 99.9%] were used as the starting materials for the $BaZrO_3$ nanoparticles, and sodium hydroxide (Fisher Scientific, 97.7%) was used as the precipitating agent. The microemulsion system used in the study consisted of n-octane (Alfa Aesar, 99%) as the continuous oil phase, cetyl trimethyl ammonium bromide (CTAB) (Alfa Aesar – 99%) as the surfactant, 1-butanol (Alfa Aesar, 99.4%) as the co-surfactant and an aqueous solution as the dispersed phase. A solution containing 0.12 M Ba^{2+} and Zr^{4+} was prepared by dissolving 0.627 g of $Ba(NO_3)_2$ and 0.555 g of $ZrO(NO_3)_2 \times H_2O$ in 20 mL of deionized water. This solution was dispersed in a mixture of 28 g of n-octane, 6 g of 1-butanol, and 8 g of CTAB to form a microemulsion. Another microemulsion of similar composition using 20 mL of 0.72 M $(OH)^-$ solution (0.576 g of NaOH in 20 mL of deionized water) was prepared. The two microemulsions were mixed together using a magnetic stirrer for 1 h. The white precipitate that formed was extracted by centrifuging at 10,000 rpm for 10 min. The precipitate was then washed with methanol and dried in an oven at 110ºC. After grinding, the dried powders were heat-treated in separate batches for 30 min in stagnant air at temperatures increasing in increments of 100ºC from 100 to 700ºC.

Characterization of the powders was performed through XRD in both the as-processed and heat-treated conditions. Samples for TEM were prepared from the as-processed and 700ºC treated particles. For TEM, the particles were suspended in a solution of methanol and mixed in a sonicator for approximately 5 min prior to sampling. Type-A lacey carbon films purchased from Ted Pella, Inc., were used to support the particles for electron microscopy. Prior to sampling, the formvar backing of the lacey carbon film was removed by dipping the vertically oriented TEM grid in and out of chloroform for approximately 20 s. After air drying, the TEM grids were dipped four times in and out of the sonicated particle suspensions. Extra care was taken in cleaning all glassware and tweezers used so as not to introduce foreign particles or to cross-contaminate.

The as-processed and post-heat-treated samples were examined with a Philips CM200 TEM operated at 200 kV in both conventional and nano-probe modes. EDS was also carried out on the particles. The distribution and agglomeration of the particles on the lacey carbon films was found to be adequate for analysis.

2.16.3. Results and Discussion

The XRD θ-2θ scan for the as-processed sample (Fig. 2.74) revealed a predominantly amorphous structure for the particles. However, some peaks were determined to be associated with the $Ba(OH)_2(H_2O)_3$ and $Zr_{0.95}O_2$ phases, although they were not positively identified until TEM analysis was conducted. Heat-treatment of the batches of as-processed powders in air for 0.5 h revealed no development of crystallinity for temperatures below 700ºC. For comparison, the XRD scan of the crystallized powders from the 700ºC treatment is shown with that of the as-processed powders in Fig. 2.74. Clearly defined peaks of $BaZrO_3$ are observed within the θ-2θ scan, along with minor peaks associated with the ZrO_2 phase. In both the as-processed and heat-treated samples, the zirconium oxide particles were determined to be tetragonal. This coincided with previous reports as to the tetragonal structure being stable at particle sizes below the range of 30 nm with larger particle sizes favoring the monoclinic structure [20–22].

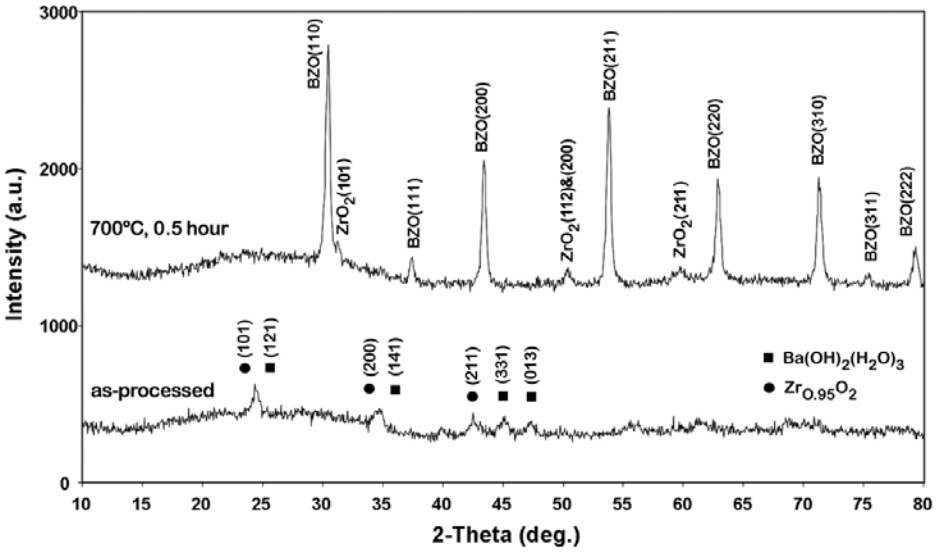

Fig. 2.74. Comparison of XRD scans for the as-processed and 700°C heat-treated samples showing the development of $BaZrO_3$ (BZO). In addition to the $BaZrO_3$ phase, a small quantity of ZrO_2 phase was also observed. The X-ray intensity for the heat treated sample has been shifted upward for clarity.

Examination of the as-processed particles through TEM confirmed the amorphous structure of the particles as indicated by XRD analysis. Figure 2.75(a) is a low-magnification image of a particle agglomeration with the insert showing the amorphous pattern of the selected area diffraction (SAD) image taken of the particles. The particles were found to be more easily identifiable when agglomerated in groups suspended over the edge of a hole on the carbon film rather than as individual particles spread out over the carbon film due to the lack of contrast associated with their amorphous structure. The amorphous structure of the particles is also evident in the higher magnification image of Fig. 2.75(b).

The average diameter of the amorphous Ba-Zr-O particles, measured from several TEM micrographs at high magnification was found to be approximately 7.5 nm with a spread of ± 2 nm. The lack of contrast associated with the amorphous particles made it too difficult to obtain a statistically accurate particle size distribution. However, the particles observed were within the 4- to 10-nm hydrodynamic diameter range for reverse micelle structures as reported in references [9] and [13]. The investigation of multiple particle agglomerations collected on the sample grid at different areas, was unsuccessful in identifying any crystalline $Zr_{0.95}O_2$ particles as detected by XRD analysis. An EDS spectrum taken from an agglomeration of the as-processed particles is shown in Fig. 2.76(a). The presence of Cu within the spectrum arises from the mesh grid supporting the lacey carbon film. In addition, levels of K, Ca and Br were also detected within the particle agglomeration from the process solution producing the nanoparticles. The level of Ba detected in the EDS spectrum of the as-processed material appeared to be slightly depleted in comparison to the spectrum taken from a $BaZrO_3$ particle of the post-heat-treated sample [Fig. 2.76(b)]. This was likely due to the presence of the $Zr_{0.95}O_2$ particles within the agglomeration analyzed. In addition to the nanoparticles, Ba-rich rod-like structures were observed in the as-processed sample, further skewing the nominal composition of the agglomeration towards that of Ba lean.

The rod-like particles [Fig. 2.75(c)] identified though EDS as a Ba-oxide were consistent in size with average diameters of 62 nm and lengths of 1.5 μm, although some particles were broken in two. The rods typically had a curvature to them of varying degrees. While XRD identified these particles as $Ba(OH)_2(H_2O)_3$, interaction with the electron beam of the microscope transformed these particles to the BaO_2 structure. The rods appeared to be composed of multiple grains or subgrains of the barium hydroxide phase, which upon exposure to the electron beam developed into a segmented particle consisting of smaller grains of BaO_2 linked together by a twined interface. A high-resolution image of a

twinned interface within one of the converted BaO_2 particles is shown in Fig. 2.75(d). Twinning of the interface was determined to be on the {112} planes of the tetragonal BaO_2. The fast Fourier transformation (FFT) of the lattice image clearly illustrates this twinning.

An increase in particle size was observed for the crystalline samples that had been heat-treated at 700ºC over that of the amorphous as-deposited material [Fig. 2.77(a)]. No rod-like $Ba(OH)_2(H_2O)_3$ particles were observed following heat-treatment. Through electron diffraction, it was revealed that the particles were a mixture of two different crystallographic phases. Examination of the ring pattern [Fig. 2.77(b)] revealed that all the intensities observed could not be associated with the $BaZrO_3$ phase alone. Based on confirmation through EDS that these particle groupings contained no additional atomic species in the form of contamination, the ring pattern was checked against different mixed Ba-Zr-O species. The tetragonal ZrO_2 phase was found to account for the additional reflections observed within the ring pattern (Table 2.9) while also sharing an overlap with some of the $BaZrO_3$ intensities, confirming what was observed through XRD. Sintering or attachment points between the particles were not observed in TEM investigation of the heat-treated particles.

The mean particle diameter of the heat-treated sample containing both $BaZrO_3$ and ZrO_2 phases was determined to be 17.3 nm, and is shown statistically in Fig. 2.78. This was determined from several bright-field TEM images of particle agglomerations, providing a total of 150 individually measured particles. To differentiate the chemical makeup of the particles and to provide some statistics as to the size and quantity of ZrO_2, a series of bright-field and dark-field images were taken of several different particle

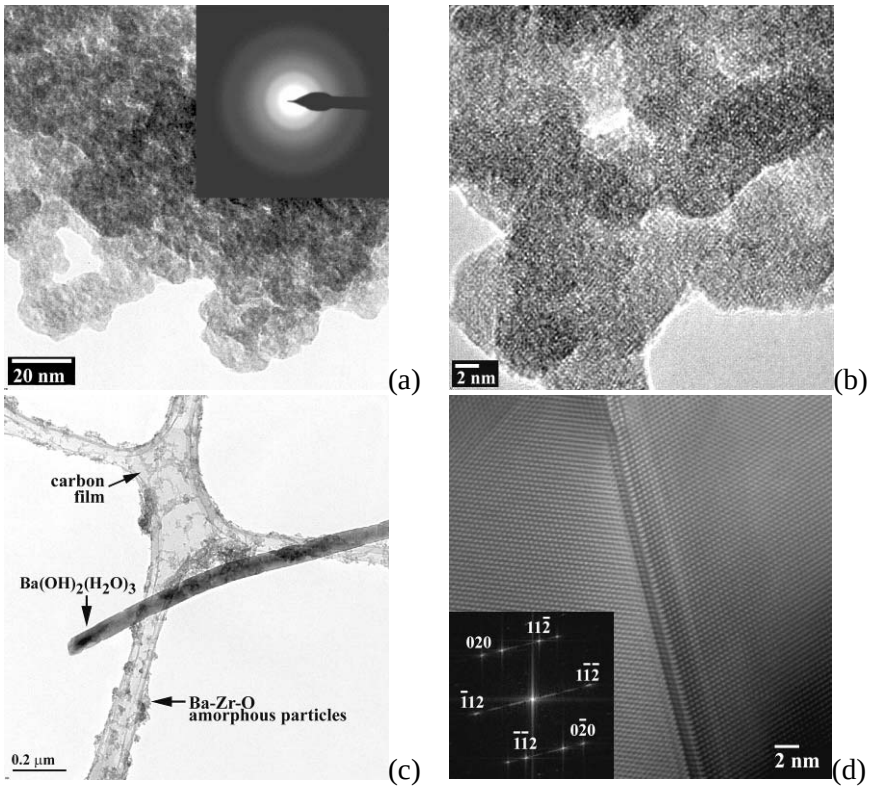

Fig. 2.75. TEM micrographs of the as-processed Ba-Zr-O sample. **(**a) Low-magnification image of the amorphous particles. Inset: Amorphous SAD pattern. (b) High-magnification image. (c) Low-magnification image showing $Ba(OH)_2(H_2O)_3$ rod-like particles caught on the lacey carbon grid. (d) Lattice image, b=[201], of a {112} twinned interface contained within the BaO_2 particles following beam-induced transformation from the $Ba(OH)_2(H_2O)_3$ phase by the microscope. Inset: fast Fourier transformation of the lattice image illustrating the twin.

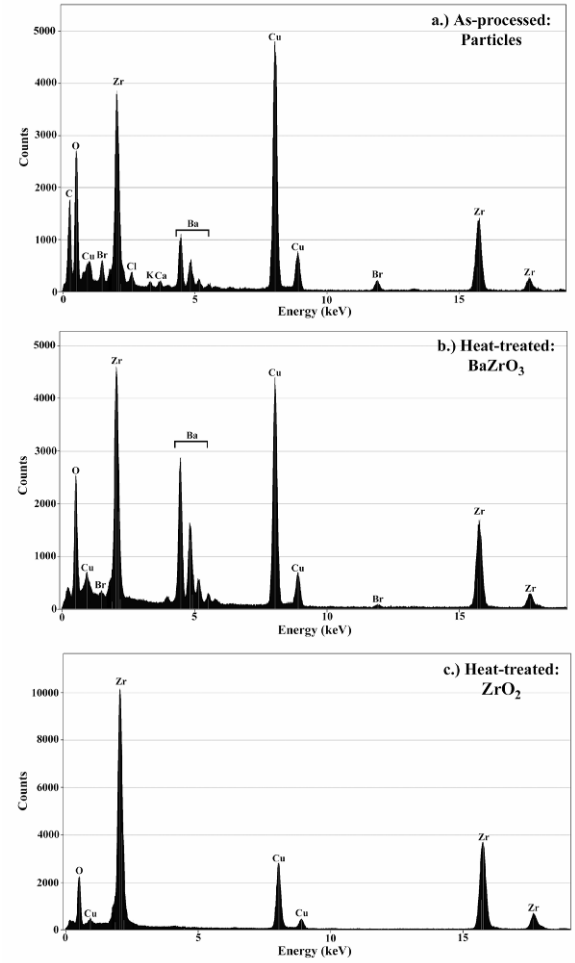

Fig. 2.76. EDS spectra. (a) As-processed nanoparticles. (b) $BaZrO_3$ and (c) ZrO_2 particles from the post-heat-treated samples.

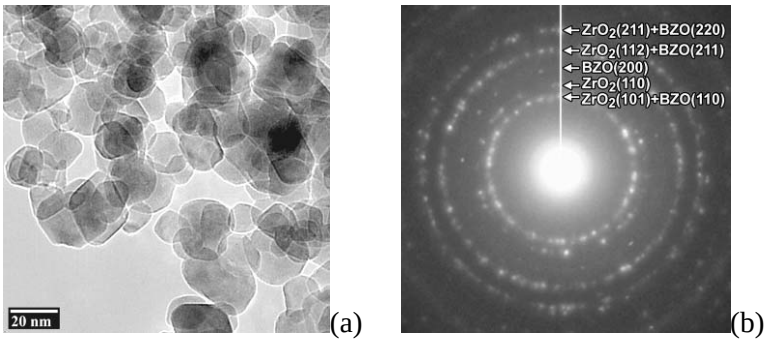

Fig. 2.77. TEM micrographs of nanoparticles following heat treatment at 700ºC for 0.5 h in air. (a) Low-magnification image illustrating the size distribution of particles. (b) selected area diffraction pattern showing a mixture of $BaZrO_3$ and ZrO_2 phases.

agglomerations. Each of the dark-field images used a selected {110} diffracting plane of the ZrO_2 particles identified within the ring-like SAD pattern of the particle agglomeration [similar to that of Fig. 2.77(b)]. The particle size distribution of 40 individually measured ZrO_2 particles from this method is also shown in Fig. 2.78. The average ZrO_2 particle size was determined to be 13.8 nm with the distribution slightly shifted to smaller particle sizes than that of the combined $BaZrO_3$ and ZrO_2 data. Although this was useful in providing data on the particle size distribution of ZrO_2, a rough estimate as to the number of ZrO_2 to $BaZrO_3$ particles was approximately 1 to 25. The quantity of ZrO_2 to $BaZrO_3$ should not be taken directly from the histograms shown in Fig. 2.78, as they are only representations of the particle size distributions. Because only a select number of {110} ZrO_2 planes could be utilized in a given series of dark-field images, confidence in the quantity of ZrO_2 particles within a given agglomeration is low. While accurate determination of the chemical composition of individual particles had to be done through EDS, differentiating the two phases could be done on a first approximation through the particle morphology.

An example of one of the larger particles determined to be $BaZrO_3$ is shown in Fig. 2.79(a), oriented with its [110] direction normal to the image or in parallel with the electron beam. The EDS spectrum from this particle is shown in Fig. 2.80(b). The insert within the high-resolution image of the particle in Fig. 2.79(a) is an FFT taken from of a region within the $BaZrO_3$ particle not overlapped with its neighbors.

A smaller particle determined to be ZrO_2 [Fig. 2.80(a)], is shown oriented with its [010] direction parallel to the beam. The EDS spectrum taken from this particle is shown in Fig. 2.76(c). Though HREM lattice images of the $BaZrO_3$ and ZrO_2 particles at first appear to be similar, well defined differences are clearly illustrated within the FFT taken from each image and are translated into the general shape of the particles.

Both the $BaZrO_3$ and ZrO_2 particles have a faceted morphology and consist of defect-free single crystals. The [110] projection of the $BaZrO_3$ particle shows a near hexagonal shape with four {111} and

Table 2.9. Measured interplanar spacing (*d*) from selected area diffraction pattern showing a mixture of $BaZrO_3$ and ZrO_2 phases compared with values for $BaZrO_3$ and ZrO_2 from powder diffraction file numbers 6-0399 and 88-1007, respectively

Ring No.	d measured (Å)	$BaZrO_3$ (cubic) (hkl); d (Å)	ZrO_2 (tetragonal) (hkl); d (Å)
1	2.999	(110); 2.964	(101); 2.950
2	2.543		(110); 2.545
3	2.113	(200); 2.096	
4	1.798	(211); 1.712	(112); 1.810
5	1.492	(220); 1.482	
6	1.534		(103); 1.549

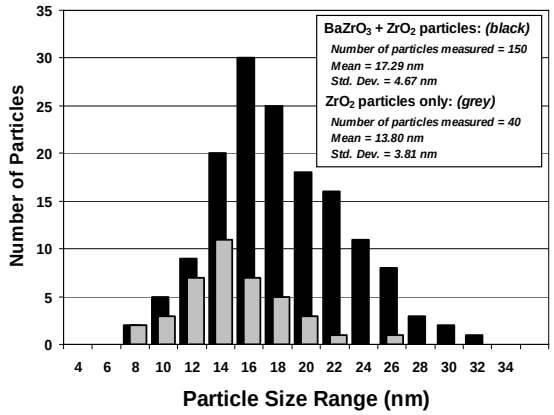

Fig. 2.78. Nanoparticle size distribution histograms after a 700ºC, 0.5-h exposure in air for measured diameters of $BaZrO_3$ plus ZrO_2 particles from bright-field TEM images and of ZrO_2 particles measured from dark-field images.

two {002} surfaces [Fig. 2.79(b) and (c)]. These particles can be described as an octahedral with {111} faces and {002} truncated surfaces. This is the same shape and surface features that have been commonly observed for nanoparticles of CeO_2 [23–25]. The faceted surfaces reported on for CeO_2 are clear experimental evidence to the earlier modeling predictions by Sayle et al. [26,27] and Conesa [28]. These predictions suggested that {111} planes are the most energetically favorable for termination in the CeO_2 structure followed by {110} and {211}, while {100} plans are energetically unstable due to a net dipole moment normal to the surface. However, removal of 50% of the atoms from the outermost O^{2-} layer allows for the {100} surface to maintain a zero net dipole moment.

The appearance of the {111} and {100} surfaces in the perovskite structured $BaZrO_3$ has led us to briefly review the stability of these surfaces due to the important interest in $BaZrO_3$ nanoparticles in areas of electronics, fuel cells and as substrate materials. The surface terminations in the perovskite structure are a little more complicated than that of the fluorite structure of CeO_2. Illustrations of the (100), (110) and (111) surfaces viewed from both the top and tangentially as if perfectly cleaved are shown in Figs. 2.81 through 2.83, respectively. The (100) surface (Fig. 2.81) is an example of a type I surface which consists of layers that are charge neutral and have no net dipole moment in their repeating unit [29].

The (100) surface can either be a BaO-terminated surface or ZrO_2-terminated surface [30], though experimental evidence and theoretical calculations suggest that surface terminations incorporating the tetravalent species is typical for the $BaTiO_3$ and $SrTiO_3$ perovskites [30–34]. Ideally both surfaces are charge neutral and non-polar, though perovskites such as $SrTiO_3$ are not fully ionic creating weakly polar (100) surfaces [29]. The (100) surface has the lowest energy as it demonstrates the lowest coordination deficiency for its surface atoms, requiring no further modification to the charges at its surface or its stoichiometry in order to maintain a non-polar surface.

This is not the case for the (110) surface which consists of charged planes (O_2-BaZrO-O_2-BaZrO-) arranged symmetrically (Fig. 2.82) [35]. If the O_2 terminated (110) surface is ideally cleaved (as shown in the figure), it would have an infinite dipole moment perpendicular to the surface and therefore be unstable. Through removal of every other oxygen atom at the surface, the structure maintains a surface with charged planes but a zero net dipole moment in its repeating unit characteristic of a type-II surface.

The removal of the oxygen from the top surface layer maintains a chemical stoichiometry through the material as delineated by the dashed lines in Fig. 2.82. Atomistic structure calculations of the polar (110) surfaces in perovskite crystals have been studied considerably, in both the asymmetric configuration shown in Fig. 2.82 and for similar oxygen terminated and metal terminated configurations [35–37]. While the configuration presented in Fig. 2.82 possess one of the lowest calculated energies, the removal of half

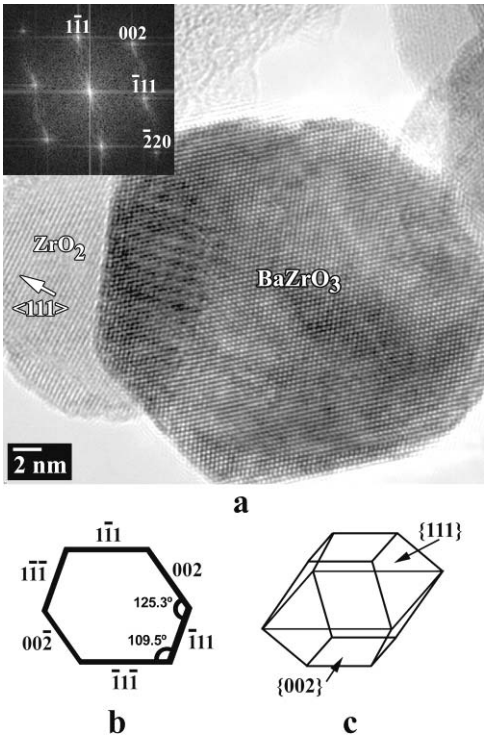

Fig. 2.79. (a) HREM image of $BaZrO_3$ particle. Inset: fast Fourier transformation of the lattice image. Schematic illustrations of (b) the [110] projection of the $BaZrO_3$ particle observed in the HREM image and (c) the three dimensional particle shape characterized as a truncated octahedral with eight {111} and two {002} surfaces.

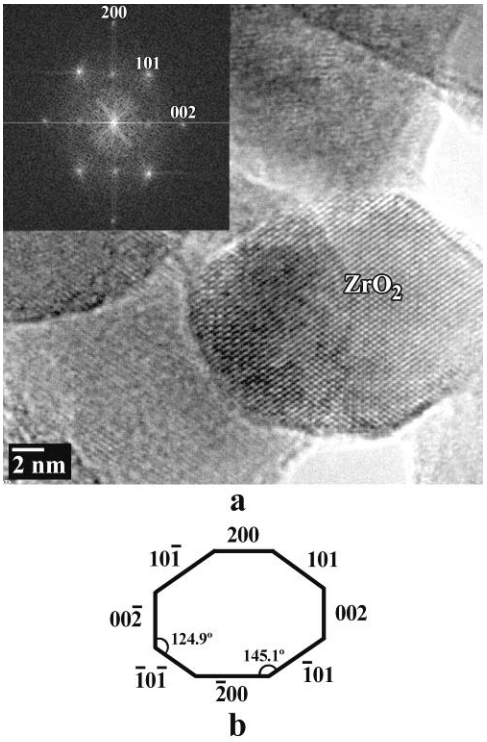

Fig. 2.80. (a) HREM image of a ZrO_2 particle aligned with its [010] parallel to the beam. Inset: fast Fourier transformation of the nonoverlapping portion of the lattice image. (b) Schematic illustrations of the [010] projection of the ZrO_2 particle shown in the HREM image.

of the oxygen atoms would disturb the balance of interatomic forces along the surface and is possibly the reason why it was not observed experimentally in this study. Though (110) surfaces have been experimental produced in $SrTiO_3$ following ultrahigh vacuum annealing, they consisted of reconstructed step ledge surfaces rather than a planar (1 × 1) surface structure [38–39].

The (111) surface consists of alternating polar layers of BaO_3^{4-} and Zr^{4+} [40] and is shown in Fig. 2.83 in both top and side views. Limited experimental and theoretical work is available on the structure of the (111) surface. Earlier experimental studies on $SrTiO_3$ have shown that stable (1 × 1) structures on (111) are possible when prepared by Ar bombardment and subsequent annealing at 600 K [41,42], with later work showing that the unreconstructed surface was stable up to 1373 K [43] with the top layer being either SrO_{3-x} or Ti terminated. Similarly, scanning tunneling microscopy observations on $BaTiO_3$ showed that (1 × 1) (111) surface was producible in Ar bombarded samples annealed at 1470 K in oxygen, though distinction as to BaO_3^{4-} or Ti^{4+} termination could not be made [44]. Different preparation conditions for $SrTiO_3$ surfaces

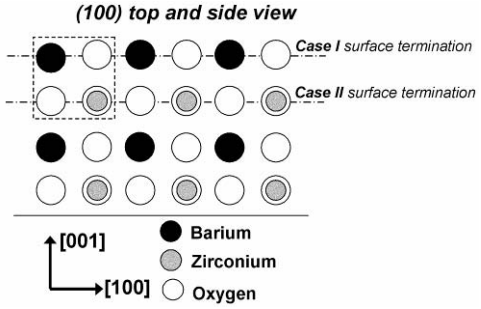

Fig. 2.81. $BaZrO_3$ perovskite structure. Termination of the (100) surface may either be on the BaO or ZrO_2 nonpolar layers. The repeating unit is outlined by the dashed box.

were found to yield reconstructed Ti-rich faces showing terraces and steps [45]. Theoretical investigation of the electronic and atomic structures of the $SrTiO_3$ (110) and (111) (1 × 1) surfaces using a total-energy, semiempirical Hartree-Fock method have been performed for various surface termination stoichiometry [46,47]. In this work, the stability of the various (110) and (111) surface terminations were examined in terms of surface energy. It was determined that for the (111) surfaces the surface energy was relatively independent of surface composition and was marginally higher than that for the (110) surfaces. It was also noted in their work that the surface energies were considerably lower than those of non-stoichiometric reconstructed surfaces. Though the (110) surfaces possessed a slightly lower energy in the calculations, the values of the surface energies are not indicative of the overall stability of the crystal and give no information as to which termination is the most stable under varying experimental conditions.

The appearance of the (111) surface on the $BaZrO_3$ nanoparticles in this investigation offers further experimental evidence for the stability of this surface in perovskite materials. In the particles that were observed through TEM, no evidence of a step-ledge or reconstructed surfaces was observed for the (100)
and (111) surfaces. Further work on evaluating these surfaces and examining possible termination structures is currently being investigated.

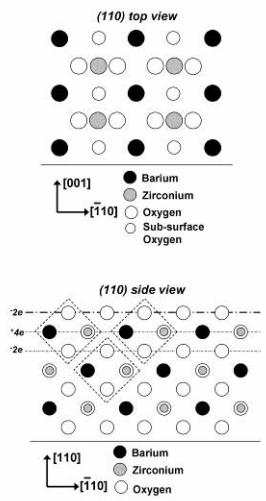

Fig. 2.82. Schematic views of the ideally cleaved (110) oxygen terminated surface of $BaZrO_3$. Side view reveals charged polar layers of O_2 and BaZrO producing an infinite dipole moment perpendicular to the surface unless 50% of the surface oxygen atoms are removed, resulting in a stoichiometrically correct zero dipole moment surface.

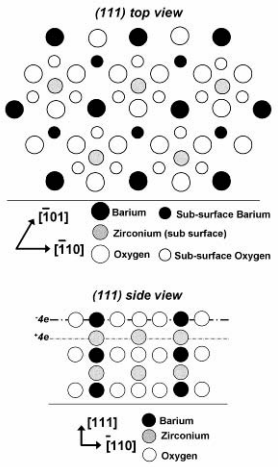

Fig. 2.83. Schematic views of the ideally cleaved (111) BaO_3^{4-} terminated surface of the $BaZrO_3$ crystal. The surface construction consists of layers of charged layers alternating between BaO_3^{4-} and Zr^{4+}.

2.16.4. Summary

Nanoparticles of the perovskite-structured $BaZrO_3$ were prepared through reverse micelle synthesis, a novel and cost-effective approach to produce nanoscale materials. The as-processed powder was a mixture of amorphous Ba-Zr-O and crystalline $Zr_{0.95}O_2$ particles with an average diameter of approximately 7.5 nm. Heat treatment of the powders to 700ºC in air for 0.5 h was sufficient to convert the material to crystalline $BaZrO_3$, though a minor quantity of ZrO_2 particles was still present. Average particle size of the heat-treated powder was increased to 17.3 nm. Both the crystalline $BaZrO_3$ and ZrO_2 particles exhibited a faceted morphology, with the shape of the $BaZrO_3$ particles exhibiting {100} and polar {111} surface terminations. In addition to observing the relatively stable {100}, the appearance of the {111} surface instead of {110} suggests a lower surface energy and more stable surface configuration.

2.16.5 References

1. M. Gotic, I. Czako-Nagy, S. Popovic,and S. Music, *Phil. Mag. Letters* **78**, 193–201 (1998).
2. J. E. Schaefer, H. Kisker, H. Kronmüller, R. Würschum, *Nanostructured Materials* **1(**6), 523–29 (1992).
3. S. D. Sartale and C.D. Lokhande, *Indian J. Eng. Mater. Sci.* 7, 404 (2000).
4. U. Erb, *Nanostructured Materials* **6(**5–8) 533–38 (1995).

5. S. Komarneni, M.C. D'Arrigo, C. Leionelli, G.C. Pellacani, and H. Katsuki, *J. Am. Ceramic Soc.* **81**, 3041 (1998).
6. A. Chatterjee, D. Das, S. K. Pradhan, and D. Chakravorty, *J. Magnetism and Magnetic Mater.* **127(**1–2) 214–18 (1993).
7. R. D. K. Misra, S. Gubbala, A. Kale, and W. F. Egelhoff, Jr., *Mat. Sci. and Eng.* **B111**, 164174 (2004).
8. T. Sugimoto and K. Kimijima, *J. Phys. Chem. B*, **107** 10753–59 (2003).
9. S. G. Dixit, A. R. Mahadeshwar, and S. K. Haram, *Colloids and Surfaces A: Physicochem. and Eng. Aspects* **133** 69–75 (1998).
10. M. C. McLeod, R. S. McHenry, E. J. Beckman, and C. B. Roberts, *J. Phys. Chem. B* **107**, 2693–2700 (2003).
11. W. Sun, L. Xu, Y. Chu, and W. Shi, *J. of Colloid and Interface Sci.* **266** 99–106 (2003).
12. M. Yuasa, G. Sakai, K. Shimanoe, Y. Teraoka, and N. Yamazoe, *J. of the Electrochemical Society* **151**(9), A1477–82 (2004).
13. J. H. Fendler, *Chem. Rev.* **87**, 877–99 (1987).
14. J. J. Urban, W. S. Yun, Q. Gu, and H. Park, *J. Am. Chem. Soc.* **124(**7), 1186–87 (2002).
15. A. Sin, B. El Montaser, P. Odier, and F. Weiss, *J. Amer. Ceramic Soc*. **85**(8), 1928–32 (2002).
16. Z. Lu, Y. Tang, L. Chen, and Y. Li, *J. of Crystal Growth* **266**, 539–44 (2004).
17. M. Paranthaman, S. S. Shoup, D. B. Beach, R. K. Williams, and E. D. Specht, *Mater. Res. Bulletin* **32**(12), 1697–1704 (1997).
18. J. L. Macmanus-Driscoll, S. R. Foltyn, Q. X. Jia, H. Wang, A. Serquis, L. Civale, B. Maiorov, M. E. Hawley, M. P. Maley, and D. E. Peterson, *Nature* **3**, 439–43 (2004).
19. D. Christen, *Nature* **3**, 421–22 (2004).
20. F. C. M. Woudenberg, W. F. C. Sager, N. G. M. Sibelt, and H. Verweij, *Adv. Mater.* **13**(7), 514–16 (2001).
21. S. S. Shankar, H. Joshi, R. Pasricha, N. R. Pavaskar, A. B. Mandale, and M. Sastry, *J. of Colloid and Interface Sci.*, **269**, 126–130 (2004).
22. P. Shen and W. H. Lee, *Nano Letters* **1**(12), 707–11 (2001).
23. F. Zhang, Q. Jin and S-W. Chan, *J. of Applied Physics* **95(**8), 4319–26 (2004).
24. L. Wu, H. J. Wiesmann, A. R. Moodenbaugh, R.F. Klie, Y. Zhu, D.O. Welch, and M. Suenaga, *Physical Review B* **69**, 125415 (2004).
25. S. Sathyamurthy, K. J. Leonard, R. T. Debastani, and M. P. Paranthaman, *Nanotechnology* (submitted 2005).
26. T. X. T. Sayle, S. C. Parker, and C. R. A. Catlow, *Surface Sci.* **316**, 329–36 (1994).
27. D. C. Sayle, T. X. T. Sayle, S. C. Parker, C. R. A. Catlow, and J. H. Harding, *Physical Review B*, **50**(19), 14498–505 (1994).
28. J. Conesa, *Surface Sci.* **339**, 337–52 (1995).
29. C. Noguera, *J. Phys.: Condens. Matter* **12**, R367–R410 (2000).
30. J. Padilla and D. Vanderbilt, *Physical Review B* **56(**3), 1625–31 (1997).
31. E. Heifets, R. I. Eglitis, E. A. Kotomin, J. Maier, and G. Borstel, *Surface Sci.* **513**, 211–20 (2002).
32. B. Cord and R. Courths, *Surface Sci.* **162**, 34–38 (1985).
33. T. Hikita, T. Hanada, M. Kudo and M. Kawai, *J. Vac. Sci. Technol. A* **11**, 2649–54 (1993).
34. T. Hikita, T. Hanada, M. Kudo, and M. Kawai, *Surface Sci.* **287–288**, 377–81 (1993).
35. E. Heifets, R. A. Evarestov, E. A. Kotomin, S. Dorfman, and J. Maier, *Sensors and Actuators B* **100**, 81–87 (2004).
36. E. A. Kotomin, E. Heifets, S. Dorfman, D. Fuks, A. Gordon, and J. Maier, *Surface Sci.* **566–568**, 231–35 (2004).
37. E. A. Kotomin, E. Heifets, J. Maier, and W. A. Goddard III, *Phys. Chem. Chem. Phys.* **5**, 4180–84 (2003).
38. J. Brunen and J. Zegenhagen, *Surface Sci.* **389**, 349–65 (1997).

39. H. Bando, Y. Aiura, Y. Haruyama, T. Shimizu, and Y. Nishihara, *J. Vac. Sci. Technol. B* **13**(3), 1150–54 (1995).
40. A. Asthagiri, C. Niederberger, A. J. Francis, L. M. Porter, P. A. Salvador, and D. S. Sholl, *Surface Sci.* **537**, 134–52 (2003).
41. W. J. Lo and G. A. Somorjai, *Phys. Rev. B* **17**, 4942–50 (1977).
42. S. Ferreer and G. A. Somorjai, *Surface Sci.* **94**, 41–56 (1980).
43. H. Tanaka and T. Kawai, *Surface Sci.* **365**, 437–42 (1996).
44. C. Hagendorf, K-M. Schindler, T. Doege, and H. Neddermeyer, *Surface Sci.* **402–04**, 581–5 (1998)
45. W. M. Sigmund, M. Rotov, Q. D. Jiang, J. Brunen, J. Zegenhagen,and F. Aldinger, *Applied Phys. A* **64**,219–20 (1997).
46. A. Pojani, F. Finocchi, and C. Noguera, *Appl. Surface Sci.* **142**, 177–81 (1999).
47. A. Pojani, F. Finocchi, and C. Noguera, *Surface Sci.* **442,** 179–98 (1999).

2.17 Growth of Rare Earth Niobate Based Pyrochlores on Textured Ni-W Substrates with Ionic Radii Dependency

M. S. Bhuiyan, M. Paranthaman, S. Sathyamurthy, D. B. Beach, and A. Goyal (ORNL); K. Salama (University of Houston)

Thin films with pyrochlore structures have been used as potential buffer layers for YBCO coated conductors, due to their thermal stability and their chemical and structural compatibility with the substrates and superconducting layers. Basic pyrochlores are ternary compounds with an $A_2B_2O_7$ stoichiometry, where A is a larger and trivalent cation and B is a smaller and tetravalent cation. The ideal pyrochlore structure possesses cubic symmetry with space group Fd3m, and there are eight molecules per unit cell. The pyrochlore structure, as shown in Fig. 2.84, is related to fluorite structure.

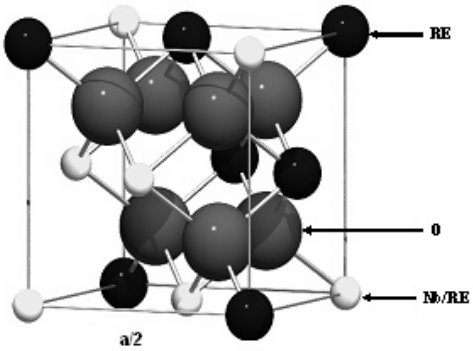

Fig. 2.84. Schematic of a pyrochlore structure (one-eighth of unit cell). Medium sphere represents RE^{3+} cation, small- Nb^{5+}/RE^{3+} cation and large- O^{2-}.

Pyrochlore structure (Fd3m) can be derived from the fluorite structure (Fm3m) by ordering the cation sub lattice and creating ordered oxygen vacancies in such a way that coordination of A atoms remains cubic, as in fluorite, but coordination of B cations decreases to octahedral. Ordering causes pyrochlore unit cell to double with respect to the fluorite unit cell. Due to the extensive compositional range of the compounds which exhibit the pyrochlore structure, there are a variety of actual and potential applications for these materials. Examples include dielectric materials, catalysts, solid electrolytes and thermal barrier coatings as well as actinide host phases for nuclear waste encapsulation. However, the phase stability for any $A_2B_2O_7$ pyrochlore compound (where A is a 3+ rare earth cation ranging in size from Lu^{3+} to La^{3+} and B is a 4+ cation ranging in size from Ti^{4+} to Pb^{4+}) is not well characterized. It was demonstrated that rare earth (RE) containing titanates and zirconates, $A_2B_2O_7$ pyrochlore with R_A/R_B (R = ionic radius) from 1.45 to 1.80 crystallize in the pyrochlore structure, where these pyrochlores were prepared as powders from solid-state synthesis and as single crystals grown from PbF_2 flux. Bulk superconductivity with a T_c = 9.6 K was reported in a pyrochlore-related oxide KOs_2O_6.

The pyrochlore structure under study has the chemical formula A_3BO_7, where A (Lu to La) is a larger trivalent and B (Nb) is a smaller pentavalent cation. If we consider one-eight of a pyrochlore unit cell then A cations are occupying the face centered position and the B cations the corner position. Of the pyrochlores there exists selected phase diagram of the compound Y_3NbO_7 from the series of A_3BO_7. A pyrochlore solid solution region having a nominal composition 3 Y_2O_3.Nb_2O_5 was found between 20 and

31.5% Nb_2O_5 and no solid solubility of Y_2O_3 in Nb_2O_5 was found. No study of pyrochlore phases, regarding ionic radii dependency, in the form of thin film have been reported so far.

Here we report the successful growth of epitaxial films of rare earth niobates, RE_3NbO_7, on Ni-W substrates and its ionic radius dependency on the formation of pyrochlore structure. Various rare-earth oxides and rare-earth pyrochlore films have been grown epitaxially on biaxially textured Ni and Ni-3 at.% W (Ni-W) substrates by solution-based methods as buffer layers for YBCO coated conductors. Since chemical solution based deposition of buffer layers are potentially lower cost, we believe that the solution-deposited RE_3NbO_7 films with good epitaxy and lattice matching to Ni-W and YBCO are potential candidates for buffer layers for coated conductors.

The precursor solutions for the rare-earth niobates were prepared using two different routes, namely sol-gel and MOD, depending on the solution chemistry. By the sol-gel precursor route, La, Y, Eu, and Gd niobates were prepared; by the MOD precursor route, Ce, Nd, Sm, Ho, and Yb niobates were prepared. All solution manipulations for sol-gel precursors were carried out under an atmosphere of argon using standard Schlenk techniques, and the starting reagents were weighed in an argon-filled, inert-atmosphere glove box. The chemical reagents La isopropoxide (Alfa, La 40%), Y isopropoxide (Alfa, 92–95%), niobium ethoxide (Alfa, 99.999%) and 2-methoxyethanol (Alfa, spectrophotometric grade) were used as received from Alfa Aesar, whereas Eu acetate and Gd acetate were purified beforehand. For the purification of Eu acetate, first, Eu acetate was prepared by the reaction of europium oxide (Alfa, 99.99%) with a fivefold excess of 25% acetic acid at 80°C for 1 h. The resulting clear solution was filtered, and the solvent was removed. The precipitate was dried at 120°C under dynamic vacuum for 16 h. A small amount of sample was allowed to react with excess water and then was dried to constant weight at 35°C to form the hydrated sample. The weight gain of this sample allowed us to estimate that the degree of hydration of the europium acetate after vacuum drying was about 1.5 ± 0.2. A similar procedure was followed for the purification of Gd acetate.

Europium methoxyethoxide solution in 2-methoxyethanol was prepared by charging a flask with 0.987 g of europium acetate and 10 mL of 2-methoxyethanol. The flask was refluxed for 1 h at 130°C, and 0.318 g of niobium ethoxide was added. The contents were rediluted with additional 2-methoxyethanol, and the distillation/redilution cycle was repeated twice more to ensure complete formation of europium methoxyethoxide. The final concentration was adjusted to produce 10 mL of a 0.50 M stock solution.

All the MOD precursor solutions were prepared in ambient atmosphere. The reagents Ce acetylacetonate (Alfa, hygroscopic), Nd acetylacetonate (Alfa, 99.9%), Sm acetate (Alfa, 99.9%), Ho acetate (Alfa, 99.9%), Yb acetylacetonate (Alfa, 99.9%), niobium ethoxide (Alfa, 99.999%), acetic acid (Alfa, 99.9985%), and methanol (Alfa, 99.9%) were used as received from Alfa Aesar. The precursor solution for Ce niobate was prepared by dissolving 0.656 g of Ce acetylacetonate in acetic acid and methanol with continuous stirring for 10 min in a hot plate at 60°C. Then 0.16 g of Nb ethoxide was added, and the final volume of the solution was adjusted to obtain 0.4 M precursor solution. The chemical reagents, solvents, and the molarities for all the precursors are listed in Table 2.10. These solutions were spin-coated onto short (2 × 1 cm), cube-textured Ni-W substrates at 4000 rpm for 30 s, followed by heat treatment in a reducing atmosphere of Ar-4% H_2. After a 5-min purge with Ar-4% H_2 gas mixture at room temperature, the samples were introduced into a preheated furnace. At the end of heat treatment cycle, the samples were quenched to room temperature in the same atmosphere. The heating and cooling rates were in the range of 350 to 400°C/min, annealing time 15~30 min; the annealing temperatures were about 1050 to 1100°C. Except for Eu niobate, which was heat treated at 1050°C for 15 min due to the phase instability at higher temperature, all the other niobates were heat-treated at 1100°C for 15 to 30 min.

The RE_3NbO_7 films were characterized by using XRD for phase purity and texture, SEM for homogeneity and microstructure, and AFM for surface roughness analysis. A Philips model XRG3100 diffractometer with CuKα radiation was used to record the θ–2θ XRD patterns. The texture analysis was performed using a Picker four-circle diffractometer. Phase analysis was done using XRD patterns, and the lattice parameters were determined using the MDI-JADE 6 program. The microstructure analyses of these

Table 2.10. Starting chemicals, solvents, and molarities for the RE_3NbO_7 precursors

Rare-earth niobates, RE_3NbO_7 (RE)	Chemical reagents	Stoichiometric quantity (g)	Solvent and reactant	Final molarity (M)
La	La-isopropoxide/Nb-ethoxide	1.1857/0.398	2 methoxyethanol	0.5
Ce	Ce-acetylacetonate/Nb-ethoxide	0.656/0.16	Acetic acid and Methanol	0.4
Nd	Nd-acetylacetonate/Nb-ethoxide	0.662/0.16	Acetic acid and Methanol	0.4
Sm	Sm-acetate/ Nb-ethoxide	0.5783/0.16	Acetic acid and Methanol	0.4
Eu	Eu-acetate/ Nb-ethoxide	0.9873/0.318	2 methoxyethanol	0.4
Gd	Gd-acetate/ Nb-ethoxide	1.003/0.318	2 methoxyethanol	0.4
Ho	Ho-acetate/ Nb-ethoxide	0.415/0.12	Acetic acid and Methanol	0.3
Y	Y-isopropoxide/Nb-ethoxide	0.998/0.398	2 methoxyethanol	0.5
Yb	Yb-acetylacetonate/Nb-ethoxide	0.9587/0.199	Acetic acid and Methanol	0.5

samples were performed using a Hitachi S-4100 field emission SEM and Digital Instruments nanoscope AFM in contact mode.

X-ray diffraction data for the solution deposited RE_3NbO_7 films grown on Ni-W substrates were collected at room temperature. From the XRD data, it was found that the niobates of Sm, Eu, Gd, Ho, Y and Yb grow epitaxially with pyrochlore structure, whereas the niobates of Ce and Nd crystallize without any preferred orientation and the La niobate decomposes to mixed phases of $LaNbO_4$ and La_2O_3 under the experimental conditions used. Although these phases are stable between 800 and 1100°C, Eu_3NbO_7 partially decomposes to Eu_2O_3 and Nb_2O_5 at temperature above 1050°C. Room-temperature XRD patterns for the pyrochlore phase RE_3NbO_7 thin films deposited on Ni-W substrates are shown in Fig. 2.85. Due to highly *c*-axis (004) oriented films there are no (222) peaks present in the patterns. There is a clear indication of (004) peak shifting to the right as a result of decreasing ionic radii of the rare earth elements. Therefore, the lattice parameters of the pyrochlore phase increases with increase in ionic radii.

Figure 2.86, shows the cell parameters of the RE_3NbO_7 pyrochlore as a function of the ionic radius ratio, and as expected, the cell parameters increase linearly with ionic radius. The data in Fig. 2.86 are the actual experimental values calculated from the XRD patterns using MDI-JADE 6 program. From the linear equation shown inside the graph, cell parameters for other RE_3NbO_7 pyrochlores can be easily calculated. From Sm to Yb niobates the cell parameter decreases from 10.7204 Å to 10.3894 Å, which is about a 3% decrease.

To grow a textured film using chemical solution deposition, a highly textured substrate is very important. Cube-textured Ni-W substrates serve the purpose with an excellent in-plane (phi scan) and out-of-plane (omega scan) texture of about 8.0° and 5.77° FWHM, respectively. All the RE_3NbO_7 films grown by solution deposition on Ni-W substrates have the out-of-plane texture with FWHM value in the range of 6.25 to 8° and the in-plane texture in the range of 8.0 to 9.35°. The ω (out-of-plane) and ϕ (in-plane) scans of Eu_3NbO_7 films on the Ni-W substrates are shown in Fig. 2.87. The Eu_3NbO_7 film has a good out-of-plane and in-plane texture with FWHM of 6.26° and 8.67°, respectively. These values are well comparable to those of Ni-W substrates ($\Delta\omega = 5.77°$, $\Delta\phi = 8.0°$). A list of FWHM values for the RE_3NbO_7 films is given in Table 2.11.

The typical (222) pole figures for all the six RE_3NbO_7 films grown on the Ni-W substrate are shown in Fig. 2.88, which indicates single cube-on-cube epitaxy. Microstructure studies of the RE_3NbO_7 films

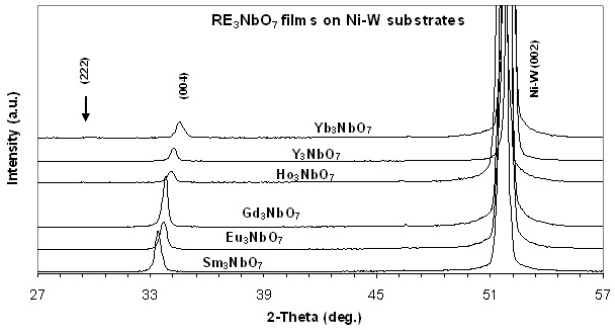

Fig. 2.85. A typical θ-2θ scan for RE_3NbO_7 (RE = Sm, Eu, Gd, Ho, Y, and Yb) films grown on biaxially textured Ni-W substrates using chemical solution deposition. RE_3NbO_7 films have preferred c-axis orientation.

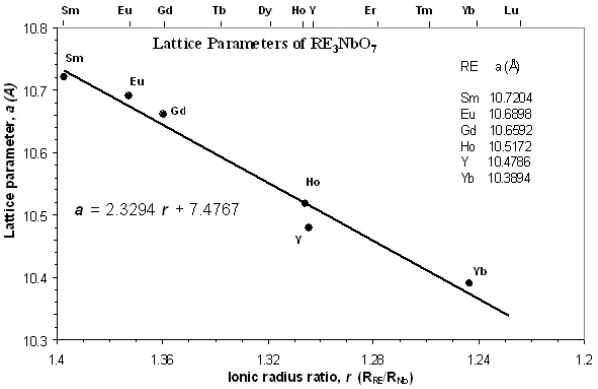

Fig. 2.86. Lattice parameters of the solution-grown RE_3NbO_7 films on Ni-W substrates. All data points represent experimental value calculated by MDI-JADE6 software.

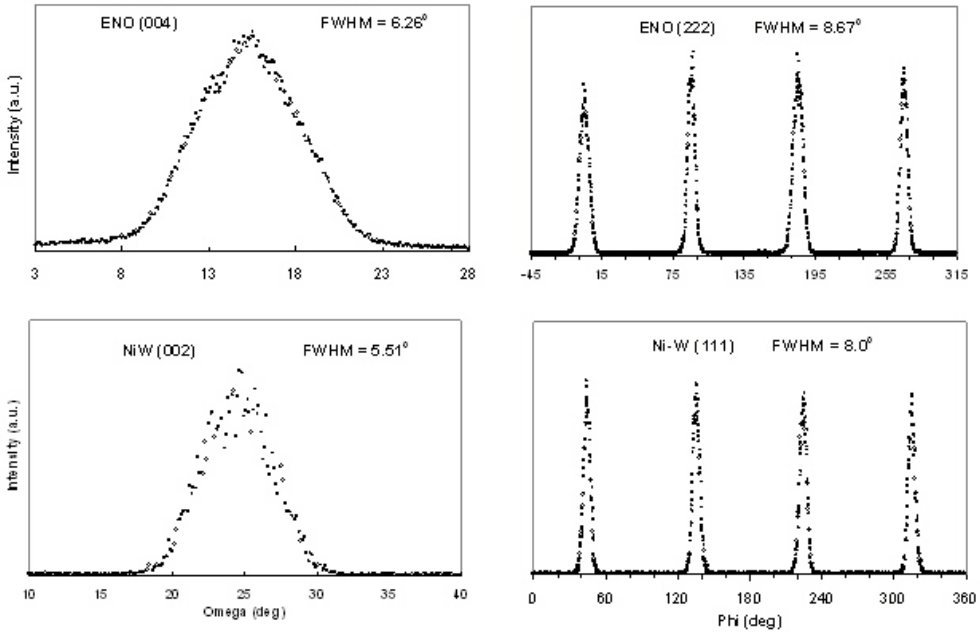

Fig. 2.87. The ω and ϕ scans obtained for a 80-nm-thick Eu_3NbO_7 film grown on textured Ni-W substrate. The FWHM values for each scan are shown inside the patterns.

exhibit a uniform, smooth, and crack-free surface morphology. As an example, a SEM micrograph for Eu_3NbO_7 film on rolled Ni-W substrate using spin-coating is shown in Fig. 2.89(a). Most of the Ni-W grain boundary grooves on the Ni-W surface were found to be well covered. Figure 2.89(a) also shows that the film surface is continuous as well as crack free. An AFM image of the same sample is shown in Fig. 2.89(b). It reveals a root-mean-square roughness of the Eu_3NbO_7 film as 1.6 nm.

Lattice matching between the substrates and the films play a key role in the epitaxial growth. The pseudo cubic cell parameters for the RE_3NbO_7 films closely follow that of the Ni-W substrates as shown in the comparative Table 2.12. Since, the films were grown epitaxially with a 45° rotation with respect to the substrates, the pseudo cubic cell parameters were calculated by dividing cubic cell parameter with $2\sqrt{2}$. The percentage lattice mismatch between these films and the substrates is 4 to 8%. The lattice mismatch between the niobate buffers and YBCO is much smaller and in the range of -0.5 to -4%, which

Table 2.11. Texture data of RE niobate films on Ni-W substrates

Rare-earth niobates	FWHM of RE_3NbO_7		FWHM of Ni-W substrates	
	ω scans (deg.) (004)	ϕ scans (deg.) (222)	ω scans (deg.) (002)	ϕ scans (deg.) (111)
Sm_3NbO_7	7.47	9.35	5.4	7.61
Eu_3NbO_7	6.26	8.67	5.77	8.0
Gd_3NbO_7	7.15	8.0	5.47	6.7
Ho_3NbO_7	8.0	8.92	5.4	7.62
Y_3NbO_7	7.72	8.23	5.47	6.7
Yb_3NbO_7	7.21	8.58	5.66	7.91

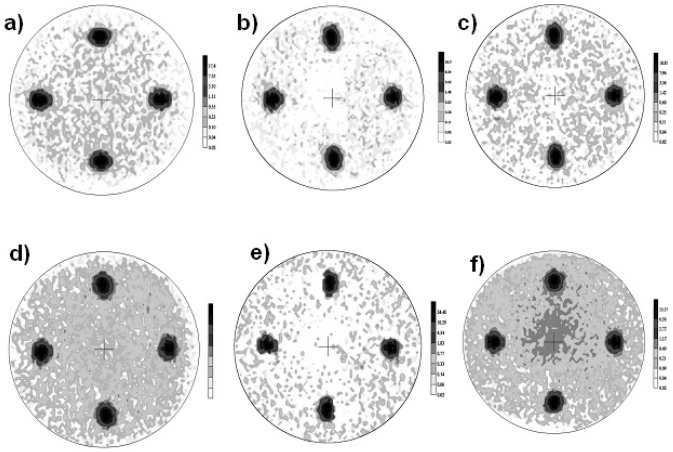

Fig. 2.88. Typical (222) log scale pole figures.
(a) Sm_3NbO_7, (b) Eu_3NbO_7, (c) Gd_3NbO_7, (d) Ho_3NbO_7, (e) Y_3NbO_7, and (f) Yb_3NbO_7 films grown on textured Ni-W substrate.

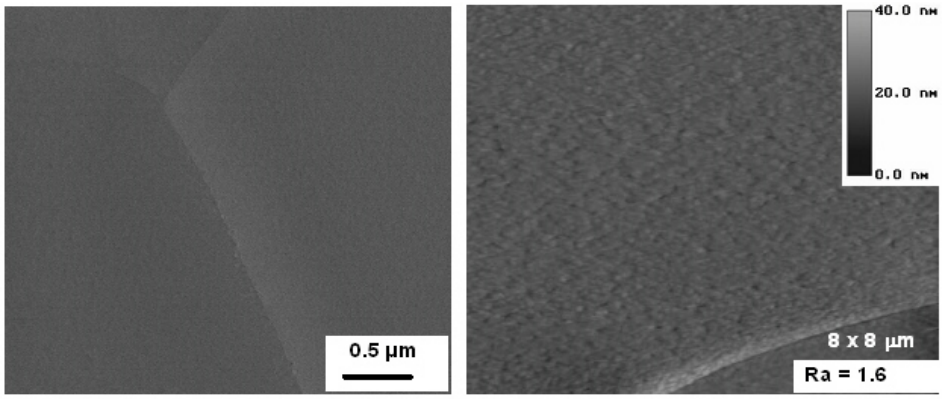

Fig. 2.89. 80-nm-thick Eu_3NbO_7 film surface. (a) SEM micrograph and (b) AFM image.

Table 2.12. List of lattice parameters for RE_3NbO_7
(Ni; a = 3.524 Å, YBCO; a = 3.823 Å, b = 3.887 Å, c = 11.68 Å)

Rare-earth niobates	Lattice parameter, a (Å)	Pseudo lattice parameter, a/2√2 (Å)	Lattice mismatch vs Ni (%)	Lattice mismatch vs YBCO (%)
Sm_3NbO_7	10.720	3.790	7.56	-0.85
Eu_3NbO_7	10.690	3.779	7.25	-1.14
Gd_3NbO_7	10.659	3.769	6.95	-1.42
Ho_3NbO_7	10.517	3.718	5.52	-2.74
Y_3NbO_7	10.479	3.705	5.13	-3.1
Yb_3NbO_7	10.389	3.673	4.23	-3.92

unfolds the possibility for RE_3NbO_7 films as a potential buffer layers for coated conductor. Efforts are under way to deposit YBCO by PLD/MOD technique on these films. As an initial demonstration, a YBCO film with a critical current density of 1.1×10^6 A/cm^2 in self-field at 77 K has been grown on single Gd_3NbO_7-buffered Ni-W substrate using pulsed laser deposition.

We have grown textured RE_3NbO_7 (RE = Sm, Eu, Gd, Ho,Y and Yb) films on cube textured Ni-W substrates using chemical solution deposition, and we demonstrated the strong dependency of epitaxy on the ionic radii of the rare earth elements. Niobates of the rare earth elements with an ionic radius ratio, r < 1.40, grow as an epitaxial pyrochlore phase on Ni-W substrates. Microstructure studies reveal a continuous, smooth, dense, and crack-free surface of the films deposited on rolled Ni substrates using solution process. Such epitaxial, dense, and crack-free RE_3NbO_7 buffer layers may be suitable buffer candidates for YBCO coated conductors.

3. Summary of Technology Partnership Activities

3.1 Background

Oak Ridge National Laboratory (ORNL) is a key participant in the U.S. Department of Energy's (DOE's) national effort on electric power applications of high-temperature superconductivity (HTS). ORNL has formed effective teams that combine the resources of the Laboratory with the entrepreneurial drive of private companies. New technology partnership mechanisms, a feature of the ORNL Superconducting Technology Program for Electric Power Systems since its inception in 1988, have resulted in 42 superconductivity "pilot center" cooperative agreements and 17 cooperative research and development agreements (CRADAs). Ten cooperative agreements and two interagency agreements were active during FY 2005. In addition, licensing agreements, joint inventions, and joint publications with the private industry partners have ensured that there *is* technology transfer throughout the program.

Technology partnering on Laboratory-industry teams can occur in several ways. In the ORNL program, the cooperative development level of technology partnering is emphasized: joint Laboratory-industry teams work on problems that (1) require combined resources and expertise and (2) have a clear objective of precompetitive research and technology development. For the project to succeed, each partner depends on the success of the other. Most of the cooperative projects with private industry and the Laboratory precompetitive research and development (R&D) projects involve developing key technology in which commercialization of the results is expected to occur after a minimum of 3 to 5 years.

3.2 Relationship to the DOE Mission

The ORNL program mission is that of its program sponsor, DOE's Office of Electricity Delivery and Energy Reliability Superconductivity Program: to develop the technology base necessary for industry to proceed to commercialization of electric energy applications of HTS. HTS will enable new energy-efficient motors, transformers, and transmission lines and will also provide electric power equipment manufacturers with strategic technology for global competitiveness. Electric utilities can defer acquisition of new transmission rights-of-way with successful introduction of superconducting cables. System stability and protection will be enhanced with the introduction of fault-current limiters. Distributed utility systems in the future, which will include distributed generation systems, will benefit from the small size and light weight of the next generation of electric power equipment. In addition, oil-free power transformers and cables will provide a cost-effective, more environmentally friendly option for the utility sector.

3.3 Funding

DOE funding for the ORNL program and a summary of funds-out cooperative agreements in 2005 are shown in Table 3.1. Funds-out to industry, universities, and other federal agencies (e.g., the National Institute of Standards and Technology) was more than $3 million in FY 2005.

3.4 Technology Partnership Approach

An interdisciplinary approach uses many of the resources available at ORNL to meet the program goals for joint Laboratory-industry development of HTS technology for electric power applications. The superconductivity agreement mechanism interlinks R&D projects with industry and universities that optimize utilization of facilities, expertise, and program resources for the benefit of all participants. This program also coordinates the ORNL activities with the other national laboratories, government agencies, university centers, and industry groups.

Cooperative agreements ensure that technology development is industry-driven. The ORNL Office of Technology Transfer and Economic Development and patent counsel work together to place these agreements. Where appropriate, these efforts are coordinated with projects within ORNL that are funded by the DOE Office of Science as well as Work for Others and ORNL Laboratory Director's R&D Fund projects.

Effective funds-out to industry is used to supplement industry cost share. In FY 2005, $3 million in funds-out to industry and universities was provided through cooperative agreements and subcontracts. To keep industry involved from the start of the program and to ensure commercialization potential, all of these technology-partnering mechanisms are augmented by CRADAs, user agreements, and licensing activities.

Responsiveness to American industry has high priority in this program. An ORNL ad hoc technical review committee, consisting of a project manager, a scientific coordinator, a manager for conductor development, and a manager for applications development, reviews all inquiries from industry and recommends projects for possible funding. This review ensures that (1) the proposed work fits the program mission, (2) the work is collaborative, (3) there is legitimate commercial interest, and (4) the work is feasible. Substantial private-sector cost share is required on cooperative agreements.

ORNL provides support to the DOE Headquarters (DOE-HQ) Superconductivity Program for Electric Power Systems by identifying, guiding, and monitoring R&D at ORNL and ORNL subcontractor sites and by performing coordination, analysis, and planning of activities related to the national program.

ORNL works with the other program laboratories to address such issues as communication among program participants, workshop and meeting implementation, planned competitive solicitations and superconductivity agreements, and coordination of technical and economic assessments. ORNL leads the Superconductivity Partnerships with Industry Technical Review Committee and manages the Cryogenics Initiative subcontracts on behalf of all the program stakeholders.

3.5 Program Inventions

A summary of the new invention disclosures for FY 2005 is shown in Table 3.2. Patents issued in FY 2005 are shown in Table 3.3, and all patents issued since 1994 are shown in Table 3.4.

Table 3.1. Superconductivity Program summary of cooperative agreements as of September 30, 2005

Participant	Approved term	Type[a]	Total agreement cost share ($K)			Technology Area
			By DOE		By industry	
			To ORNL	To Industry		
American Superconductor	4/5/01–4/4/06	C	2,400	0	2,400	HTS conductors for electric power applications; Wire Development Group; and YBCO wires
American Superconductor	8/29/05–5/29/06	C(FI)	0	0	99	Low-cost fabrication of 2G wire for ac applications
General Electric Company	8/2/02–7/08	C	1,050	0	1,050	Design and development of a 100-MVA HTS generator
Metal Oxide Technologies	7/5/05–7/4/07	C	370	0	425	Develop HTS research targeted to power intensive commercial applications
NIST-Gaithersburg	12/1/00–12/31/05	IAG	0	1,110	1,110	YBCO phase diagram support
NIST-Boulder	3/98–2/29/07	IAG	0	1,497	1,497	Electromechanical properties for superconductor applications
Oxford Instruments	1/94–12/31/05	C	1,450	0	1,675	Develop technology for dip-coated BSCCO-2212 wire and RABiTS
Reliance Electric Company	8/12/05–8/11/06	C	75	0	75	HTS Motor Coil Quench Model
Southwire Company	2/1/97–9/30/06	FO	12,066	500	12,631	Develop HTS cable technology
SuperPower, Inc.	10/8/02–9/30/06	C	500	0	500	Produce high current density YBCO coated conductors
SuperPower, Inc.	07/01/04–02/28/07	C	850	0	850	Matrix fault current limiter SPI
Waukesha Electric Systems	6/15/97–9/30/06	FO	3,197	250	2,556.4	HTS transformer
Total active agreements			21,958	3,357	24,868	
Total completed agreements			16,104	5,845.6	20,807.7	
Totals			38,062	9,203	45,676	

[a]NFE = no-funds-exchange; FO = funds-out; FI = funds-in; IAG = interagency agreement; and C = CRADA.

Table 3.2. Invention disclosures during FY 2005

I.D. No.	Title	Inventor
1556	Method to fabricate a low aspect ratio substrate for epitaxial growth of materials	A. Goyal
1557	Graphite fiber reinforced Cu alloy composites for overhead transmission conductor cores	A. Goyal
1590	Novel process for fabrication of high flux-density transformer core materials	A. Goyal
1594	Novel method for fabrication of cost-effective, high performance hydrogen membrane fuel cell	A. Goyal

Table 3.3. Patents issued in FY 2005

Patent No./ID No.	Date Issued	Title
2 217 822 Canadian (1640-X)	November 23, 2004	Structures Having Enhanced Biaxial Texture and Method of Fabricating Same
6,846,344 B2 (316.07)	January 25, 2005	Biaxially Textured Articles Formed by Powder Metallurgy
03601830 Japan (1640-X)	October 1, 2004	Structures Having Enhanced Biaxial Texture and Method of Fabicating Same
6,890,369 B2 (316.6)	May 10, 2005	Biaxially Textured Articles Formed by Powder Metallurgy
6,902,600 B2	June 7, 2005	Biaxially Textured Articles Formed by Powder Metallurgy

Table 3.4. Cumulative listing of patents

Patent No./ID No.	Date Issued	Title
5,357,756 (1185-X)	October 25, 1994	Bipolar Pulse Field for Magnetic Refrigeration
5,395,821 (1039-X)	March 7, 1995	Method of Producing Pb-Stabilized Superconductor Precursors and Method of Producing Superconductor Articles Therefrom
5,525,583 (1471-X)	June 11, 1996	Superconducting Magnetic Coil (with AMSC)
5,546,261	August 13, 1996	Hermetically Sealed Superconducting Magnet Motor
5,646,097	July 8, 1997	Method of Fabricating a (1223) Tl-Ba-Ca-Cu-O Superconductor
5,739,086 (1640-X)	April 14, 1998	Structures Having Enhanced Biaxial Texture and Method of Fabricating Same
5,741,377 (1640-X)	April 21, 1998	Structures Having Enhanced Biaxial Texture and Method of Fabricating Same
5,830,828 (1193-X)	November 3, 1998	Process for Fabricating Continuous lengths of Superconductor
5,846,912 (1512-X)	December 8, 1998	Method for Preparation of Textured $YBa_2Cu_3O_x$ Superconductor
5,898,020 (1640-X)	April 27, 1999	Structures having Enhanced Biaxial Texture and Method of Fabricating Same
5,958,599 (1640-X)	September 28, 1999	Structures Having Enhanced Biaxial Texture
5,964,966	October 12, 1999	Method of Forming Biaxially Textured Alloy Substrates and Devices Thereon
5,968,877 (18-19)	October 19, 1999	High Tc YBCO Superconductor Deposited on Biaxially Textured Ni Substrate
5,972,847 (458)	October 26, 1999	Method for Making High-Critical-Current-Density $YBa_2Cu_3O_7$ Superconducting Layers on Metallic Substrates.
6,055,446 (1193)	April 25, 2000	Continuous Lengths of Oxide Superconductors
6,077,344 (223)	June 20, 2000	Sol-Gel Deposition of Buffer Layers on Biaxially Textured Metal Substances
6,106,615 (368)	August 22, 2000	Method of Forming Biaxially Textured Alloy Substrates and Devices Thereon
6,114,287 (534) (HTSPC-023)	September 5, 2000	Method of Deforming a Biaxially Textured Buffer Layer on a Textured Metallic Substrate and Articles Therefrom
6,150,034 (467)	November 21, 2000	Buffer Layers on Rolled Nickel, or Copper as Superconductor Substrates
6,156,376 (467)	December 5, 2000	Buffer Layers on Metal Surfaces having Biaxial Texture as Superconductor Substrates
6,159,610 (467)	December 12, 2000	Buffer Layers on Metal Surfaces having Biaxial Texture as Superconductor Substrates
6,180,570 B1 (312)	January 30, 2001	Biaxially Textured Articles Formed by Plastic Deformation
6,256,521 B1 (1784, new 148)	July 3, 2001	Preferentially Oriented, High Temperature Superconductors by Seeding and a Method for their Preparation
6,261,704 B1 (218)	July 17, 2001	MGO Buffer Layers on Rolled Nickel or Copper as Superconductor Substrates
6,270,908 B1 (734)	August 7, 2001	Rare Earth Zirconium Oxide Buffer Layers on Metal Substrates
6,286,194 B (1193)	September 11, 2001	Apparatus for Fabricating Continuous Lengths of Superconductor
6,296,701 B1 (296)	October 2, 2001	Method of Depositing An Electrically Conductive Oxide Film on a Textured Metallic Substrate and Articles Formed Therefrom
6,331,199 B1	December 18, 2001	Biaxially Textured Articles Formed by Powder Metallurgy
6,375,768 B1 (312)	April 23, 2002	Method for Making Biaxially Textured Articles by Plastic Deformation
6,385,835 B1	May 14, 2002	Apparatus for Fabricating Continuous Lengths of Superconductor

Table 3.4 (continued)

Patent No./ID No.	Date Issued	Title
6,399,154 B1 (734)	June 4, 2002	Laminate Article
6,440,211 B1 (649)	August 27, 2002	Method of Depositing Buffer Layers on Biaxially Textured Metal Substrates
6,447,714 B1 (316)	September 10, 2002	Method for Forming Biaxially Textured Articles by Powder Metallurgy
6,451,450 B1 (749)	September 17, 2002	Method of Depositing a Protective Layer over a Biaxially Textured Alloy Substrate and Composition Therefrom
6,468,591 (218)	October 22, 2002	Method for making MgO buffer layers on rolled nickel or copper as superconductor substrates
6,486,100 B1	November 26, 2002	Method for Preparing Preferentially Oriented, High Temperature Superconductors Using Solution Reagents
6,555,256 B1	April 29, 2003	Method of Depositing an Electrically Conductive Oxide Film on a Textured Metallic Substrate and Articles Formed Therefrom
6,599,346 B2 (316.3)	July 29, 2003	Biaxially Textured Articles Formed by Powder Metallurgy
6,602,313 B2 (316.2)	August 5, 2003	Biaxially Textured Articles Formed by Powder Metallurgy
6,607,839 B2 (316.9)	August 19, 2003	Biaxially Textured Articles Formed by Powder Metallurgy
6,610,413 (316.5)	August 26, 2003	Biaxially Textured Articles Formed by Powder Metallurgy
6,610,414 (316.11)	August 26, 2003	Biaxially Textured Articles Formed by Powder Metallurgy
6,617,283 B2 (889)	September 9, 2003	Method of Depositing an Electrically Conductive Oxide Buffer Layer on a Textured Substrate and Articles Formed Therefrom
6,635,097 B2 (316.4)	October 21, 2003	Biaxially Textured Articles Formed by Powder Metallurgy
6,645,313 B2 (1697-X)	November 11, 2003	Powder-in-Tube and Thick-Film Methods of Fabricating High Temperature Superconductors having Enhanced Biaxial Texture
6,663,976 B2 (649.2)	December 16, 2003	Laminate Articles on Biaxially Textured Metal Substrates
6,700,297 B2	March 2, 2004	Superconducting PM Undiffused Machines with Stationary Superconducting Coils
6,716,795 B2 (726.2)	April 6, 2004	Buffer Architecture for Biaxially Textured Structures and Method of Fabricating Same
6,740,421 B1 (1205)	May 25, 2004	Rolling Process for Producing Biaxially Textured Substrates
6,764,770 B2 (1047)	July 20, 2004	Buffer Layers and Articles for Electronic Devices
6,784,139 B1 (375)	August 31, 2004	Conductive and Robust Nitride Buffer Layers on Biaxially Textured Substrates
6,790,253 B2 (316.13)	September 14, 2004	Biaxially Textured Articles Formed by Powder Metallurgy
6,797,030 (316.12)	September 28, 2004	Biaxially Textured Articles Formed by Powder Metallurgy
2 217 822 Canadian (1640-X)	November 23, 2004	Structures Having Enhanced Biaxial Texture and Method of Fabricating Same
6,846,344 B2 (316.07)	January 25, 2005	Biaxially Textured Articles Formed by Powder Metallurgy
03601830 Japan (1640-X)	October 1, 2004	Structures Having Enhanced Biaxial Texture and Method of Fabicating Same
6,890,369 B2 (316.6)	May 10, 2005	Biaxially Textured Articles Formed by Powder Metallurgy
6,902,600 B2	June 7, 2005	Biaxially Textured Articles Formed by Powder Metallurgy

4. Events, Honors, and Awards

4.1 Amit Goyal Edits Book on Second-Generation High-Temperature Superconductors

Amit Goyal, team leader in the ORNL Superconductivity Program and member of the Metals and Ceramics Division Functional Materials Group, is the editor of *Second Generation HTS Conductors*, the first book to be published on this important class of HTS conductors (Fig. 4.1). The book summarizes the progress to date in the entire field as well as future research directions. It is an excellent reference for people working in this research area. Plenum Corporation (Kluwer Academic Publishers) invited Goyal to put the book together by seeking input from international leaders in the field. Several chapters were written by fellow ORNL staff members in the Superconductivity Program.

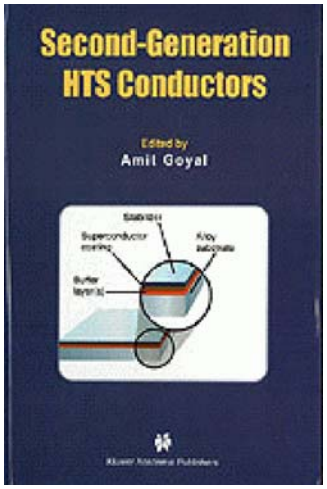

Fig. 4.1. *Second-Generation High-Temperature Superconductors*, published in FY 2005, is the first book in the field.

4.2 Team Members Elected Fellows

Amit Goyal and Parans Paranthaman (Fig. 4.2) were elected fellows by professional organizations in FY 2005. Goyal is one of four ORNL staff members to be elected fellows of the American Association for the Advancement of Science. The election of fellow is the highest honor of the association, which is the world's largest general scientific society and publisher of the journal *Science*. The association's mission is to advance science through policy initiatives, international programs, science education, and related avenues. Goyal is honored for his distinguished contributions to the field of high-temperature superconductivity and for the invention and development of the Rolling-Assisted Biaxially Textured Substrates (RABiTS™) process.

Fig. 4.2. Amit Goyal and Parans Paranthaman.

Goyal was also named a consulting fellow of the World Innovation Foundation (WIF). The WIF was founded by the late Glenn Seaborg, a Nobel Laureate. The current president is Nobel Laureate Jerome Karle. The WIF is an international, multidisciplinary consultative research group that advises nations and their governments. Currently, the WIF has about 2000 members and fellows throughout the world, including 57 Nobel laureates. For each governmental or major international topic, about 30 members and

fellows will undertake consultations in concert but separately over a period of 8 weeks to provide their personal input.

Parans Paranthaman, task leader of the HTS Chemistry Projects in the ORNL Superconductivity Program, is one of three ORNL staff members to be elected fellows of the Institute of Physics, based in London. He was elected in recognition of his status in the physics community as the co-inventor of the RABiTS™ technology to fabricate high-performance second-generation superconducting wires and for his contribution to the Institute of Physics as a member of an editorial board. Parans served as the technical editor for the Applied Superconductivity Conference's 2004 Materials Section. He completed his assignment for two coated-conductor sessions and submitted the accepted papers to the IEEE transactions. The papers were published in a three-volume set of the June 2005 issue of the *IEEE Transactions on Applied Superconductivity*. Parans also gave a short course, "Superconducting Materials Development—Current Status and Future Directions: YBCO Coated Conductors," at the Applied Superconductivity Conference (ASC) 2004, Jacksonville, Florida, October 3, 2004. Parans also served as editor for the recently published *High-Temperature Superconductor Materials, Devices, and Applications, Ceramic Transactions*, Vol. 160, which is a part of the 13-volume *Proceedings of the 106th Annual Meeting of the American Ceramic Society*, held in Indianapolis, Indiana, in the fall of 2004.

4.3 Joint US-Japan Workshop on AC Losses

ORNL hosted a group of researchers from the United States and Japan in October 2004 for a workshop on AC Losses in High-Temperature Superconductors (Fig. 4.3). The purpose of the workshop was to exchange experimental and theoretical modeling results achieved in the past year.

Fig. 4.3 Attendees to US-Japan Workshop on AC Losses. Front row (l–r): O. Tsukamoto (Yakohama National University), Y. Yamada (SRL-ISTEC), N. Chikumoto (SRL-ISTEC), T. Machi (SRL-ISTEC), M. Iwakuma (Kyushu University), A. Gurevich (University of Wisconsin), M. Suenaga (BNL), T. Kisu (Kyushu University). Second row (l–r): M. Inoue (Kyushu University), M. Gouge (ORNL), F. List (ORNL), A. Contractor (Ohio State), N. Amemiya (Yokohama University), F. Kazuo (Kyushu University), D. Christen (ORNL), P. Martin (ORNL), P. Barnes (AFRL), M. Paranthaman (ORNL), D. Lee (ORNL), T. Izumi (SRL-ISTEC), A. Goyal (ORNL), Y. Zie (SuperPower), Y. Shiohara (SRL-ISTEC). Back row (l–r): R. Hawsey (ORNL), M. Sumption (Ohio State), A. Ijaduola (ORNL), J. Thompson (ORNL), C. Rey (ORNL), S. Ashworth (LANL), T. Watanabe (SRL-ISTEC), and R. Duckworth (ORNL).

4.4 International Energy Agency Committee on Superconductivity

ORNL hosted the annual meeting of the Committee on Superconductivity of the International Energy Agency, October 11–3, at the River Terrace Resort and Convention Center in Gatlinburg (Fig. 4.4). Day two of their meeting included a tour of HTS facilities at ORNL.

Fig. 4.4 Front row (l–r): O. Tsukamoto (Japan), J. F. Daley (United States), P. Komarek (Germany), R. Flukiger (Switzerland), and M. Hoshino (IEA-Paris). Middle row (l–r): A. Goyal (ORNL), Y. Morishita (Japan), Y. Milstein (Israel), L. Martini (Italy), and A. Sjodin (Sweden). Back row (l–r): D. Rose (UK), A. Wolsky (ANL), D. Lindsay (Ultera-Southwire), G. Deutscher (Israel), R. A. Hawsey (ORNL), and M. J. Gouge (ORNL).

4.5 Three New CRADAs Signed During Quarter

Three new CRADAs were signed during the last quarter of 2005:

- American Superconductor for "Low-Cost Fabrication of 2G Wire for AC Applications,"
- Reliance Electric Company for "HTS Motor Coil Quench Model," and
- Metal Oxide Technologies for "Development of High Temperature Superconductors" (Fig. 4.5).

Fig. 4.5. CRADA partner Metal Oxide Technologies, Inc. (Houston, Texas) visited ORNL's Metals and Ceramics Division to evaluate using a unique rolling mill facility for preparation of RABiTS™ templates. The rolling facility is unique among the national labs and is critical to the preparation of roll-textured and annealed nickel alloy templates for second-generation superconducting wires. As a result of this visit MetOx decided to proceed with plans to use the ORNL mill in 2005 as part of a CRADA funded by the Office of Electric Transmission and Distribution.

4.6 Summer Interns in Superconductivity Program

The ORNL Superconductivity Program hosted seven summer interns in FY 2005 (see Table 4.1 and Figs. 4.6–4.11).

Table 4.1. 2005 Summer Intern Program information

Name	Institution	DOE Program	ORNL Mentor
Jennifer Carney	University of Tennessee	Science Undergraduate Laboratory Internships (SULI)	Robert Duckworth
Namita Bisaria	Princeton University	SULI	Parans Paranthaman
Kartik Venkataraman	University of Wisconsin-Madison	Visiting researcher	Parans Paranthaman
Brandon Killian	North Carolina A&T University	Faculty and Student Teams (FaST)	David Christen Albert Gapud
Bethany Spencer	North Carolina A&T University	FaST	David Christen Tolga Aytug
David Gettman	California State University	Pre-service Teachers (PST)	Amit Goyal
Mehmet Ertugrul	Ataturk University (Turkey)	Higher Education Research Experiences (HERE) at ORNL	David Christen

Fig. 4.6. Namita Bisaria, Princeton University.

Fig. 4.7. Kartik Venkataraman, University of Wisconsin-Madison.

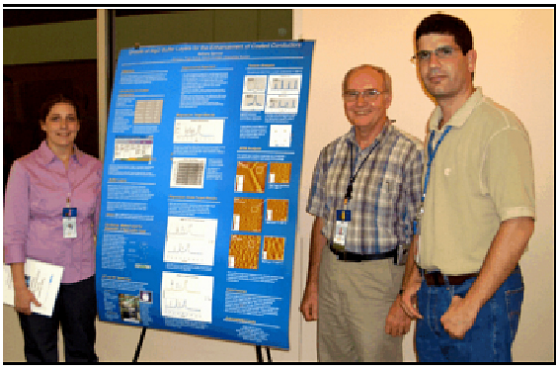

Fig. 4.8 Bethany Musgrave (North Carolina A&T University) with Dave Christen and Tolga Aytug.

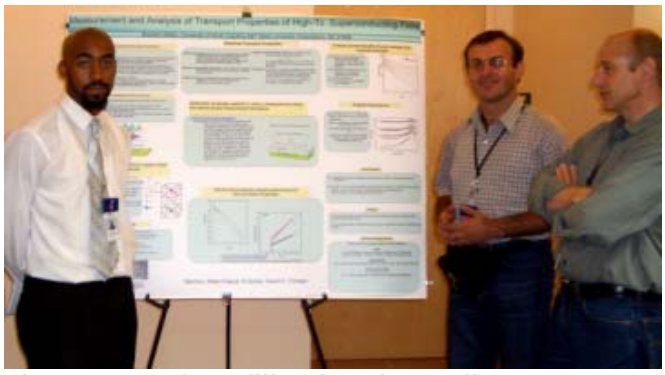

Fig. 4.9. Brandon Killian (North Carolina A&T University) with Mehmet Ertugrul (Ataturk University) and Ron Feenstra.

Fig. 4.10. David Gettman, California State University.

Fig. 4.11. Jennifer Carney, University of Tennessee, with Mike Gouge and Robert Duckworth.

4.7 Goyal Receives "Outstanding Young Tennessean (OYT)" Award

Amit Goyal, team leader in the ORNL superconductivity program and a member of the Metals and Ceramics Division's Functional Materials Group received the Outstanding Young Tennessean Award on September 25, 2004, from the Tennessee Junior Chamber of Commerce. The award recognizes people who have risen to the top of their chosen fields and who now act as role models for America's youth. In the field of sports, NBA player Shane Battier of the Memphis Grizzlies received the OYT award this year. Past recipients of the OYT award include former U.S. Vice President Al Gore, present Congressman Harold Ford, from Memphis, present Congressman Zack Wamp, from Oak Ridge, the late Elvis Presley, and many more. The awards were presented at a special ceremony in Nashville in conjunction with the annual meeting of the Tennessee Junior Chamber of Commerce.

4.8 ORNL Scientists Co-organized and Led the 2005 DOE Superconducting Wire Development Workshop

Parans Paranthaman, Dominic Lee, and Mike Gouge from the ORNL Superconductivity Program were part of the seven-member workshop organizing committee. The DOE Wire Development Workshop was held in St. Petersburg, Florida, during January 19 and 20, 2005, and was sponsored by the Office of Electric Transmission and Distribution (OETD). It was a very successful workshop. All the presentations are now available on-line: http://www.energetics.com/wire05.html.

5. FY 2005 Presentations/Publications

Published

Aytug, T., M. Paranthaman, H. Y. Zhai, A. A. Gapud, K. J. Leonard, P. M. Martin, A. Goyal, J. R. Thompson, and D. K. Christen, "An Approach for Electrical Self-Stabilization of High-Temperature Superconducting Wires for Power Application," *Appl. Phys. Lett.* **85** (14) 2887–89 (October 2004).

Aytug, T., M. Paranthaman, H. Y. Zhai, K. J. Leonard, A. A. Gapud, J. R. Thompson, P. M. Martin, A. Goyal, and D. K. Christen, "Iridium: An Oxygen Diffusion Barrier and a Conductive Seed Layer for RABiTS-Based Coated Conductors," *IEEE Transactions on Applied Superconductivity* **15** (2), 2977–80 (June 2005).

Bhuiyan, M. S., M. Paranthaman, S. Kang, D. F. Lee, and K. Salama, "Growth of Epitaxial Y_2O_3 Buffer Layers on Biaxially Textured Ni-W Substrates for YBCO Coated Conductors by MOD Approach," *Physica C* **422**, 95–101 (June 2005).

Bhuiyan, M. S., M. Paranthaman, S. Sathyamurthy, A. Goyal, and K. Salama, "Growth of Rare-Earth Niobate-Based Pyrochlores on Textured Ni-W Substrates with Ionic Radii Dependency," *J. Mater. Res.* **20** (4), 904–909 (April 2005).

Bhuiyan, M. S., M. Paranthaman, D. Beach, L. Heatherly, A. Goyal, E. A. Payzant, and K. Salama, "Epitaxial Growth of Eu_3NbO_7 Buffer Layers on Biaxially Textured Ni-W Substrates," *Ceramic Transactions, High Temperature Superconductor Materials, Devices, and Applications*, ed. M. Paranthaman et al., **160**, 35–41 (2004).

Cantoni, C., D. K. Christen, E. D. Specht, M. Varela, J. R. Thompson, A. Goyal, and S. J. Pennycook, "Buffer Layers for Development of High-J_c Cu-Based Coated Conductors," p. 81 in *Applied Superconductivity 2003*, Vol. 181, ed. A. Andreone, G. P. Pepe, R. Cristiano, and G. Masullo, Institute of Physics, Dirac House, Temple Back, Bristol BS1 6BE, United Kingdom (December 2004). Invited.

Cantoni, C., A. Goyal, U. Schoop, X. Li, M. W. Rupich, C. Thieme, A. A. Gapud, T. Aytug, M. Paranthaman, K. Kim, J. D. Budai, and D. K. Christen, "Investigation of TiN Seed Layers for RABiTS Architectures with a Single-Crystal-Like Out-of-Plane Texture," *IEEE Transactions on Applied Superconductivity* **15** (2), 2981–84 (June 2005).

Cantoni, C., D. T. Verebelyi, E. D. Specht, J. Budai, and D. K. Christen, "Anisotropic Nonmonotonic Behavior of the Superconducting Critical Current in Thin $YBa_2Cu_3O_{7-\delta}$ Films on Vicinal $SrTiO_3$ Surfaces," *Phys. Rev. B* **71**, 054509 (February 2005).

Christen, H. M., D. F. Lee, F. A. List, S. W. Cook, K. J. Leonard, L. Heatherly, P. M. Martin, M. Paranthaman, A. Goyal, and C. M. Rouleau, "Pulsed Electron Deposition of Fluorine-Based Precursors for $YBa_2Cu_3O_{7-x}$-Coated Conductors," *Supercond. Sci. Technol.* **18**, 1168–75 (September 2005).

Cook, L. P., W. Wong-Ng, and R. Feenstra, "$Ba(OH)_2$ Equilibria in the System Ba-O-H-F, with Application to the Formation of $Ba_2YCu_3O_{6.5+x}$ from BaF_2-Precursors," *J. Res. Natl. Inst. Stand. Technol.* **110** (2), 115–26 (March–April 2005).

Demko, J. A., J. W. Lue, R. C. Duckworth, M. A. Young, M. J. Gouge, D. Lindsay, J. Tolbert, M. Roden, D. Willen, and C. Traeholt, "Testing of a 1.5 m Single Phase Short Sample Cable Made with Copper Laminated HTS Tapes at ORNL," *IEEE Transactions on Applied Superconductivity* **15** (2), 1755–51 (June 2005).

Duckworth, R. C., M. J. Gouge, J. Caughman, J. W. Lue, J. A. Demko, J. Tolbert, C. L. H. Thieme, and D. T. Verebelyi, "On the Effect of NiW on the Inductance and AC Loss of HTS Cables," *IEEE Transactions on Applied Superconductivity* **15** (2), 1578–82 (June 2005).

Duckworth, R. C., M. J. Gouge, J. W. Lue, C. Thieme, and D. T. Verebelyi, "Substrate and Stabilization Effects on the Transport AC Losses in YBCO Coated Conductors," *IEEE Transactions on Applied Superconductivity* **15** (2), 1583–86 (June 2005).

Feenstra, R., A. A. Gapud, F. A. List, E. D. Specht, D. K. Christen, T. G. Holesinger, and D. M. Feldmann, "Critical Currents I_c (77 K) > 350 A/cm-Width Achieved in ex situ YBCO Coated Conductors Using a Faster Conversion Process," *IEEE Trans. Appl. Supercond.* **15** (2) 2803 (June 2005).

Feldmann, D. M., D. C. Larbalestier, T. Holesinger, R. Feenstra, A. A. Gapud, and E. D. Specht, "Evidence for Extensive Grain Boundary Meander and Overgrowth of Substrate Grain Boundaries in High Critical Current Density ex situ $YBa_2Cu_3O_{7-x}$ Coated Conductors," *J. Mater. Res.* **20** (8), 2012–20 (August 2005).

Gapud, A. A., D. Kumar, S. K. Viswanathan, C. Cantoni, M. Varela, J. Abiade, S. J. Pennycook, and D. K. Christen, "Enhancement of Flux Pinning in $YBa_2Cu_3O_{7-\delta}$ Thin Films Embedded with Epitaxially Grown Y_2O_3 Nanostructures using a Multi-Layering Process," *Supercond. Sci. Technol*. **18**, 1502–1505 (October 2005).

Gapud, A. A., R. Feenstra, D. K. Christen, J. R. Thompson, and T. G. Holesinger, "Temperature and Magnetic Field Dependence of Critical Currents in YBCO Coated Conductors with Processing-Induced Variations in Pinning Properties," *IEEE Transactions on Applied Superconductivity* **15** (2), 2578–81 (June 2005).

Gonzalez, J. C., N. Mestres, T. Puig, J. Gazquez, F. Sandiumenge, X. Obradors, A. Usoskin, Ch. Jooss, H. C. Freyhardt, and R. Feenstra, "Biaxial Texture Analysis of $YBa_2Cu_3O_7$ Coated Conductors by Micro-Raman Spectroscopy," *Phys. Rev. B* **70** (9), 094525 (September 2004).

Gouge, M. J., D. T. Lindsay, J. A. Demko, R. C. Duckworth, A. R. Ellis, P. W. Fisher, D. R. James, J. W. Lue, M. L. Roden, I. Sauers, J. C. Tolbert, C. Traeholt, and D. Willen, "Tests of Tri-Axial HTS Cables," *IEEE Transactions on Applied Superconductivity* **15** (2) 1827–30 (June 2005).

Goyal, A., S. Kang, K. J. Leonard, P. M. Martin, A. A. Gapud, M. Varela, M. Paranthaman, A. E. Ijaduola, E. D. Specht, J. R. Thompson, D. K. Christen, S. J. Pennycook, and F. A. List, "Irradiation-Free, Columnar Defects Comprised of Self-Assembled Nanodots and Nanorods Resulting in Strongly Enhanced Flux-Pinning in $YBa_2Cu_3O_{7-\delta}$ Films," *Supercond. Sci. Technol.* **18**, 1533–38 (October 2005).

Grabovickic, R., D. R. James, I. Sauers, A. R. Ellis, P. C. Irwin, K. Weeber, L. Li, and A. D. Gadre, "Measurements of Temperature Dependence of Partial Discharge in Air Gaps between Insulated Bi-Sr-Ca-Cu-O Tapes," *IEEE Transactions on Applied Superconductivity* **15** (2), 3668–71 (June 2005).

Grabovickic, R., D. R. James, I. Sauers, and A. R. Ellis (ORNL); P. C. Irwin, K. Weeber, L. Li, and A. D. Gadre (GE), "Partial Discharge and Accelerated Pulsed Aging of Insulation between Parallel Plane-Plane Stainless Steel Electrodes and between Bi-Sr-Ca-Cu-O Tapes at Room Temperature," pp. 286–89 in *Proc. of the 2004 Conference on Electrical Insulation and Dielectric Phenomena* (2004).

Haugan, T. J., P. N. Barnes, T. A. Campbell, A. Goyal, A. Gapud, L. Heatherly, and S. Kang, "Deposition of $(Y_2BaCuO_5/YBa_2Cu_3O_{7-x})xN$ Multilayer Films on Ni-Based Textured Substrates," *Physica C* **425** (1–2) 21–26 (September 2005).

Holesinger, T. G., P. N. Arendt, R. Feenstra, A. A. Gapud, E. D. Specht, D. M. Feldmann, and D. C. Larbalestier, "Liquid Medicated Growth and the Bi-Modal Microstructure of $YBa_2Cu_3O_{7-}$ Films made by the ex situ Conversion of Physical Vapor Deposited BaF_2 Precursors," *J. Mater. Res.* **20** (5), 1216–33 (May 2005).

Kim, K., D. P. Norton, C. Cantoni, T. Aytug, A. A. Gapud, M. P. Paranthaman, A. Goyal, and D. K. Christen, "(La, Sr) TiO_3 as a Conductive Buffer for High-Temperature Superconducting Coated Conductors," *IEEE Trans. Appl. Supercond.* **15** (2) 2997 (June 2005).

Lee, D. F., F. A. List, R. Feenstra, H. M. Christen, L. Heatherly, K. J. Leonard, A. Goyal, and M. Paranthaman, "Ex situ Conversion of PVD Precursors: A Strategic Component of RABiTS CC R&D," extended abstract published in *Proc. International Workshop on Coated Conductors for Applications*, November 19–20, 2004, Kanagawa, Japan.

Leonard, K. J., S. Sathyamurthy, and M. Paranthaman, "Characterization of $BaZrO_3$ Nanoparticles Prepared by Reverse Micelle Synthesis," *Chem. Mater*. **17 (**15), 4010–17 (July 2005).

List, F. A., P. G. Clem, L. Heatherly, J. T. Dawley, K. J. Leonard, D. F. Lee, and A. Goyal, "Low-Pressure Conversion Studies for YBCO Precursors Derived by PVD and MOD Methods," *IEEE Transactions on Applied Superconductivity* **15** (2), 2656–58 (June 2005).

List, F. A., L. Heatherly, D. F. Lee, K. J. Leonard, and A. Goyal, "Oxidation of Carbon on Nickel-Based Metallic Substrates: Implications for High-Temperature Superconductor Coated Conductors, *J. Mater. Res.* ***20***, No. 3, 765-773 (March 2005).

Lu, Zigui, and J. Zhu (Tenn. Tech. Univ); E. A. Payzant and M. P. Paranthaman (ORNL), "Electrical Conductivity of the Manganese Chromite Spinel Solid Solution," *J. Am. Ceram. Soc.* **88** (4), 1050–53 (April 2005).

Lue, J. W., R. C. Duckworth, and M. J. Gouge, "Over-Current Testing of HTS Tapes," *IEEE Transactions on Applied Superconductivity* **15** (2), 1835–38 (June 2005).

McConnell, B. W., "Applications of High Temperature Superconductors to Direct Current Electric Power Transmission and Distribution," *IEEE Transactions on Applied Superconductivity* **15** (2), 2142–45 (June 2005).

Palau, A., T. Puig, X. Obradors, R. Feenstra, and H. C. Freyhardt, "Effect of Strain on Grain and Grain-Boundary Critical Currents of YBCO Coated Conductors," *IEEE Trans. Appl. Supercond.* **15** (2), 2790 (June 2005).

Paranthaman, M. P., T. Aytug, H. Y. Zhai, L. Heatherly, A. Goyal, and D. K. Christen, "Growth of YBCO Films on MgO-Based Rolling-Assisted Biaxially Textured Substrates Templates," *Supercond. Sci. Technol*. **18** (3) , 223–28 (March 2005).

Paranthaman, M. P., S. Sathyamurthy, M. S. Bhuiyan, A. Goyal, T. Kodenkandath, X. Li, W. Zhang, C. L. H. Thieme, U. Schoop, D. T. Verebelyi, and M. W. Rupich, "Improved YBCO Coated Conductors using Alternate Buffer Architectures," *IEEE Transactions on Applied Superconductivity* **15** (2), 2632–34 (June 2005).

Paranthaman, M. P., T. Aytug, H. Y. Zhai, L. Heatherly, A. Goyal, and D. K. Christen, "Growth of YBCO Films on MgO-Based Rolling-Assisted Biaxially Textured Substrate Templates," *Supercond. Sci. Technol.* **18**, 223–28 (2005).

Paranthaman, M., M. S. Bhuiyan, S. Sathyamurthy, H. Y. Zhai, and A. Goyal (ORNL); K. Salama (University of Houston), "Epitaxial Growth of Solution-Based Rare-Earth Niobate, RE_3NbO_7, Films on Biaxially Textured Ni-W Substrates," *J. Mater. Res.* **20** (10), 6–9 (January 2005).

Sathyamurthy, S., M. Paranthaman, M. S. Bhuiyan, E. A. Payzant, D. F. Lee, and A. Goyal, "Solution Deposition Approach to High J_c Coated Conductor Fabrication," *IEEE Transactions on Applied Superconductivity* **15** (2), 2974–76 (June 2005).

Sathyamurthy, S., K. J. Leonard, R. T. Debestani, and M. P. Paranthaman, "Reverse Micellar Synthesis of Cerium Oxide Nanoparticles," *Nanotechnology* **16** (9), 1960–64 (September 2005).

Schoop, U., M. W. Rupich, C. Thieme, D. T. Verebelyi, W. Zhang, X. Li, T. Kodenkandath, N. Nguyen, E. Siegal, L. Civale, T. Holesinger, B. Maiorov, A. Goyal, and M. Paranthaman, "Second Generation HTS Wire Based on RABiTS Substrates and MOD YBCO," *IEEE Transactions on Applied Superconductivity*, **15** (2), 2611–16 (June 2005).

Shu, Q. S., G. F. Cheng, J. Susta, D. Li, J. R. Hull, J. A. Demko, C. P. Britcher, J. E. Fesmire, S. D. Augustnowicz, F. Werfel, and E. C. Bonnema, "A Six-Meter-Long Prototype of the Mag-Lev Cryogen Transfer Line," *IEEE Transactions on Applied Superconductivity (*15), **2**, 2297–300 (June 2005).

Thompson, J. R., K. D. Sorge, C. Cantoni, H. R. Kerchner, D. K. Christen, and M. P. Paranthaman, "Vortex Pinning and Slow Creep in High-J_c MgB_2 Thin Films: A Magnetic and Transport Study," *Supercond. Sci. Technol.* **18**, 970–76 (June 2005).

Venkataraman, K., E. E. Hellstrom, and M. Paranthaman, "Growth of Lanthanum Manganate Buffer Layers for Coated Conductors via a Metal-Organic Decomposition Process," *IEEE Transactions on Applied Superconductivity*, **15** (2), 3005–3008 (June 2005).

Weber, C. S., C. T. Reis, D. W. Hazelton, S. W. Schwenterly, M. J. Cole, J. A. Demko, E. F. Pleva, S. Mehta, T. Golner, and N. Aversa, "Design and Operational Testing of a 5/10-MVA HTS Utility Power Transformer," *IEEE Transactions on Applied Superconductivity*, **15** (2), 2210–13 (June 2005).

Xu, Y., A. Goyal, K. Leonard, and P. Martin, "High Performance YBCO Films by the Hybrid of Non-Fluorine Yttrium and Copper Salts with Ba-TFA," *Physica C* 421, 67–72 (2005).

Wong-Ng, W., I. Levin, R. Feenstra, L. P. Cook, and M. Vaudin, "Phase Evolution of $Ba_2YCu_3O_{6+x}$ Films During the BaF_2 Process," *Supercond. Sci. Technol*. **17** S548–56 (September 2004).

Wong-Ng, W., L. P. Cook, J. Suh, I. Levin, and R. Feenstra, "Melting Investigation of the System BaF_2-BaO-$1/2Y_2O_3$-H_2O," *Supercond. Sci. Technol.* **18**, 442–53 (2005).

Wong-Ng, W., L. P. Cook, I. Levin, M. Vaudin, J. Suh, and R. Feenstra, "Coated Conductors: Phase Relations in the Ba-Y-Cu-F-O-H System," p. EE2.9.1 in *Frontiers in Superconducting Materials–New Materials and Applications Symposium*, Vol. EXS-3, ed. V. Matias, J. Talvacchio, X. Xi, Z. Han, and H. W. Neumuller, Materials Research Society, Warrendale, Pennsylvania (2004).

Wong-Ng, W., L. P. Cook, I. Levin, J. Suh, R. Feenstra, T. Haugan, and P. Barnes, "Phase Equilibria of Ba-R-Cu-O for Coated Conductor Applications (R= Lanthanides and Y)," *Physica C* 408–10, 20–22 (August 2004).

Xu, Y., A. Goyal, K. Leonard, L. Heatherly, and P. Martin, "Liquid Phase Enhanced Hybrid MOD Approach for High Performance YBCO Films Development," *IEEE Transactions on Applied Superconductivity*, **15** (2), 2617–19 (June 2005).

Yethiraj, M., D. K. Christen, A. A. Gapud, D. M. Paul, S. J. Crowe, C. D. Dewhurst, R. Cubitt, L. Porcar, and A. Gurevich, "Temperature and Field Dependence of the Flux-Line Lattice Symmetry in V_3Si," *Phys. Rev.* ***B*** **72** (6), 060504 (August 2005).

Yoo, J., K. J. Leonard, H. S. Hsu, L. Heatherly, F. A. List, D. F. Lee, A. A. Gapud, P. M. Martin, S. Cook, M. Paranthaman, A. Goyal, and D. M. Kroeger, "The Growth of YBCO Films with High Critical Current at Reduced Pressures using the BaF_2 ex situ Process," *Supercond. Sci. Technol.* **17** (10) 1209–14 (October 2004).

Young, M. A., M. J. Gouge, M. O. Pace, J. A. Demko, R. C. Duckworth, J. W. Lue, and A. Fathy, "An Investigation of the Current Distribution in The Triaxial Cable and Its Operational Impacts on a Power System," *IEEE Transactions on Applied Superconductivity*, **15** (2), 1751–54 (June 2005).

Zhai, H.-Y., H. M. Christen, R. Feenstra, F. A. List, A. Goyal, K. J. Leonard, Y. Xu, D. K. Christen, K. Venkataraman, and V. A. Maroni, "Pulsed Electron Deposition for Coated Conductor Applications," p. EE1.8.1 in *Frontiers in Superconducting Materials–New Materials and Applications Symposium*, **EXS-3**, ed. V. Matias, J. Talvacchio, X. Xi, Z. Han, and H. W. Neumuller, Materials Research Society, Warrendale, Pennsylvania (2004).

Zhang, Y., R. Feenstra, J. R. Thompson, A. A. Gapud, T. Aytug, and D. K. Christen, "High Critical Current Density $YBa_2Cu_3O_{7-}$ Thin Film Growth by Post-Deposition Processing at Low Pressures," p. EE5.11.1 in *Frontiers in Superconducting Materials—New Materials and Applications Symposium*, **EXS-3**, ed. V. Matias, J. Talvacchio, X. Xi, Z. Han, and H. W. Neumuller, Materials Research Society, Warrendale, Pennsylvania (2004).

Zhang, Y., R. Feenstra, and D. K. Christen, "X-Ray Photoelectron Spectroscopy Study on E-beam Co-Evaporated YBCO Precursors and their Post-Deposition Conversion," p. C7.9 in *Recent Advances in Superconductivity—Materials Synthesis, Multiscale Characterization, and Functionally Layered Composite Conductors*, **868E**, ed. T. Holesinger, T. Izumi, J. L. MacManus-Driscoll, D. Miller, W. Wong-Ng, Materials Research Society, Warrendale, Pennsylvania (2005).

Zhang, Y., M. P. Paranthaman, R. Feenstra, T. Aytug, and D. K. Christen, "Comparison of $YBa_2Cu_3O_{7-\delta}$ Precursors Made using TFA-MOD and BaF_2 Ex-Situ Processes and Their Post-Deposition Processing Under Low Pressure Conditions," *IEEE Transactions on Applied Superconductivity*, **15** (2) 2659–62 (June 2005).

Submitted

Aytug, T., M. Paranthaman, K. J. Leonard, H. Y. Zhai, M. S. Bhuiyan, E. A. Payzant, A. Goyal, S. Sathyamurthy, D. B. Beach, P. M. Martin, and D. K. Christen (ORNL); X. Li, T. Kodenkandath, U. Schoop, and M. W. Rupich (AMSC); and H. E. Smith (AFRL), "Assessment of Chemical Solution Synthesis and Properties of $Gd_2Zr_2O_7$ Thin Films as Buffer Layers for Second Generation High-Temperature Superconductor Wires," submitted to *J. Mater. Res.*

Aytug, T., M. Paranthaman, A. A. Gapud, S. Kang, H. M. Christen, K. J. Leonard, P. M. Martin, J. R. Thompson, and D. K. Christen (ORNL); R. Meng, I. Rusakova, and C. W. Chu (University of Houston), "Enhancement of Flux Pinning and Critical Currents in $YBa_2Cu_3O_{7-\delta}$ Films by Nanoscale Iridium Pretreatment of Substrate Surfaces," submitted to *J. Appl. Physics*.

Lee, D. F., H. M. Christen, F. A. List, L. Heatherly, K. J. Leonard, C. M. Rouleau, S. W. Cook, P. M. Martin, M. Paranthaman, and A. Goyal, "R&D of RABiTS-Based Coated Conductors: Conversion of ex-situ YBCO Superconductor using a Novel Pulsed Electron-Beam Deposited Precursor," submitted to *Physica C*.

Leonard, K. J., S. Sathyamurthy, and M. Paranthaman, "Characterization of $BaZrO_3$ Nanoparticles Prepared by Reverse Micelle Synthesis," *Mater. Science and Engineering B.*

Sathyamurthy, S., M. Paranthaman, L. Heatherly, P. M. Martin, E. D. Specht, and A. Goyal (ORNL); T. Kodenkandath, Xiaoping Li, and M. Rupich (AMSC), "Solution Processed Lanthanum Zirconium Oxide as a Barrier Layer for High I_c Coated Conductors," submitted to *J. Mater. Res.*

Presentations

Christen, H. M., M. Varela, C. Cantoni, D. H. Kim, M. F. Chisholm, H. N. Lee, D. P. Norton, and D. H. Lowndes, "Electronic Configuration at $LaMnO_3/SrTiO_3$ Interfaces and in Related Heterostructures" 2005 Fall Materials Research Society Meeting, Boston, Massachusetts (November 28–December 2, 2005).

Feenstra, R., A. A. Gapud, E. D. Specht, Y. Zhang, D. K. Christen, T. G. Holesinger, D. M. Feldmann, X. Song, D. C. Larbalestier, A. Palau, T. Puig, and X. Obradors, "Growth and Structure Effects in ex-situ YBCO Films," The 12th US-Japan Workshop, Delavan, Wisconsin (October 10–12, 2005).

Demko, J. A., R. C. Duckworth, P. W. Fisher, M. J. Gouge, C. M. Rey, M. A. Young, D. Lindsay, M. Roden, J. Tolbert, D. Willen, C. Traeholt, "Testing of a Liquid Nitrogen Cooled 5-meter, 3000 Tri-Axial High Temperature Superconducting Cable System," abstract submitted to CEC-ICMC 2005.

Feenstra, R., A. A. Gapud, E. D. Specht, Y. Zhang, and D. K. Christen (ORNL); T. G. Holesinger (LANL); D. M. Feldmann, X. Song, and D. C. Larbalestier (Uwi); and A. Palau, T. Puig, and X. Obradors (Institut de Ciencia de Materials de Barcelona), "Improving the Thickness Dependence of J_c in BaF_2 ex situ YBCO Coated Conductors," The International Workshop on Coated Conductors for Applications CCA2005, Santa Fe, N.M. (December 4–7, 2005).

Goyal, A., "Nature of Grain Boundaries, Long-Range Current Flow, and Significant Enhancement in Flux-Pinning for YBCO Films on RABiTS," 17th International Symposium on Superconductivity (ISS2004), Nigata, Japan (November 23–26, 2004).

Goyal, A., "Epitaxial Growth of High Performance Superconducting Wires on Rolling-Assisted Biaxially-Textured Substrates (RABiTS)," 2005 TMS Annual Meeting & Exhibition (Feb. 14–17).

Goyal, A., F. A. List, C. Cantoni, T. Aytug, S. Sathyamurthy, L. Heatherly, A. Ijadoula, J. R. Thompson, K. J. Leonard, M. Paranthaman, D. F. Lee, S. Kang, J. Yoo, and D. K. Christen, "Recent Progress in the Fabrication of RABiTS," CCA2004 International Workshop on Coated Conductors for Applications, Kanagawa, Japan (November 18–21, 2004).

Goyal, A., S. Kang, K. J. Leonard, M. Varela, A. Gapud, A. Ijadoula, J. R. Thompson, M. Paranthaman, D. F. Lee, F. A. List, and D. K. Christen, "Enhanced Flux-pinning in YBCO on RABiTS," CCA2004 International Workshop on Coated Conductors for Applications, Kanagawa, Japan (November 18–21, 2004).

Hawsey, R. A., "Status of Coated Conductor Research and Development," The International Workshop on Coated Conductors for Applications (CCA2005), Santa Fe, NM (December 4–7, 2005).

Lee, D. F., F. A. List, R. Feenstra, H. M. Christen, L. Heatherly, K. J. Leonard, A. Goyal, and M. P. Paranthaman, "Ex-Situ Conversion of Physical Vapor Deposited YBCO Precursors on RABiTS," CCA2004 International Workshop on Coated Conductors for Applications, Kanagawa, Japan (November 18–21, 2004).

Schwenterly, S. W., and R. C. Duckworth (ORNL); D. W. Hazelton (SuperPower); and F. Breuer (Nexans), "Thermal Property Measurements on Bulk Bi-2212 MCP Materials,"abstract submitted to CEC-ICMC (2005).

INTERNAL DISTRIBUTION

1. D. B. Beach
2. C. A. Blue
3. P. F. Britt
4. M. V. Buchanan
5. D. K. Christen
6. J. F. Cooke
7. F. V. Damiano
8. E. C. Fox
9. M. J. Gouge
10. A. Goyal
11. G. R. Gruzalski
12. R. A. Hawsey
13. L. L. Horton
14. J. Johnson, OTIC
15. W. Koncinski
16-25. D. F. Lee
26. S. L. Milora
27. M. Paranthaman
28. M. Reeves
29. S. J. Zinkle

EXTERNAL DISTRIBUTION

30. N. Aversa, Consultant, Waukesha Electric Systems, 400 S. Prairie Ave., Waukesha, WI 53186-5937
31. J. Badin, Energetics Inc., 7164 Gateway Dr., Columbia MD 21046
32. P. N. Barnes, Air Force Research Laboratory, AFRL/PRPG, 2645 Fifth Street, WPAFB, OH 45433-7919
33. R. Bhattacharya, National Renewable Energy Laboratory, 1617 Cole Blvd., Golden, CO 80401
34. J. W. Bray, Physicist/Program Manager, General Electric Corporate Research and Development, P.O. Box 8, Schenectady, NY 12301
35. S. W. Butler, Texas Center for Superconductivity at the University of Houston, Houston Science Center 206, Houston TX 77204-5002
36. L. Castellani, Metal Oxide Technologies Inc., 8807 Emmott Rd., Suite 100, Houston, TX 77040
37. H. S. Chhabra,OE-2, U.S. Department of Energy, 6H-034/FORS, 1000 Independence Ave., S.W., Washington, DC 20585
38. P. G. Clem, Sandia National Laboratories, MS 1411, P.O. Box 5800, Albuquerque, NM 87185-1405
39. G. Crabtree, Argonne National Laboratory, ET/212, 9700 South Cass Ave., Argonne, IL 60439-4838
40. S. J. Dale, Florida Adv Power Lab, Florida State University, 2000 Levy Ave., Bldg. A, Tallahassee, FL 32310
41. J. G. Daley, OE-2, U.S. Department of Energy, 6H-034/FORS, 1000 Independence Ave., S.W., Washington, DC 20585
42. J. Ekin, National Institute of Standards and Technology, 325 Broadway, Boulder, CO 80303
43. S. Fleshler, American Superconductor Corporation, Two Technology Dr., Westborough MA 01581
44. H. Harshavardhan, Neocera, 10000 Virginia Manor Rd., Beltsville, MD 20705
45. D. Haught, EE-2D, U.S. Department of Energy, 1000 Independence Ave., S.W., Washington, DC 20585
46. P. F. Herz, Technology & Management Services Inc., 18757 North Frederick Road, Gaithersburg MD 20879

47. X. Huang, General Electric Corporate Research and Development, EP-113, P. O. Box 8, Schenectady, NY 12301
48. K. Kolevar, OE-1, U.S. Department of Energy, 1000 Independence Ave., S.W., Washington, DC 20085
49. V. Kruse, Southwire Company, P. O. Box 1000, Carrollton, GA 30119
50. D. C. Larbalestier, University of Wisconsin–Madison, Applied Superconductivity Center, 1500 Engineering Drive, Madison, WI 53706-1687
51. W. C. Lin, U.S. Department of Energy, Office of Assistant Manager for Energy Research and Development, Oak Ridge Field Office, P.O. Box 2008, Oak Ridge, TN 37831-6269
52. D. Lindsay, Ultera-Southwire Company, P. O. Box 1000, Carrollton, GA 30119
53. A. P. Malozemoff, American Superconductor Corporation, Two Technology Dr., Westborough MA 01581
54. K. R. Marken, Jr., Oxford Superconducting Technology, P.O. Box 429, Carteret, NJ 07008-0429
55. V. Maroni, Argonne National Laboratory, Chemical Technology, 9700 South Case Ave., Bldg. 205, Argonne IL 60439
56. S. P. Mehta, Waukesha Electric Systems, 400 S. Prairie Ave., Waukesha, WI 53186-5937
57. P. N. Overholt, OE-2, U.S. Department of Energy, 1000 Independence Avenue, S.W., Washington, DC 20585
58. S. M. Parker, Oxford Superconducting Technology, P.O. Box 429, Carteret, NJ 07008- 0429
59. W. P. Parks, Jr., OE-1, U.S. Department of Energy, 1000 Independence Avenue, S.W., Washington, DC 20585
60. P. Pellegrino, SuperPower, Inc., 450 Duane Avenue, Schenectady, NY 12305
61. D. E. Peterson, Los Alamos National Laboratory, Superconductivity Technology Center, P.O. Box 1663, MS K763, Los Alamos, NM 87545
62. E. Pleva, Waukesha Electric Systems, 400 S. Prairie Ave., Waukesha, WI 53186-5937
63. M. W. Rupich, American Superconductor Corporation, Two Technology Drive, Westborough, MA 01581
64. R. F. Schiferl, Rockwell Automation Power Systems, 26391 Curtiss Wright Pkwy, Suite 102, Richmond Heights, OH 44143
65. V. Selvamanickam, SuperPower, Inc., 450 Duane Avenue, Schenectady, NY 12305
66. V. F. Solovyov, Brookhaven National Laboratory, Materials Science Dept., Bldg. 480, P. O. Box 5000, Upton, NY 11973-5000
67. H. Weinstock, Physics and Electronics, Air Force Office of Scientific Research, AFOSR/NE, 4015 Wilson Blvd., Room 713, Arlington VA22203-1954
68. W. Wong-Ng, National Institute of Standards and Technology, Ceramics Division, Building 223, A-256 Materials, Gaithersburg, MD 20899
69. G. Yurek, American Superconductor Corporation, Two Technology Drive, Westborough, MA 01581